Universitat Autònoma de Barcelona

Thin film based all-solid-state lithium-ion batteries and operando characterization methods

Valerie Siller

Thin film based all-solid-state lithium-ion batteries and operando characterization methods

Author

Valerie Siller

Catalan Institute of Energy Research

PhD thesis

Doctor of Philosophy in

Materials Science

Directors:

Albert Tarancón Rubio and Alejandro Morata

Catalan Institute of Energy Research

Tutor:

Gemma Garcia Alonso

Autonomous University of Barcelona

Barcelona November 2020

Baterías de litio de estado sólido en capa delgada y métodos de caracterización en operación

Autora

Valerie Siller

Institut de Recerca en Energia de Catalunya

Tesis doctoral

Programa de Doctorado en

Ciencia de Materiales

Directores:

Albert Tarancón Rubio y Alejandro Morata

Institut de Recerca en Energia de Catalunya

Tutora:

Gemma Garcia Alonso

Universitat Autònoma de Barcelona

Barcelona Noviembre 2020

Declaration

El Dr. Albert Tarancón Rubio y el Dr. Alejandro Morata, investigadores del Instituto de Investigación en Energía de Cataluña (IREC), CERTIFICAN:

Que la memoria titulada **Thin film based all-solid-state lithium-ion batteries and operando characterization methods** presentada por Valerie Siller para optar al grado de Doctor en el Programa de Cienca de Materiales de la Universitat Autònoma de Barcelona ha sido realizada bajo su dirección en el Institut de Recerca en Energia de Catalunya (IREC).

Barcelona, Noviembre de 2020

Dr. Albert Tarancón Rubio

Dr. Alejandro Morata

Acknowledgement

This thesis has seen great support and efforts in contribution of many different people and I hereby wish to express my dearest gratitude to everyone who accompanied this work. First of all, I would like to thank my supervisors and thesis directors Albert and Alex for giving me this great opportunity of professional and personal development, which was accompanied by the joy of entering a great, international team and the friendly atmosphere I have experienced.

This said, I would like to thank also all my colleagues which have accompanied me in the past years at IREC. Especially thank you to Aitor for being always by my side (literally) and the great help you always provided. Special thanks also to Marc & Marc, Lucile, Mercè, Iñigo, Nerea, Federico, Julien, Gotzon, Juan Carlos and Miguel for all your support. Further I would like to thank my fellow PhD students, especially Francesco, Simone and Arianna for their company and great help over all the years spent. Another great thank you to Marco, Yunqing, José, Juande, Maritta, Natalia, Carolina, Marina, Marie-Carmen, Cecilia, Elba, Gerard, Taisiia, Hemesh and Tammy for all your help, patience and good company. I would also like to thankfully acknowledge the contribution of Víctor Román to this work.

In addition, I would like to express a special thank you to Diouldé Sylla and Jordi Jacas for their great help and council over the past years, as well as to Rafael Trócoli for all the useful knowledge in the field of batteries he provided me with, Michel Stchakovsky for the fruitful collaboration, Collins Erinmwingbovo and Fabio La Mantia for their supportive and interesting contributions to our work, Marta Cazorla Soult and her colleagues from Imec for the good collaboration, Raul Arenal for the wonderful STEM results, Juan Miguel López del Amo for the interesting results on NMR, José Santiso and José Manuel Caicedo for your great interest and support in our work, and last, thank you for the interesting discussions I very much enjoyed with our collaborators Ainara Aguadero and Mónica Burriel.

I happily appreciate all the time spent in the past years and have it memorized forever as my first years in research and as well in Barcelona. I wish you all the best and I am looking forward for our paths to hopefully cross again in the future.

Vielen Dank an meine Familie,
für euer Verständnis und all die Unterstützung. Diese Arbeit ist in großen Teilen ebenso euer Verdienst und wäre ohne euch nicht möglich gewesen.
Ich danke euch von ganzem Herzen.

Gracias a Emanuel, Diego y Anna, Juanita, Maggie, Guillermina y Deborah por darme algunos de los momentos más felices de los últimos meses.
Gracias a Alicia, Marta, Simo, Eduardo, Franzi, Philipp y Hannes por siempre pensar en mi.

Abstract

This thesis aims to contribute to the development of all-solid-state batteries (ASSBs) on lithium-ion basis by the investigation of thin film materials fabricated by Pulsed Laser Deposition (PLD), holding opportunity of producing large-areas (up to 4 inch) covered by homogeneous thin layers. Thin films enable high surface-to-volume ratios and generate a unique material engineering, which is of great advantage for lower internal resistances, higher energy densities and good rate capability. Bottleneck for battery performance remains the solid-state electrolyte, which needs to be improved by tailoring mass transport and reducing interfacial degradation processes.

A suitable target of NASICON-like $Li_{1+x}Al_xTi_{2-x}(PO_4)_3$ (LATP) solid-electrolyte has been fabricated and first layer depositions in a large-area PLD have been optimized under variation of the background gas pressure. Thin film electrochemical performances have been evaluated accordingly, demonstrating good ionic conductivities ~ 10^{-6} S cm^{-1} as-deposited, comparable to conventional solid electrolytes (such as phosphorous oxynitrates) currently under application in thin film batteries. An additional heat treatment revealed an increase of two orders of magnitude in ionic conductivity and a significant drop in overall activation energies, providing values close to the bulk material with ~ 10^{-4} S cm^{-1} and 0.37 eV, respectively. All these features make the developed LATP thin films excellent candidates for their application as electroytes in ASSBs.

A new PLD approach for the deposition of spinel intercalation materials $LiMn_2O_4$ (LMO) and $Li_4Ti_5O_{12}$ (LTO) is further presented by multi-layer pulsed laser co-deposition with Li_2O addition. In the aim of compensating for typically appearing lithium losses during thin film fabrication, lithium concentration can be varied and different phases stabilized. Resulting layer thicknesses, microstructure and lithium content have a great impact on the electrochemical performance.

Summed to their direct application potential in thin film ASSB, the developed layers constitute interesting systems for the study of the fundamental properties of materials. Thin films provide high fabrication control and more direct access than bulk systems to some phenomena inducing interfacial resistances and material instabilities, which are calling for a deeper understanding upon device operation.

Seeking for non-destructive in-situ/operando techniques of low cost, facile use and realistic device operation conditions, Raman spectroscopy and Spectroscopic Ellipsometry (SE) are applied to the operando monitoring in the lithium storage. Raman spectroscopy is already well known in the field of in-situ probing for lithium-ion migration, but SE, although it is widely established for the optical analysis of thin films and complex multi-layer systems, it remains unexplored for the time-resolved analysis of battery performance. In this thesis, SE is used for probing lithium-ion movements in real-time for LMO and $LiMn_{1.5}Ni_{0.5}O_4$ (LMNO) thin films in ionic liquids. The accurate time-resolution for changes in the ionic oxidation states upon lithium (de-) intercalation and the high surface and interface sensitivity make operando SE a powerful technique for the observation of time-transient electrochemical processes at the solid-solid interface.

Resumen

La presente tesis aspira a contribuir al desarrollo de baterías totalmente sólidas mediante la investigación de materiales de capa fina fabricados con la técnica de depósito por láser pulsado (PLD). Las capas delgadas pueden proporcionar una gran ratio superficie-volumen y permiten una ingeniería de material única, lo que supone una gran ventaja para reducir resistencias internas, incrementar la densidad de energía y mejorar la capacidad de ciclado. En la persecución de un mayor rendimiento, el cuello de botella sigue siendo el electrolito sólido, que necesita mejoras en su capacidad de transporte iónico y una reducción de los procesos de degradación de las superficies de contacto con los electrodos.

Un target de NASICON $Li_{1+x}Al_xTi_{2-x}(PO_4)_3$ (LATP) electrolito sólido ha sido fabricado y los primeros depósitos por PLD han sido optimizados mediante una variación de la presión del gas de proceso. El comportamiento electroquímico de las capas depositadas ha sido evaluado. Éstas han demostrado una adecuada conductividad iónica del orden de 10^{-6} S cm^{-1}, comparable a as ostentadas por electrolitos sólidos convencionales, como los oxinitruros de litio (LiPON), de aplicación común en baterías de capa delgada actuales. Un tratamiento térmico adicional ha facilitado un incremento de dos órdenes de magnitud en la conductividad iónica, así como un descenso significativo en sus energías de activación, proporcionando valores cercanos a los del material en volumen (10^{-4} S cm^{-1} y 0.37eV, respectivamente). Estas características dotan las capas delgadas de LATP desarrolladas de excelente potencial para su aplicación en baterías de estado sólido.

Un nuevo método para el depósito de materiales de intercalación en fase espinela $LiMn_2O_4$ (LMO) y $Li_4Ti_5O_{12}$ (LTO) es presentado, consistente en el co-depósito de los materiales en cada caso alternando un blanco de Li_2O. Con la finalidad de compensar las típicas perdidas de Li durante la fabricación de capas delgadas, la concentración de litio puede ser variada y diferentes fases pueden ser estabilizadas. Los grosores de capa, la microestructura y el contenido de litio resultantes tienen un gran impacto en el rendimiento electroquímico.

Sumado a su gran potencial de aplicación en baterías de estado sólido, las capas desarrolladas constituyen sistemas interesantes para el estudio de propiedades

fundamentales de los materiales. Las capas delgadas proporcionan un mayor control en la fabricación y un acceso más directo que los sistemas voluminosos a muchos de los fenómenos que llevan a resistencias de intercara e inestabilidades, los cuales necesitan de una comprensión profunda durante la operación de los dispositivos. En una búsqueda de métodos operando no destructivos, de bajo coste y de fácil aplicación en condiciones de operación realistas, dos técnicas de caracterización óptica, espectroscopia Raman y elipsometría espectroscópica (SE), han sido implementada para la monitorización del contenido de litio en capas finas. La espectroscopia Raman es bien conocida en el campo para la medida in situ de la migración de Li. Por otro lado, la SE, a pesar de tratarse de una técnica madura y bien instaurada para el análisis óptico de capas delgadas y sistemas multi-capa complejos, su aplicación al análisis del rendimiento de baterías con resolución temporal permanece inexplorada. En esta tesis, la SE se utiliza por primera vez para monitorizar el movimiento de litio a tiempo real en capas delgadas de LMO y $LiMn_{1.5}Ni_{0.5}O_4$ (LMNO) inmersas en líquidos iónicos. La precisa resolución temporal para cambios del estado de oxidación de los materiales frente a la intercalación de Li y la gran sensibilidad y resolución espacial hacen de la SE una técnica muy poderosa para su aplicación en el campo de las baterías electroquímicas, especialmente en la observación de procesos electroquímicos transitorios en las intercaras sólido-sólido.

Index

List of acronyms

A	Annealed
ABL	Artificial Buffer Layers
ac	Alternating Current
AD	As-Deposited
ADF	Annular Dark Field
AFM	Atomic Force Microscope
ALD	Atomic Layer Deposition
ASS	All-Solid-State
ASSB	All-Solid-State Battery
BF	Bright Field
BSE	Back-Scattered Electrons
CA	Chronoamperometry
CCD	Charge-Coupled Device
CE	Counter Electrode
CF	Crystal Field
CG	Columnar Growth
CP	Chronopotentiometry
CPE	Constant Phase Element
CV	Cyclic Voltammetry
CT	Charge Transfer
DFT	Discrete Fourier Transform
DMC	Dimethyl carbonate $C_3H_6O_3$
DMFA	Dynamic Multi-Frequency Analysis
DOS	Density of States
DSC	Differential Scanning Calorimetry
DTG	Dynamic Thermogravimetry
EC	Ethylene carbonate $C_3H_4O_3$
EDS	Energy Dispersive X-ray Spectroscopy
EELS	Electron Energy-Loss Spectroscopy
EMA	Effective Media Approximation
EIS	Electrochemical Impedance Spectroscopy
EPMA	Electron Probe Micro-Analyzer
ESW	Electrochemical Stability Window
EV	Electronic Vehicle
FEG	Field Emission Gun
FEM	Finite Element Method
FFT	Fast Fourier Transform
FIB	Focused Ion Beam
FM	Frank-van der Merwe growth
FTIR	Fourier Transform Infrared
FWHM	Full Width at Half Maximum
GISAXS	Grazing Incidence SAXS
GI-XRD	Grazing Incidence XRD
HAADF	High-Angle Annular Dark Field
HL	High-Loss
HOMO	Higher Occupied Molecular Orbital
HR-TEM	Highr Resolution TEM

IFFT	Inverse Fast Fourier Transform
IHP	Inner Helmholtz Plane
IR	Infrared
LA-PLD	Large Area Pulsed Laser Deposition
LATP	$Li_{1+x}Al_xTi_{2-x}(PO_4)_3$
LIB	Lithium Ion Battery
LISICON	Lithium Superionic Conductor
LL	Low-Loss
LMO	$LiMn_2O_4$
LMNO	$LiMn_{1.5}Ni_{0.5}O_4$
LTO	$Li_4Ti_5O_{12}$
LUMO	Lowest Unoccupied Molecular Orbital
MAS-NMR	Magic Angle Spinning NMR
MBE	Molecular Beam Epitaxy
MEMS	Micro Electro-Mechanical Systems
MWL	Mulit Wavelength
NASICON	Sodium (Na) Super Ionic Conductor
NMR	Nuclear Magnetic Resonance
OC	Open Circuit
pc	Pseudo-cubic
PDE	Partial Differential Equation
PLD	Pulsed Laser Deposition
RE	Reference Electrode
RF	Radio Frequency
SAXS	Small Angle X-ray Scattering
SE	Secondary Electrons
SE	Spectrocscopic Ellipsometry
SEI	Solid Electrolyte Interphase
SEM	Scanning Electron Microscope
SERS	Surface Enhanced Raman Spectroscopy
SF	Step-flow growth
SK	Stranski-Krastanov growth
SOC	State Of Charge
SSA	Specific Surface Area
SSE	Solid State Electrolyte
STEM	Scanning Transmission Electron Microscope
TEM	Transmission Electron Microscop
TERS	Tip Enhanced Raman Spectroscopy
TGA	Thermogravimetric Analysis
UHV	Ultra High Vacuum
UV	Ultra Violet
VM	Volmer-Weber growth
WAXS	Wide Angle X-ray Scattering
WDS	Wavelength Dispersive X-ray Spectroscopy
WE	Working Electrode
XRD	X-ray Diffraction

List of symbols and abbreviations

et al.	et alia (lat.)
etc.	et cetera (lat.)
e.g.	exempli gratia (lat.)
Eq.	Equation
Fig.	Figure
Tab.	Table
C	C-rate [h^{-1}]
C_{th}	Theoretical capacity [Ah]
Q_c	Accumulated charge [Ah]
E	Specific energy [Wh kg^{-1}]
P	Specific power [W kg^{-1}]
V_{cell}	Cell voltage [V]
m_a	Active mass electrode material [g]
t	time [s]
R_i	Internal resistance [Ω cm^{-2}]
r_p	Particle radius [cm]
δ_p	Particle density [particle cm^{-2}]
mol %	Molar-percent
wt %	Weight-percent
p	Pressure ambient [Pa, bar, Torr]
λ	Wavelength [nm]
F	Laser fluence [J cm^{-2}]
f	Frequency [Hz]
d_{ST}	Target-to-substrate distance [cm]
U_o	Cohesive energy [eV]
t_p	Pulse width [s]
P	Power [W]
R_{st}	Front position of laser plume [cm]
pO_2	Partical Oxygen pressure [mbar]
$m_{G,H,L}$	Atomic weight of background gas (G), heavy element (H) or light element (L)
M_p	Mass of plume species [atoms per pulse]
v_0	Plume front velocity [m s^{-1}]
S_T	Surface ablated spot size
δ_a	In-depth etch rate [nm per pulse]
ρ_T	Density target [g cm^{-3}]
γ	Surface energy on interfaces [???] between substrate (s), film (f) and vapor (v)
θ_s	Surface contact angle [°]
a, b, c	Lattice parameters
a_0, b_0, c_0	Initial lattice parameters
pc	Pseudo-cubic
(hkl)	Miller indices of reciprocal lattice planes
V	Voltage [V]
I	Current [A]
h	Planck's constant = 6.62607015×10^{-34} Js = $4.135667696\times10^{-15}$ eV s

m_0	Eelectrons rest mass = 9.10938370×10^{-28} g
e	Elementary charge = 1.60217662×10^{-19} C
E	Kinetic energy [eV]
Z	Atomic number
θ	Glanzing angle, Bragg angle [º]
d_{hkl}	Atomic inter-planar spacing real lattice [nm]
n	Positive integer
i, j	Complex integer
G_{hkl}	Reciprocal lattice vector
$\vec{k}$	Waver vector
β_P	Particle size broadening
t	Apparent particle size
R_g	Radius of gyration [nm]
ω	Incident angle [º] used for GI-XRD
$\alpha_{i,f,c}$	Shallow scattering angle [º] as incident (i), exit (f) and critical (c) for total reflection
n_r	Refractive index
δ_d	Dispersion
β_a	Absorption
$q_{x,y,z}$	Spatial scattering directions
ψ_0	Out-of-plane angle X-ray scattering [º]
$\tilde{\nu}$	Wavenumber [cm^{-1}]
N	Spin state
l	Nuclear spin quantum number
B_0	Magnetic field
δ_0	Chemical shift [ppm]
e	Euler number = 2,718281829
ω	Angular frequency
φ	Phase shift [º]
V_0, I_0	Amplitudes in *ac* voltage or current wave
Z	Impedance, with (‘) real and (“) imaginary
Re, Im	Real and Imaginary part of the Impedance
d	Distance between electrical contacts
L	Length of electrical contacts
t_f	Thickness of thin film [nm]
R, C, I	Resistor, Capacitor, Inductor
R_p	Polarization resistance
C_{dL}	Double-layer Capacitor
τ	Time constant
α	Dispersive factor
Q	Pseudo-capacitance
Z_W	Warburg Impedance
σ_W	Warburg coefficient [$\Omega cm^2\ s^{-1/2}$]
D	Diffusin coefficient
δ_{dL}	Double-layer thickness
E_a	Energy of activation [eV]
ϕ_0	Brewster angle = 70º
k	Extinction coefficient
Δ	Difference in phase shift ellipsometry
Ψ	Amplitude ratio ellipsometry

c_i	concentration of species i in domain j
g	Source element
J	Diffusion flux
∇	Nabla operator for n-dimensional gradient
Ψ_i	Basic function for small domain in FEM
D	Diffusion coefficient [$cm^2\ s^{-1}$]
E_{WE}	Potential at working electrode [V]
j	Current density [$mA\ cm^{-2}$]
v	Scan rate [$mV\ s^{-1}$]

1. Introduction

1.1 Motivation

Energy harvesting and consumption in the global age of digitalization are demanding the development of electrical-energy-storage systems, if we are to succeed in meeting the world's population ever-growing desire for electronic devices, mobility and domestic energy supply. Among that, the consumption of finite energy resources and further environmental pollution, causing disastrously irreversible changes in the global climate, urges to be resolved. With the goal of carbon-neutrality, the research in renewable energies and (hybrid) electronic vehicles (EV) boosted the development of rechargeable batteries in the past decades, especially in the lithium-ion based chemistry.[1] Lithium-ion batteries (LIB), with their high energy and power density, both gravimetric and volumetric, perfectly meet the requirements for developing a renewable energy supply grid withstanding high peak-currents, as well as providing light-weighted power sources for portable electronic devices and EVs.[2] Self-powered and self-supported micro devices in the field of portable electronics profit from miniaturized batteries and supercapacitors at the micro-scale,[3–6] involving micro-fabrication techniques, especially for the deposition of thin film electrodes and solid electrolytes for replacing common button-batteries.

Thin film deposition methods have proven to enable a precise control of the material stoichiometry and solid-solid interfaces,[7,8] as reoccurring instabilities and degradation phenomena especially evolve from the materials specific defect chemistry and the nature of interfaces. The solid electrolyte acts as the charge mediator and hence controls the battery performance by its ionic mass transport properties and intrinsic electrochemical stability window towards the electrode materials. Facing the challenges for providing deeper insight into complex charge and mass transport mechanisms under realistic operation conditions, great interest has been taken in advancing in-situ/operando techniques for the investigation of battery materials and devices.[9]

In this thesis, the following section concentrates on the all-solid state lithium-ion thin film batteries, their current state of the art and future challenges, with the emphasis on the importance of developing suitable thin film solid electrolytes and electrode materials and their in-situ investigation under operating conditions.

1.2 Solid-state lithium-ion batteries

Non-aqueous, rechargeable lithium-ion batteries have been introduced for the first time in the early 60s with the motivation of high energy densities and long cycle life. Since then the economically more favorable and safer intercalation material based lithium-ion chemistry has experienced a steady improvement towards increased safety, non-toxicity and cycling stability, in respect to lithium metal batteries with poor cycling efficiency and short circuits resulting from lithium dendrite growth and corrosion.[10,11] The typical configuration for a standard lithium-ion battery is shown in **Fig. 1.2.1 (a)** with a classic cylindrical cell setup involving mixed ionic-electronic conducting materials (electrodes) in stable solution with solely ionic conducting liquids (electrolyte), separated through a semi-permeable membrane (separator) leaving passage to the ionic charge without intermixing the liquids. The electronic charge exchanged during the redox-reactions is collected on metallic contacts (current collectors) placed upon the electrodes, protected from the electrolyte. Electrodes are defined as anode (negative) or cathode (positive), both consisting of intercalation materials having a layered structure for the storage of lithium, e.g. between graphite sheets or CoO_6 octahedra, respectively.[12]

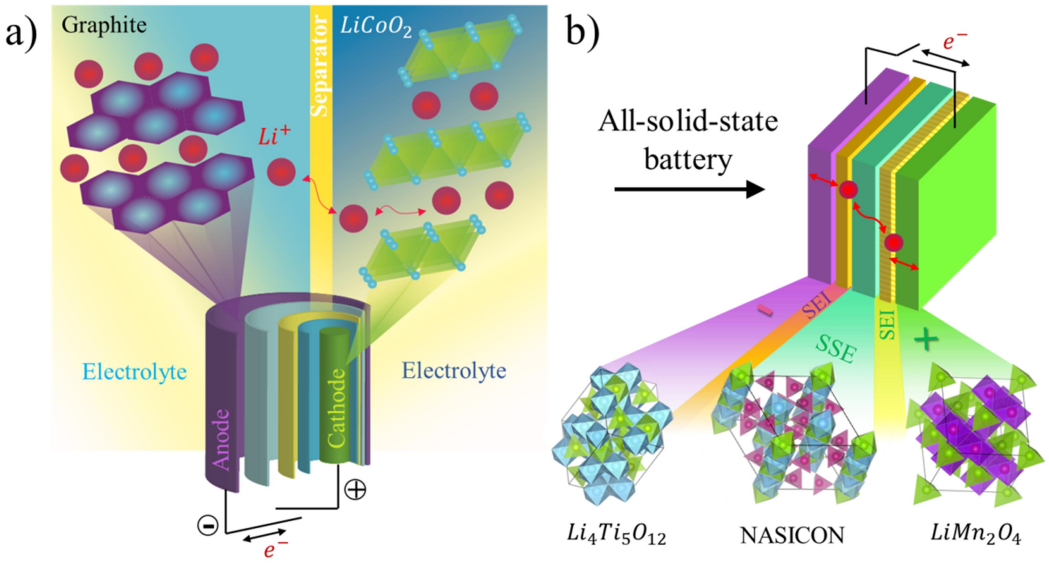

Fig. 1.2.1: Battery concept in (a) for the lithium-ion battery as cylindrical cell involving liquid electrolytes (e.g. $LiPF_6$ EC/DMC) and intercalation materials as electrodes, e.g. graphite as anode (-) and $LiCoO_2$ as cathode (+).[12] In (b) the scheme of an all-solid-state battery is demonstrated, replacing the ionic liquid with a ceramic solid-state electrolyte (SSE), e.g. NASICON-like compounds. Intercalation materials such as transition metal oxides are commonly used, e.g. $Li_4Ti_5O_{12}$ as anode and $LiMn_2O_4$ as cathode. The formation of a solid-electrolyte interface (SEI) is common for both liquid and all-solid-state cells.

The resulting voltage for powering electronic devices is generated by the redox-reaction between anode and cathode. The transfer of ionic charge resolves in the donation or acceptance of electronic charge, which causes a change in the oxidation states of the transition metal ions. This typical redox processes will be discussed with more detail in **Section 2.4** concerning electrode materials and the evolution of their electrochemical potentials on the example of spinel $LiMn_2O_4$ and $Li_4Ti_5O_{12}$.

Further **Fig. 1.2.1 (b)** is demonstrating the schematic setup of an all-solid-state battery (ASSB) under replacement of the ionic liquids with an adequate solid-state electrolyte (SSE), such as NASICON-like (polianionic phosphates) or LISICON-like (sulfides and thiphosphates) conductors, as well as Perovskites, Garnets and many others.[13,14] All-solid-state batteries are considered as the future replacement of common battery systems consisting of cylindrical, coin or pouch cells of relatively large spatial dimensions, solving their safety hazards evolving from the liquid carbonaceous electrolytes and the use of metallic lithium.[2,14,15] Together with the increased desire for miniaturization, geometrical limitations in the application of liquid electrolytes are reached and the development of suitable solid electrolytes pushed forward. Their good stability towards changes in ambient conditions, high lithium-ion conduction at room temperature and negligible electronic conductivities, help to avoid cell shorting with the result in an improved safety and benign environmental impacts. The possibility of implementing those materials in thin film deposition techniques enables their shape adaptation for microbatteries and flexible electronics, strongly increasing the capability of high specific capacities on a small volume (energy density), for the development of self-sustaining portable microelectronic devices.[2,14]

In the following sections the current state of the art for all-solid-state batteries will be elucidated in **Section 1.2.1**, with special emphasis on the solid-solid interface nature in **Section 1.2.2** and its overall great impact on the solid-state battery performance. In **Section 1.2.3** the current capabilities of thin film deposition techniques for manufacturing especially microbatteries are given in a quick overview, with deeper insight in the Pulsed Laser Deposition (PLD) as the preferred thin film deposition technique applied in this thesis.

1.2.1 State-of-the-art for all-solid-state batteries

Although all-solid-state batteries promise a safe alternative to overcome physicochemical limitations evolving from liquid systems,[11] certain drawbacks are being faced especially when it comes to interface stabilities, fast kinetics, as well as competing power densities compared to commercial LIBs.[16,17] State-of-the-art volumetric and gravimetric energy densities of liquid systems reach 770 Wh l^{-1} and 260 Wh kg^{-1}, respectively, for cycling rates greater than 1C.[16,18] ASSBs struggle to reach those values, not only due to higher resistances at the solid-solid interfaces and lower ionic conductivities of the SSE, but also due to further complications arising from the inverse relationship between the specific power and specific energy.[19] For following explanations, the battery conventions referred to in the next section are defined in **Eq. 1.2.1**, whereas the theoretical capacity C_{th} of a material can also be expressed as an energy, when multiplying the accumulated charge ($Q_c = I \cdot t = C_{th}$) with the cell voltage (V_{cell}). Hence the specific energy E is defined as the power (P) over time per mass (m_a) of the active material (gravimetric) or the cell volume (energy density).[18–20]

$$\text{specific energy [Wh} \cdot \text{kg}^{-1}\text{]: } E = \frac{V_{cell} \cdot C_{th}}{m_a} = \frac{P \cdot t}{m_a} \qquad \text{(Eq. 1.2.1a)}$$

$$\text{specific power [W} \cdot \text{kg}^{-1}\text{]: } P = \frac{E}{T} \qquad \text{(Eq. 1.2.1b)}$$

Low energy densities can be counteracted with a higher amount of electrode active material (thickness and density dependent), usually resolving in thick electrode configurations, at the expense of power densities due to the insulating character of intercalation- and conversion-type electrode materials.[21] The incorporation of conductive additives in the cathode/anode composite and the use of SSEs of high-rate capability may counteract these limitations, leading to ASSBs capable of specific energies higher than 400 Wh kg^{-1}, energy densities above 1000 Wh l^{-1} and a specific power beyond 250 W kg^{-1} (exclusive cell casing) in the near future, as it is indicated in **Fig. 1.2.2** for the Ragone plot.[18,19,21]

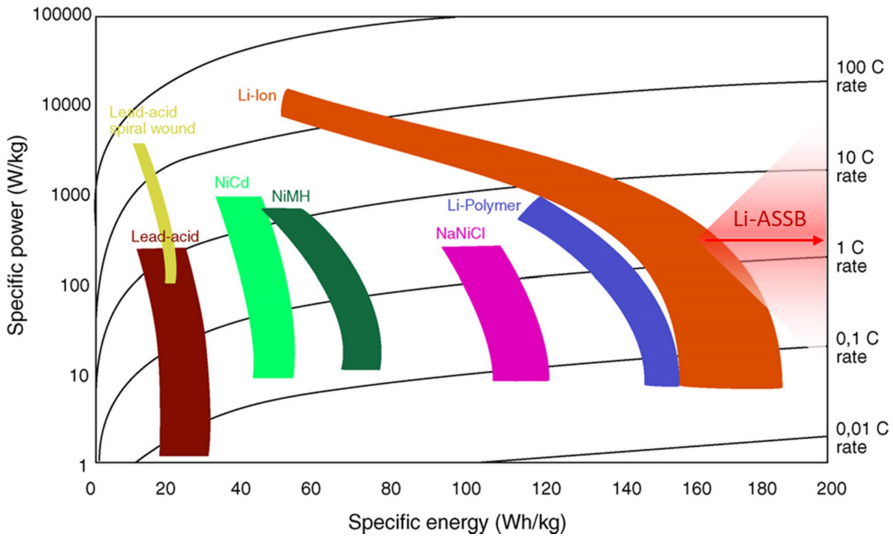

Fig. 1.2.2: Ragone plot comparing the specific power and specific energy along different C-rates for a variety of battery technologies,[22] complemented by the recent projection on lithium ASSBs by *Randau et al.*[18] Reproduced and adapted from *Van den Bossche et al.*,[22] with permission from Elsevier.

Only recent studies by *Randau et al.*[18] on benchmarking the current performance of all-solid-state cells offered deeper insight in the limiting criteria for reaching high specific power and specific energies to mostly depend on internal resistances and layer thicknesses. In their projection for lithium metal ASSBs they conclude that it is recommended to restrict the overall internal resistance to $R_i < 40\ \Omega\ cm^{-2}$, supported by separator thicknesses of less than 50 µm and in-situ created anodes for higher energy densities. Further recommendation concerns the area capacities (cell capacity per cross-sectional area) to range above 5 mAh cm^{-2} and the hypothetical (separated) cathode specific energy above 500Wh kg^{-1}, being the limiting factor for the maximum achievable specific energies of the cell. Leading performances in ASSBs so far have been demonstrated by lithium metal and graphite based intercalation- or conversion-type cells including SSE composed of ternary and quaternary sulfides and thiophosphates.[16,18] The future goal of eliminating lithium metal and graphite as negative electrodes would cause a huge drop in the energy densities, as they exhibit great specific capacities, high electronic conductivities and high cell voltages. Unfortunately, due to severe safety concerns and remaining instability issues, mainly resulting from anodic oxidation, their replacement is inevitable.[11] Although solid electrolytes seem to prevent some of those safety issues, most of the SSEs exhibit a non-matching electrochemical stability window (ESW) towards the standard potential of metallic lithium or graphite,[16] and further lower ionic

conductivities in the solids hinder the accessibility of the full electrodes theoretical capacity.[18] Given the current limitations, it is absolutely necessary to invest further research in highly capacitive and high rate performing electrode materials, fast ionic conducting SSEs,[19] an improved tailoring of the interfacial behavior[23,24] and to take advantage of size effects at the nano-scale,[25,26] in order to improve mass transport and charge storage across lithium-ion ASSBs.

1.2.2 The solid-solid interface

One of the main concerns in improving battery performance is the electrode-electrolyte interface in solids, which is defined by certain chemical and electrochemical interdiffusion phenomena and material stabilities, as well as local lattice distortions and the mechanical contact between the different components.[27,28] The universal goal is to control the interface and to avoid material degradation. Excessive volume expansion causing chemo-mechanically induced layer cracking and detachment, as well as the formation of lithium dendrites and highly resistive interfaces need to be supressed.[24,29] For a better understanding of the physicochemical limitations at the solid-solid interface, **Fig. 1.2.3** describes the evolution of the energy and potential across the ASSB.

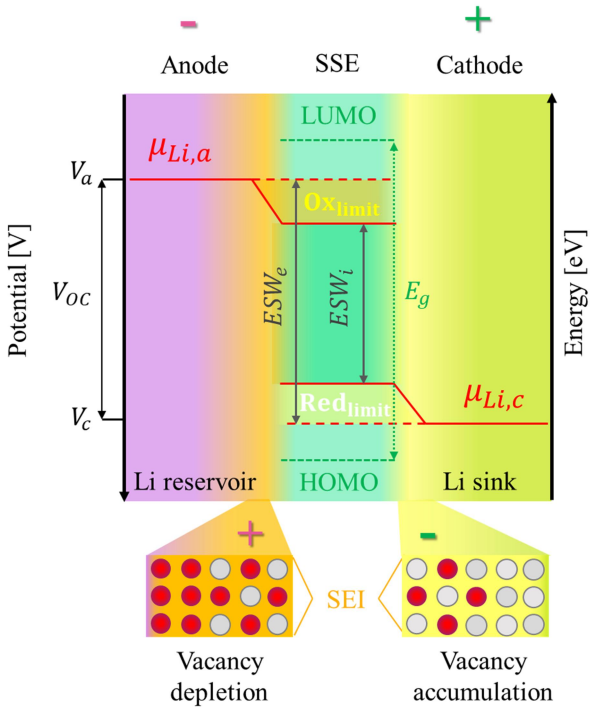

Fig. 1.2.3: Schematic illustration of the energy diagram across an all-solid state battery consisting of anode|SSE|cathode during open-circuit (OC). The y-axes indicate the cell

voltage V and chemical potential μ of lithium in the anode (index a) and cathode (index c). Electrochemical stability window (ESW) is shown for the initial (index i) and extended case (index e), delimited by the oxidation (Ox_{Limit}) and reduction potential (Red_{Limit}) of the electrolyte evolving from the HOMO/LUMO energy gap E_g, and the electrodes chemical potentials. Solid-electrolyte interfaces (SEIs) are forming on the electrode-electrolyte interface, depleting or accumulating vacancies (vice versa interstitials). Adapted from *Pervez et al.*[27] Copyright © 2019, American Chemical Society. Adapted by permission from Springer Nature *Famprikis et al.*,[29] Copyright © 2019.

The thermodynamic stability of an electrolyte in contact with an electrode is governed by the difference between the Fermi level of the electrode and the highest occupied molecular orbital (HOMO) or the lowest unoccupied molecular orbital (LUMO) levels of the electrolyte. An anode holding a Fermi Level above the LUMO of the electrolyte will generate the driving force to reduce it. Similarly, a cathode with a Fermi level below the HOMO of the electrolyte will lead to its oxidation. Either of the cases will lead to the decomposition of the SSE and interphase layer formation, known as the solid-electrolyte interphase (SEI). Therefore the electrochemical stability window (ESW) in **Fig. 1.2.3** resulting from the HOMO/LUMO of the SSE has to be chosen wide enough to prevent continuous material decomposition. Two different types of SEI layers are distinguishable in **Fig. 1.2.3**, as one is mainly built by the accumulation of interstitials (Li-rich) and the other by the accumulation of vacancies (Li-poor), building a positive and negative space charge area respectively. If the resulting SEI layer is stable or not depends on its electronic character. Electron-insulating layers appear to stably passivate the solid-solid interface, with no further SSE degradation, resulting in a mediated energy profile across the battery device, extending the ESW of the electrolyte. Electronically conducting layers on the other hand may not achieve electrode passivation and continue to decompose the electrolyte, leading to a continuous increase in the interface resistance. The latter has been a known issue for the application of sulfide-based SSEs in combination with Li metal and common metal oxides, such as $LiCoO_2$, due to certain instabilities with Li and the interdiffusion of S and Co compounds.[27,30] On the other side, sulfide and thiophosphate SSEs have been reported to perform as most promising ASSBs due to their exceptionally high ionic conductivities (~ 10^{-2} S cm^{-1}) and resulting high specific energies, which resolves a huge interest in overcoming certain interfacial instabilities.[18] The scenario described in **Fig. 1.2.3** shows the preferred situation in which the negative electrode (anode) and positive electrode (cathode) with their

chemical potentials μ_{Li} are placed inside the reduction and oxidation limit of the electrolyte.

The phenomenon of electronically conductive interlayer formation may partially be suppressed by limiting the overall cell voltage V_{OC} to be in a comfortable limit of the thermodynamic stability window of the SSE.[27] Further, additional interface engineering by synthetically produced SEIs, so-called artificial buffer layers (ABL) have reached great attention.[24,28] ABLs selectively influence the interfacial space charge region by introducing inactive ions in the shape of a thin passivating barrier, blocking the compound interdiffusion and protecting the electrode-electrolyte interphase.[31] Furthermore lattice mismatches (mainly occurring in thin film batteries) can be counteracted.[28] Commonly implemented ABLs consist of Al-based[31–33] or Mg-based[34] thin film coatings, which tend to incorporate the inactive ions in the active composites surface, forming some kind of core-shell structure during electrochemical processing at the interface. This greatly improves cycle life stability and safety in all battery devices across the field, as well as it allows for the combination of different material chemistries with controlled or diminished compound interdiffusion. ABLs generally are in need of suitable thin film deposition techniques, similar to the ones described in **Section 1.2.3.2** for the fabrication of thin film batteries.

1.2.3 Thin film microbatteries

The development of microbatteries experienced a great proliferation upon the increasing interest in portable micro devices, such as autonomous micro-electromechanical systems (MEMS), wireless micro-sensors and transceivers, or implantable health monitoring devices.[4–6] All-solid-state miniaturized batteries and supercapacitors with their compact shape are therefore substantial for enabling high specific power, while maintaining good stability and safety.[4,35] Thin film batteries (TFBs) have demonstrated in the past to greatly increase the rate capability of ASSBs, unfortunately at the cost of energy densities, as demonstrated in **Fig. 1.2.4**.

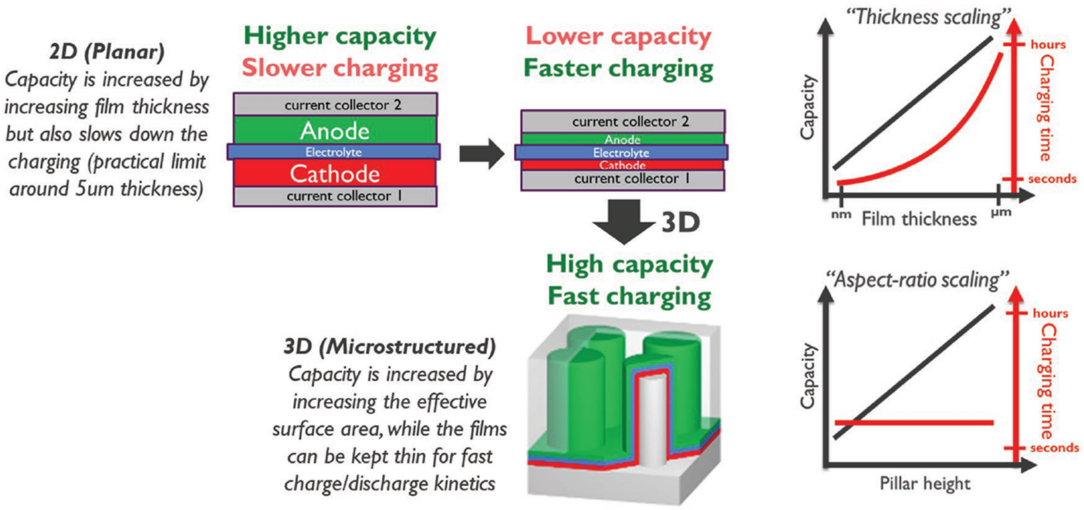

Fig. 1.2.4: Correspondence between specific energy (capacity) and specific power (charging rate) on scaling properties in the planar or 3D configuration of thin-film batteries. Reproduced from *Moitzheim et al.*,[36] Copyright © 2019 Wiley-VCH.

This could be counteracted by improving the surface-to-volume ratio in 3D-microstructuring the battery device, leading to increased energy densities while maintaining the high rate capability evolving from the reduced internal resistance of the TFB device. TFBs are commonly associated with the combined effects of introducing nano-structures in the charge storage,[26] plus enabling densely packed and controlled interfaces, providing short diffusion paths and reduced internal resistances by the use of thin film deposition techniques.[8,25,36]

1.2.3.1 Nanostructured materials

Nano-size effects are greatly impacting the battery performance on different levels, ranging from the impact of high aspect ratios on the surface-to-volume ratio to the transform of bulk material properties, e.g. phase stabilization, increasing robustness and better cyclability.[26,37] Vital mechanistic steps in lithium transportation across the battery device can be divided in (i) the Li^+ ion transport across the electrolyte, (ii) its absorption at the electrolyte-electrode interface and (iii) the final chemical Li^+ intercalation inside the electrode lattice (and vice versa). Fundamental driving force originates from a Li concentration gradient $(\delta/\delta x) \cdot c_{Li}$ as a result of different chemical potentials μ_{Li} of the electrodes, as well as the transport coefficient of the chemical Li^+ diffusion D_{Li}.[25] From the second law of diffusion, the correlation between intercalation time τ and diffusion path length L can be described as in **Eq. 1.2.2**, with adapted boundary conditions.[26]

$$\tau = \frac{L^2}{D_{Li}} \qquad \text{(Eq. 1.2.2)}$$

Hence rate capabilities greatly depend on the length of lithium diffusion paths as their shortage improves the material flux, which is simply realized by decreasing layer thicknesses. Transport coefficients on the contrary mainly depend on the carrier concentration and certain defect accumulations, common for surfaces and interfaces. During electrode polarization the materials symmetry is rearranged, leading to carrier accumulations and localized intrinsic effects on the materials electronic band structure (level bending).[25] Especially small particle sizes allow for a complete disappearance of domain boundaries between differently occupied states, promoting fast reaction kinetics under the formation of solid-solutions as a result of really short diffusion paths.[38] Hence, the more surface available, the greater the free energy, leading to improved material contact, higher lithium-ion fluxes and a better accommodation towards charge-induced strain. Nonetheless, nano-shapes also bare some obstacles for battery performances, mainly originating from undesired side-reactions due to higher reactivities at electrode/electrolyte interfaces and difficulties of particle synthesis and electrode densification.[37] Therefore thin film deposition techniques, with their great control in stoichiometric compositions, smooth surfaces and high layer densification, demonstrate a good viability for the realization of nano-shapes of controllable size and sufficient interfacial contact.[35,36]

1.2.3.2 Thin film deposition of Li-ion battery components

In most of the cases, deposition techniques for all-solid-state thin film lithium-ion batteries include physical (PVD) or chemical (CVD) vapor deposition (besides others, such as sol-gel processing or ion plating),[8] with either vaporizing the materials source onto a substrate in a low-pressure, controlled gas atmosphere or utilizing thin film formation under gas-phase induced reactions on the substrate surface, respectively. Classic representatives for the fabrication of TFB and ABLs of PVD techniques include the sputter deposition (magnetron and radio-frequency), thermal and electron beam evaporation, molecular beam epitaxy (MBE) and the pulsed laser deposition (PLD). CVD techniques commonly used range from plasma-enhanced and laser-induced methods, to low-pressure applications and the layer-by-layer formation through atomic layer deposition (ALD). Their

applicability strongly depends on the desired material properties, substrates and layer adhesion, layer thickness and correlated deposition rates, as well as the maximum lateral dimensions of the substrate for obtaining good layer uniformity.[35]

Thin films of common lithium intercalation materials, e.g. $LiMn_2O_4$ and $Li_4Ti_5O_{12}$, as well as solid electrolytes, e.g. LiPON, perovskites and garnets, have been greatly implemented for depositions in the radio frequency (RF) magnetron sputtering and PLD,[7,39–43] under the typical addition of 15 wt% Li_2O in the target materials for compensating the loss of volatile lithium (see details in **Section 2.3.3**). As these are vacuum techniques, which only allow for low background gas pressures during deposition, resulting layers usually exhibit a certain off-stoichiometry at the anionic side. Lithium and oxygen deficiencies during thin film deposition are undoubtedly the source of lower amounts of active material and therefore resulting capacitive restrictions, as well as the formation of undesired secondary phases. Ionic conductivities of thin film SSEs suffer a significant drop compared to their bulk counterparts, if lithium loss is not accurately balanced.[7,17] Additional annealing for re-oxidation purposes of oxide compounds usually improves film stoichiometry, relaxes strain and increases the structural order and crystallinity.[8] On the other side, its necessity induces again lithium loss and delimits the application of certain substrates and materials of lower temperature stability (e.g. LiPON).[44,45] Alternatives to the fixed lithium amount in the pelletized material source emerged over the past years, as sputtering and PLD methods offer the possibility of applying multiple targets in an alternating manner in the same deposition setting, allowing adaptable lithium content for accurate compensation. Only recent progress in co-depositing garnet SSEs in combination with additional Li_2O[17] or Li_3N[46] layers enabled ionic conductivities ~ 10^{-4} S cm^{-1}, close to bulk values of SSEs. This approach appears universally viable for any compound of TFBs, as it has been previously demonstrated by our group to provide excellent properties in $LiMn_2O_4$ cathode thin films deposited by PLD, as reported by *Fehse et al.*[47–49] The concept of the alternating multi-layer deposition between two different targets is schematically shown in **Fig. 1.2.5**.

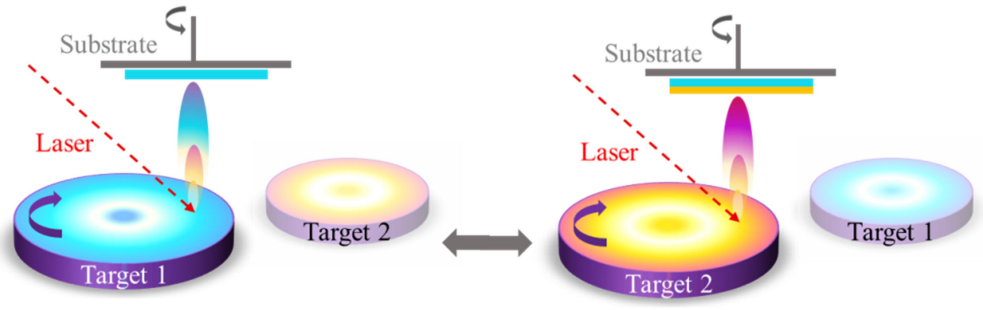

Fig. 1.2.5: Multi-layer deposition in the PLD under application of alternating targets for the compensation of volatile materials during thin film deposition. A complete cycle consists of the separated ablation of each target material for a fixed amount of pulses. Cycles can be repeated unlimited until the desired thickness and crystallinity are reached.

Thin films of LMO deposited by this approach showed reversible charge capacities of 289 mAh cm^{-3} with capacity retention of 99.996 % per cycle at extraordinary high rates of 348 C over 3500 cycles could be obtained in an aqueous electrolyte and remain widely unmatched by other research groups providing comparable results only at much lower rates of 18 C.[50,51] The multi-layered thin films have also been applied in a dual-metal-ion rechargeable microbattery comprising of LMO|Li_2SO_4:$ZnSO_4$|Zn in an aqueous environment, capable of providing high specific power densities of 3400 W kg^{-1} with coulombic efficiency of 99.94% over 300 cycles and a typical specific energy for Li-ion batteries ~100 Wh kg^{-1}.[49,52]

In summary, the use of PLD for the fabrication of thin film microbatteries allows for a precise stoichiometric transfer of complex multicomponent oxides, a smooth surface and good control of the interface.[7] It further provides the opportunity for industrial up-scaling,[53] which makes it an attractive technique for commercialized applications, as thin film and micro-fabrication techniques are no inexpensive fabrication methods.[36]

1.3 Solid-state electrolyte materials

The main objective for the use of all-solid-state batteries clearly evolves from the drawbacks in the use of carbonaceous, aprotic liquid electrolytes, bringing forth the need of adequate solid replacements of comparable ionic conductivities in the range of 10^{-2} S cm^{-1} at room temperature.[14] This is conflicted by the nature of the solid-state itself and requires specific material properties, such as high ionic mobility paired with low intrinsic electronic conduction. The development of solid-state electrolytes (SSE) undoubtedly got boosted in the past decades by the continuous

development of new material families providing fast lithium ion kinetics up to 10^{-4} and 10^{-2} S cm^{-1}, slowly on their way of even exceeding reaction kinetics of liquid systems.[27] Additionally the lithium transference number for suitable solid electrolytes is much higher (~1) than for aprotic liquids (0.2 – 0.5), as well as their thermal stability. Together with a certain non-flammability and agitating as some kind of physical barrier for lithium dendrite growth, SSEs enable good cycle life stability and safety for ASSBs.[13] Furthermore, their thermodynamic stability over a great temperature gradient and insignificant electronic conductivity open the opportunity for applications at very low or elevated temperatures,[13,54] without suffering severe self-discharge phenomena or explosion.[11]

Different chemical families for suitable SSEs are briefly presented in the following (**Section 1.3.1**). The Al-substituted NASICON-like compound $Li_{1+x}Al_xTi_{2-x}(PO_4)_3$ (LATP) and its characteristic material properties are further elucidated in **Section 1.3.2**. In the light of thin film microbatteries, a short overview of reported thin film applications of common SSEs is given in **Section 1.3.3**.

1.3.1 SSE material families

Fast ionic migration has been connected to originate from the materials anionic sublattices with preferable orientation in the body-centered cubic and the mobile species to be dislocated from its usual coordination environment.[13] This provides a great amount of vacant lattice sites and a 3D framework of migration channels surrounded by anions of a high polarizability, enabling high ionic mobilities. Further low migration enthalpies are recommendable to facilitate the long- and short-range hopping of lithium ions across the interstitial sites.[27]

Conventional solid electrolyte families can be divided into LISICON-like (Lithium Superionic Conductor), NASICON-like (Sodium (Na) Superionic Conductor), Garnets and Perovskites, as shown in **Fig. 1.3.1**, comparing their corresponding ionic conductivities at room temperature. Besides material compositions involving Argyrodite thiophosphates, also nitrides, hydrides and halides are currently providing potential SSE materials for the application in ASSB devices.

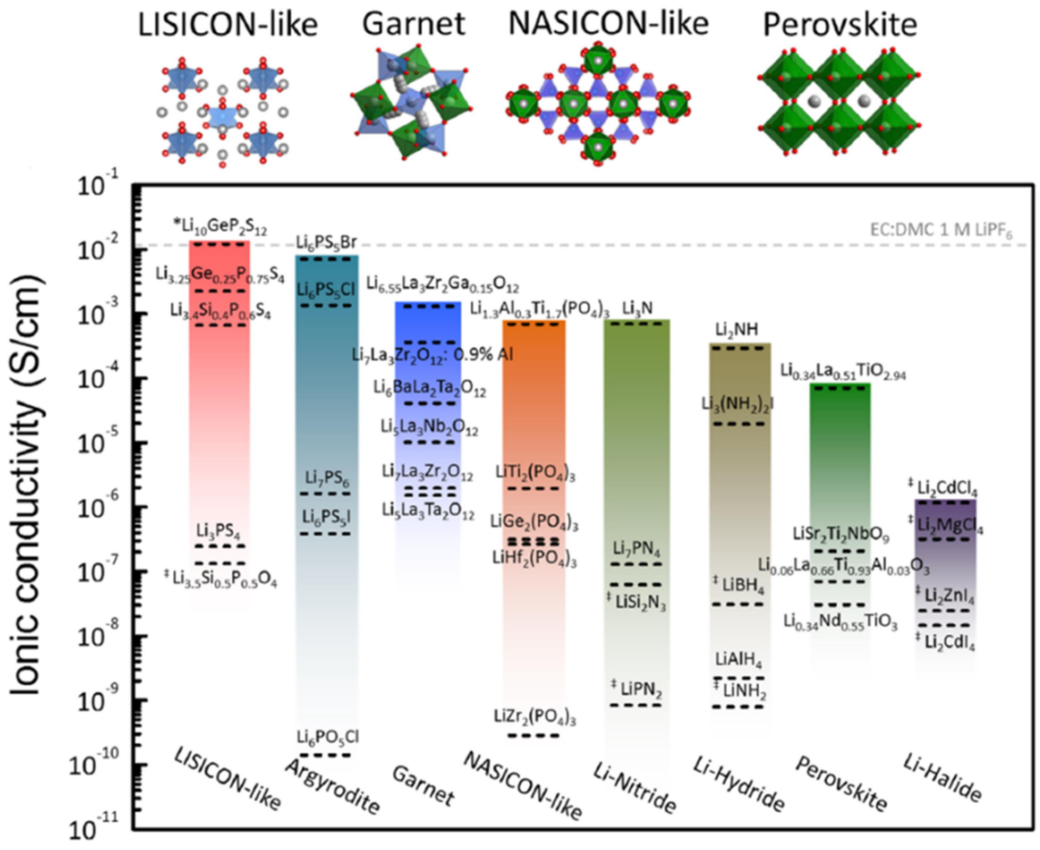

Fig. 1.3.1: Total ionic conductivities of solid-state lithium-ion conductors at room temperature for different SSE families. The lithium-ion conductivity of the common carbonaceous liquid electrolyte 1 M $LiPF_6$ EC/DMC is shown for comparison as horizontal dashed grey line. Reprinted from *Bachman et al.*[13] Copyright © 2016, American Chemical Society.

LISICON-like structures are crystallizing in the orthorhombic *Pnma* lattice with structural similarity to γ-Li_3PO_4. Their greatest advantage evolves from a high temperature stability and compatibility with aqueous environments, but their low ionic conductivities (~ 10^{-7} S cm^{-1}), instability towards Li metal and CO_2 reactivity are obstacles to their successful implementation as SSE. The replacement of O^{2-} with bigger S^{2-} anions of higher polarizability, as well as the aliovalent substitution of P^{5+} with tetravalent cations (M = Si, Ge and Sn) gives rise to much higher ionic conductivities in $Li_{10}MP_2S_{12}$, commonly known as *thio*-LISICON ionic conductors.[13] Their excellent ionic conductivities of ~ 10^{-2} S cm^{-1} and above, together with low activation energies (E_A) between 0.20 – 0.25 eV are current benchmarks for SSEs and tend to even exceed the ionic mobility in aprotic ionic liquids when compared to $LiPF_6$ EC/DMC in **Fig. 1.3.1**. Current drawbacks in their application evolve from their hazardous reactivity with water and high sensitivity to moisture (formation of poisonous H_2S gas), as well as their very limited ESW due

to the reduction of M-cations in contact with Li-metal at low redox-potentials, as shown in **Fig. 1.3.2**. Glassy sulfide electrolytes in the Li_2S-P_2S_5 system allow for similar high ionic conductivities of 10^{-2} – 10^{-3} S cm^{-1}, a ductile nature and better stabilities towards Li, but still remaining safety concerns when in contact with water or ambient moisture. Comparable electrolyte materials such as Argyrodites of the composition Li_6PS_5X (X = Cl, Br and I) are facing similar issues and even greater limitations in their ESW, although ionic conductivities are just as high and activation energies can be greatly reduced to 0.16 eV.[27]

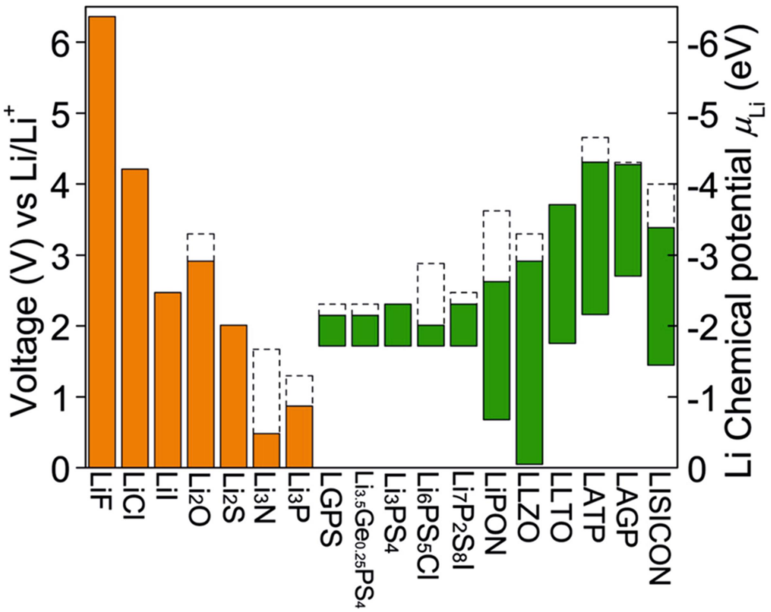

Fig. 1.3.2: Electrochemical stability window in respect to the chemical potential of Li for commonly used SSEs (green bars), initially (solid bars) and extended (dashed lines) to their oxidation potential under complete delithiation. Binary decomposition products commonly occurring in contact with lithium are shown in addition (orange bars). Reproduced by permission from Springer, Journal of Electoceramics, *Lotsch et al.*,[55] Copyright © 2017.

Another dominant family of SSE materials is provided in the crystallographic shape of garnet materials, generally described with A_3B_2 $(XO_4)_3$ with a cubic unit cell in the $Ia\bar{3}d$ space group. A promising representative amongst the garnet electrolytes is $Li_7La_3Zr_2O_{12}$ (LLZO), demonstrating ionic conductivities as high as 10^{-3} – 10^{-4} S cm^{-1}, with good stability towards lithium and a very broad electrochemical stability window, as can be seen in **Fig. 1.3.2**.[13,56] Only remaining disadvantages evolve from their brittle nature and certain instabilities towards moisture, forming insulating carbonates and hydroxides on the material surface.[27] Similar to the garnets, perovskite structures of the general ABO_3 formula in $Pm\bar{3}m$ exhibit good ionic conductivities of 10^{-3} S cm^{-1} and typical activation energies around 0.3 – 0.4

eV for $Li_{3x}La_{2/3-x}\square_{1/3-2x}TiO_3$ (LLTO) with $0 < x < 0.16$. The aliovalent substitution of lanthanum with lithium leads to a modification in the concentration of both La ions and vacancies (□), resolving different Li/□ ordering upon doping with significant effect on the ionic conduction. LLTO has been reported to be stable towards air and surrounding humidity, as well as towards higher temperature gradients between 4 K – 1600 K.[27] As drawback remains the typical reduction of Ti^{4+} versus lithium around 1.5 V, making it unstable when used in contact with metallic Li and graphite.[13] Nonetheless, the observed ESW in **Fig. 1.3.2** is sufficiently broad and can be considered for the application in ASSBs with high-voltage performing cathodes.

NASICON-like structures, as another popular material class of SSEs, have drawn much attention in the past years. Their general formula can be described as $LiM_2(XO_4)_3$ with M = Ti, Ge, Zr and X= P, As, S crystallizing in the rhombohedral space group of $R\bar{3}c$. Typical lithium ion mobilities compose of ionic conductivities around 10^{-3} – 10^{-4} S cm^{-1} and low activation energies of 0.3 – 0.4 eV. Maximum conducitivites could be obtained by aliovalent doping with trivalent Al (also Ga, Sc, In and Y) on the Ti^{4+} site, leading to a greater amount of lithium charge incorporation in the lattice for $Li_{1+x}Al_xTi_{2-x}(PO_4)_3$ with $0.2 \leq x \leq 0.5$.[13,27,57] A great stability towards humidity (see applications for aqueous lithium-air batteries[58]) and high temperatures, as well as a sufficiently broad ESW and the low electronic contribution (10^{-10} – 10^{-11} S cm^{-1})[59–61] are promising prerequisites for their application in ASSBs. However, a similar issue with $Ti^{4+/3+}$ transition as reported for perovskites occurs, leading to the material degradation in contact with lithium. This may be counteracted by replacing the $Ti^{4+}$with Ge^{4+}, which is more difficult to be reduced by Li, but suffers small incisions in the ionic conductivity and ESW.[62]

Deeper insight on the ionic conduction mechanism in LATP is provided in the following sections, as its outstanding stability towards humidity and temperature, in combination with its good electrochemical performance, are providing excellent preconditions for its application in thin film deposition for TFBs or as ABL. Further attention will be paid on this material in **Section 3** of the present thesis, devoted to the development of LATP electrolyte material in bulk and thin film form.

1.3.2 LATP solid electrolyte

Superionic conducting glass-ceramics in the NASICON structure $A_xM_2(XO_4)_3$ such as $Li_{1+x}M'_xTi_{2-x}(PO_4)_3$ were first studied by *Aono et al.*,[63] with trivalent M' e.g. Al^{3+}, Ga^{3+} and Fe^{3+}, concluding an improvement in ionic conductivity upon partial substitution of the tetravalent Ti^{4+} cations. The extent of ionic conductivity is determined by the areal size of vacant triangles, formed by oxygen between corner-sharing TiO_6 octahedra and PO_4 tetrahedra, as shown in **Fig. 1.3.3 (a)**, constituting the "bottlenecks" in the conduction channels responsible for charge transfer limitations in the bulk.[64–66] Under the partial replacement of tetravalent M_{2-x} transition-metal ions with trivalent M'_x cations, the "bottlenecks" can be broadened and the connecting oxygen differently polarized, both acting as possible source in accelerating ionic conduction for the interstitial ions at Li1 and Li3 sites (as shown in **Fig. 1.3.3. (a)**).[57,65]

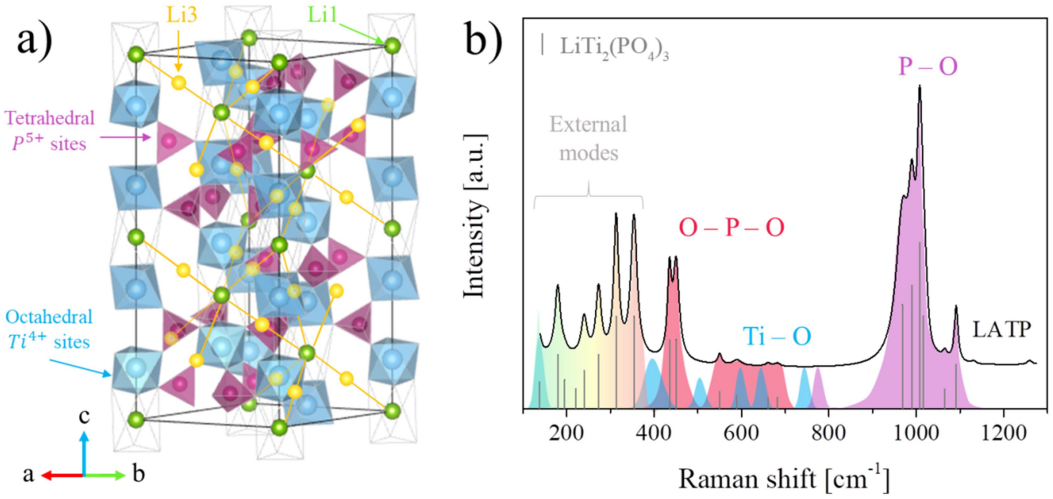

Fig. 1.3.3: NASICON-like crystal structure of $Li_{1+x}Al_xTi_{2-x}(PO_4)_3$ with x = 0.5 in (a) indicating Li-interstitial sites Li1 and Li3. Adapted from *Breuer et al.*[57] Copyright © 2015 The Royal Society of Chemistry. Raman spectrum in (b) of LATP pellet for x ≈ 0.2 (compare *Dashjav et al.*)[67] indicating raman vibrational modes of the host lattice $LiTi_2(PO_4)_3$ (grey vertical lines) reported by *Giarola et al.*,[65] with further assignments for distinctive molecule vibrations concerning phosphates and titanates.[68–70]

Wyckoff cell positions are occupied by Li^+ (6b), Ti^{4+} (12c), P^{5+} (18e) and by O^{2-} (36f) for the host-lattice of $LiTi_2(PO_4)_3$.[65] With site occupation of Li at 6b (Li1) only, the mobility of the ions is blocked.[71] Hence doping with Al^{3+} leads to mixed occupation of the 12c site between Ti and Al, as well as the occupation of different lithium interstitial voids besides Li1, with additional charge distribution on Li2 (6a or 18e) or Li3 (36f),[60,71–73] providing possible pathways for fast Li^+ conduction. In

Fig. 1.3.3 (b) Raman active modes are indicated for LATP, which primarily evolve from the symmetric and asymmetric intramolecular stretching/bending between (O-)P-O and (O-)Ti-O bonds. The resulting 108 possible degrees of freedom in the $LiTi_2(PO_4)_3$ unit cell (36 atoms) anticipate 25 Raman active vibrational modes obtained from group theory calculations.[65,68] External bands (lattice phonon modes) are composed of different vibrations for Li^+, $Ti^{3+/4+}$ and P^{5+} interactions with O^{2-}, which makes their assignment to specific bonds difficult due to their strong overlap. *Burba et al.*[68] and *Dashjav et al.*[67] reported the possibility of determining the lithium content by the change in local disorder of the PO_4^{3-} anion, as a result of Al and Li intercalation into the lattice. Mainly the relative intensities of vibration bands around 430 - 440 cm^{-1} and the broad band of 900 – 1100 cm^{-1} are affected by the Li uptake, with increasingly sharp peaks in the region of 1000 cm^{-1} indicating higher PO_4^{3-} symmetry and therefore relatively low disturbances by dopant and lithium incorporation. Furthermore, Raman spectra allow for a good identification of common secondary phases evolving upon the loss in lithium, such as titania (mainly Rutile and Anatase),[70] $LiTiOPO_4$[69] or $AlPO_4$.[74]

Ionic conductivities of LATP have been reported to be the highest in the bulk, for compositions between $0.3 \leq x \leq 0.5$ with ~ 10^{-3} S cm^{-1} and very low activation energies of 0.13 – 0.19 eV,[57,75,76] characteristic for the typical interstitial lithium diffusion mechanism for the bulk.[77] Hence grain boundaries (GB) are considered an obstacle for the ionic conduction, as their activation energies are much higher and interrupt the bulk ion hopping, causing E_A around 0.3 – 0.4 eV.[57,78] High resistances at the GB may have various origins, such as a certain off-stoichiometry and defect concentration at the interface, causing a distorted atomic order which may hinder the ionic transport. Space-charge areas (Mott-Schottky barriers),[79] commonly associated to the high activation energies at the GB for proton conducting materials, was excluded by *Gellert et al.*[78,80] to be the case in NASICON-like LATP. The discrepancy in ionic conductivities between bulk and GBs was rather associated to highly defective layers between differently oriented grains with a thickness between 5 - 10 nm, adding a number of serial barriers to the ion hopping process. The higher the dissimilar orientation between neighboring grains, the more amorphous appears the separating GB-layer between them, which *Gellert et al.*[80] associated to be very resistive in comparison to the bulk material. On

the other side, the formation of a glassy, amorphous phase is typical for glass-ceramic materials and necessary for their densification, as also previous studies on LATP have shown to improve its electrochemical performance upon improved crystallite contact.[81,82] The formation of a thin, glassy, lithium ion conducting phase between crystallites has shown to improve the ionic conduction, formed either by intrinsically present secondary phases such as $LiTiOPO_4$[83,84] or other compounds of the quaternary Li_2O-Al_2O_3-TiO_2-P_2O_5 system.[85] Even amorphous $AlPO_4$ is known to be present at sintering temperatures below 900 ºC. Although providing much lower ionic conductivites, it still improves the grain-to-grain contact.[82] Glassy phases have been reported by Soman et al.[85] to be present for annealing temperatures up to 850 ºC, which beyond that tend to slowly decompose into crystalline $AlPO_4$. Additionally, the synthetic engineering of a glassy matrix at the GB has been reported for LATP-Bi_2O_3 composites with a slight decrease in activation energies for Li^+ migration.[86]

Therefore, the amorphization of GBs for highly disoriented grains is an ubiquitous phenomenon in the LATP microstructure of great impact on the electrochemical properties. Hence, it requires the attention of certain heat treatments and directed layer compositions in order to achieve a better tailoring of glassy phases and their ionic conductivities across the SSE.

1.3.3 Thin film solid electrolytes

Besides the constant thrive of new material compositions for potential solid ionic conductors with higher ionic conductivities and better overall stabilities, the engineering of the characteristics for already existing SSEs can be carried on at the level of micro-fabrication and cell design, especially in the light of miniaturization for TFBs and 3D microbatteries. Classical thin film deposition techniques such as RF- and ion-beam-sputtering, PLD, MBE, ALD, thermal and electron beam evaporation, as well as sol-gel spin coating are commonly used.[8,35] As it has already been lined out in **Section 1.2.3**, the material properties can be greatly modified from their bulk characteristics when introducing nano-size effects.[25,26,37]

Generally, SSEs applicable in thin film deposition techniques can be divided in amorphous and crystalline layers and have been reviewed in literature.[7,8,35] Amorphous materials allow for dense films with fast isotropic ion conduction

without grain domains as obstacles. Typical glassy electrolytes compose of oxides (Li_2O) and sulfides (Li_2S) as modifiers of the covalent oxide (such as SiO_2, P_2O_5, B_2O_3, etc.) or sulfide (such as SiS_2, P_2S_5, B_2S_3, etc.) glass matrix. Additional doping (usually lithium halides or sulfates) allows for the implementation of a wide range of possible material compositions and high ionic conductivities.[8] Sulfide glassy electrolytes have not experienced as much attention in thin films as in bulk, mainly due to their hygroscopic nature and corrosive reaction in contact with silica, one of the most common substrates used in micro-fabrication (high earth abundance, low cost, good micro- and nano-structurability). Those factors complicate the handling in air and increase the cost, as special substrates and suitable deposition techniques (under protective atmosphere) are essential. Therefore oxide electrolytes are preferably used, which in particular promoted the implementation of lithium phosphorous oxynitride glasses (N-doped Li_3PO_4 as xLi_2O:yP_2O_5:zPON),[87] commonly known as LiPON, which lead to the first commercialized TFBs.[88,89] Its broad ESW of 0.0 – 5.0 V vs. Li/Li^+ (see **Fig. 1.3.2** partially extended by common decomposition products of LiPON such as Li_2O, Li_3P and Li_3N)[88] and good stability towards both lithium and transition metal oxides, in combination with negligible electronic leakage ($< 10^{-14}$ S cm^{-1}) have made it the dominating SSE and ABL material in thin film applications.[8,36] Still it lacks in ionic conductivities in comparison to bulk SSEs, with a maximum of ~10^{-6} S cm^{-1} at 25 ºC being only moderately high,[36] and a typical sensitivity towards air and moisture.[90] Further its amorphous character only persists for rapid heat treatments around 250 ºC at maximum,[91] which generally does not account as high temperature stability and limits the application of LiPON in TFBs, as electrode crystallization usually requires subsequent annealing or relatively high deposition temperatures.[36]

Therefore crystalline SSEs are widely studied, as they exhibit excellent stabilities at higher temperatures.[8] Especially LLZO thin film applications are clearly dominating the research interest, with their high ionic conductivity ~10^{-4} S cm^{-1},[17,46] low activation energies ~ 0.3 eV, broad ESW and good stability towards lithium metal, as well as scalable low electronic conductivities of ~10^{-8} S cm^{-1} and facile synthesis.[56] Therefore Garnets are meeting multiple criteria for a successful application in battery devices, but also exhibit certain drawbacks concerning their

instability towards moisture, eventual dendrite penetration due to their brittle nature,[27,56] as well as the necessity for usually high crystallization temperatures (> 800ºC),[35,86] which only recently could be reduced by co-deposition of Li_2O or Li_3N below 700 ºC or even 400 ºC, respectively.[17,46] Perovskite LLTO as well has been studied as suitable thin film SSE, but is further facing problems in the stability towards lithium metal due to the $Ti^{3+/4+}$ redox-couple, which causes severe electronic conductivity in the material producing a higher risk for self-discharge and cell shorting.[8] A solution of this issue occurred, when depositing amorphous layers of LLTO, which largely inhibit the electronic conductivity and lead to a good stability towards Li. The amorphization happens at the cost of ionic conductivity of $10^{-5} – 10^{-6}$ S cm^{-1}.[7,35]

Regarding LISICON- and NASICON-like electrolytes, these have been only rarely applied as thin films, although especially NASICON-based structures may yield certain advantages for TFBs due to their high ionic bulk conductivities, low electronic contributions and extraordinary stability towards air and moisture. LATP in particular is just as instable towards Li as LLTO and undergoes a redox-reaction around 2.4 V vs. Li/Li^+, but exhibits much lower electronic conductivity ~ 10^{-11} S cm^{-1}, which still allows for its application as SSE in combination with intercalation electrode materials at higher redox potentials.[8,61]

1.4 Intercalation electrode materials

Key for eliminating degradation phenomena arising from lithium corrosion and dendrite growth is the development of new topotactic transition metal oxides for the reversible lithium-ion transfer. First positive intercalation materials were found in the chalcogenides, which later were successfully replaced by transition metal oxides, such as Li_xCoO_2 (LCO) and Li_xNiO_2 (LNO), promising the desired high energy densities, although their high working potential resulting from the cation related redox reactions added another obstacle to be overcome for the stability of the surrounding electrolytic liquid.[92–94] A variety of lithium intercalation materials, anodes as well as cathodes, has been developed over the past decades, especially addressing high-voltage applications for cathodes and suitable replacements for metallic lithium or graphite anodes. **Fig. 1.4.1 (a)** gives a brief overview of current electrode materials in respect to their specific gravimetric capacities achievable

under full lithium de-intercalation. In **Fig. 1.4.1 (b)** the simplified density of states N(ε) of the electrode potential forming versus metallic lithium is given a general outline, with the ESW of the surrounding electrolyte indicated with HOMO and LUMO levels for the electrolyte oxidation or reduction limits, respectively.

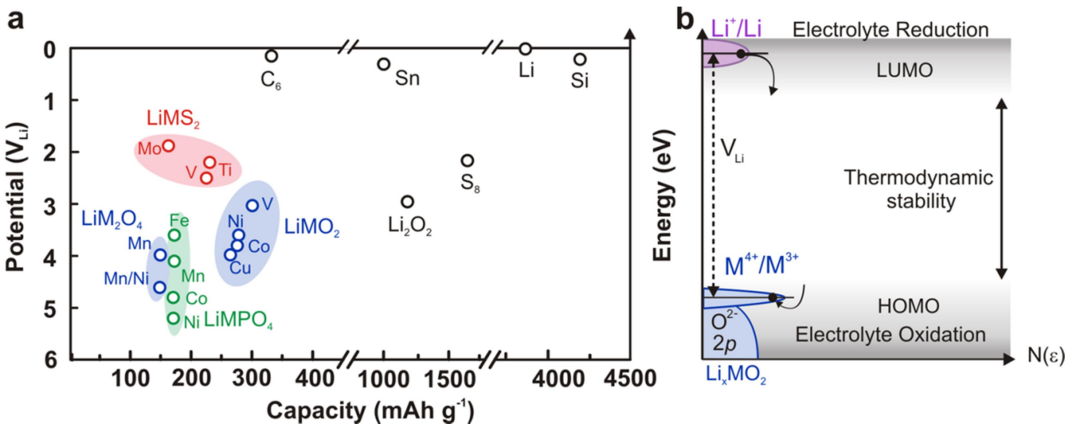

Fig. 1.4.1: Potentials and expected capacities in (a) of various lithium storage materials calculated from full lithium extraction. In (b) the density of states N(ε) is schematically depicted for an electrode material and its energy levels in respect to metallic lithium, indicating the electrode redox potential. HOMO/LUMO positions of the surrounding electrolyte denote the thermodynamic stability window (ESW) between electrolyte reduction and oxidation. Reprinted from *Gauthier et al.*[95] Copyright © 2015, American Chemical Society.

Although LCO and LNO provide high specific capacities, remaining environmental issues and safety hazards in contact with aprotic electrolytes, as well as high cost and eventual health risks associated to mining Co and Ni, led to the simultaneous development of spinel $LiMn_2O_4$ (LMO) as cathode of low cost, high cycling efficiency and a benign environmental impact.[10,96–98] As those materials may suffer certain instabilities due to oxygen release at higher potentials (especially LCO), polyanionic structures in order to strengthen the oxygen bonds have seen further application.[99] Much higher capacities are currently reached using Si, Sn or lithium oxides as intercalation materials, as shown in **Fig. 1.4.1 (a)**.[95] Additionally, new anode materials are provided by Li-In alloys or $Li_4Ti_5O_{12}$ (LTO).[29] Therefore, transition metal oxides as anode or cathode intercalation materials are promising materials for the Li-ion storage and can be divided into layered oxides (e.g. LCO, LNO, Li_2MnO_3), spinel (e.g. LMO, LTO, $LiMn_{1.5}Ni_{0.5}O_4$ (LMNO)) and polyanionic olivine structures (e.g. $LiFePO_4$).[12]

The following sections will be focused on electrodes in the spinel structure, such as LMO and LMNO (cathode), as well as LTO (anode). Due to their high specific

capacities, high rate capability and low volumetric changes upon electrochemical cycling (below 5 %),[40,100] they are of major interest in the fabrication of TFBs and will be the focus of study on subsequent **Sections 4** and **5** in this thesis.

1.4.1 $LiMn_2O_4$ cathode

LMO crystallizes in the spinel structure of crystallographic symmetry $Fd\bar{3}m$, which can generally be described as $A_{1+x}B_{2+x}X_4$, with O^{2-} as X anions occupying the 32e sites, forming a face-centered cubic (fcc) lattice. The octahedral 16d positions are half-occupied by Mn cations (B) and one-eighth of tetrahedral 8a sites is populated by Li^+ (A). The formula can be written as $Li_{(8a)}Mn_{2(16d)}O_{4(32e)}$ with a mixed valence of interconnected six-fold corner-sharing $Mn^{3+/4+}$, creating a migration bottleneck at the 16c octahedral interstitial sites, perpendicular to the plane of Li ion conduction pathways.[96,101,102] The cubic spinel structure causes a strong O_{2p}-Mn_{3d} hybridization, leading to the density of states (DOS) described in **Fig. 1.4.2 (a)** with a splitting of the crystal field in the 3d orbital, assigned to t_{2g} and e_g intraband transitions between the valence and conduction band.[94,103] The difference between the Fermi energy (E_F) of cathode and anode (lithium used as reference) denotes the resulting electrochemical potential of the electrode (here LMO cathode).

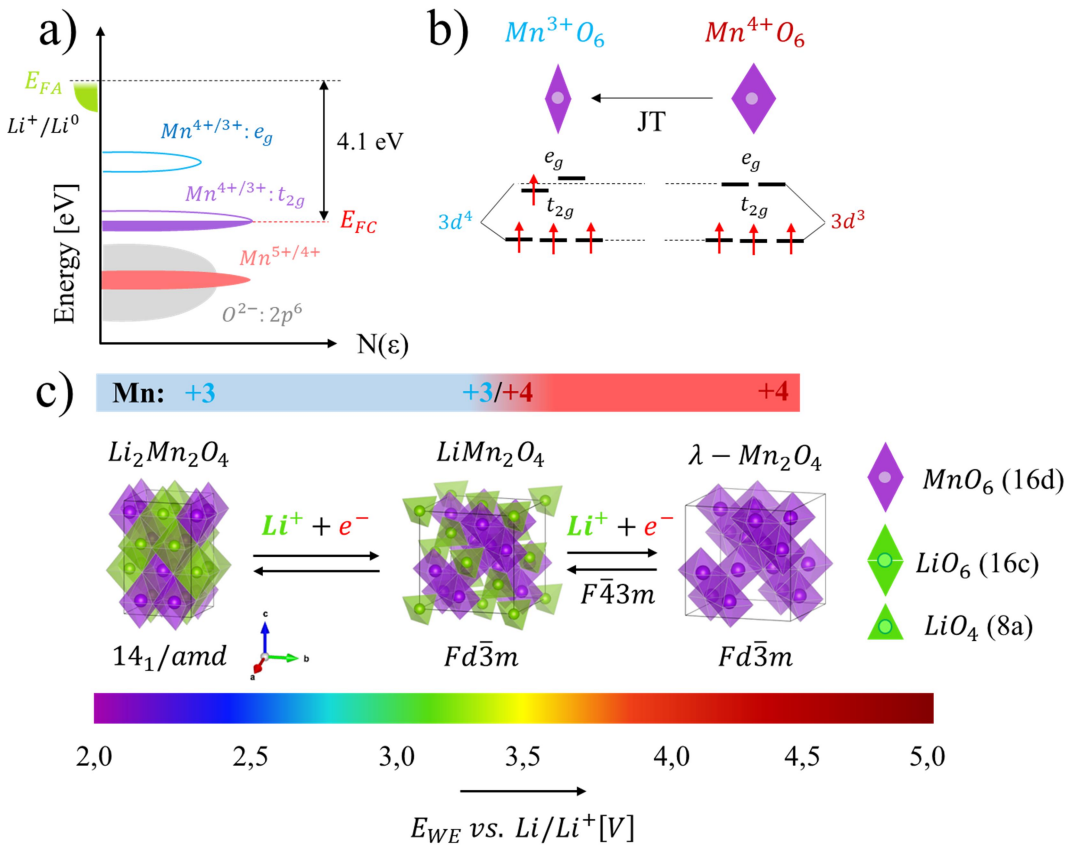

Fig. 1.4.2: Simplified representation of the density of states N(ε) for spinel cathode material $LiMn_2O_4$ in (a) with the energetic difference of 4.1 eV between the Fermi level E_F of anode and cathode.[104] In (b) the crystal-field split of the hybridized 3d orbital is shown for Mn^{3+} and Mn^{4+} octahedra, with JT indicating the Jahn-Teller structural distortion.[105] In (c) the evolution of Mn oxidation states with their corresponding crystal lattices and Wyckoff cell positions, illustrated in dependency of the electrochemical electrode potential vs. Li/Li^+. Structural data for LMO has been deduced from literature.[106,107]

A classical phenomenon of lattice-disordering and associated lattice volume changes in the spinel structure is the Jahn-Teller (JT) effect, occurring for the transition metal ligands with octahedrally coordinated bonds.[40,108] When transforming from Mn^{4+} to Mn^{3+} with the additional spin occupation in the e_g-band, its rearrangement towards lower energies leads to a volume change in the MnO_6 octahedra, as demonstrated in **Fig. 1.4.2 (b)**. The JT-introduced mechanical stress can cause severe material damage until electrode pulverization and therefore should be limited to a minimum.[26] In literature it is generally distinguished between the 4 V and 3 V region (or plateau) vs. Li/Li^+,[40,109] which can be associated with the lattice transformation inside the cubic $Fd\bar{3}m$ and $F\bar{4}3m$ (4 V)[110] or a tetragonal transition towards $I4_1/amd$ (3 V) when LMO is lithiated to $Li_2Mn_2O_4$ (compare **Fig. 1.4.2 (c)**). Specific capacities arising from the complete lithium de-intercalation for

LMO are 148 mAh g^{-1} in the 4 V region, whereas operation in the complete electrochemical window between 2.0 – 4.5 V vs. Li/Li^+ provides 296 mAh g^{-1}.[40] The onset of the JT distortion appears when more than half of the Mn valence states are transformed to the +III oxidation state, which is the case when lithiating below 3.5 V vs. Li/Li^+.[40,109] Reversible redox-reactions upon electrode polarization are located at different standard redox potentials, typical for the $Mn^{3+/4+}$ transform and evolving from the change in the E_{FC} in **Fig. 1.4.2 (a)**. A two-step reaction mechanism occurs for the 4 V region during electrochemical lithium extraction from LMO, under combination of (i) interfacial processes for the reversible (de-) insertion of Li^+ into $LiMn_2O_4$ and (ii) bulk Li^+ diffusion phenomena inside the spinel lattice, as described for **Eq. 1.4.1 (a-c)**.[52,111–113] In the case of solid-liquid interfaces the charge at the interface undergoes an additional (de-) solvation of Li_ε^+ and their adsorption as Li_i^+ in the inner Helmholtz plane (IHP) at the electrode surface, as denoted in **Eq. 1.4.1 (a)**.[52]

$$Li_\varepsilon^+ \rightleftharpoons Li_i^+ \qquad \text{(Eq. 1.4.1a)}$$

$$\frac{1}{2}Li_i^+ + LiMn_2O_4 + \frac{1}{2}e^- \rightleftharpoons Li_{0.5}Mn_2O_4 \qquad \text{(Eq. 1.4.1b)}$$

$$\frac{1}{2}Li_i^+ + Li_{0.5}Mn_2O_4 + \frac{1}{2}e^- \rightleftharpoons \lambda - Mn_2O_4 \qquad \text{(Eq. 1.4.1c)}$$

Under exploration of the 3 V plateau, the so-called overdischarge of LMO towards $Li_{1+x}Mn_2O_4$, the occupation of lithium on the tetrahedral 8a sites in the cubic spinel shifts to octahedral 16c voids in the tetragonal lattice, creating the distorted spinel $Li_{2(16c)}Mn_{2(16d)}O_{4(32e)}$ in the tetragonal crystal system $I4_1/amd$.[40,97,109] The intercalation mechanism can be described as in **Eq. 1.4.2**, with $0 < x < 1$.

$$xLi_i^+ + LiMn_2O_4 + xe^- \rightleftharpoons Li_{1+x}Mn_2O_4 \qquad \text{(Eq. 1.4.2)}$$

The Mn oxidation state completely changes from tetravalent to trivalent, causing an expansion of the unit cell for 6.2 % and a strong increase in the unit cell edge ratio a/c for 16 %.[109] Besides the strong JT-distortion, the problem of manganese dissolution exclusively occurs in liquid electrolytes, mainly due to the disproportionation reaction of manganese Mn^{3+} into Mn^{4+} and soluble Mn^{2+}, leading to the irreversible formation of MnO as described in **Eq. 1.4.3**.[109]

$$Li_2Mn_2O_4 \longrightarrow Li_2MnO_3 + MnO \qquad \text{(Eq.1.4.3)}$$

Stabilization of the 3 V plateau by nano-structuring,[26] coating or doping[40] as nano-shaped materials has shown some improvement to increase stability upon electrochemical lithium insertion at lower potentials, which makes micro-fabrication techniques essential for accessing the potentially high specific material capacities achievable upon additional lithium intercalation.

Furthermore, the Mn^{4+} state can be preserved and the JT-distortion limited, as well as the Mn^{2+} dissolution suppressed by doping LMO with divalent nickel in the Mn/Ni ratio of 3:1, forming $LiMn_{1.5}Ni_{0.5}O_4$ (LMNO) in the cubic (ordered) spinel *P4₃32*, as shown in **Fig. 1.4.3 (a)**.[114] Mn and Ni occupy octahedral 4a and 12d sites, with lithium at tetrahedral 8c sites and two different oxygen sites at 8c and 24e.[115]

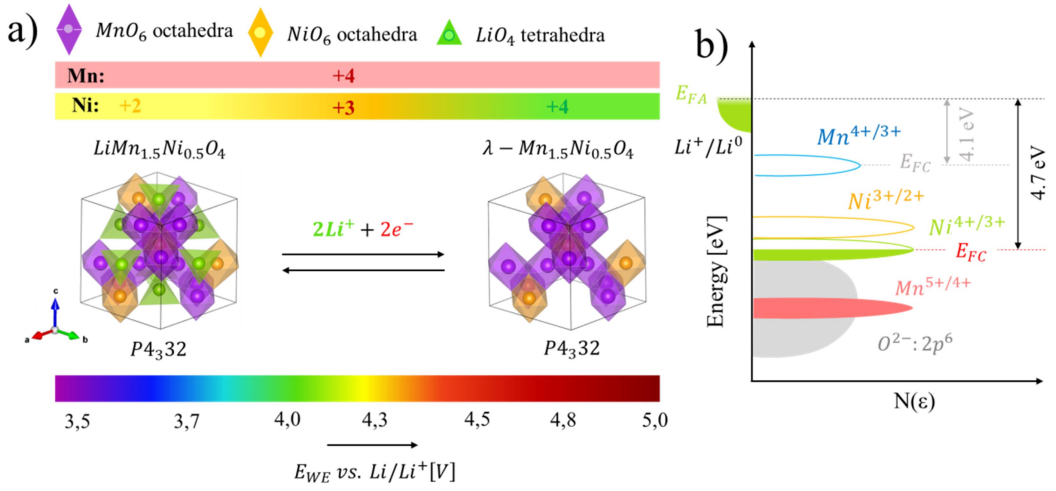

Fig. 1.4.3: Cubic lattice in *P4₃32* of $LiMn_{1.5}Ni_{0.5}O_4$ at different Mn and Ni oxidation states for the corresponding electrochemical electrode potential vs. Li/Li^+ in (a). Simplified representation of the DOS in (b) of $LiMn_{1.5}Ni_{0.5}O_4$ and the corresponding chemical potential of the redox couples relative to the Fermi energy level E_F of the lithium anode.[104,116] Structural data for LMNO has been deduced from literature.[107,117,118]

Band positions of the 3d-orbital in **Fig. 1.4.3 (b)** are complemented by the $Ni^{4+/3+}$ and $Ni^{3+/2+}$ t_{2g}-e_g intraband transitions between conduction band and valence band, leading to a lower Fermi level of the cathode and an increase in the electrode standard potential ~ 4.7 V.[118] Such high redox-potentials require stable electrolytes, which is one of the main issues for the electrochemical stability of LMNO, as electrolyte decomposition leads to the formation of a SEI, which continuously decomposes the cathode material.[118] Ideally, if LMNO exists in the ordered spinel structure *P4₃32*, trivalent charges of Mn^{3+} and Ni^{3+} are only present in very low amounts and hence the potential step between the two redox-couples upon lithium insertion or extraction is fairly small. Often the lithium (de-) intercalation procedure

is referred to only $Ni^{2+/4+}$ as redox couple, as the energy gap between their electronic states is small (see **Fig. 1.4.3 (b)**).[116] On the contrary, disordered spinels crystallizing in the $Fd\bar{3}m$ are slightly oxygen deficient $LiMn_{1.5}Ni_{0.5}O_{4-\delta}$ with a greater content of trivalent charges in the conduction band, slightly increasing the energy gap between $Ni^{3+/4+}$ and $Ni^{3+/2+}$ (compare in **Fig. 1.4.3 (b)**).[115] The site occupation of LMO is restored, with Mn and Ni sharing the 16d octahedral positions.

1.4.2 $Li_4Ti_5O_{12}$ anode

A promising intercalation material for the anodic side of lithium ion batteries has been found in spinel $Li_4Ti_5O_{12}$, best known for its very low lattice expansion of 0.2 – 0.3 % upon lithium uptake, qualifying it as "zero strain" intercalation material, leading to better safety and long cycle lifetimes in batteries.[100,102] As well as LMO it exhibits the spinel typical fcc configuration in the $Fd\bar{3}m$ space group of the primitive cell $A_{1+x}B_{2-x}X_4$. Lithium ions of A are distributed in two tetrahedral 8a sites and *2x* octahedral 16d sites, partially shared with *4-2x* titanium ions of B at the 16d sites (cation ratio A:B of 1:5) and X corresponds to eight oxide ions occupying the 32e sites. Hence the structural formula can be written as $Li_{4(8a)}[LiTi_5^{4+}]_{(16d)}O_{4(32e)}$.[119] The strong Ti-O-hybridization forming TiO_6 octahedra between the O_{2p} and Ti_{3d} orbitals is defining the evolution of electronic states in the conduction and valence bands when inserting or extracting lithium.[102] The simplified representation of the DOS for octahedral Ti^{3+} and Ti^{4+} in the 3d orbital is shown in **Fig. 1.4.4 (a)** and **(b)**, respectively.

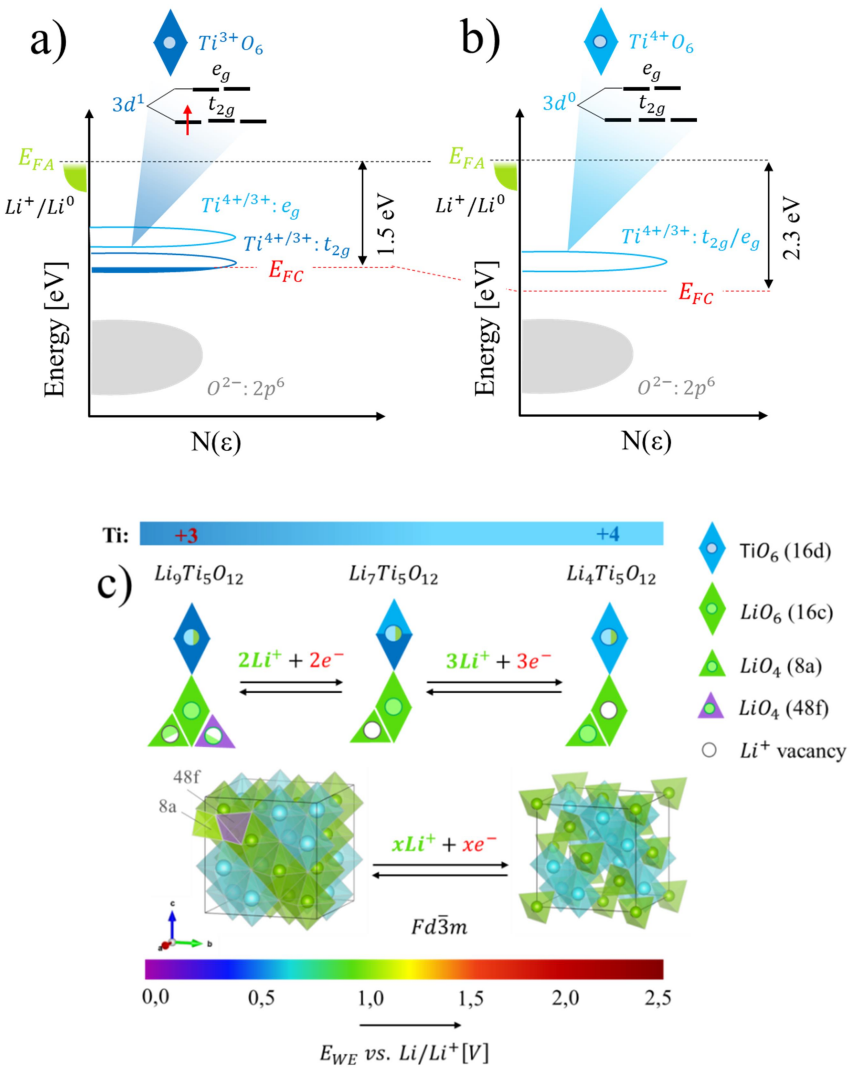

Fig. 1.4.4: Simplified representation of the density of states N(ε) for $Li_7Ti_5O_{12}$ and the corresponding 3d orbital split in the crystal field for Ti^{3+} in (a) and for $Li_4Ti_5O_{12}$ and the corresponding Ti^{4+} in (b).[102,120–123] Transformation of lithium occupancy in LTO during charge/discharge is shown in (c). Strucutral data for LTO has been deduced form literature.[107,121,124]

The insulating character and therefore broad energy band gap ~2.3 eV (1.8 – 3.8 eV in literature)[122,125–129] arise from the empty states in the T_{3d} orbital, leading to a low intrinsic diffusion coefficient and poor rate capability.[102,126] During lithium intercalation into $Li_{4+x}Ti_5O_{12}$ the oxidation state of titanium +IV is changed to +III and lithium occupation transfers from the tetrahedral 8a sites to octahedral 16c sites as described in **Eq. 1.4.4,** with the standard redox potential of 1.5 V and a theoretical capacity of 175 mAh g^{-1}.[119,122]

$$Li_{3(8a)}[LiTi_5^{4+}]_{(16d)}O_{12(32e)} + 3Li_i^+$$

$$+3e^- \rightleftharpoons Li_{6(16c)}[LiTi_3^{3+}Ti_2^{4+}]_{(16d)}O_{12(32\ )} \qquad \text{(Eq. 1.4.4)}$$

Recent studies showed that lithium uptake is not limited to its accommodation by vacant octahedral sites, as $Li_7Ti_5O_{12}$ is capable of accepting additional two lithium ions under reduction of the remaining Ti_2^{4+} and occupation of tetrahedral 8a sites by Li^+, as described in **Eq. 1.4.5**.

$$Li_{6(16c)}[LiTi_3^{3+}Ti_2^{4+}]_{(16d)}O_{12(32e)} + 2Li_i^+ + 2e^- \rightleftharpoons Li_{2(8a)}Li_{6(16c)}[LiTi_5^{3+}]_{(16d)}O_{12(32\ )} \qquad \text{(Eq. 1.4.5)}$$

The resulting theoretical capacity hence is bound to the content of tetravalent titanium ions and can be extended to 239 mAh g^{-1} for lithium uptake between 0.01 – 2.5 V vs. Li/Li^+. As *Liu et al.*[130] could demonstrate high reversibility, minor lattice volume changes and the formation of a stable SEI layer upon lithiation to such low potentials, the extension of the operational window of LTO allows for higher cell voltages and a greater specific energy for lithium-ion batteries as safe alternative to common graphite anodes.

1.5 In-situ and operando techniques

Nature and driving forces of electrochemical reactions are exposed to a multitude of influences and require detailed understanding in order to avoid cell failure. In-situ and operando techniques are capable of revealing reaction kinetics, phase transformations, volume changes and buried interfaces under an approximation of operating conditions.[131] With the recognition of interfacial phenomena being the main cause for battery degradation and high internal resistances, the availability of suitable characterization techniques expanded rapidly over a broad field of popular and highly sophisticated methods, which have seen elaborate reviews in literature,[9,132] and can be distinguished as mechanical, chemical and electrochemical characterization, as demonstrated in **Fig 1.5.1 (a)** with a brief summary of corresponding techniques.[131] Especially electrochemical in-situ characterization is of outermost importance, as interfacial phenomena are transient without electrode polarization and ex-situ performed chemical characterization lacks of the proximity to realistic in-time operation conditions.

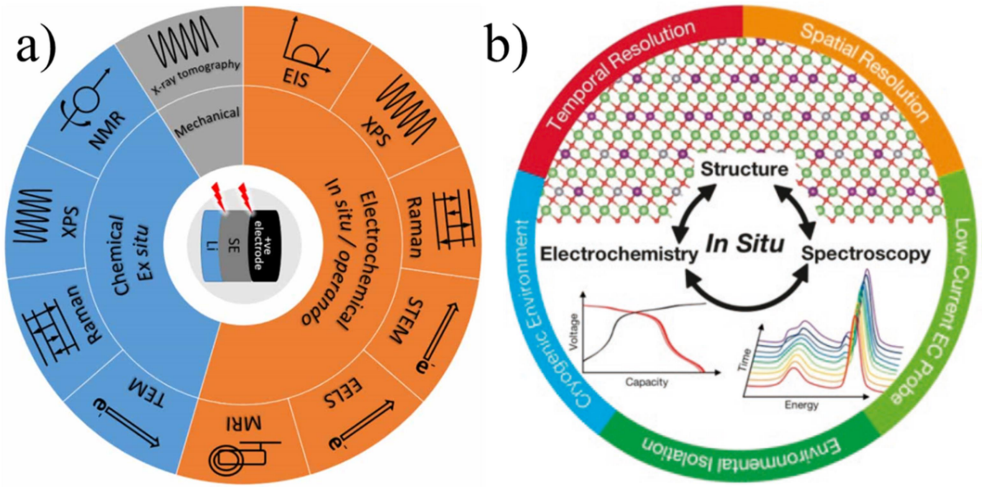

Fig. 1.5.1: Schematic illustration of commonly used ex-situ and in-situ/operando techniques in (a)for monitoring electrochemically induced phenomena at the interfaces in all-solid-state lithium-ion batteries. Reprinted with permission from *Pasta et al.*[131] Copyright © 2020 IOP publishing, Ltd. In (b) the required developments for improved in-situ characterization of electrochemical, structural and elemental changes upon device operation are listed, namely enhanced time and spatial resolution, low current measurements and environmental isolation. Reproduced from *Wynn et al.*[132] Copyright © Materials Research Society 2018.

Applications of in-situ analysis spread over a great variety of different techniques such as (scanning) transmission electron microscopy (S)TEM[133,134] including electron holography (EH)[135,136] and electron energy loss spectroscopy (EELS),[137,138] secondary ion mass spectroscopy (SIMS) under isotopic ion exchange,[139] X-ray diffraction (XRD)[140] and imaging,[141] synchrotron X-ray[142–149] or neutron diffraction (ND),[110] X-ray photoelectron spectroscopy (XPS),[150] X-ray tomography,[151] Raman spectroscopy[152–154] and shell-isolated nanoparticles enhanced Raman spectroscopy (SHINERS),[155] Fourier transform infrared spectroscopy (FTIR),[156,157] dynamic electrochemical impedance spectroscopy (EIS),[52,140] solid-state nuclear magnetic resonance (NMR) with in-situ magnetic resonance imaging (MRI),[158] as well as probe-induced surface potential mapping with scanning probe microscopy (SPM),[159,160] e.g. Kelvin probe force microscopy (KPFM),[161] etc.[9] Certain drawbacks for the broad applicability of some in-situ/operando methods evolve from complicated and expensive sample preparation (e.g electron-transparent lamellas for TEM-related analysis), beam damage (e.g. X-ray, electron beam or certain laser wavelengths for Raman), special ambient conditions for the precise observation of electron and ion movements (e.g. vacuum, cryogenic systems, ionic liquids for SIMS) or certain material properties (e.g. bulk, powder, thin film, sensitivity to air and/or moisture, etc.). The remaining challenges can be

summarized as shown in **Fig. 1.5.1 (b)**, concerning especially low signal-to-noise ratios due to disturbances by high applied currents or voltages, as well as low time resolutions, unsuitable for the monitoring of fast reaction kinetics. Additionally, high spatial resolution is required for the observation of nano-metric interfaces and a better isolation of the environment for achieving realistic material and operation conditions.[132] Therefore, some techniques may not always be non-destructive or in good proximity of reality, as well as their availability maybe limited by high acquisition cost and expensive sample preparation.

In summary, the search for facile and inexpensive in-situ/operando techniques for device characterization and the development of stable all-solid-state battery technology may both profit from mutual improvements. Especially optical techniques give opportunity to a non-destructive device characterization, which in combination with direct observations on the level of electronic band transitions is a powerful tool for in-situ/operando probing reaction kinetics. In **Section 5** of this thesis, the capabilities of operando Raman spectroscopy and Spectroscopic Ellipsometry (SE) for probing lithium-ion migration upon device operation are evaluated in greater detail.

1.6 Scope of the thesis

This thesis is devoted to the fabrication of thin film battery components by Pulsed Laser Deposition (PLD) for the application in solid-state lithium-ion microbatteries and the understanding of lithium migration processes at solid-solid interfaces, as well as the implementation of operando optical techniques for a facile and inexpensive monitoring of charge transfer phenomena during electrochemically induced material transitions. The necessity for high specific energy and specific power battery devices have made thin films attractive to overcome certain limitations in rate capabilities of bulk materials and internal resistances caused by layer thicknesses of solid electrolytes, as well as by passivating layers at the electrode-electrolyte interface. Suitable in-situ techniques for the better understanding of charge/discharge phenomena, state of charge (SOC) and interface resistances are essential but also complicated to be realized at the nano-scale and require sensitive spatial and time resolution, while maintaining ambient probing conditions as close as possible to the device reality.

In order to provide a good understanding of the thin film synthesis and specific material characteristics of thin film battery components, this thesis has been organized with the following sections:

- **Section 2** contains a detailed description of the synthesis techniques used for the preparation of bulk glass-ceramics by solid-state synthesis and the subsequent thin film deposition by PLD. Further analytical techniques via optical or electrochemical material probing are introduced for ex-situ characterization, as well as for operando monitoring in the spectroscopic ellipsometry.

- **Section 3** is dedicated to the fabrication of solid-state electrolyte thin films composed of the NASICON-like $Li_{1+x}Al_xTi_{2-x}(PO_4)_3$ (LATP) by large-area (LA) PLD. Further the effect of a post-deposition heat treatment is elucidated as pursue of layer optimization for thin film battery applications, with special remark on the differences in bulk and grain boundary behavior.

- **Section 4** deals with the thin film deposition of spinel $LiMn_2O_4$ (LMO) cathode and spinel $Li_4Ti_5O_{12}$ (LTO) anode materials, under application of a

multi-layering/co-deposition approach in the LA-PLD. General structural and microstructural, as well as optical and electrochemical characterization are carried out for both systems. Special attention is paid to the electrochemical behavior of LMO thin films in the 3 V plateau, as well to the effect of different lithium content in LTO layers on their electrochemical properties.

- **Section 5** is devoted to the time resolved monitoring of lithium insertion and extraction in thin film cathodes composed of LMO and LMNO ($LiMn_{1.5}Ni_{0.5}O_4$) under application operando Raman spectroscopy and operando Spectroscopic Ellipsometry (SE). The aptitude of SE as novel optical operando technique in the field of electrochemical storage devices is further elaborated concerning the resolution of electronic band transitions upon charge/discharge and the materials SOC.

- **Section 6** provides a summary of the overall conclusions, concerning the applicability of LATP thin films in all-solid-state battery devices, the electrochemical performance of spinel electrode thin films fabricated by the PLD co-deposition approach, as well as the applicability of operando SE for the time-resolved monitoring of electrochemical charge storage mechanisms.

References

(1) Tarascon, J. Key Challenges in Future Li-Battery Research. *Philos. Trans. R. Soc. A* **2010**, *368*. https://doi.org/10.1098/rsta.2010.0112.

(2) Wang, Y.; Liu, B.; Li, Q.; Cartmell, S.; Ferrara, S.; Deng, Z. D.; Xiao, J. Lithium and Lithium Ion Batteries for Applications in Microelectronic Devices: A Review. *J. Power Sources* **2015**, *286*, 330–345.

(3) Liao, G.; Mahrholz, T.; Geier, S.; Wierach, P.; Wiedemann, M. Nanostructured All-Solid-State Supercapacitors Based on NASICON-Type Li1.4 Al0.4 Ti1.6 (P O4)3 Electrolyte. *J. Solid State Electrochem.* **2018**, *22* (4), 1055–1061.

(4) Soavi, F.; Bettini, L. G.; Piseri, P.; Milani, P.; Santoro, C.; Atanassov, P.; Arbizzani, C. Miniaturized Supercapacitors: Key Materials and Structures towards Autonomous and Sustainable Devices and Systems. *J. Power Sources* **2016**, *326*, 717–725. https://doi.org/10.1016/j.jpowsour.2016.04.131.

(5) Ning, H.; Pikul, J. H.; Zhang, R.; Li, X.; Xu, S.; Wang, J.; Rogers, J. A.; King, W. P.; Braun, P. V. Holographic Patterning of High-Performance on-Chip 3D Lithium-Ion Microbatteries. *Proc. Natl. Acad. Sci.* **2015**, *112* (21), 6573–6578. https://doi.org/10.1073/pnas.1423889112.

(6) Wu, F.; Yu, P.; Mao, L. Self-Powered Electrochemical Systems as Neurochemical Sensors: Toward Self-Triggered in Vivo Analysis of Brain Chemistry. *Chem. Soc. Rev.* **2017**, *46* (10), 2692–2704. https://doi.org/10.1039/c7cs00148g.

(7) Julien, C. M.; Mauger, A. Pulsed Laser Deposited Films for Microbatteries. *Coatings* **2019**, *9* (6), 386. https://doi.org/10.3390/coatings9060386.

(8) Xia, H.; Wang, H. L.; Xiao, W.; Lai, M. O.; Lu, L. Thin Film Li Electrolytes for All-Solid-State Micro-Batteries. *Int. J. Surf. Sci. Eng.* **2009**, *3* (1–2), 23–43.

(9) Liu, D.; Shadike, Z.; Lin, R.; Qian, K.; Li, H.; Li, K.; Wang, S.; Yu, Q.; Liu, M.; Ganapathy, S.; others; Qin, X.; Yang, Q.-H.; Wagemaker, M.; Kang, F.; Yang, X.-Q.; Li, B. Review of Recent Development of In Situ/Operando Characterization Techniques for Lithium Battery Research. *Adv. Mater.* **2019**, *31* (28), 1806620. https://doi.org/10.1002/adma.201806620.

(10) Broussely, M.; Biensan, P.; Simon, B. Lithium Insertion into Host Materials : The Key to Success for Li Ion Batteries. *Electrochim. Ac* **1999**, *45*, 3–22.

(11) Mauger, A.; Julien, C. M. Critical Review on Lithium-Ion Batteries : Are They Safe? Sustainable? *Ionics (Kiel).* **2017**, *23*, 1933–1947. https://doi.org/10.1007/s11581-017-2177-8.

(12) Goodenough, J. B.; Park, K. S. The Li-Ion Rechargeable Battery: A Perspective. *J. Am. Chem. Soc.* **2013**, *135* (4), 1167–1176. https://doi.org/10.1021/ja3091438.

(13) Bachman, J. C.; Muy, S.; Grimaud, A.; Chang, H.-H.; Pour, N.; Lux, S. F.; Paschos, O.; Maglia, F.; Lupart, S.; Lamp, P. Inorganic Solid-State Electrolytes for Lithium Batteries: Mechanisms and Properties Governing Ion Conduction. *Chem. Rev.* **2015**, *116* (1), 140–162.

(14) Sun, C.; Liu, J.; Gong, Y.; Wilkinson, D. P.; Zhang, J. Recent Advances in All-Solid-State Rechargeable Lithium Batteries. *Nano Energy* **2017**, *33*, 363–386. https://doi.org/10.1016/j.nanoen.2017.01.028.

(15) Richards, W. D.; Miara, L. J.; Wang, Y.; Kim, J. C.; Ceder, G. Interface Stability in

Solid-State Batteries. *Chem. Mater.* **2016**, *28* (1), 266–273. https://doi.org/10.1021/acs.chemmater.5b04082.

(16) Janek, J.; Zeier, W. G. A Solid Future for Battery Development. *Nat. Publ. Gr.* **2016**, *1* (September), 1–4. https://doi.org/10.1038/nenergy.2016.141.

(17) Sastre, J.; Priebe, A.; Döbeli, M.; Michler, J.; Tiwari, A. N.; Romanyuk, Y. E. Lithium Garnet Li 7 La 3 Zr 2 O 12 Electrolyte for All-Solid-State Batteries : Closing the Gap between Bulk and Thin Film Li-Ion Conductivities. *Adv. Mater. Interfaces* **2020**, *7* (2000425). https://doi.org/10.1002/admi.202000425.

(18) Randau, S.; Weber, D. A.; Kötz, O.; Koerver, R.; Braun, P.; Weber, A.; Ivers-tiffée, E.; Adermann, T.; Kulisch, J.; Zeier, W. G.; Richter, F. H.; Janek, J. Benchmarking the Performance of All-Solid-State Lithium Batteries. *Nat. Energy* **2020**, *5*, 259–270. https://doi.org/10.1038/s41560-020-0565-1.

(19) Kato, Y.; Hori, S.; Saito, T.; Suzuki, K.; Hirayama, M.; Mitsui, A.; Yonemura, M.; Iba, H.; Kanno, R. High-Power All-Solid-State Batteries Using Sulfide Superionic Conductors. *Nat. Energy* **2016**, *1* (April), 1–7. https://doi.org/10.1038/NENERGY.2016.30.

(20) Linden, D.; Reddy, T. B. Handbook of Batteries: Third Edition. McGraw Hill 2002.

(21) Kato, Y.; Shiotani, S.; Morita, K.; Suzuki, K.; Hirayama, M.; Kanno, R. All-Solid-State Batteries with Thick Electrode Configurations. *J. Phys. Chem. Lett.* **2018**, *9*, 607–613. https://doi.org/10.1021/acs.jpclett.7b02880.

(22) Van den Bossche, P.; Vergels, F.; Van Mierlo, J.; Matheys, J.; Van Autenboer, W. SUBAT : An Assessment of Sustainable Battery Technology. *J. Power Sources* **2006**, *162*, 913–919. https://doi.org/10.1016/j.jpowsour.2005.07.039.

(23) Kanno, R.; Murayama, M.; Inada, T.; Kobayashi, T.; Sakamoto, K.; Sonoyama, N.; Yamada, A.; Kondo, S. A Self-Assembled Breathing Interface for All-Solid-State Ceramic Lithium Batteries. *Electrochem. Solid-State Lett.* **2004**, *7* (12), 455–458. https://doi.org/10.1149/1.1809553.

(24) Du, M.; Liao, K.; Lu, Q.; Shao, Z. Recent Advances in the Interface Engineering of Solid-State Li-Ion Batteries with Artificial Buffer Layers: Challenges, Materials, Construction, and Characterization. *Energy Environ. Sci.* **2019**.

(25) Maier, J. Size Effects on Mass Transport and Storage in Lithium Batteries. *J. Power Sources* **2007**, *174* (2), 569–574. https://doi.org/10.1016/j.jpowsour.2007.06.246.

(26) Armstrong, M. J.; O'Dwyer, C.; Macklin, W. J.; Holmes, J. D. Evaluating the Performance of Nanostructured Materials as Lithium-Ion Battery Electrodes. *Nano Research*. Tsinghua University Press December 4, 2014, pp 1–62. https://doi.org/10.1007/s12274-013-0375-x.

(27) Pervez, S. A.; Cambaz, M. A.; Thangadurai, V.; Fichtner, M. Interface in Solid-State Lithium Battery : Challenges , Progress , and Outlook. *ACS Appl. Mater. Interfaces* **2019**, *11*, 22029–22050. https://doi.org/10.1021/acsami.9b02675.

(28) Hirotoshi, Y. Interfaces of Solid Electrolytes: Fundamentals and Applications. *J. Indian Inst. Scinece* **2016**, *96* (4), 315–324.

(29) Famprikis, T.; Canepa, P.; Dawson, J. A.; Islam, M. S.; Masquelier, C. Fundamentals of Inorganic Solid-State Electrolytes for Batteries. *Nat. Mater.* **2019**, *18*, 1278–1291.

(30) Wenzel, S.; Sedlmaier, S. J.; Dietrich, C.; Zeier, W. G.; Janek, J. Interfacial Reactivity and Interphase Growth of Argyrodite Solid Electrolytes at Lithium Metal Electrodes.

Solid State Ionics **2018**, *318* (July 2017), 102–112. https://doi.org/10.1016/j.ssi.2017.07.005.

(31) Kim, C.; Phillips, P. J.; Xu, L.; Dong, A.; Buonsanti, R.; Klie, R. F.; Cabana, J. Stabilization of Battery Electrode/Electrolyte Interfaces Employing Nanocrystals with Passivating Epitaxial Shells. *Chem. Mater.* **2015**, *27*, 394–399.

(32) Liu, Y.; Sun, Q.; Zhao, Y.; Wang, B.; Kaghazchi, P.; Adair, K. R.; Li, R.; Zhang, C.; Liu, J.; Kuo, L.-Y.; Hu, Y.; Sham, T.-K.; Zhang, L.; Yang, R.; Lu, S.; Song, X.; Sun, X. Stabilizing the Interface of NASICON Solid Electrolyte against Li Metal with Atomic Layer Deposition. *ACS Appl. Mater. Interfaces* **2018**, *10* (37), 31240–31248. https://doi.org/10.1021/acsami.8b06366.

(33) Venkateswara Rao, C.; Soler, J.; Katiyar, R.; Shojan, J.; West, W. C.; Katiyar, R. S. Investigations on Electrochemical Behavior and Structural Stability of Li1.2 Mn0.54 Ni0.13 Co0.13 O2 Lithium-Ion Cathodes via in-Situ and Ex-Situ Raman Spectroscopy. *J. Phys. Chem. C* **2014**, *118* (26), 14133–14141. https://doi.org/10.1021/jp501777v.

(34) Alva, G.; Kim, C.; Yi, T.; Cook, J. B.; Xu, L.; Nolis, G. M.; Cabana, J. Surface Chemistry Consequences of Mg-Based Coatings on Li Ni0.5 Mn1.5 O4 Electrode Materials upon Operation at High Voltage. *J. Phys. Chem. C* **2014**, *18*, 10596–10605.

(35) Liang, X.; Tan, F.; Wei, F.; Du, J. Research Progress of All Solid-State Thin Film Lithium Battery. *IOP Conf. Ser. Earth Environ. Sci.* **2019**, *218* (1), 12138. https://doi.org/10.1088/1755-1315/218/1/012138.

(36) Moitzheim, S.; Put, B.; Vereecken, P. M. Advances in 3D Thin-Film Li-Ion Batteries. *Adv. Mater. Interfaces* **2019**, *1900805*, 1–17. https://doi.org/10.1002/admi.201900805.

(37) Bruce, P. G.; Scrosati, B.; Tarascon, J. Nanomaterials for Rechargeable Lithium Batteries. *Angew. Chemie Int. Ed.* **2008**, *47*, 2930–2946. https://doi.org/10.1002/anie.200702505.

(38) Okubo, M.; Mizuno, Y.; Yamada, H.; Kim, J.; Hosono, E.; Zhou, H.; Kudo, T.; Honma, I. Fast Li-Ion Insertion into Nanosized LiMn 2 O 4 without Domain Boundaries. *ACS Nano* **2010**, *4* (2), 741–752.

(39) Quan, Z.; Ohguchi, S.; Kawase, M.; Tanimura, H.; Sonoyama, N. Preparation of Nanocrystalline LiMn2O4 Thin Film by Electrodeposition Method and Its Electrochemical Performance for Lithium Battery. *J. Power Sources* **2013**, *244*, 375–381. https://doi.org/10.1016/j.jpowsour.2012.12.087.

(40) Put, B.; Vereecken, P. M.; Labyedh, N.; Sepulveda, A.; Huyghebaert, C.; Radu, I. P.; Stesmans, A. High Cycling Stability and Extreme Rate Performance in Nanoscaled LiMn2O4 Thin Films. *ACS Appl. Mater. Interfaces* **2015**, *7* (40), 22413–22420. https://doi.org/10.1021/acsami.5b06386.

(41) Simmen, F.; Lippert, T.; Novák, P.; Neuenschwander, B.; Döbeli, M.; Mallepell, M.; Wokaun, A. The Influence of Lithium Excess in the Target on the Properties and Compositions of Li1+x Mn2 O4-δ Thin Films Prepared by PLD. *Appl. Phys. A* **2008**, *93* (3), 711–716. https://doi.org/10.1007/s00339-008-4701-1.

(42) Julien, C.; Haro-Poniatowski, E.; Camacho-Lopez, M. A.; Escobar-Alarcon, L.; Jimenez-Jarquin, J. Growth of LiMn2O4 Thin Films by Pulsed-Laser Deposition and Their Electrochemical Properties in Lithium Microbatteries. *Mater. Sci. Eng. B Solid-State Mater. Adv. Technol.* **2000**, *72* (1), 36–46. https://doi.org/10.1016/S0921-5107(99)00598-X.

(43) Rho, Y. H.; Dokko, K.; Kanamura, K. Li+ Ion Diffusion in LiMn2O4 Thin Film Prepared by PVP Sol-Gel Method. *J. Power Sources* **2006**, *157* (1), 471–476.

https://doi.org/10.1016/j.jpowsour.2005.07.050.

(44) Nazri, G. A.; Pistoia, G. *Lithium Batteries: Science and Technology*; Springer US, 2008.

(45) Li, D.; Ma, Z.; Xu, J.; Li, Y.; Xie, K. High Temperature Property of All-Solid-State Thin Film Lithium Battery Using LiPON Electrolyte. *Mater. Lett.* **2014**, *134*, 237–239. https://doi.org/10.1016/j.matlet.2014.07.092.

(46) Pfenninger, R.; Struzik, M.; Garbayo, I.; Stilp, E.; Rupp, J. L. M. A Low Ride on Processing Temperature for Fast Lithium Conduction in Garnet Solid-State Battery Films. *Nat. Energy* **2019**, *4* (6), 475–483. https://doi.org/10.1038/s41560-019-0384-4.

(47) Fehse, M.; Trócoli, R.; Hernández, E.; Ventosa, E.; Sepúlveda, A.; Morata, A.; Tarancón, A. An Innovative Multi-Layer Pulsed Laser Deposition Approach for LiMn2O4 Thin Film Cathodes. *Thin Solid Films* **2018**, *648*, 108–112. https://doi.org/10.1016/j.tsf.2018.01.015.

(48) Fehse, M.; Trócoli, R.; Ventosa, E.; Hernández, E.; Sepúlveda, A.; Morata, A.; Tarancón, A. Ultrafast Dischargeable LiMn2O4 Thin-Film Electrodes with Pseudocapacitive Properties for Microbatteries. *ACS Appl. Mater. Interfaces* **2017**, *9* (6), 5295–5301.

(49) Trócoli, R.; Morata, A.; Fehse, M.; Stchakovsky, M.; Sepúlveda, A.; Tarancón, A. High Specific Power Dual-Metal-Ion Rechargeable Microbatteries Based on Li Mn2 O4 and Zinc for Miniaturized Applications. *ACS Appl. Mater. Interfaces* **2017**, *9* (38), 32713–32719. https://doi.org/10.1021/acsami.7b08883.

(50) Singh, D.; Kim, W.-S.; Craciun, V.; Hofmann, H.; Singh, R. K. Microstructural and Electrochemical Properties of Lithium Manganese Oxide Thin Films Grown by Pulsed Laser Deposition. *Appl. Surf. Sci.* **2006**, 516–521. https://doi.org/10.1007/s11581-007-0134-7.

(51) Tang, S. B.; Lai, M. O.; Lu, L.; Tripathy, S. Comparative Study of LiMn 2 O 4 Thin Film Cathode Grown at High , Medium and Low Temperatures by Pulsed Laser Deposition. *J. Solid State Chem.* **2006**, *179*, 3831–3838. https://doi.org/10.1016/j.jssc.2006.08.025.

(52) Erinmwingbovo, C.; Siller, V.; Nuñez, M.; Trócoli, R.; Brogioli, D.; Morata, A.; La Mantia, F. Dynamic Impedance Spectroscopy of LiMn2O4 Thin Films Made by Multi-Layer Pulsed Laser Deposition. *Electrochim. Acta* **2020**, *331*. https://doi.org/10.1016/j.electacta.2019.135385.

(53) Greer, J. A.; Tabat, M. D. Large-Area Pulsed Laser Deposition: Techniques and Applications. *J. Vac. Sci. Technol. A Vacuum, Surfaces, Film.* **1995**, *13* (3), 1175–1181. https://doi.org/10.1116/1.579857.

(54) Robertson, A. D.; West, A. R.; Ritchie, A. G. Review of Crystalline Lithium-Ion Conductors Suitable for High Temperature Battery Applications. *Solid State Ionics* **1997**, *104* (1–2), 1–11.

(55) Lotsch, B. V; Maier, J. Relevance of Solid Electrolytes for Lithium-Based Batteries : A Realistic View. *J. Electroceramics* **2017**, *38*, 128–141. https://doi.org/10.1007/s10832-017-0091-0.

(56) Wang, C.; Fu, K.; Kammampata, S. P.; Mcowen, D. W.; Samson, A. J.; Zhang, L.; Hitz, G. T.; Nolan, A. M.; Wachsman, E. D.; Mo, Y.; Thangadurai, V.; Hu, L. Garnet-Type Solid-State Electrolytes : Materials , Interfaces , and Batteries. *Chem. Rev.* **2020**, *120* (10), 4257–4300. https://doi.org/10.1021/acs.chemrev.9b00427.

(57) Breuer, S.; Prutsch, D.; Ma, Q.; Epp, V.; Preishuber-Pflügl, F.; Tietz, F.; Wilkening, M.

Separating Bulk from Grain Boundary Li Ion Conductivity in the Sol-Gel Prepared Solid Electrolyte Li1.5 Al0.5 Ti1.5 (P O4)3. *J. Mater. Chem. A* **2015**, *3* (42), 21343–21350.

(58) Hasegawa, S.; Imanishi, N.; Zhang, T.; Xie, J.; Hirano, A.; Takeda, Y.; Yamamoto, O. Study on Lithium/Air Secondary Batteries-Stability of NASICON-Type Lithium Ion Conducting Glass-Ceramics with Water. *J. Power Sources* **2009**, *189* (1), 371–377. https://doi.org/10.1016/j.jpowsour.2008.08.009.

(59) Popovici, D.; Nagai, H.; Fujishima, S.; Akedo, J. Preparation of Lithium Aluminum Titanium Phosphate Electrolytes Thick Films by Aerosol Deposition Method. *J. Am. Ceram. Soc.* **2011**, *94* (11), 3847–3850. https://doi.org/10.1111/j.1551-2916.2011.04551.x.

(60) Monchak, M.; Hupfer, T.; Senyshyn, A.; Boysen, H.; Chernyshov, D.; Hansen, T.; Schell, K. G.; Bucharsky, E. C.; Hoffmann, M. J.; Ehrenberg, H. Lithium Diffusion Pathway in Li1.3 Al0.3 Ti1.7 (P O4)3 (LATP) Superionic Conductor. *Inorg. Chem.* **2016**, *55* (6), 2941–2945.

(61) Wu, X. M.; Li, X. H.; Wang, S. W.; Wang, Z.; Zhang, Y. H.; Xu, M. F.; He, Z. Q. Preparation and Characterization of Lithium-Ion-Conductive Li1.3 Al0.3 Ti1.7 (P O4)3 Thin Films by the Solution Deposition. *Thin Solid Films* **2003**, *425* (1–2), 103–107. https://doi.org/10.1016/S0040-6090(02)01094-5.

(62) Li, L.; Zhang, Z.; Luo, L.; Jiao, J.; Huang, W.; Wang, J.; Li, C.; Han, X.; Chen, S. Enhancing the Interface Stability of Li 1.3 Al 0.3 Ti 1.7 (PO4)3 and Lithium Metal by Amorphous Li 1.5 Al 0.5 Ge 1.5 (PO4)3 Modification. *Ionics (Kiel).* **2020**, *26*, 3815–3821.

(63) Aono, H. Ionic Conductivity of Solid Electrolytes Based on Lithium Titanium Phosphate. *J. Electrochem. Soc.* **1990**, *137* (4), 1023. https://doi.org/10.1149/1.2086597.

(64) Wang, G. X.; Bradhurst, D. H.; Dou, S. X.; Liu, H. K. LiTi2(PO4)3 with NASICON-Type Structure as Lithium-Storage Materials. *J. Power Sources* **2003**, *124* (1), 231–236. https://doi.org/10.1016/S0378-7753(03)00609-8.

(65) Giarola, M.; Sanson, A.; Tietz, F.; Pristat, S.; Dashjav, E.; Rettenwander, D.; Redhammer, G. J.; Mariotto, G. Structure and Vibrational Dynamics of NASICON-Type Li Ti2 (P O4)3. *J. Phys. Chem. C* **2017**, *121* (7), 3697–3706.

(66) Arbi, K.; Hoelzel, M.; Kuhn, A.; García-Alvarado, F.; Sanz, J. Local Structure and Lithium Mobility in Intercalated Li3 Alx Ti2-x (P O4)3 NASICON Type Materials: A Combined Neutron Diffraction and NMR Study. *Phys. Chem. Chem. Phys.* **2014**, *16* (34), 18397–18405. https://doi.org/10.1039/c4cp02938k.

(67) Dashjav, E.; Ma, Q.; Xu, Q.; Tsai, C.-L.; Giarola, M.; Mariotto, G.; Tietz, F. The Influence of Water on the Electrical Conductivity of Aluminum-Substituted Lithium Titanium Phosphates. *Solid State Ionics* **2018**, *321*, 83–90. https://doi.org/10.1016/j.ssi.2018.04.010.

(68) BURBA, C.; FRECH, R. Vibrational Spectroscopic Study of Lithium Intercalation into Li Ti2 (P O4)3. *Solid State Ionics* **2006**, *177* (17–18), 1489–1494. https://doi.org/10.1016/j.ssi.2006.07.015.

(69) Eddahaoui, K.; Benmokhtar, S.; Manoun, B.; Belaaouad, S.; Lazor, P. Vibrational Spectra and Factor Group Analysis of M0.50 Ti O P O4 Oxyphosphates (M=Mg, Zn, Ni, Co, Fe and Cu). *Spectrochim. Acta. A. Mol. Biomol. Spectrosc.* **2012**, *99*, 81–89. https://doi.org/10.1016/j.saa.2012.08.033.

(70) Lakshmi-Narayana, A.; Hussain, O. M.; Mauger, A.; Julien, C. Transport Properties of Nanostructured Li2 Ti O3 Anode Material Synthesized by Hydrothermal Method. *Sci*

2019, *1* (39), 1–16.

(71) Pérez-Estébanez, M.; Isasi-Marín, J.; Többens, D. M.; Rivera-Calzada, A.; León, C. A Systematic Study of Nasicon-Type Li1+x Mx Ti2-x (P O4)3 (M: Cr, Al, Fe) by Neutron Diffraction and Impedance Spectroscopy. *Solid State Ionics* **2014**, *266*, 1–8. https://doi.org/10.1016/j.ssi.2014.07.018.

(72) Dashjav, E.; Tietz, F. Neutron Diffraction Analysis of NASICON-Type Li1+x Alx Ti2-x P3 O12. *Zeitschrift für Anorg. und Allg. Chemie* **2014**, *640* (15), 3070–3073. https://doi.org/10.1002/zaac.201400195.

(73) Arbi, K.; Hoelzel, M.; Kuhn, A.; García-Alvarado, F.; Sanz, J. Structural Factors That Enhance Lithium Mobility in Fast-Ion Li1+x Ti2-x Alx (P O4)3 ($0 \leq x \leq 0.4$) Conductors Investigated by Neutron Diffraction in the Temperature Range 100-500 K. *Inorg. Chem.* **2013**, *52* (16), 9290–9296. https://doi.org/10.1021/ic400577v.

(74) Cîntă Pînzaru, S.; Onac, B. P.; Pînzaru, S. C.; Onac, B. P. Raman Study of Natural Berlinite from a Geological Phosphate Deposit. *Vib. Spectrosc.* **2009**, *49* (2), 97–100. https://doi.org/10.1016/j.vibspec.2008.05.003.

(75) Kotobuki, M.; Koishi, M. Preparation of Li1.5 Al0.5 Ti1.5 (P O4)3 Solid Electrolyte via a Co-Precipitation Method. *Ceram. Int.* **2013**, *39* (4), 4645–4649. https://doi.org/10.1016/j.ceramint.2012.10.206.

(76) Yoon, Y.; Kim, J.; Park, C.; Shin, D. The Relationship of Structural and Electrochemical Properties of NASICON Structure Li1.3 Al0.3 Ti1.7 (P O4)3 Electrolytes by a Sol-Gel Method. *J. Ceram. Process. Res.* **2013**, *14* (4), 563–566.

(77) Lang, B.; Ziebarth, B.; Elsässer, C. Lithium Ion Conduction in Li Ti2 (P O4)3 and Related Compounds Based on the NASICON Structure: A First-Principles Study. *Chem. Mater.* **2015**, *27* (14), 5040–5048. https://doi.org/10.1021/acs.chemmater.5b01582.

(78) Mariappan, C. R.; Gellert, M.; Yada, C.; Rosciano, F.; Roling, B. Grain Boundary Resistance of Fast Lithium Ion Conductors: Comparison between a Lithium-Ion Conductive Li-Al-Ti-P-O-Type Glass Ceramic and a Li1.5 Al0.5 Ge1.5 P3 O12 Ceramic. *Electrochem. commun.* **2012**, *14* (1), 25–28.

(79) Kjølseth, C.; Fjeld, H.; Prytz, Ø.; Inge, P.; Estournès, C.; Haugsrud, R.; Norby, T. Space – Charge Theory Applied to the Grain Boundary Impedance of Proton Conducting Ba Zr0.9 Y0.1 O3-D. *Solid State Ionics* **2010**, *181*, 268–275. https://doi.org/10.1016/j.ssi.2010.01.014.

(80) Gellert, M.; Gries, K. I.; Yada, C.; Rosciano, F.; Volz, K.; Roling, B. Grain Boundaries in a Lithium Aluminum Titanium Phosphate-Type Fast Lithium Ion Conducting Glass Ceramic: Microstructure and Nonlinear Ion Transport Properties. *J. Phys. Chem. C* **2012**, *116* (43), 22675–22678. https://doi.org/10.1021/jp305309r.

(81) Schell, K. G.; Bucharsky, E. C.; Lemke, F.; Hoffmann, M. J. Effect of Calcination Conditions on Lithium Conductivity in Li1.3 Ti1.7 Al0.3 (P O4)3 Prepared by Sol-Gel Route. *Ionics (Kiel).* **2017**, *23* (4), 821–827.

(82) Yu, S.; Mertens, A.; Gao, X.; Gunduz, D. C.; Schierholz, R.; Benning, S.; Hausen, F.; Mertens, J.; Kungl, H.; Tempel, H.; Eichel, R.-A. Influence of Microstructure and AlPO 4 Secondary-Phase on the Ionic Conductivity of Li1.3 Al0.3 Ti1.7 (P O4)3 Solid-State Electrolyte. *Funct. Mater. Lett.* **2016**, *09* (05), 1650066. https://doi.org/10.1142/S1793604716500661.

(83) Hupfer, T.; Bucharsky, E. C.; Schell, K. G.; Hoffmann, M. J. Influence of the Secondary Phase LiTiOPO 4 on the Properties of Li1+x Alx Ti2-x (P O4)3 (x = 0; 0.3). *Solid State Ionics* **2017**, *302*, 49–53. https://doi.org/10.1016/j.ssi.2016.10.008.

(84) Hupfer, T.; Bucharsky, E. C.; Schell, K. G.; Senyshyn, A.; Monchak, M.; Hoffmann, M. J.; Ehrenberg, H. Evolution of Microstructure and Its Relation to Ionic Conductivity in Li1+x Alx Ti2-x (P O4)3. *Solid State Ionics* **2016**, *288*, 235–239. https://doi.org/10.1016/j.ssi.2016.01.036.

(85) Soman, S.; Iwai, Y.; Kawamura, J.; Kulkarni, A. Crystalline Phase Content and Ionic Conductivity Correlation in LATP Glass-Ceramic. *J. Solid State Electrochem.* **2012**, *16* (5), 1761–1766. https://doi.org/10.1007/s10008-011-1592-4.

(86) Lee, S.-D.; Jung, K.-N.; Kim, H.; Shin, H.-S.; Song, S.-W.; Park, M.-S.; Lee, J.-W. Composite Electrolyte for All-Solid-State Lithium Batteries: Low-Temperature Fabrication and Conductivity Enhancement. *ChemSusChem* **2017**, *10* (10), 2175–2181. https://doi.org/10.1002/cssc.201700104.

(87) Schlesinger, H. I.; Brown, H. C.; Finholt, A. E.; Bates, X. Y. J. B.; Jellison, G. E.; Hart, F. X. A Stable Thin-Film Lithium Electrolyte : Lithium Phosphorus Oxynitride. *J. Electrochem. Soc.* **1997**, *144* (2), 524–532.

(88) Jiang, Z.; Han, Q.; Wang, S.; Wang, H. Reducing the Interfacial Resistance in All-Solid-State Lithium Batteries Based on Oxide Ceramic Electrolytes. *ChemElectroChem* **2019**, *6* (12), 2970–2983. https://doi.org/10.1002/celc.201801898.

(89) Dudney, N. J. Thin Film Micro-Batteries. *Electrochem. Soc. Interface* **2008**, *17* (3), 44–48.

(90) Wang, L.; Wang, Q.; Jia, W.; Chen, S.; Gao, P.; Li, J. Li Metal Coated with Amorphous Li 3 PO 4 via Magnetron Sputtering for Stable and Long-Cycle Life Lithium Metal Batteries. *J. Power Sources* **2017**, *342*, 175–182. https://doi.org/10.1016/j.jpowsour.2016.11.097.

(91) Neudecker, B. J.; Dudney, N. J.; Bates, J. B. " Lithium-Free " Thin-Film Battery with In Situ Plated Li Anode. *J. Electrochem. Soc.* **2000**, *147* (2), 517–523.

(92) Mizushima, K.; Jones, P. C.; Wiseman, P. J.; Goodenough, J. B. Lix CoO2 (0 < x < 1): A New Cathode Material for Batteries of High Energy Density. *Mater. Res. Bull.* **1980**, *15*, 783–789.

(93) Park, J.-K. Principles and Applications of Lithium Secondary Batteries https://books.google.es/books?hl=de&lr=&id=papHH-urMVYC&oi=fnd&pg=PP10&ots=kxTs9AMJkD&sig=GWyusNo5m-zW0EB8T9t5I-oGKDE&redir_esc=y#v=onepage&q&f=false (accessed Oct 13, 2020).

(94) Liu, C.; Neale, Z. G.; Cao, G. Understanding Electrochemical Potentials of Cathode Materials in Rechargeable Batteries. *Mater. Today* **2016**, *19* (2), 109–123. https://doi.org/10.1016/j.mattod.2015.10.009.

(95) Gauthier, M.; Carney, T. J.; Grimaud, A.; Giordano, L.; Pour, N.; Chang, H.; Fenning, D. P. Electrode-Electrolyte Interface in Li-Ion Batteries: Current Understanding and New Insights. *J. Phys. Chem. Lett.* **2015**, *6* (22), 4653–4672.

(96) Thackeray, M. M.; David, W. I. F.; Bruce, P. G.; Goodenough, J. B. Lithium Insertion into Manganese Spinels. *Mater. Res. Bull.* **1983**, *18* (4), 461–472. https://doi.org/10.1016/0025-5408(83)90138-1.

(97) Thackeray, M. M.; Mansuetto, M. F.; Bates, J. B. Structural Stability of LiMn2O4 Electrodes for Lithium Batteries. *J. Power Sources* **1997**, *68* (1), 153–158. https://doi.org/10.1016/S0378-7753(96)02624-9.

(98) Bencko, V.; Wagner, V.; Wagnerova, M.; Zavázal, V. Human Exposure to Nickel and Cobalt: Biological Monitoring and Immunobiochemical Response. *Environ. Res.* **1986**,

40 (2), 399–410. https://doi.org/10.1016/S0013-9351(86)80115-3.

(99) Masquelier, C.; Croguennec, L. Polyanionic (Phosphates , Silicates , Sulfates) Frameworks as Electrode Materials for Rechargeable Li (or Na) Batteries. *Chem. Rev.* **2012**.

(100) Cunha, D. M.; Hendriks, T. A.; Vasileiadis, A.; Vos, C. M.; Verhallen, T.; Singh, D. P.; Wagemaker, M.; Huijben, M. Doubling Reversible Capacities in Epitaxial Li4 Ti5 O12 Thin Film Anodes for Microbatteries. *ACS Appl. Energy Mater.* **2019**, *2* (5), 3410–3418. https://doi.org/10.1021/acsaem.9b00217.

(101) Hoang, K. Understanding the Electronic and Ionic Conduction and Lithium Over-Stoichiometry in Li Mn2 O4 Spinel. *J. Mater. Chem. A* **2014**, *2* (43), 18271–18280. https://doi.org/10.1039/C4TA04116J.

(102) Liu, Y.; Lian, J.; Sun, Z.; Zhao, M.; Shi, Y.; Song, H. The First-Principles Study for the Novel Optical Properties of LiTi2O4, Li4Ti5O12, Li2Ti2O4 and Li7Ti5O12. *Chem. Phys. Lett.* **2017**, *677*, 114–119. https://doi.org/10.1016/j.cplett.2017.04.009.

(103) Berg, H.; Göransson, K.; Noläng, B.; Thomas, J. O. Electronic Structure and Stability of Li1+(x)Mn2-(x)O4 Spinels. *J. Mater. Chem.* **2000**, *10* (6), 1437–1441. https://doi.org/10.1039/a908746j.

(104) Julien, C. M.; Mauger, A.; Zaghib, K.; Groult, H. Comparative Issues of Cathode Materials for Li-Ion Batteries. *Inorganics* **2014**, *2*, 132–154. https://doi.org/10.3390/inorganics2020132.

(105) Janiak, C.; Meyer, H.-J.; Gudat, D.; Alsfasser, R. *Riedel Moderne Anorganische Chemie*; Riedel, E., Meyer, H.-J., Eds.; DE GRUYTER: Berlin, Boston, 2012. https://doi.org/10.1515/9783110249019.

(106) Eckhoff, M.; Blöchl, P. E.; Behler, J. Hybrid Density Functional Theory Benchmark Study on Lithium Manganese Oxides. *Phys. Rev. B* **2020**, *101* (205113). https://doi.org/10.1103/PhysRevB.101.205113.

(107) Jain, A.; Ong, Shyue Ping Hautier, G.; Chen, W.; Richards, W. D.; Dacek, S.; Cholia, S.; Gunter, D.; Skinner, D.; Ceder, Gerbrand Persson, K. Commentary: The Materials Project: A materials genome approach to accelerating materials innovation https://www.materialsproject.org (accessed Nov 19, 2020). https://doi.org/https://doi.org/10.1063/1.4812323.

(108) Sturge, M. D. The Jahn-Teller Effect in Solids. *Acad. Press* **1968**, *20*, 91–211.

(109) Kosilov, V. V; Potapenko, A. V; Kirillov, S. A. Effect of Overdischarge (Overlithiation) on Electrochemical Properties of Li Mn2 O4 Samples of Different Origin. *J. Solid State Electrochem.* **2017**, *21* (11), 3269–3279. https://doi.org/10.1007/s10008-017-3671-7.

(110) Bianchini, M.; Suard, E.; Croguennec, L.; Masquelier, C. Li-Rich Li1+x Mn2-x O4 Spinel Electrode Materials: An Operando Neutron Diffraction Study during Li+ Extraction/Insertion. *J. Phys. Chem. C* **2014**, *118* (45), 25947–25955.

(111) Bruce, P. G.; Saidi, M. Y. A Two-Step Model of Intercalation. *Solid State Ionics* **1992**, *51* (3–4), 187–190. https://doi.org/10.1016/0167-2738(92)90198-X.

(112) Kobayashi, S.; Uchimoto, Y. Lithium Ion Phase-Transfer Reaction at the Interface between the Lithium Manganese Oxide Electrode and the Nonaqueous Electrolyte. *J. Phys. Chem. B* **2005**, *109* (27), 13322–13326. https://doi.org/10.1021/jp044283j.

(113) Vassiliev, S. Y.; Sentyurin, V. V.; Levin, E. E.; Nikitina, V. A. Diagnostics of Lithium-Ion Intercalation Rate-Determining Step: Distinguishing between Slow Desolvation and

Slow Charge Transfer. *Electrochim. Acta* **2019**, *302*, 316–326. https://doi.org/10.1016/j.electacta.2019.02.043.

(114) Hallot, M.; Demortière, A.; Roussel, P.; Lethien, C. Sputtered Li Mn1.5 Ni0.5 O4 Thin Films for Li-Ion Micro-Batteries with High Energy and Rate Capabilities. *Energy Storage Mater.* **2018**, *15* (August), 396–406. https://doi.org/10.1016/j.ensm.2018.08.012.

(115) Samarasingha, P. B.; Andersen, N. H.; Sørby, M. H.; Kumar, S.; Nilsen, O.; Fjellvåg, H. Neutron Diffraction and Raman Analysis of Li Mn1.5 Ni0.5 O4 Spinelt Type Oxides for Use as Lithium Ion Battery Cathode and Their Capacity Enhancements. *Solid State Ionics* **2016**, *284*, 28–36. https://doi.org/10.1016/j.ssi.2015.11.018.

(116) Song, J.; Shin, D. W.; Lu, Y.; Amos, C. D.; Manthiram, A.; Goodenough, J. B. Role of Oxygen Vacancies on the Performance of Li[Ni 0.5-x Mn1.5+x]O4 (X= 0, 0.05, and 0.08) Spinel Cathodes for Lithium-Ion Batteries. *Chem. Mater.* **2012**, *24*, 3101–3109. https://doi.org/10.1021/cm301825h.

(117) Manthiram, A.; Chemelewski, K.; Lee, E. A Perspective on the High-Voltage Li Mn1.5 Ni0.5 O4 Spinel Cathode for Lithium-Ion Batteries. *Energy Environ. Sci.* **2014**, *7*, 1339–1350. https://doi.org/10.1039/c3ee42981d.

(118) Matsui, M.; Dokko, K.; Kanamura, K. Surface Layer Formation and Stripping Process on LiMn[Sub 2]O[Sub 4] and LiNi[Sub 1⁄2]Mn[Sub 3⁄2]O[Sub 4] Thin Film Electrodes. *J. Electrochem. Soc.* **2010**, *157* (2), A121. https://doi.org/10.1149/1.3262622.

(119) Ge, H.; Li, N.; Li, D.; Dai, C.; Wang, D. Study on the Theoretical Capacity of Spinel Lithium Titanate Induced by Low-Potential Intercalation. *J. Phys. Chem. C* **2009**, *113*, 6324–6326.

(120) Joshi, Y.; Saksena, A.; Hadjixenophontos, E.; Schneider, J. M.; Schmitz, G. Electrochromic Behavior and Phase Transformation in Li 4 + x Ti 5 O 12 upon Lithium-Ion Deintercalation / Intercalation. *ACS Appl. Mater. Interfaces* **2020**, *12*, 10616–10625. https://doi.org/10.1021/acsami.9b19683.

(121) Sarantuya, L.; Sevjidsuren, G.; Altantsog, P. Synthesis , Structure and Electronic Properties of Li 4 Ti 5 O 12 Anode Material for Lithium Ion Batteries. *Solid State Phenom.* **2018**, *271*, 9–17. https://doi.org/10.4028/www.scientific.net/SSP.271.9.

(122) Raja, M. W.; Mahanty, S.; Kundu, M.; Basu, R. N. Synthesis of Nanocrystalline Li 4 Ti 5 O 12 by a Novel Aqueous Combustion Technique. *J. Alloys Compd.* **2009**, *468*, 258–262. https://doi.org/10.1016/j.jallcom.2007.12.072.

(123) Walsh, A.; Sokol, A. A.; Buckeridge, J.; Scanlon, D. O.; Catlow, C. R. A. Oxidation States and Ionicity. *Nat. Mater.* **2018**, *17* (November). https://doi.org/10.1038/s41563-018-0165-7.

(124) Schmidt, W.; Bottke, P.; Sternad, M.; Gollob, P.; Hennige, V.; Wilkening, M. Small Change - Great Effect : Steep Increase of Li Ion Dynamics in Li 4 Ti 5 O 12 at the Early Stages of Chemical Li Insertion. *Chem. Mater.* **2015**, *27*, 1740–1750. https://doi.org/10.1021/cm504564k.

(125) Liu, D.; Ouyang, C.; Shu, J.; Jiang, J.; Wang, Z.; Chen, L. Theoretical Study of Cation Doping Effect on the Electronic Conductivity of Li 4 Ti 5 O 12. *Phys. status solidi* **2006**, *1841* (8), 1835–1841. https://doi.org/10.1002/pssb.200541404.

(126) Jhan, Y. R.; Duh, J. G. Electrochemical Performance and Low Discharge Cut-off Voltage Behavior of Ruthenium Doped Li 4Ti 5O 12 with Improved Energy Density. *Electrochim. Acta* **2012**, *63*, 9–15. https://doi.org/10.1016/j.electacta.2011.12.014.

(127) Meng, X.; Wang, X.; Zhou, Y.; Tong, L.; Zeng, X.; Chen, X. Spinel Lithium Titanate

from Brookite Nanocrystallites. *Ceram. Int.* **2014**, *40* (3), 4989–4993. https://doi.org/10.1016/j.ceramint.2013.08.054.

(128) Özen, S.; Şenay, V.; Pat, S.; Korkmaz, Ş. Optical, Morphological Properties and Surface Energy of the Transparent Li4Ti5O12 (LTO) Thin Film as Anode Material for Secondary Type Batteries. *J. Phys. D. Appl. Phys.* **2016**, *49* (10). https://doi.org/10.1088/0022-3727/49/10/105303.

(129) Ge, H.; Tian, H.; Song, H.; Liu, D.; Wu, S.; Shi, X. Study on the Energy Band Structure and Photoelectrochemical Performances of Spinel Li 4 Ti 5 O 12. *Mater. Res. Bull.* **2014**, *61*, 459–462. https://doi.org/10.1016/j.materresbull.2014.10.064.

(130) Liu, H.; Zhu, Z.; Huang, J.; He, X.; Chen, Y.; Zhang, R.; Lin, R.; Li, Y.; Yu, S.; Xing, X.; Yan, Q.; Li, X.; Frost, M. J.; An, K.; Feng, J.; Kostecki, R.; Xin, H.; Ong, S. P.; Liu, P. Elucidating the Limit of Li Insertion into the Spinel Li 4 Ti 5 O 12. *ACS Mater. Lett.* **2019**, *1*, 96–102. https://doi.org/10.1021/acsmaterialslett.9b00099.

(131) Pasta, M.; Armstrong, D.; Brown, Z. L.; Bu, J.; Castell, M. R.; Chen, P.; Cocks, A.; Corr, S. A.; Gussen, E. J.; Darnbrough, E.; Deshpande, V.; Doerrer, C.; Dyer, M. S.; El-Shinawi, H.; Fleck, N.; Grant, P.; Gregory, G. L.; Grovenor, C.; Hardwick, L. J.; Irvine, J. T. S.; Lee, H. J.; Li, G.; Liberti, E.; Mcclelland, I.; Monroe, C.; Nellist, P. D.; Shearing, P. R.; Shoko, E.; Song, W.; Jolly, D. S.; Thomas, C. I.; Turrell, S. J.; Vestli, M.; Williams, C. K.; Zhou, Y.; Bruce, P. G. 2020 Roadmap on Solid-State Batteries. *J. Phys. Energy* **2020**, *2* (3).

(132) Wynn, T. A.; Lee, J. Z.; Banerjee, A.; Meng, Y. S. In Situ and Operando Probing of Solid-Solid Interfaces in Electrochemical Devices. *MRS Bull.* **2018**, *43* (10), 740–745. https://doi.org/10.1557/mrs.2018.235.

(133) Gong, Y.; Zhang, J.; Jiang, L.; Shi, J.-A.; Zhang, Q.; Yang, Z.; Zou, D.; Wang, J.; Yu, X.; Xiao, R.; others. In Situ Atomic-Scale Observation of Electrochemical Delithiation Induced Structure Evolution of Li Co O2 Cathode in a Working All-Solid-State Battery. *J. Am. Chem. Soc.* **2017**, *139* (12), 4274–4277.

(134) Gong, Y.; Chen, Y.; Zhang, Q.; Meng, F.; Shi, J. A.; Liu, X.; Liu, X.; Zhang, J.; Wang, H.; Wang, J.; Yu, Q.; Zhang, Z.; Xu, Q.; Xiao, R.; Hu, Y. S.; Gu, L.; Li, H.; Huang, X.; Chen, L. Three-Dimensional Atomic-Scale Observation of Structural Evolution of Cathode Material in a Working All-Solid-State Battery. *Nat. Commun.* **2018**, *9* (1), 1–8. https://doi.org/10.1038/s41467-018-05833-x.

(135) Aizawa, Y.; Yamamoto, K.; Sato, T.; Murata, H.; Yoshida, R.; Fisher, C. A. J.; Kato, T.; Iriyama, Y.; Hirayama, T. In Situ Electron Holography of Electric Potentials inside a Solid-State Electrolyte: Effect of Electric-Field Leakage. *Ultramicroscopy* **2017**, *178*, 20–26.

(136) Yamamoto, K.; Iriyama, Y.; Asaka, T.; Hirayama, T.; Fujita, H.; Nonaka, K.; Miyahara, K.; Sugita, Y.; Ogumi, Z. Direct Observation of Lithium-Ion Movement around an in-Situ-Formed-Negative-Electrode/Solid-State-Electrolyte Interface during Initial Charge--Discharge Reaction. *Electrochem. commun.* **2012**, *20*, 113–116.

(137) Yamamoto, K.; Iriyama, Y.; Asaka, T.; Hirayama, T.; Fujita, H.; Fisher, C. A. J.; Nonaka, K.; Sugita, Y.; Ogumi, Z. Dynamic Visualization of the Electric Potential in an All-Solid-State Rechargeable Lithium Battery. *Angew. Chemie Int. Ed.* **2010**, *49* (26), 4414–4417.

(138) Yamamoto, K.; Yoshida, R.; Sato, T.; Matsumoto, H.; Kurobe, H.; Hamanaka, T.; Kato, T.; Iriyama, Y.; Hirayama, T. Nano-Scale Simultaneous Observation of Li-Concentration Profile and Ti-, O Electronic Structure Changes in an All-Solid-State Li-Ion Battery by Spatially-Resolved Electron Energy-Loss Spectroscopy. *J. Power Sources*

2014, *266*, 414–421.

(139) Zhu, Z.; Zhou, Y.; Yan, P.; Vemuri, R. S.; Xu, W.; Zhao, R.; Wang, X.; Thevuthasan, S.; Baer, D. R.; Wang, C.-M. In Situ Mass Spectrometric Determination of Molecular Structural Evolution at the Solid Electrolyte Interphase in Lithium-Ion Batteries. *Nano Lett.* **2015**, *15* (9), 6170–6176. https://doi.org/10.1021/acs.nanolett.5b02479.

(140) Wi, S.; Park, J.; Lee, S.; Kim, J.; Gil, B.; Yun, A. J.; Sung, Y. E.; Park, B.; Kim, C. Insights on the Delithiation/Lithiation Reactions of LixMn0.8Fe0.2PO4 Mesocrystals in Li+ Batteries by in Situ Techniques. *Nano Energy* **2017**, *39*, 371–379. https://doi.org/10.1016/j.nanoen.2017.07.016.

(141) Ohmer, N.; Fenk, B.; Samuelis, D.; Chen, C. C.; Maier, J.; Weigand, M.; Goering, E.; Schütz, G. Phase Evolution in Single-Crystalline LiFePO4 Followed by in Situ Scanning X-Ray Microscopy of a Micrometre-Sized Battery. *Nat. Commun.* **2015**, *6*, 1–7. https://doi.org/10.1038/ncomms7045.

(142) Mukerjee, S.; Thurston, T. R.; Jisrawi, N. M.; Yang, X. Q.; McBreen, J.; Daroux, M. L.; Xing, X. K. Structural Evolution of Li x Mn2 O 4 in Lithium-Ion Battery Cells Measured In Situ Using Synchrotron X-Ray Diffraction Techniques. *J. Electrochem. Soc.* **1998**, *145* (2), 466–472. https://doi.org/10.1149/1.1838286.

(143) Bressler, C.; Chergui, M. Ultrafast X-Ray Absorption Spectroscopy. *Chem. Rev.* **2004**, *104* (4), 1781–1812. https://doi.org/10.1021/cr0206667.

(144) Chen, Y.-C.; Chen, J.-M.; Hsu, C.-H.; Lee, J.-F.; Yeh, J.-W.; Shih, H. C. In-Situ Synchrotron X-Ray Absorption Studies of LiMn0.25Fe0.75PO4 as a Cathode Material for Lithium Ion Batteries. *Solid State Ionics* **2009**, *180* (20), 1215–1219. https://doi.org/https://doi.org/10.1016/j.ssi.2009.06.013.

(145) Robert, R.; Zeng, D.; Lanzirotti, A.; Adamson, P.; Clarke, S. J.; Grey, C. P. Scanning X-Ray Fluorescence Imaging Study of Lithium Insertion into Copper Based Oxysulfides for Li-Ion Batteries. *Chem. Mater.* **2012**, *24* (14), 2684–2691. https://doi.org/10.1021/cm3005375.

(146) Finegan, D. P.; Scheel, M.; Robinson, J. B.; Tjaden, B.; Hunt, I.; Mason, T. J.; Millichamp, J.; Di Michiel, M.; Offer, G. J.; Hinds, G.; Brett, D. J. L.; Shearing, P. R. In-Operando High-Speed Tomography of Lithium-Ion Batteries during Thermal Runaway. *Nat. Commun.* **2015**, *6*, 6924.

(147) Ding, Y.; Li, Z.-F.; Timofeeva, E. V; Segre, C. U. In Situ EXAFS-Derived Mechanism of Highly Reversible Tin Phosphide/Graphite Composite Anode for Li-Ion Batteries. *Adv. Energy Mater.* **2018**, *8* (9), 1702134. https://doi.org/10.1002/aenm.201702134.

(148) Boesenberg, U.; Fittschen, U. E. A. 2D and 3D Imaging of Li-Ion Battery Materials Using Synchrotron Radiation Sources. In *Rechargeable Batteries: Materials, Technologies and New Trends*; Zhang, Z., Zhang, S. S., Eds.; Springer International Publishing: Cham, 2015; pp 393–418. https://doi.org/10.1007/978-3-319-15458-9_14.

(149) Lin, F.; Liu, Y.; Yu, X.; Cheng, L.; Singer, A.; Shpyrko, O. G.; Xin, H. L.; Tamura, N.; Tian, C.; Weng, T.-C.; Yang, X.-Q.; Meng, Y. S.; Nordlund, D.; Yang, W.; Doeff, M. M. Synchrotron X-Ray Analytical Techniques for Studying Materials Electrochemistry in Rechargeable Batteries. *Chem. Rev.* **2017**, *117* (21), 13123–13186. https://doi.org/10.1021/acs.chemrev.7b00007.

(150) Fears, T. M.; Doucet, M.; Browning, J. F.; Baldwin, J. K. S.; Winiarz, J. G.; Kaiser, H.; Taub, H.; Sacci, R. L.; Veith, G. M. Evaluating the Solid Electrolyte Interphase Formed on Silicon Electrodes: A Comparison of: Ex Situ X-Ray Photoelectron Spectroscopy and in Situ Neutron Reflectometry. *Phys. Chem. Chem. Phys.* **2016**, *18* (20), 13927–13940.

https://doi.org/10.1039/c6cp00978f.

(151) Alam, M. F.; Haque, A.; Ranjith, P. G. A Study of the Particle-Level Fabric and Morphology of Granular Soils under One-Dimensional Compression Using Insitu X-Ray CT Imaging. *Materials (Basel).* **2018**, *11* (919), 1–24. https://doi.org/10.3390/ma11060919.

(152) Drewett, N. E.; Aldous, I. M.; Zou, J.; Hardwick, L. J. In Situ Raman Spectroscopic Analysis of the Lithiation and Sodiation of Antimony Microparticles. *Electrochim. Acta* **2017**, *247*, 296–305. https://doi.org/https://doi.org/10.1016/j.electacta.2017.07.030.

(153) Krause, A.; Tkacheva, O.; Omar, A.; Langklotz, U.; Giebeler, L.; Dörfler, S.; Fauth, F.; Mikolajick, T.; Weber, W. M. In Situ Raman Spectroscopy on Silicon Nanowire Anodes Integrated in Lithium Ion Batteries. *J. Electrochem. Soc.* **2019**, *166* (3), A5378–A5385. https://doi.org/10.1149/2.0541903jes.

(154) Lei, J.; McLarnon, F.; Kostecki, R. In Situ Raman Microscopy of Individual LiNi0.8Co0.15Al0.05O2 Particles in a Li-Ion Battery Composite Cathode. *J. Phys. Chem. B* **2005**, *109* (2), 952–957. https://doi.org/10.1021/jp046027c.

(155) Galloway, T. A.; Cabo-Fernandez, L.; Aldous, I. M.; Braga, F.; Hardwick, L. J. Shell Isolated Nanoparticles for Enhanced Raman Spectroscopy Studies in Lithium-Oxygen Cells. *Faraday Discuss.* **2017**, *205*, 469–490. https://doi.org/10.1039/c7fd00151g.

(156) Matsui, M.; Kuwata, H.; Imanishi, N. In Operando FTIR Spectroscopy for Lithium-Ion Batteries. *Meet. Abstr.* **2014**, *MA2014-02* (4), 247.

(157) Streich, D.; Novák, P. Electrode-Electrolyte Interface Characterization of Carbon Electrodes in Li-O2 Batteries: Capabilities and Limitations of Infrared Spectroscopy. *Electrochim. Acta* **2016**, *190*, 753–757. https://doi.org/https://doi.org/10.1016/j.electacta.2015.12.061.

(158) Oukali, G.; Salager, E.; Ammar, M. R.; Dutoit, C. E.; Sarou-Kanian, V.; Simon, P.; Raymundo-Piñero, E.; Deschamps, M. In Situ Magnetic Resonance Imaging of a Complete Supercapacitor Giving Additional Insight on the Role of Nanopores. *ACS Nano* **2019**, *13*, 12810–12815. https://doi.org/10.1021/acsnano.9b04998.

(159) Zhu, J.; Lu, L.; Zeng, K. Nanoscale Mapping of Lithium-Ion Diffusion in a Cathode within an All-Solid-State Lithium-Ion Battery by Advanced Scanning Probe Microscopy Techniques. *ACS Nano* **2013**, *7* (2), 1666–1675. https://doi.org/10.1021/nn305648j.

(160) Breitung, B.; Baumann, P.; Sommer, H.; Janek, J.; Brezesinski, T. In Situ and Operando Atomic Force Microscopy of High-Capacity Nano-Silicon Based Electrodes for Lithium-Ion Batteries. *Nanoscale* **2016**, *8* (29), 14048–14056. https://doi.org/10.1039/C6NR03575B.

(161) Zhu, J.; Zeng, K.; Lu, L. In-Situ Nanoscale Mapping of Surface Potential in All-Solid-State Thin Film Li-Ion Battery Using Kelvin Probe Force Microscopy. *J. Appl. Phys.* **2012**, *111* (6), 63723.

2. Experimental methods

2.1 Introduction

In the following, the fabrication of thin film electrodes and electrolytes, applicable in microbatteries and thin film supercapacitors, is lined out in **Section 2.2** and **2.3.** Starting with the synthesis of $Li_{1+x}Al_xTi_{2-x}(PO_4)_3$ solid electrolyte powders, the general aspects of solid-state reactions and the routine chosen to fabricate LATP are described in **Section 2.2.2**. While the synthesis and application of powder and bulk LATP solid electrolyte has already seen a vast exploration in literature,[1–3] on the contrary its implementation in thin films is rarely represented.[4–6] To further explore its thin film properties, the pulsed laser deposition (PLD) is selected for its ability to control stoichiometry and interfaces precisely, as described in **Section 2.3**, with the opportunity to be applied on an industrial scale of thin film fabrication by Large-Area (LA) PLD (see **Section 2.3.6**).

Further the synthesized materials in powder, bulk and thin film form are analyzed by a variety of methods relating to their material characteristics. The information gained for structural and microstructural material properties described in **Section 2.4** mainly results from the interaction of matter with radiation (e.g. Radio waves, UV/NIR Lasers, X-Rays) and the excitation of electronic states or scattering phenomena on the crystal lattice due to the interaction with electrons. Functional properties are characterized in **Section 2.5**, concerning the materials electrical, optical and electrochemical behavior by induced electro-magnetic fields for the study of mass transport phenomena. The opportunity to observe the *in-situ* or *in-operando* performance of the electrode materials is given under coupling the signals with optical techniques, such as described in **Section 2.6**. The interest in time-resolved operando techniques for the study of interfaces has strongly increased in the past years. In this thesis, the aim to study electrochemically active interfaces reaches for the implementation of techniques, fairly simple to be applied with no need of complicated sample preparation and special safety requirements. In-situ observation of electrochemical properties has been chosen based on the coupling with optical, non-destructive techniques, such as Raman spectroscopy (see **Section 2.6.1**) and Spectroscopic ellipsometry (see **Section 2.6.2**).

2.2 Solid-state synthesis

As the basis to begin with, to realize thin films with high stoichiometry, density and good ionic conductivity in batteries, the synthesis routine chosen to obtain a pure material is crucial. Each reaction step has to be evaluated carefully, as deviations from the intended stoichiometry may form a different phase or lead to the segregation of secondary phases, possibly inhibiting a barrier-free mass transport. Besides material composition, the microstructure and density will further impact the ionic conductivity, as compressed reacted powders may deviate in their density from the values theoretically expected.

In this thesis, the powders of $Li_{1+x}Al_xTi_{2-x}(PO_4)_3$ were prepared via solid-state synthesis and sintered to a dense target for the deposition of thin films in LA-PLD.

2.2.1 Transition metal oxides and glass-ceramics

Different synthesis routines have been designed for transition metal oxides and glass-ceramics, mainly divided between solid (e.g. ceramic method, hydrothermal method, high-pressure or microwave assisted methods) and liquid (e.g. sol-gel synthesis, flux method, molten salt electrolysis) reactants.[7] Herein the focus is placed on lithium-based materials, especially on the fabrication of LATP glass-ceramics. Most synthesis routines explored are based on solid-solid ceramic reactions, sol-gel reactions, melt-quenching or mechano-chemical milling.[8–10] In order to obtain dense glass-ceramics, reacted powders are pressed in (cylindrically shaped) pellets and annealed afterwards. The purpose of annealing or sintering is the material densification by increasing the contact area between the single crystals, which can be improved with partial liquid-phase sintering, introducing an additional phase of a lower melting point as so-called sintering aid, e.g. Bismuth-based compounds or lithium-oxide.[11] Further sintering can be assisted by microwaves, spark plasma or high pressure.[12,13]

The ceramic method (solid-solid direct reaction of precursors) is very common, as it is fairly easy to perform and implement in comparison to so-called soft chemistry routines such as solution-based sol-gel synthesis, although they show several advantages. Higher densities, phase purities and ionic conductivities can be obtained due to two reasons with sol-gel/co-percipitation methods, as (i) the contact

between the precursors in sol-gel mixtures is much better and (ii) therefore the temperatures needed for effective sintering are much lower. In particular for lithium-based materials, lower sintering temperatures prevent volatile lithium to evaporate as oxide from the structure, as this may already appear above 500 °C.[14]

In this thesis, LATP synthesis is explored, first in bulk and later in thin film form. Despite the advantages deriving from soft chemistry synthesis (e.g. sol-gel), the quantity of reacted powders producible in a relatively short amount of time is small in comparison to solid-solid reactions. As described in detail for **Section 2.3.6**, thin film depositions were performed in a LA-PLD, being applicable for the production of thin films on an industrial scale. A target of relatively large spatial dimensions is needed, in order to suit the specific requirements of the system. Hence a solid-state synthesis routine is chosen to fabricate sufficient quantities of LATP pre-reacted powders.

2.2.2 Ceramic method

For the direct reaction between solid precursors, the diffusion lengths between the reactants should be small and the particle contact good, so the reaction rate is high. Therefore nano- or micro-sized powder precursors are used in order to maximize the specific surface area (*SSA*[§]) of the mixture.[7,15] Moreover, higher reactivity is achieved with the increase in temperature, as powders are reacted in high-temperature stable crucibles (typically Al_2O_3, ZrO_2 or very stable metals, such as Platinum or Tungsten). Side reactions may occur under elevated temperatures, such as with the crucible side walls or the evaporation of humidity and organics from the precursors. As any volatile compound will evaporate, for lithium compounds a certain excess of the Li-precursors is introduced, usually calculated with 5 – 15 mol% surplus Li.[14,16] To reduce possible contaminants and off-stoichiometry, precursors should be pre-dried prior to weighing, and first mixtures are pre-reacted (calcined) at intermediate temperatures to remove humidity and organics from precursors, such as CO_2 and NH_3.[17] Before and after each reaction step, the powders are mixed repeatedly, either manually in a mortar or by using a high energetic ball milling, with the purpose of material homogenization and reduction of particle and crystallite sizes. If particle sizes are irreducible, pressure can be

[§] Surface specific area SSA, where $SSA \cdot r_p \cdot \delta_p = 3$, with r_p as particle radius and δ_p as its density.[7]

applied in order to increase their contact area. Completing the reaction with a final annealing, the reacted powders are pressed into pellets and heated to sintering temperatures $T_S = 2\,T_M/3$ for the melting point T_M of the lower melting component.[15] The final densification is aiming for values close to the theoretical densities of crystalline materials.

In this thesis, a solid-state reaction was carried out between Li_2CO_3 (99.997 % Sigma-Aldrich), Al_2O_3 (99.999 % Sigma-Aldrich), TiO_2 (99.999 % Sigma-Aldrich) – all nano-powders – and $NH_4H_2PO_4$ (99.999 % Sigma-Aldrich). Precursors were pre-dried and weighed for obtaining x = 0.5 in $Li_{1+x}Al_xTi_{2-x}(PO_4)_3$, with additional 15 wt% of Li_2CO_3 to compensate eventual losses in lithium that might lead to the segregation of $AlPO_4$ as secondary phase. The powders were first mixed and ground in a mortar, then milled with zirconia balls and reacted in a Platinum crucible. Calcination was performed at very slow heating rates, with 3 $^oC\ min^{-1}$ and intermediate dwelling steps at 180 – 300 – 400 – 500 ^oC for 2 h, up to 650 ^oC and dwelling for 5 h, in ambient atmosphere and a conventional muffle furnace from Hobersal TR-25MFF. After cooling, the powders were ground, mixed and milled, again reacted in a platinum crucible and heated 5 $^oC\ min^{-1}$ up to 950 ^oC and dwelled for 2 h. After re-grinding and milling again the powder, it was cold-pressed at 20 MPa, reground and pressed again at 20 MPa in a pellet of 3” diameter and 0.5 cm of approx. thickness and finally sintered at 1000 ^oC, a fast heating ramp of 5 $^oC\ min^{-1}$, dwelling for 2 h, and a very slow cooling of 1 $^oC\ min^{-1}$. In order to prevent the formation of lithium-deficient surface layers or any stoichiometry different from the rest of the target, the entire pellet was covered in a sacrificial layer of reacted powders (top, bottom, sides) on an alumina plate, which could easily be removed after sintering. The obtained 3” target was carefully polished, manually with abrasive paper, in order to level the surface and remove eventual irregularities. All the optimization in synthesis carried out in this work is summarized in **Section 3**, under the study of phase evolution in bulk LATP upon temperature.

2.3 Pulsed laser deposition of thin films

Pulsed Laser Deposition (PLD) is a film growth technique used for the evaporation of various materials and their compounds onto a great selection of conductive or non-conductive substrates, hence securing a precise control of the desired

stoichiometry and crystal structure with the ability to support the complexity of multicationic transfer and its reproducibility.[18] Compared to other techniques in the field of physical vapour deposition for the transfer of complex stoichiometries, such as Molecular Beam Epitaxy (MBE) and Sputtering, the high energy of the laser-induced gas phase, favours the PLD application in the growth of epitaxial thin films and superlattices of heterostructures.[7]

Exploration of this technique has started just with the invention of the laser itself in the 1960s,[19,20] but first competitive applications arose in the late 1980s from the deposition of superconducting oxide thin films based on Y-Ba-Cu, operating under a high critical transition temperature T_c and therefore facilitating cooling with the use of liquid nitrogen.[21,22] Further applications followed with the rising interest in microelectronics and microelectromechanical systems (MEMS), with the need of dense thin films and controlled interfaces and the chance of industrial upscaling for mass production as demonstrated by Large-Area (LA) PLD.[23] In search of new solutions to meet the world's growing energy consumption on several levels of scale, thin films for energy harvesting, conversion and storage, as discussed in **Section 1.2.1.2** for microbatteries, came into stronger focus.[24,25]

In this thesis, pulsed laser deposition has been used to fabricate thin films of electrochemically active materials, such as spinel electrodes of lithium manganates and titanates, but also the NASICON solid electrolyte of Li-Al-Ti-P-O as a fairly new material combination to be applied in the PLD. The synthesis of an appropriate LATP target is described in **Section 2.2.2**. The targets for depositing spinel $LiMn_2O_4$ (LMO) and $Li_4Ti_5O_{12}$ (LTO) are commercial targets (purchased from Neyco France), as well as the Li_2O target (provided by Codex). Materials were deposited to be studied first individually, ranging from polycrystalline thin films on amorphous to crystalline substrates, to oriented layers with a certain epitaxy evolving from single crystalline substrates. Further multi-layer combinations among different materials were tried with the aim of finally achieving an all-solid state thin film microbattery of multiple heterostructures fully deposited by LA-PLD.

2.3.1 Definition of PLD method

The deposition of thin films by a pulsed laser is based on the ablation and evaporation of a target material by focusing the laser onto its surface and creating a highly directed plasma plume, propagating from target surface towards substrate. A general schematic setup of the PLD system used in this thesis is shown as model example in **Fig. 2.3.1** consisting of the laser beam passing through the optical system into the ultra-high vacuum (UHV) chamber, where the incident beam penetrates the target on a focused spot of pre-defined size and shape. As the plasma plume evolves perpendicular between target and substrate surface, the substrate holder is situated above, surrounded by a heating system. Both, target and substrate can be rotated around their own vertical axes, in which the target also can be moved horizontally at a fixed height for a so-called rastering, leading to an overall homogenization of the formed layer.

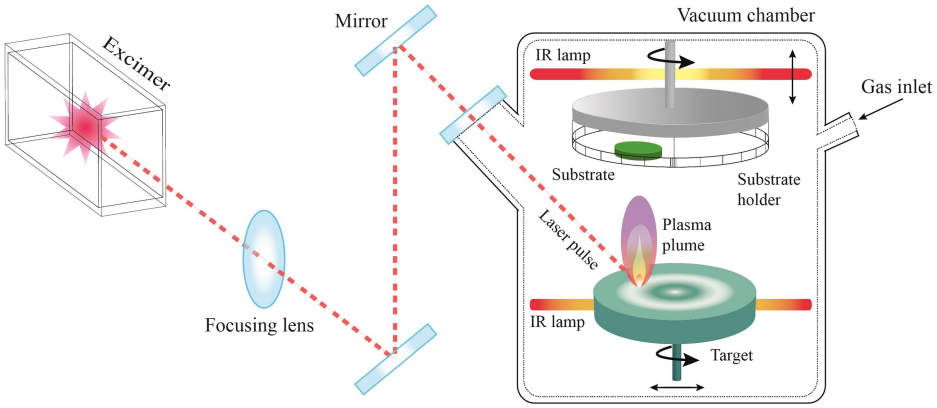

Fig. 2.3.1: Schematic setup for a common pulsed laser deposition.

While the setup of the system seems fairly simple, the interactions taking place in order to create a thin layer of the desired properties, concerning stoichiometry, materials density and orientation, are complex in their involved parameters and kinetic models. For simplicity they are divided in different sections of (i) laser-solid interactions described in **Section 2.3.2**, (ii) plasma plume propagation, see **Section 2.3.3** and (iii) the interactions of impinging species on the substrate surface and (iv) the resulting dynamics of the layer formation, as described in **Section 2.3.4**. The majority of layer properties will highly depend on the plume composition, which is a strong result from the laser-matter interactions between the target and the background gas. Different kinds of lasers, such as CO_2, Nd-YAG, Ti-sapphire and

excimer laser are commonly used for the illumination of the target material within the frequency range of ultra-violet (UV) light.[26] Further the background gas can have a great impact on the interactions between gas molecules and the evaporated species, depending on the gas molecule weight and density in the chamber, not only changing the plume composition, but also its propagation dynamics above experimental pressures of 10^{-3} mbar. For the deposition of oxide compounds usually O_2 serves as background gas for compensating certain losses, but moreover the application of inert gases such as Ar, or reactive gases like N_2, NH_3 and O_3 has been explored.[27] In order to limit unknown interactions with contaminants and to provide a good material flux towards the substrate, the necessity to create an UHV inside the chamber before ablation is evident. Additionally, the growth conditions can be optimized by a uniform rotation of the target and substrate, and even more with a homogeneous beam rastering over the target surface (further also protecting the target from damage), eliminating local off-stoichiometries and geometrical inhomogeneities. In the case for crystalline thin films their degree of crystallization can be tuned with an additional heating system for the substrate, consisting of either a resistive heater, infra-red (IR) lamps or a laser itself.

In this thesis, a careful evaluation and adaption for the deposition parameters of LMO, LTO and LATP is conducted, for the creation of electrochemically active materials. Particularly NASICON-like compounds seem to be complicating the stoichiometric transfer due to their complex multi-cationic structure. As there has not been a study laying out a clear evaluation of their preferable deposition conditions by pulsed laser deposition yet and only very few studies have been collected on their fabrication as thin films,[4–6] the following work aims to fill in this gap. Herein the focus is placed on (i) interactions of the laser with the target, (ii) scattering of ablated cations within the background gas, (iii) species condensation on the substrate surface and (iv) the layer nucleation and growth. Further, special care has to be taken for ablations within a Large-Area (LA) PLD configuration (see **Section 2.3.6**), as distances between target and substrate, as well as the spotsize of the ablated area are enlarged and contribute to a change in the plume propagation and material flux. The effect of certain parameters in the PLD is further discussed in the results for **Section 3**, directing the optimization of LATP thin film depositions, as well as the depositions made for LMO and LTO in **Section 4**.

2.3.2 Laser-solid interactions

One main advantage of applying a pulsed laser onto a material, is the high dose of energy being absorbed by a small spatial area of the target in a very short time interval (about 1,000 K ns^{-1}), resulting in the controlled ejection of primarily low-mass species at single and multi-atomic level, as well as electrons and neutrons. Suitable laser sources therefore operate at UV wavelengths between 100 – 400 nm, as most materials exhibit optical absorption in this range. The laser typically penetrates depths of 10 – 100 nm, depending on the wavelength (short λ present lower penetration), material specific absorption and conductivity.[26,28] Among many different lasers being applicable for ablation, the once suitable for pulsed laser deposition are mainly solid state crystal or glass laser (Nd-YAG, Ruby, Ti-sapphire, etc.), molecular gas laser (CO_2 or CO) and excimer laser (KrF, XeCl, etc.). In order to reach low thermal impact on the target and high homogeneity in the plume-composition, a sharp top-flat single-pulse energy plateau and short pulse widths of pico- to nanoseconds (possibly femtoseconds) are desirable, as common for Ti-sapphire and excimer lasers.[18,26,28,29]

Under photon absorption of the material in the UV, the valence electrons of the covalent atomic bonds are being excited and therefore emitted. The positive atomic nucleus develops a repulsive force towards similar charged nuclei, generating huge amounts of localized heat exceeding the materials melting point up to several thousands of kelvin, close to the thermodynamically critical temperature. As a result, the material surface experiences an evaporation and boiling, or even explosive release (Coulomb explosion) of nano- and micro-sized particles consisting of atoms, ions, neutrons and electrons. Considering the particle size present in the plume, and so the layer smoothness, density and stoichiometry, the laser fluence is crucial. For higher laser irradiance ($> 10^{10}$ W cm^{-2}) three problems may occur: (i) explosive subsurface boiling, (ii) the risk of ejecting bigger particulates, (iii) the amount of material ejected is so high, that a stronger shadowing of the incoming beam intensity occurs. For lower laser fluence, there might be a pre-dominant evaporation of volatile components due to their low cohesive energy as a measure of surface bonding strength.[7,28–30]

In this thesis, for laser ablation at UV wavelengths of λ = 248 nm, a Coherent (formerly Lambda Physik) COMPex PRO 205 KrF excimer laser was used, with a pulse width t_p of 20 ns, maximum power P of 30 W, maximum pulse energy of 700 mJ and the maximum pulse repetition rate f of 50 Hz, while depositions are mainly performed between 1 – 10 Hz. Approximate target penetration depth at this wavelength of the laser is about 100 nm,[28] and the average laser fluence was calculated to be 1.2 – 1.4 J cm^{-2} (spot size ~15 mm^2).

2.3.3 Plasma plume propagation

After material ejection, with a typical ablation yield of 10^{15} – 10^{16} atoms per pulse, the plume interacts with the laser light under continuous light absorption and becomes ionized under the effects of photoexcitation and inversed bremsstrahlung, leading to a strong increase of temperature in the plume (10,000 K and above) and the creation of a plasma. At first the plasma plume expands one-dimensional during the laser pulse with pressures as high as 5 – 10 bars, away from the target surface into the vacuum or a background gas (regime I). After pulse termination, the gas layer thickness is around 100 µm and expands adiabatically in all three dimensions (regime II), with a broader angular distribution of ejected material with smaller spot size. The final forward peaked plume shape is more distinctive with higher laser fluences, caused by a gradient in the initial plume pressure, accumulating most of the plume species in its front. In vacuum this motion remains free, but in a background gas, upon interaction with the ablated species, the plume gets trapped inside the gas and slowed down drastically. Further expansion is leading to the plume division in a vacuum-like component, moving forward rapidly and another diffusion-like component of damped velocity (regime III). Propagation continues in a shock-wave manner, finally trapping the plume at high pressures, as all plume particles are eventually slowed down and thermalized (regime IV). In the following diffusive regime, the background gas becomes the mediator of kinetic particles arriving at the substrate surface and being adsorbed.[18,28–30] The distance at which the plume front comes at rest is described as R_{ST} and depends on the mass of the plume species M_p, its initial velocity v_0 and the ambient pressure p as seen in **Eq. 2.3.1**. Further the plume mass derives from the spot size ablated surface area S_T, the in-depth etch rate in nm per pulse δ_a and the target density ρ_T. It is equal to the mass of the background gas at R_{ST}.[27,31]

$$R_{ST} \propto \left(\frac{M_p v_0^2}{p}\right)^{\frac{1}{3}} \qquad \text{(Eq. 2.3.1)}$$

This expression evolves from the assumption that the propagating plume front resembles to a thin, hemispherical shock layer (at room temperature),[31,32] rather than a parabolic expansion as it is expected under vacuum.[30,33] Elevated temperatures, although they are often neglected, can have a strong influence on the particle velocity and background gas density. With increasing deposition temperatures, the plume front transforms towards a rather elliptical shape, as similar for high laser fluence, having a higher velocity of impinging species. A shift of R_{ST} closer to the substrate surface appears, also as the background gas exhibits a higher permeability towards the plume species.[31] In **Fig. 2.3.2 (a)** the differences of plume shape and propagation depending on the weight of the compounds in the ablation of spinel $LiMn_2O_4$ is depicted for each of its components.

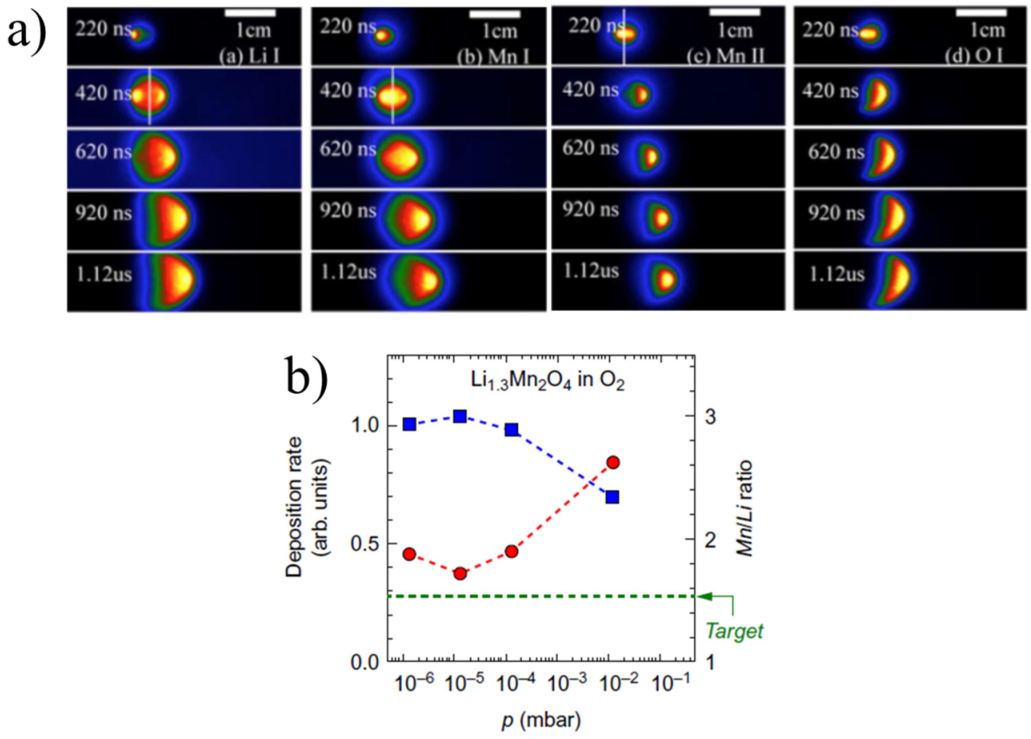

Fig. 2.3.2: Plasma plume propagation time- and component-resolved for $LiMn_2O_4$ for 0.2 mbar of oxygen partial pressure pO_2 and a plasma fluence F = 2 J cm^{-2} illustrated in (a). Reproduced from *Canulescu et al.*,[34] with the permission of AIP Publishing. In (b) the deposition rate (blue squares) and Mn/Li ratio (red circles) for $LiMn_2O_4$ are plotted against the pO_2 at F = 0.6 J cm^{-2} and substrate-target distance d_{ST} = 5 cm.[27,35] Reproduced from *Amoruso et al.*,[27] with permission from Elsevier.

The impact of the plume mass, the mass of background gas (m_G) and the angular distribution of high (m_H) and low (m_L) mass species will be evaluated in the

following, as the stoichiometric transfer of especially light components strongly relies on their interactions with the background gas.[29,36–38] Under any elastic collision between light and heavy elements, the lighter species will be scattered to broader plume angles than the heavier component, leading to its abundant presence on the plume center and deposited thin film. In conclusion, the ablated target area lacks the ablated heavier compound more than the light compound. With increasing the laser fluence and/or decreasing the background gas pressure, the mean free path of the species increases and due to less scattering events an increased amount of m_L populates the strongly forward directed plume.[39] In **Fig. 2.3.2 (b)** the effect of various partial oxygen pressures (pO_2) on the $m_H|m_L$ ratio and deposition rate is depicted for $Li_xMn_2O_{4-y}$. Lithium transfer is favoured especially at low pO_2, but still is light in comparison to O_2 (m_G = 32) or Ar (m_G = 40), and hence always suffers some losses in its transfer from the initial target composition. To generally reduce the amount of scattering events of light elements, different measures can be applied, such as (i) shorter target-to-substrate distances, (ii) lower background gas pressures and (iii) higher laser fluence, additionally reducing the evaporation of light elements as described previously in **Section 2.3.2**. But these parameters have to be balanced carefully, in order to avoid an increasing amount of defects and the resputtering of light compounds by interactions of the film material with impinging species of high energies. Further the increase in deposition temperature may slightly favour the transfer of heavier compounds in respect to the mass of the background gas.[27]

In this thesis, a variety of different background gas pressures was examined for the deposition of the Li – Al – Ti – P – O multi-cationic oxide, ranging from $2.67 \cdot 10^{-2}$ – 10^{-1} mbar (20 – 200 mT). Background gases applicable in the system are N_2, Ar and O_2, of which O_2 was used throughout the majority of depositions conducted with a mass flow between 5 – 10 sccm. Only first preliminary experiments for the deposition of the solid-electrolyte based on the NASICON-like structure were carried out under Ar-atmosphere, as some literature for component related phosphoric olivine structures (e.g. $LiFePO_4$) have reported good stoichiometric transfers in Ar.[40,41] But as O_2 is comparably light, its interaction with heavier compounds destabilizes the stoichiometric transfer and further Ar exhibits an even stronger scattering of light elements, such as Li, Al and P. Hence an O_2-atmosphere

secures a better stoichiometric transfer from the target, as it is further elaborated in **Section 3** for the deposition of LATP.[6,18] In general for the fabrication of lithium compounds in the PLD, there is an expected loss in lithium, and further oxygen. Many deposition routines try to balance the losses with the compensation through Li- or Li_2O-excess inside the targets by 7.5 – 15 wt %,[16,34,42] or with the deposition of alternating multi-layers from the desired compound with an additional target of Li_2O.[43–45] For the deposition of alternating multi-layers of Li_2O and LMO or LTO, some deposition parameters remained fixed as they have been previously optimized, such as the substrate-to-target distance at 90 mm, pulse frequency of 10 Hz, pO_2 of $2.67 \cdot 10^{-2}$ mbar (20 mT), the substrate temperature of 650 ºC and the laser fluence fixed to ~ 1.3 J cm^{-2} (spot size 0.15 cm^2).[45] For further improvement, ablation ratios of alternated pulses have been studied in order to optimize the stoichiometry of the thin film electrode materials of spinel LMO and LTO, as it is described in **Section 4**.

2.3.4 Layer nucleation

2.3.4.1 Surface phenomena and growth modes

The species condensing near the substrate surface will either undergo an adsorption and chemical bonding, or depending on their energy upon arrival and their mass, be re-evaporated from the substrate surface.[46] Once the plume species has been adsorbed, there can be five different regimes of layer nucleation expected, depending on the material flux of the impinging species, the diffusion coefficient of the adhered atoms, their adhesion energy, the substrate temperature, the substrate surface morphology (e.g. terraces or roughness) and its misfit in lattice parameters towards the film growing. Hence the growth modes are divided into (i) step-flow, (ii) layer-by-layer, (iii) layer plus island, (iv) island and (v) columnar growth.[47] For high surface diffusivities, 2D[§] layer growth modes are more likely to occur resulting in oriented thin films of very high quality. With less surface energies and mobility, 3D[‡] growth is preferably initiated, leading to higher surface roughness

[§] 2D growth modes are step-flow (SF) and Frank- van der Merwe (FM) layer-by-layer growth. The species exhibits stronger bonds towards the substrate than to each other.[47]

[‡] 3D growth modes are layer plus island (SK – Stranski-Krastanov) and island (VW – Volmer-Weber) growth. Columnar growth (CG) appears as intermediate of SK and VW, but oriented grains remain as single islands without layer formation and lattice energy adaption throughout defect and dislocation formation.[7,47–49]

and an increased polycrystallinity. The spatial expansion evolves upon a stronger bonding between the adatoms and a diminished influence of the substrate. Island growth can be thermodynamically favoured for small diffusion coefficients, as film and substrate may be inhomogeneous and the bonding between film species to each other is stronger. Step-flow and columnar grain growth are usually more common for epitaxial films, while the other nucleation mechanisms are applicable for both, epitaxial and non-epitaxial film growth, but will lead to a different surface roughness.[7,47–49]

2.3.4.2 Roughness evolution for hetero- and non-epitaxial growth

The wetting properties of the adsorbed species, described by the contact angle θ_c, can determine the growth mode to be expected, as this is a result from the interfacial surface energies γ of the contact between substrate (*s*), film (*f*) and vapour (*v*). This relation is described in Young's equation in **Eq. 2.3.2**.[50]

$$\gamma_{sv} = \gamma_{fs} + \gamma_{fv} \cdot cos\theta_c \qquad \text{(Eq. 2.3.2)}$$

Layer-by-layer growth therefore occurs for good surface wetting with $\theta_c \sim 0$, and island growth appears for $\theta_c > 0$. Roughness can be pre-determined by the initial growth process, but further evolves in different mechanisms after the coverage of the substrate by the first layer. For VW and SK growth modes, arriving droplets forming islands may reduce the surface energy upon formation of coalescent bondings and tend to reduce the surface area (smoother surface). But for materials of higher melting points, these bonds require a bigger amount of energy to be formed and the initial islands grown are unable to complete coalescence for the entire thin film. Therefore the surface roughness can be amplified, increasing the growth rate inconstantly by positive feedback growth or resolving in a constant growth rate by a non-positive feedback on the surface roughness. Positive feedback can enlarge certain particles locally due to shadowing of others below, or due to concentration and temperature gradients existent. The non-positive feedback can favour the growth along a specific crystallographic plane by the change in surface energy for each plane. Roughness evolving upon this progressively fast growing planes is often related to as texture.[49]

In this thesis, different substrates have been applied for the growth of thin films by PLD. The complete study of LATP solid electrolyte thin films in **Section 3** has

been conducted on Si-substrates covered in amorphous SiO_2 (100 nm) and Si_3N_4 (300 nm) for blocking eventual lithium diffusion into Si. Further depositions have also been carried out on glassy SiO_2 substrates especially necessary for the solid state NMR conducted in **Section 3.3.2.3**. Other thin film depositions, for LATP as well as for LMO and LTO have been carried out on Pt-covered (80 nm) $Si|SiO_2|Si_3N_4$-substrates, with a thin adhesive layer of TiN or TiO_2 (about 10 nm) typically between, see **Section 3-5**.

2.3.5 Interface engineering of thin films

2.3.5.1 Material defects

As already mentioned in the previous **Section 2.3.4**, due to certain deficiencies and eventual resputtering effects on the deposited layer, there is a variety of defects that may occur upon fabrication of thin films by PLD. Those are divided into point defects of intrinsic and extrinsic nature, such as oxygen vacancies or interstitials of host atoms or dopants. Further line defects (dislocations) or surface defects, such as stacking faults, twins and domain boundaries, as well as volumetric defects of pores, inclusions or precipitates of secondary phases may occur.[47] A strong impact on the electronic band structure and the materials energy landscape to enable electrochemical reactions or certain transport properties evolves mainly from point, line and surface defects, as they can locally impact the oxidation states of the cations.[51,52]

2.3.5.2 Lattice Strain

Engineering of the energy landscape can be provided with strained lattices, as they can locally transform bond energies and create reactivity for certain processes as a result of mechano-chemical coupling.[53] Strain can be induced upon deposition, depending on the lattice mismatch and the surface energy of adatoms, determining their wetting properties on the substrate surface (Young's equation).[47,50] If lattices are perfectly matching, they will exhibit the same crystal system and lattice parameters. A slight offset will induce strain in the growing layer, expanding towards one of its lattice parameters. For the lattice to extend even further, there will be a limit reached where strain releases into the formation of a defect.[50] For some application, strain is maintained for the purpose of energy landscape

modification. It has to be applied thoroughly to not eventually relax or transform the lattice.[53]

2.3.5.3 Annealing

Further thin films can be strained simply by the circumstance of their deposition procedure, without the intention to influence their properties. Relaxation of the lattice towards energetically more favourable states can be provided by curing the lattice with an additional heat treatment. This may lead to the reduction or re-organization of defects and grain boundaries, towards a lower intrinsic energy and a reduced roughness.[6] Especially for oxide layers deposited in the PLD, a post-deposition oxygen re-incorporation is common in order to reduce the amount of oxygen vacancies inhabitant from the deposition as a result from the generally reductive atmosphere inside the chamber.[40] Besides re-oxidation, carbonates incorporated in the layer, as common impurities for the deposition in PLD, will be released under elevated temperatures. But further also volatile components may evaporate upon thermal curing, as it may be the case for lithium or ruthenium.[54]

In this thesis, as the loss of lithium and oxygen are reported under certain deposition conditions in the PLD of thin films,[34] the compensation of this potential loss is balanced by the alternating ablation of two targets, one containing the stoichiometric electrode material of either $LiMn_2O_4$ or $Li_4Ti_5O_{12}$, and the other being a LiO_2 target. Further the solid electrolyte thin films of Li – Al – Ti – P – O may exhibit not only a loss in lithium, but also a notable loss of Al and P due to interactions with the heavier background gas. Aluminium acts as dopant in the NASICON lattice, replacing titanium to further incorporate higher amounts of lithium.[55] After deposition, a heat treatment for the as-deposited solid electrolyte thin films was applied, with a ramp of 1 – 5 °C min^{-1} between 700 – 900 °C in ambient air. As not all substrates available for thin film deposition can withstand high temperatures, annealing was restricted to Si_3N_4, SiO_2 and Pt-substrates described in the previous **Section 2.3.4.2**, which have shown to be stable for temperatures beyond the 800 ºC.[56,57] The effect of the thermal curing is evaluated in **Section 3**, in respect of thin film composition, crystallinity, microstructure and ionic conductivity.

2.3.6 Large-Area (LA) PLD

Large-Area PLD holds the promise to be implemented in future applications for thin film deposition techniques with the PLD inherent ability to precision in film growth, interfacial pre-determination and stoichiometry, on a highly reproducible industrial scale.[18,23] Therefore the upscaling in thin film deposition techniques is an important asset, as otherwise the fabrication of devices would be inconceivably expensive. Common LA-PLD systems, exemplary shown in **Fig. 2.3.3**, are able to handle substrates of 6 – 8” in diameter and bigger, while keeping a constant thickness and stoichiometry throughout the surface.

Several changes in the setup are made, in order to keep deposition rates high on big surfaces and the performance of the method reproducible, as distances in the optical path and between the target and substrate increase. For a reasonable growth rate, the amount of ablated species per pulse has to be increased with the spotsize and the laser power, constantly rotating target and substrate for a homogeneous distribution of material. In conclusion the target-to-substrate distance has to be adjusted to the new, increased position of plume diffusive regime R_{ST} (minimum 9 cm). A programmable mirror for re-focusing the beam spot on large target surfaces and intelligent rotational windows are implemented in order to reduce the weakening of the beam by the species condensing on them.

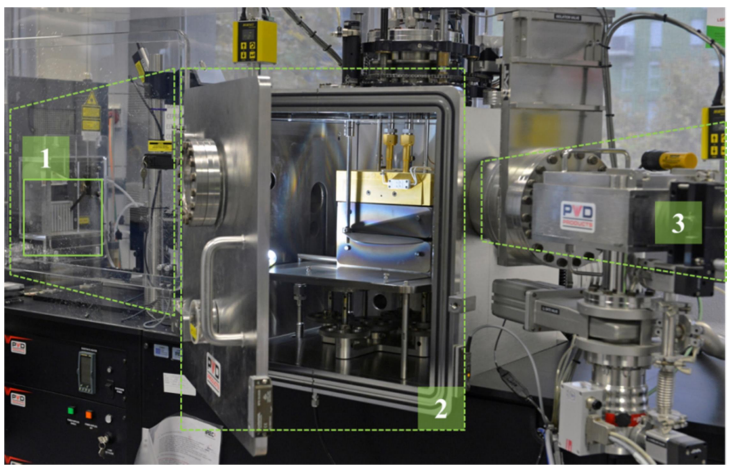

Fig. 2.3.3: Large-Area PLD from PVD Products at IREC with the optical path behind UV-protective glass and the laser exit shutter (green square) in (1), the UHV chamber opened (2) and the load lock in (3) for introducing the substrate holder while the chamber is under vacuum.

In this thesis, ablation of various thin film materials was performed inside a LA-PLD chamber, fitting at the same time four different targets on a rotational carousel of target holders inside, eliminating the need of manual target exchange (re-opening of UHV chamber) to switch between targets for multi-layers. This minimizes the amount of possible contaminants being able to attach to the layer or chamber-wall surface between the deposition of different layers. In addition, the air-exposure of the target material is minimized, as for Li-based targets there is a big attraction to moisture leading to an accelerated material decomposition. Depositions were carried out at IREC in the LA-PLD-5000 system from PVD products, operating at a minimum target-to-substrate distance of 90 mm, average spot size of 0.15 cm^2 (formerly 0.39 cm^2) and the ability to fit targets of 4" and substrates of 6" in diameter. A continuous rotation of the target holder is applied along the z-axis and an additional horizontal rastering for increased homogeneity in the stoichiometric material transfer. The substrate holder is rotated vertically with an offset of rotation towards the target, increasing the overall homogeneity and stoichiometry of deposited thin layers. The parameter adjustment and its impact on the thin layers is further demonstrated in **Section 3** for LATP and **Section 4** for spinel electrodes of LMO and LTO.

2.3.7 Related thin film deposition techniques

Thin film deposition techniques can be divided into Physical Vapor Deposition (PVD) and Chemical Vapor Deposition (CVD). The previously described pulsed laser deposition counts to the typical PVD techniques, which further amounts of thermal and electron beam evaporation, molecular beam epitaxy and the sputter deposition. Sputtering is realized under the directed bombardment on the negatively charged target with positive ions under creation of a plasma, whereas radio frequency (RF) sputtering additionally couples the target with the plasma capacitively under application of a frequency between 0.5 – 30 MHz. This allows to deposit not only conductive compounds, but also insulators and semiconductors.[58] Atomic layer deposition (ALD) is a method from the CVD which enables the growth of thin films layer-by-layer under the alternating application of precursors in the chamber, intermixing and growing the desired layer on the substrate surface.

In this thesis, $LiMn_{1.5}Ni_{0.5}O_4$ thin films have been fabricated by the Interuniversity Microelectronics Centre (Imec), Leuven, in Belgium.[59] Thin layers have been deposited by RF-sputtering on Pt coated planar substrates. The silicon substrate was covered with thermally grown 100 nm SiO_2 and 10 nm TiO_2 coating (ALD), which acts as adhesion layer below the Pt. Subsequent annealing at 800 ºC was carried out in air for 30 min in order to prevent eventual outgassing during future annealing. Substrates were finally metallized with a 70 nm conductive Pt layer deposited by DC sputtering, with Pt acting as current collector and diffusion barrier. The LMNO layer is deposited by RF sputtering (Kurt J. Lesker Company) from a 4" target (Neyco, France, 99.5% purity) at a power of 55 W, with substrate rotation at 20 rpm, and an Ar flow of 11 sccm. The as-deposited films are amorphous and appear inactive, which then changes after annealing (Annealsys) at 700 ºC for 1 h in an O_2 atmosphere, achieving pure, crystallized LMNO thin films of ~ 100 nm thickness. The thin layers have been encapsulated as described in **Section 2.6** for operando spectroscopic ellipsometry (SE) measurements in an air-tight optical chamber under electrochemical cycling, which is demonstrated in **Section 5.3.2**.

2.4 Structural and microstructural characterization

In the following, material characterization in structure and microstructure was performed, mostly through to optical characterization techniques. Arising from the wave-particle duality described by *de Broglie*, a particle is a wave and vice versa, which allows photons and electrons to penetrate matter as waves, whereas photons are neutral and electrons are negative in charge.[60] As a result of different wavelengths and hence energies exciting the material, a variety of effects can be observed characteristic for a multitude of material properties.

In this thesis, microstructural analysis is explored under the application of elastic electron scattering in the Scanning (Transmission) electron microscope (SEM/STEM) for bulk and transparent specimen. Inelastic scattering phenomena lead to the collection of energy and wavelength dispersive X-ray spectra (EDS/WDS) and electron energy-loss spectra (EELS), monitoring the material composition. Further structural analysis is performed upon X-ray diffraction and scattering (XRD/GI-XRD) and electron diffraction patterns collected from high resolution (HR)-STEM images. Laser excitation of the material and the analysis of

its vibrational modes between molecules were done by Raman spectroscopy. Apart from interactions with electrons and X-rays, the change of the near-atomic magnetic field in a molecule under application of radio waves results in further structural and compositional information detected by the nuclear magnetic resonance (NMR) spectroscopy. Away from analyzing scattering events by optical techniques, in **Section 2.4.3** another fraction of material characterization is explored, such as the thermo-gravimetric analysis (TGA) for estimating temperature induced chemical reactions, or the translation of electro-mechanical surface effects for topographic imaging in the atomic force microscopy (AFM).

2.4.1 Electron-induced interactions

Electrons are emitted from a cathode material through thermal or field emission and accelerated through an electromagnetic field. The wavelength λ and therefore kinetic energy of an electron depends on the strength of the applied voltage *V* accelerating it in vacuum. Hence de Broglie's equation combined with the electrons kinetic energy can be used to calculate λ in **Eq. 2.4.1**, with *h* being the Planck's constant, m_0 the electrons rest mass, *e* the elementary charge and *E* the kinetic energy (in *eV*).[61]

$$\lambda = \frac{h}{(2m_0 eV)^{1/2}} \sim \frac{1.22}{E^{1/2}} \qquad \text{(Eq. 2.4.1)}$$

As a result, higher voltages lead to smaller λ and higher resolutions, but with restrictions by limitations usually resulting from the system.

2.4.1.1 Scanning electron microscopy (SEM)

For typical SEM imaging, accelerating voltages can be chosen between 1 – 30 kV, providing a minimum instrument resolution around 1 nm. The electrons are focused to a beam, scanning the specimen surface. As the primary beam is absorbed by the sample, it will be deflected under interaction with electrons in the outer atomic shell creating secondary electrons (SE) for topographic contrasts (inelastic scattering event), or back scattered electrons (BSE) formed upon interaction with the atomic nuclei giving a material contrast in dependence on the *Z* atomic number (elastic scattering event). Secondary electrons are detected with either a common Everhart-Thornley detector or with a specific in-lens detector placed in the beam path,

providing especially high resolution for SE emitted near the surface of the interacting volume.[61–63]

In this thesis, the Zeiss Auriga SEM at the facilities of IREC, equipped with a 30kV Gemini FESEM column (field emission electron gun) and detectors for SE, BSE and an in-lens for higher resolutions, is used for the analysis of thin films. Operating voltages and working distances were kept low, between 3 – 5 kV and 1 – 3 mm respectively, to gain higher resolution and less charging effects on the oxide based materials. Images are collected in-plane and across-plane for the determination of roughness and thickness values. Comparison is made to values achieved in the Ellipsometer models and topography analysis by atomic force microscopy in **Section 3** and **4**.

2.4.1.2 Energy/Wavelength dispersive analysis (EDS/WDS)

As the electron beam interacts with the sample atoms, inelastic scattering events between the electrons in the atomic shell and the beam species lead to a transfer in energy. Under high accelerating voltages, the high energy of the electron bombardment can eject electrons in the inner atomic shells. The electron hole is filled by electrons of higher electronic states under energy delivery in the shape of characteristic X-ray photoemission.[63] For EDS those characteristic photon energies are detected simultaneously for all elements, in WDS they are diverted onto an analytical crystal to perform diffraction on. As only one λ at the time can fulfill Bragg's law diffraction requirements (see **Eq. 2.4.2**), the signal of only one element is analyzed at a time. Elemental sensitivity for WDS is more accurate for lighter elements such as C, N and O (limit is B), than for EDS where detection fades with elements of an atomic number *Z* lighter than Na, as the energies are in the lower detectable limit. Additional care has to be taken with possible evaporation of light elements under exposure to the electron beam, hence complicating precise analysis of volatile species even more. Further the sensitivity for trace elements in WDS is higher, with detection limits at 0.01 wt%, compared to EDS with the lowest amount detectable in theory of 0.08 wt%.[63,64]

In this thesis, qualitative and quantitative elemental analysis for the bulk powders and targets, as well as thin films deposited of LATP was performed with an EDS detector implemented in the Zeiss Auriga SEM at IREC. Working distances are

increased to 5 mm and the accelerating voltage set between 15 – 20 kV. As calibration elements Cu, Co and Si can be used, depending on the energies expected for the characteristic X-rays evolving from the elements to be analyzed. As lithium and oxygen are too light to be detected with certainty in the EDS, the cationic ratios between Al, P and Ti are comparable for different compositions. For more reliability in the results for light elements, WDS was carried out on thin film samples of LATP at accelerating voltages of 12, 15 and 20 kV and evaluated with the thin-film program STRATAGEM (SAMx France). Qualitative and quantitative results could be obtained and are compared to EDS results in **Section 3**. WDS measurements were performed at the equipment of CCiT at the University of Barcelona with multiple spectrometers mounted in an Electron probe micro-analyzer (EPMA). In addition, EDX spectra were collected with the Titan (Thermo Fisher Scientific) in STEM mode, as described in the following **Section 2.4.1.3**. The results for the analysis on LATP are presented in **Section 3**.

2.4.1.3 Transmission electron microscopy (TEM/STEM)

For thin specimen < 100 nm, the material is transparent to penetrating electrons and therefore elastic and inelastic scattering events of the primary beam before and after passing through the sample can be detected. This transmission electron microscopy (TEM) allows imaging at high resolution below 1 Å, with accelerating voltages up to 1200 kV. As in the TEM a parallel electron beam is passing through the sample, in the mode for Scanning transmission electron microscopy (STEM) the beam is converged and scanned through the samples as in the SEM and therefore enabling the elemental analysis by EDS and electron-energy loss spectroscopy (EELS), described in **Section 2.4.1.2** and **2.4.1.4** respectively. For the STEM, detectors get arranged in annular shape around the primary beam axis, detecting the signal of the species at the angles characteristic for their different scattering events. Therefore the transmitted, direct beam is used for bright field (BF) imaging. Coherent elastic scattered electrons (deviation angles 1 – 10º) indicate coulombic interactions of beam electrons with the electron cloud of the atomic shell and are used for imaging in the annular dark field (ADF) detector. Higher anlges (above 10º) indicate coulombic interaction of the beam electrons with the atomic nuclei, known as the Rutherford scattering leading to incoherent elastic forward scattered electrons. They

are detected in the high-angle annular dark field (HAADF) and indicate directly the material *Z*-contrast.[61]

Dark and bright field images result from the contrast in amplitude for different species, but the contrast in phase is visible in high resolution (HR) TEM images when passing multiple parallel electron beams through the sample. Constructive interference, where the waves remain in phase, will occur under a certain glancing angle θ, where the path difference between two waves is an integer multiple (n) of the wavelength λ, see **Fig. 2.4.1 (a)**. As the coherent electron beam wavelength is in the order of atomic inter-planar spacing d_{hkl}, the atoms of the crystal lattice act as equidistant scattering centers (slit-like) and diffraction occurs, under the condition of Bragg's law, described in **Eq. 2.4.2**.[60,61] For electron diffraction the glancing angle ranges from $0 < \theta < 1^{o}$, which is much smaller than for X-ray diffraction (see **Section 2.4.2.1**) due to the smaller wavelength of the incident electron beam.[65]

$$2 \cdot d_{hkl} \cdot \sin(\theta) = n \cdot \lambda \qquad \text{(Eq. 2.4.2)}$$

Where d_{hkl} is referring to (*hkl*) Miller indices, describing crystallographic planes with the reciprocal integer multiple *h*, *k* and *l* of the lattice parameters *a*, *b*, *c* in real space if n = 1 (parallel planes to specimen surface), otherwise the *d*-spacing results from the Laue indices as the *n*-multiple of *hkl* (in 3 dimensional crystals). The Laue indices are used to describe crystal lattices in reciprocal space, where the reciprocal lattice vector is established as G_{hkl} in **Fig. 2.4.1 (a)**, with vector description to depict the Bragg condition also in the reciprocal space. The construction of the reciprocal lattice from the unit cell in real space is described in **Fig. 2.4.1 (b)**.

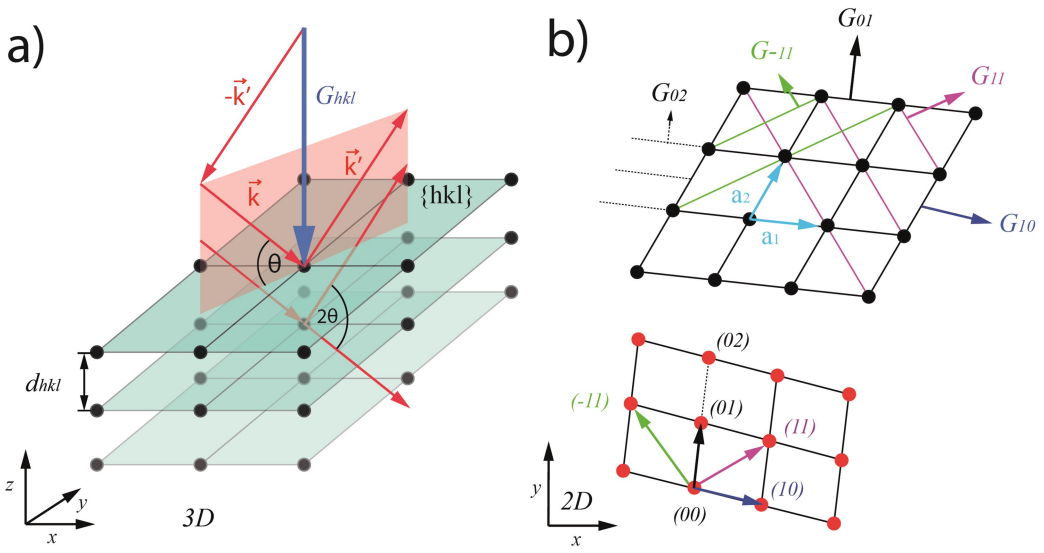

Fig. 2.4.1: The crystal lattice parallel planes *{hkl}* are shown in real space, with their vector translation into the reciprocal space in (a) under the condition of constructive interference of the parallel beam wave at a glancing angle θ. In (b) the translation of a 2D unit cell from real space into the reciprocal lattice with G_{hk0} is depicted.

Expressed in vectors, the incident beam is written as wave vector $\vec{k}$ and the elastically scattered beam as $\vec{k'}$, with $|\vec{k}| = |\vec{k'}|$ related to λ as sinusoidal wave expressed as angular frequency 2π divided by the period *k*. Hence the Bragg condition of the constructive interference is true, if the difference in wave vectors is equal to the reciprocal lattice vector $G_{hkl} = \vec{k} - \vec{k'}$, as seen in **Fig, 2.4.1 (a)**, whereas G_{hkl} is always normal to d_{hkl} and can be described with **Eq. 2.4.3**.

$$G_{hkl} = 2\pi \cdot \frac{1}{d_{hkl}} \qquad \text{(Eq. 2.4.3)}$$

As a result, under constructive interference the zone axis of the incident beam is always parallel to G_{hkl}, as well as always normal to d_{hkl} of the lattice planes. Hence for the reciprocal lattice each point describes a set of parallel lattice planes. For the imaging in HR-TEM, the signal of multiple lattice planes can be accumulated simultaneously for polycrystalline materials, giving information on the different orientations and lattice dislocations, due to their difference in phase. As the zone axis of the beam has to be normal to all of these planes, the Ewald-sphere crosses the path of G_{hkl} at the length of its radius $r = \lambda^{-1}$ for constructive interference, collecting all diffracted reflections in the crystal in one projected plane. In order to filter the accumulated and overlapping signal of all the waves with different phases, a Fast Fourier Transform (FFT) is performed, where the reflections are split upon

their different period in single periodical waves and depicted as symmetrical reflections with $1/d_{hkl}$ distance from the beam center. The FFT basically pictures the reciprocal lattice and therefore a reversed translation of the lattice in real space, with its vectors and angles of the unit cell. Further the inverse of FFT (IFFT) can be back translated, in order to obtain a clearer contrast in phase, as the noise of non-constructive interferences is subtracted.[61,66,67]

In this thesis, thin film samples of LATP deposited by PLD were prepared with a focused ion beam (FIB) of Ga-ions (FEI Dual Beam Helios NanoLab 600) for the investigation in the STEM. Lamellas were cut across the plane and polished down to thicknesses between 40 – 50 nm. The electron transparent samples were then introduced in a probe aberration corrected Titan (Thermo Fisher Scientific) equipped with a high-brightness field emission gun and operated at 300 keV Tecnai F30 (FEI company), fitted with a SuperTwin lens enabling a point resolution down to 1.9 Å. A High-angle annular dark field (HAADF) detector was used for the monitoring of the Z-contrast in STEM mode. The equipment was available at the University of Zaragoza, operating in both the TEM and STEM mode. Results on LATP thin films investigated with STEM are presented and discussed in **Section 3**.

2.4.1.4 Electron energy-loss spectroscopy (EELS)

As the primary beam electrons are transmitted through the specimen, their inelastic interactions cause a certain energy loss in favor of the energy uptake for initiated processes, such as inner-shell ionization, emission of bremsstrahlung as braking radiation and characteristic X-rays, creation of secondary electrons, phonons, plasmons and the initiation of cathodoluminescence. The beam electrons loose energy upon those interactions, which can be detected and are characteristic for the interactions that have taken place. For very thin specimen, a majority of the electrons exhibit zero loss (ZL) while their passage and therefore the signal at 0 is the strongest. In the low-loss (LL) region up to 100 eV the plasmonic features are the strongest and vary their intensity with the specimen thickness. The electronic information collected is a response from the more weakly bound conduction and valence electrons. For high-loss (HL) region above 100 eV (and below 1000 eV), the intensity drops significantly and the continuous background is constructed of bremsstrahlung. Well defined ionization edges are visible, resulting from the energy threshold for electron jumps in the inner atomic shell, being very characteristic for

the kind of atom and shell, giving additional information about the kind of bonding. As a result, EELS is very powerful for the detection of light species, as *all* species can be detected under a very high energy resolution at single-atom level below 1 eV. Hence it is possible to detect lithium and other volatile species, as this is not possible within the limits of X-ray spectroscopy.[61,65]

In this thesis, EELS were collected with the Titan (Thermo Fisher Scientific) in STEM mode. The setup includes the "Tridiem" Gatan Energy Filter (GIF), enabling Energy Filtered TEM (EFTEM) images, as well as line spectra or spectrum imaging as maps. To allow simultaneous TEM imaging, a 2k x 2k Ultrascan CCD camera (Gatan) is placed before the GIF. EELS has been carried out using the STEM mode (Spectrum-imaging acquisition[68]) and minimizing possible damages of the material structure with the electron beam. Analysis performed on the lamellas prepared from LATP thin films is described in **Section 3**, with the focus on the EELS sensitivity to especially light components, such as lithium and oxygen.

2.4.2 Photon-induced interactions

Photons are elementary particles with discrete energy values in an electro-magnetic field, neutral in charge and being characterized by their wave-particle duality in certain wavelengths, frequencies or energies. Therefore a full electro-magnetic spectrum expands upon their quantized energy levels ranging from λ as high as 10^7 m (10^4 km) down to 10^{-15} m (10^{-6} nm).

2.4.2.1 X-ray diffraction (XRD)

X-rays are photons emitted upon the interaction of accelerated electrons with matter, creating radiation in a range of λ below 10^{-2} nm up to 10 nm. Due to their small wavelength they can be scattered on objects in the size of crystal lattice unit cells and therefore deliver valuable information upon the materials structure and crystallinity. Scattering events on lattice planes parallel to the surface under the glancing angle θ, the diffraction requirements of Bragg's law in **Eq. 2.4.2** are fulfilled and the material can be systematically analyzed by moving θ on a goniometer ring over the sample between $0 < \theta < 180^{o}$. Multiple reflections may occur, all adding up to a diffractogram with a peak pattern over a broad angular range, as characteristic fingerprint of the material. But not only the peak position gives valuable information on the material properties, also line broadening of single

reflection peaks can give the apparent particle size *t*, which can be calculated by the Scherrer equation in **Eq. 2.4.4**.[69]

$$\beta_P = \lambda/(t \cdot \cos(\theta)) \qquad \text{(Eq. 2.4.4)}$$

The particle size broadening β_P can be described by the full width at half maximum (FWHM) of a diffraction peak (in radians).

In this thesis, for the structural analysis of all samples, X-Ray diffraction on powders and thin films was performed with the Bragg-Brentano Theta-2Theta setup on the goniometer ring, where the sample holder is fixed horizontally in reflection and the X-ray gun and detector are scanning symmetrically the angular range of θ. X-ray diffractograms were collected with Bruker-D8 Advance equipment utilizing Cu-Kα radiation (λ = 1.54184 Å), Ni filter and Lynx Eye detector. For measurements the coupled Theta-2Theta mode was set and for thin films on single crystalline substrates performed with a slight omega offset in order to reduce the impact of the very intense reflections from the substrate. Further In-situ measurements upon annealing of pre-reacted powders or as-deposited thin films on different substrates were performed inside the XRK 900 reactor chamber from Anton Paar GmbH with an operational range between 25 – 900 ºC and an inlet for controlled gas supply. Additional diffractograms specialized in the analysis of thin films were performed in the PANalytical X'Pert PRO MRD diffractometer using a grazing incidence (GI) setup with an incident beam angle ω between 0.33 and 0.40º at the scientific and technological center (CCiT) at the University of Barcelona. Peak broadening was determined by a fit to the Gaussian profile in OriginPro9® and the resulting FWHM. Diffraction pattern analysis was performed with X'Pert HighScore Plus® software provided by Malvern PANalytical with ICDD reference pattern database. The measurements for in-situ temperature dependent analysis in XRD are further presented in **Section 3** for LATP powders and thin films. Ex-situ XRD in ambient on thin films was performed for the characterization of LATP, LMO and LTO in **Section 3 – 4**. GI-XRD measurements have been performed for LTO thin films are presented in **Section 4**.

2.4.2.2 Raman spectroscopy

Molecules interacting with an electromagnetic field will lead to an energy uptake in their quantized electronic states, due to inelastic scattering. The energy of this transition is directly proportional to the inverted wavelength λ^{-1}, the so-called

wavenumber $\tilde{\nu}$, with 1 cm^{-1} equal to the energy difference of $1.24 \cdot 10^{-4}$ eV per molecule upon absorption/emission. If a photon hits atoms connected in an ordered structure (short- or long range order), vibrational oscillations among the atoms, so-called phonons, will mainly occur in the range of $\tilde{\nu} = 10^4 – 10^2$ cm^{-1}, known as the Raman scattering.[70] As the incident beam is usually a monochromatic light source (e.g. laser) in the visible light spectrum, the energy of incoming photons in Raman is in the order of electronic transitions, connecting electronic with vibrational and rotational states.[70,71] A change in polarizability (measure of molecule/atomic deformation in electric field) defines Raman active modes, which will lead to a deviation in the incoming light frequency and a detectable shift in the wavenumber of the emitted light in return, with each shift characteristic for the molecule and its initiated interactions upon illumination. These interactions can be presented on a spectrum of Raman shifts characteristic for the material and its vibrational and rotational modes.

For the understanding of vibrational modes visible in the Raman shift, one has to correlate the crystal structure of the material and site symmetries of the atomic Wyckoff cell positions to point group specific character tables.[70,72] From those tables the active vibrational modes of each atomic position can be calculated and usually under application of DFT calculations the shift in the Raman spectra predicted. Structural and microstructural features can further influence the empirical Raman shift, giving more profound information on the composition, crystallinity, orientation and strain.

In this thesis, Raman spectra were collected in an HORIBA Scientific iHR320 monochromator equipped with an HORIBA syncerity CCD (1024 x 256, pixel size 26 µm x 26 µm) and a laser at λ = 532 nm (green), providing a spectral range between 100 – 7700 cm^{-1} (gratings available are 600, 1200 and 1800 lines mm^{-1}). A microscope objective of 0.90/100x was used with a resulting spot diameter of 721 nm. For acquisition and analysis the LabSpec 6® Spectroscopy Suite software from Horiba Franca SAS is used. The lattice vibrations of LATP, LMO and LTO were studied for understanding their structural changes and are further elaborated in **Sections 3** to **4**. Operando measurements are described in **Section 2.6.1** and results for the measurements on LMO thin film cathodes under operation are collected in **Section 5.2**.

2.4.2.3 Nuclear magnetic resonance (NMR)

In a strong magnetic field the transition of nuclear spin levels is observed under application of radio waves.[70] Atoms with an even atomic mass number (and an even number of neutrons) do not exhibit a nuclear spin quantum number *l* and therefore are unable to change their energy level, as they remain at one spin state *N*. The detection of isotopes (odd number of neutrons) and atoms with an odd atomic *Z* is enabled due to the variety of spin states obtainable from $N = 2l+1$. Without the presence of an external magnetic field all of these states are equal. Within a uniform magnetic field B_0, the states are divided in discrete energy levels, as the unpaired spin can be flipped under the penetration of radio frequent waves and the nuclei are resonant towards B_0.[73] For the analysis in solids, the magic angle spinning (MAS) NMR is applied for higher resolution, spinning (within the range of kHz) the sample probe at 54.7º respectively towards the direction of the magnetic field.[74] NMR spectra picture the energy absorption of the nuclei to reach resonance and in the difference of this energy necessary, depending on their chemical environment, there will be shift in frequency known as chemical shift δ_0 (ppm) where resonance occurs. Hence NMR is very sensitive to certain nuclei and their local coordination environment and even quantification can be obtained.[75]

In this thesis, MAS NMR measurements were performed at Centre for Cooperative Research on Alternative Energies (CIC energiGUNE) facilities in Álava (Spain) using the Bruker Avance III 500 MHz (11.7 T) spectrometer operating at Larmor frequencies of 500.24, 194.41 and 130.35 MHz for ^{1}H, ^{7}Li and ^{27}Al respectively. Thin films of LATP deposited on glassy SiO_2 substrates were ground to powders and packed in 2.5 mm rotors. The MAS frequency was set to 20 kHz for all measurements. References for the ^{7}Li and ^{27}Al spectra consist of 0.1 M LiCl and $Al(NO_3)_3$. Single pulses were applied in all cases with non-selective π/2 pulse durations of 2.3 μs for ^{27}Al and 2.4 μs for ^{7}Li. The DMFIT software was used to reconstruct and simulate the spectra. Thin films of LATP deposited by LA- PLD on SiO_2 glass substrates as-deposited and annealed at 800 ºC for 5 h were examined by MAS-NMR concerning their ^{7}Li and ^{27}Al spectra and are compared in **Section 3**.

2.4.3 Further applied characterization methods

Optical scattering techniques include many typical characterization techniques, such as microscopy, surface analysis, chemical composition and structural analysis, but having their limits, they are complemented by thermal and chemical analysis, as well as alternative microscopy techniques.

2.4.3.1 Thermogravimetric analysis (TGA)

For dynamic measurements (DTG) the sample is linearly heated with a constant rate, monitoring the change in mass over time and giving an estimation of the reaction kinetics. Using differential scanning calorimetry (DTA/DSC), the heat flow at the sample and a blank are measured as a function of the temperature and time. Endothermic or exothermic reactions will cause peaks at discrete temperatures in the signal of the monitored heat flow, from which the thermal heat capacity and reaction enthalpy can be calculated.[76]

In this thesis, DTG and TG-DSC analysis were performed in order to study the reactions taking place between precursors of LATP pre-reacted at 600 ºC and further heated up to 950ºC in a Zirconia crucible under ambient atmosphere, monitoring the weight loss taking place in respect to a stable reference (blank) over time. The observations in TGA-DSC experiments for the LATP powder synthesis are illustrated in **Section 3**.

2.4.3.2 Atomic force microscopy (AFM)

For the imaging of surface topography in the AFM, a physical probe is scanned in very close proximity over the surface of the specimen. As the scanning probe serves a force-sensing cantilever, which by scanning over the surface encounters van der Waals, chemical, magnetic or electrostatic interactions with surface atoms, leading to attractive or repulsive bending of the tip. Hence the difference in potential energy can be expressed with a force, and the deflection of the tip in z direction is monitored by a laser beam deflected from the cantilever onto a photoelectrode detector. The AFM can operate in multiple imaging modes, such as contact, friction force, tapping or non-contact mode. In tapping mode, the cantilever is held at its resonance frequency by a piezoelectric drive, touching the surface at the bottom of

each oscillation and therefore exhibiting measureable changes in its phase or amplitude.[77,78]

In this thesis, the XE15-AFM from Park systems was operated in tapping mode at IREC facilities. Non-contact micro cantilevers by Olympus of type OMCL-AC160TS with a force constant of 26 N m^{-1} and a frequency of 300 kHz were applied. Surface roughness for the thin layers of LATP on Si_3N_4 substrates are shown in **Section 3**.

2.5 Functional characterization

The functional material properties are characterized in respect of the materials electrochemical and optical behavior. Whereas all the properties can be linked to the electronic band structure of the compounds, giving insight into the influence of transition metal valence band occupancies and their effect on electrochemical potentials and the mass transport properties in general. A variety of relative simple techniques is studied in the following, in order to investigate the phenomena taking place in transition metal oxides, glass-ceramics and their hetero- and homogeneous interfaces.

2.5.1 Electrochemical: Solid – solid interfaces

For the characterization of mass and charge transport mechanisms in electrodes and/or electrolytes across solid-solid and solid-liquid phase boundaries, the application of Electrochemical Impedance Spectroscopy (EIS) is a popular choice to resolve the unique polarization mechanisms at interfaces subjected to potential differences.[79] In the following the EIS data acquisition method, modeling of equivalent circuits and their interpretation in respect to the physical meaning will be explained in further detail, focusing on solid state chemistry. The basics will be applicable also to the analysis in liquid electrochemistry, but with some restrictions as explained in **Section 2.5.2.3**.

2.5.1.1 Electrochemcial impedance spectroscopy (EIS)

To resolve single phenomena in a system deviating from the linear ohmic behavior, such as inductance (change in magnetic fields) or capacitance (electrostatic charge storage), a sinusoidal voltage V (or current I) is imposed and polarized regions will adapt with for each process characteristic rates. To provide a description of the full

system as a function of various frequencies, the assumption of linearity is kept for small-signals, in which the system virtually occurs time-invariant and a deconvolution of single contributions is possible.[79] Hence the sinusoidal (*ac*) oscillation of current and voltage can be written as in **Eq. 2.5.1 (a)** and **(b)**, with V_o and I_o as amplitudes and φ as the phase shift imposed by the applied voltage (or current).

$$V(t) = V_0 \cdot e^{j\omega t} \qquad \text{(Eq. 2.5.1a)}$$

$$I(t) = I_o \cdot e^{j\omega t + \varphi} \qquad \text{(Eq.2.5.1b)}$$

Their quotient according to Ohm's law is the complex impedance Z, as a function of the angular frequency $\omega = 2\pi f$, demonstrated in polar **(a)** and cartesian **(b)** coordinates in **Eq. 2.5.2**.[79,80]

$$Z(\omega) = \frac{V(t)}{I(t)} = |Z| \cdot e^{-j\varphi} \qquad \text{(Eq. 2.5.2a)}$$

$$Z(\omega) = |Z|cos\varphi - j|Z|sin\varphi = Z' - jZ'' \qquad \text{(Eq. 2.5.2b)}$$

Hence linear behavior with an ohmic resistance equal to Re(Z) = Z' is achieved if the phase shift $\varphi = 0$, and non-linear behavior is included in the imaginary part Im(Z) = Z'', as summarized in **Fig. 2.5.1** in the so-called Nyquist plot.

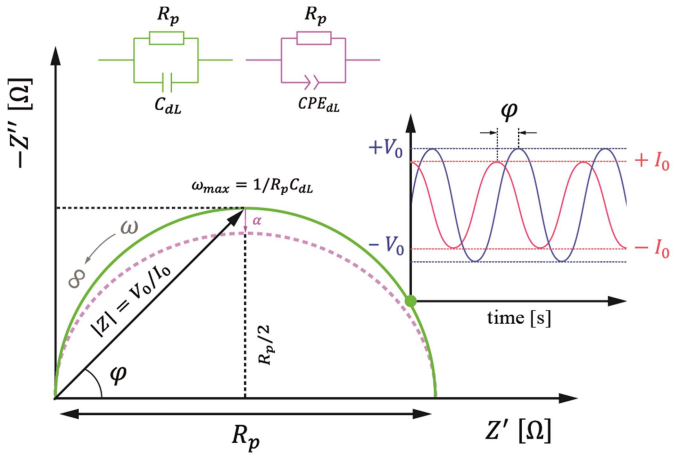

Fig. 2.5.1: Nyquist plot for RC (green) and R-CPE (purple) element and the phase shift φ between the electrical stimulus *V(t)* and the response of the current *I(t)* demonstrated for one frequency ω in the inset.

In this thesis, temperature-dependent impedance spectra were conducted in a Linkam LTS600 probe station performing in-plane and cross-plane measurements on parallel, rectangular sputtered gold electrodes applied at IREC facilities or

circular micro-electrodes fabricated at the Institute of Microelectronics of Barcelona IMB-CNM. Electrodes were connected through two tungsten tips in a pseudo-four-probe configuration to eliminate the resistance of the measurement wires. The station and the setup are shown in **Fig. 2.5.2 (a)**.

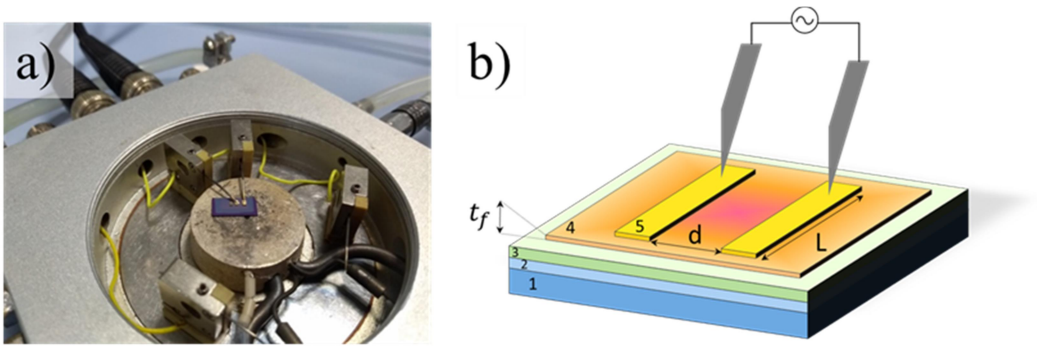

Fig. 2.5.2: Linkam THMS600 probe station with the thin film sample mounted on a resistive heating plate in the center in (a) and the in-plane setup illustrated for gold current collectors of a length L and distance d deposited on the thin film (4) with a thickness of t_f (nm) in (b). With (3) 300 nm Si_3N_4, (2) 100 nm SiO_2 and (1) Silicon substrate, respectively.

In-plane impedance measurements were carried out as schematically demonstrated in **Fig. 2.5.2 (b)** and resulting conductivities calculated with **Eq. 2.5.3**, using the parameters d as distance between the electrodes, L as their length, R as the resistance and t_f as the film thickness measured (by SEM or spectroscopic ellipsometry).

$$\sigma = \frac{1}{\mathrm{R}} \cdot \frac{d}{L \cdot t_f} \qquad \text{(Eq. 2.5.3)}$$

Measurements in *ac* were controlled by a Novocontrol Alpha-A Impedance spectrometer with ZG4 electrochemical interface and collected in a frequency range of 40 MHz to 100 mHz and a perturbation voltage of 100 mV with zero bias. Gold electrodes or any noble metal with high electrical conductivity and very low ionic conductivity can be used as current collectors, hence blocking lithium and other ionic compounds to be conducted. This is of great importance also on the triple phase boundary of the thin electrolyte, the current collector and the ambient, in order to exclude eventual leakages or additional contributions. All measurements were performed in a dry gas mixture of 79 % N_2 and 21 % O_2 and spectra were measured while heating up and cooling down from room temperature up to 450 ºC. The comparison between them should evaluate the influence of eventual humidity on the overall ionic conductivity and further secure reproducible results. Impedance

spectra collected on LATP thin films as-deposited on different substrates and after annealing at different temperatures are discussed in **Section 3.3**.

2.5.1.2 Modelling equivalent circuits

As mentioned before in **Section 2.5.1.1**, the current-time response of polarized domains is characteristic for certain mass and charge transport phenomena, and can be described for each individually with a specific time constant τ. To translate the complex impedance signal obtained in the Nyquist plot to a physical meaningful model, *ac* modules of singular phenomena combining resistors (*R*), capactiors (*C*) and inductors (*I*) in parallel, such as the RC element, are connected in series to an equivalent circuit to model the full function of impedance as a function of freuquency.[80] For a simple RC element, e.g. for a corroding system with a double layer capacitance C_{dL} and a polarization Resistance R_p, adaptions in **Eq. 2.5.2b** lead to **Eq. 2.5.4**.

$$Z(\omega) = R_p + \frac{1}{j\omega C_{dL}} = \frac{R_p}{1+j\omega R_p C_{dL}} \qquad \text{(Eq. 2.5.4)}$$

For the arc to be at its maximum in the imaginary Im(Z), the real part Re(Z) = $R_p/2$ and the time constant τ_{rc} for an RC element can be derived from the maximum frequency ω_{max}, as demonstrated in **Eq. 2.5.5**.[80]

$$\omega_{max} = 2\pi f_{max} = \frac{1}{R_p C_{dL}} = \frac{1}{\tau_{rc}} \qquad \text{(Eq. 2.5.5)}$$

The obtained time constant describes for each system characteristic relaxation times to equilibrate after the perturbation with an electrical stimulus. Under slight disturbances due to defects on interfaces, charge inhomogeneities, changes in stoichiometry, etc. the oscillations can be damped and the response dispersed with a factor $0 < \alpha < 1$, as illustrated in **Fig. 2.5.1**.[79] Hence the perfect capacitor changes to a constant phase element (CPE) with $Z_{CPE} = 1/(Q(j\omega)^{\alpha})$, defined in a pseudo-capacitance Q and the corresponding relaxation time of the R-CPE equivalent circuit is calculated from the frequency in **Eq. 2.5.6**.[81]

$$\omega_{max} = \left(\frac{1}{R_p Q}\right)^{1/\alpha} \qquad \text{(Eq. 2.5.6)}$$

Further elements for the description of diffusive phenomena can be fit with a set of impedances, which occur upon the change of surface concentration of an

electrochemically active species during the *ac* cycle. A Warburg impedance Z_W of finite-length can be applied as described in **Eq. 2.5.7**, with the Warburg coefficient σ_W ($\Omega cm^2\ s^{-1/2}$) and a double layer contribution in the imaginary part, for allowing a constant concentration profile of the species distant from the surface.

$$Z_W = \frac{\sigma_W}{\sqrt{\omega}} - j\frac{\sigma_W}{\sqrt{\omega}} \qquad \text{(Eq. 2.5.7)}$$

The diffusion coefficient D and the double layer thickness δ_{dL} are in direct correlation to ω_{max} and the resulting time constant, as shown in **Eq. 2.5.8**.

$$\omega_{max} = 2\pi \cdot 0.4 \cdot \frac{D}{\delta_{dL}^2} = \frac{1}{\tau_W} \qquad \text{(Eq. 2.5.8)}$$

The physical meaning of σ_W can be adapted depending on physical, chemical or electrochemical parameters in the nature of the electrochemical process. As bottom line it is useful to keep in mind that the construction of equivalent circuits has to be evaluated each time new regarding their physical meaning.[80]

In this thesis, the construction and fitting of equivalent circuits was carried out using ZView® software. The solid electrolyte LATP has been studied thoroughly with impedance spectroscopy in literature and certain equivalent circuits have been established and their physical meaning evaluated, as it is further elaborated in **Section 3**. Nonetheless the circuits change upon the material physical and chemical properties, and as already lined out earlier, thin film applications of LATP have been rarely investigated so far. Therefore the impedance spectra collected as a function of frequency and temperature were evaluated under construction of adapted equivalent circuits and the activation energy (E_A) for their ionic conduction processes calculated, as demonstrated in **Section 3** for LATP thin films before and after annealing.

2.5.2 Electrochemical: Solid – liquid interfaces

A different contemplation is chosen when comparing solid and liquid electrolyte systems and their interfacial phenomena. Their differences can be attributed to a reversed behavior in electronic and ionic conductivities comparing each other. Liquid solvent and aqueous based electrolytes have much higher ionic conductivities than their solid counterparts and less electronic conductivity, whereas solids have usually less ionic conductivity but can exhibit an increase in

electronic conductivity upon stoichiometric changes.[79] Advantages and disadvantages in the application of solid electrolytes for solid-state devices are elaborated in **Section 1**, with further detail on the current state of the art in their performance compared to liquid systems. The following section is dedicated to the disclosure of similarities in the behavior of polarized interfaces in electrochemical processes from solid-solid to solid-liquid domains, in order to shape their analysis in a comparable way.

In this thesis the electrochemical performance of $LiMn_2O_4$ (LMO), $LiMn_{1.5}Ni_{0.5}O_4$ (LMNO) and $Li_4Ti_5O_{12}$ thin films was performed in **Section 4 – 5**, using the following characterization techniques.

2.5.2.1 Charge and mass transport phenomena

As the electrodes and electrolyte exhibit a different electronic density of states, their concentrations of charge carriers at the interface differs and a potential drop occurs. Classic electrochemical models rely on a time-concentration dependency to describe electrochemical redox-reactions taking place on the solid-liquid interface, hence describing mass transport phenomena of charged particles depending on migration, diffusion and convection in the Nernst-Planck equation in **Eq. 2.5.9**. The uni-directional flux J of a species j is determined by the diffusion coefficient D_j, the charge z_j and the concentration C_j of the species at a certain temperature T, with the gas constant R and Faraday's constant F.[82]

$$J_j(x) = -D_j \frac{\partial C_j(x)}{\partial x} - \frac{z_j F}{RT} D_j C_j \frac{\partial \phi(x)}{\partial x} + C_j v(x) \qquad \text{(Eq. 2.5.9)}$$

The first term is the Fick's 1st law of diffusion, describing the species flux against a concentration gradient $\partial C_j(x,t)/\partial x$ as a function of time t and distance x from the electrode. Migration can be expressed under addition of the Nernst equation in the second part, as the flux of species in an electric field with a potential gradient $\partial \phi(x)/\partial x$ along the x-axis. The third part is dedicated to convection phenomena with the rate $v(x)$ of movement when stirring is applied or strong concentration gradients occur. The area between the solid – liquid interface is defined by the evolution of a diffusion controlled double layer comparable to an imperfect capacitor, just as in the solid – solid interface of electrode and electrolyte described in **Section 2.5.1.2** for polarized domains. The difference to the liquid ambient is its

thickness δ_N and composition, as in liquids the charge is surrounded by ligands of solvent molecules, inhibiting the charge transport over the mass transport within a distance of 10^{-3} – 10^{-1} cm from the electrode. Hence for diffusion dominated phenomena the thickness of the so-called Nernst diffusion layer can be calculated as $\delta_N = \sqrt{\pi D t}$.[79,82]

In order to observe the redox-reactions taking place, the electrode of interest is defined as working electrode (WE) and its potential is monitored with respect to a non-polarizable reference electrode, ideally not taking place in any reaction under an electrical stimulus. A third electrode is connected as counter (CE), mainly passing the current between WE and CE so the potential drop between WE and RE resulting from the solution resistance R_s is minimized, which can be further continued by placing the reference in close proximity to the WE. This setup is a three-electrode cell and is necessary to be used for monitoring electrochemical processes occurring at the WE for systems where the potential drop between WE and RE exceeds 2 mV. A two-electrode cell (no CE) can still be used, if applying very small currents.[82]

In this thesis, for the conduction of electrochemical measurements a three-electrode setup was established, with either LMO cathode or LTO anode thin films as working electrodes connected to a Biologic SP-50 potentiostat/galvanostat. Depending on their electrode potentials and the electrochemical stability window of the applied electrolytes, different choices in RE and CE are made. For the operation of LMO in aqueous electrolytes such as 1 M Li_2SO_4 the RE consisted of an Ag/AgCl wire introduced in 3 M KCl solution and sealed with mesoporous glass frit, exhibiting a standard electrode potential of 0.23 V vs. SHE. As CE in the three-electrode setup served a Pt-wire. The electrolytic stability window of water is narrow (1.23 V vs. SHE) and seeks extension for the operation of electrodes with unmatched electrolytic stabilities in the aqueous.[83] Therefore other solvent based electrolytes such as 1 M $LiPF_6$ with EC/DMC (1:1) are explored with a broad window up to 5 V vs. Li/Li^+, enabling anodic currents for the investigation of LTO as electrode in the potential range of 1.5 – 2.3 V vs. Li^+/Li, as well as generating accessibility to the full potential range of LMO with 2 – 4.5 V vs. Li^+/Li.[84] Those measurements have to be conducted under inert ambient, such as in a glove box with protective Argon atmosphere inside ($O_2 \leq 0.1$ ppm and $H_2O = 0.0$ ppm), due

to the electrolyte degradation under the influence of humidity, but also for many Li-based electrode materials. Further the reference and counter electrode were prepared of metallic lithium with -3.04 V vs. SHE in solution, which would react in a strong exothermic reaction with humidity and therefore it is impossible to operate in aqueous electrolytes. The electrochemical properties collected for LMO and LTO thin films are presented in **Section 4** for aqueous and non-aqueous electrolytes. Operando Spectroscopic Ellipsometry (SE) and Raman spectroscopy (see experimental details in **Section 2.6**) upon electrode operation are evaluated in **Section 5** for LMO and LMNO.

2.5.2.2 Voltamperometric techniques

Electrochemical methods can be classified in static and dynamic measurements, either being current or potential controlled. Herein the focus lies on cyclic voltammetry (CV) as a potentiostatic voltage sweep and the adjustment of the current upon the movement of charge, while maxima and minima exhibit cathodic and anodic redox-reactions taking place, changing the oxidation number and hence the valence band structure by incorporation or dissolution of cations. It is a typical indicator for the reversibility of a system and can further give information about the rate dependent charge transfer. It is usually complemented with static measurements, such as the chronoamperometry (CA) as potentiostatic technique, or chronopotentiometry (CP) as a galvanostatic technique following the charge transfer over time. As a result the specific charge and discharge capacities can be obtained and the diffusion coefficient *D* calculated. [82]

In this thesis, electrochemical polarization is controlled and data collected with the EC-Lab® software from Biologic. The electrochemical performance of LMO and LTO thin film electrodes is studied under the evaluation of their cyclic voltammograms and reversible redox-reactions, rate stability and capacity retention, conducted in **Section 4**. The change in optical properties related to the adjustment of their electrochemical density of states (EDOS) upon polarization is demonstrated for LMO and LMNO in **Section 5**, conducting operando SE and Raman spectroscopy for the optical monitoring of charge transport phenomena.

2.5.3 Optical: Ellipsometry

Polarized light, as already described in detail for the structural and microstructural characterization in **Section 2.3** in great detail, can further be extended to its capabilities in analysis of functional properties. The optical properties of a material always strongly depend on the band structure of its electronic states and are therefore a very characteristic fingerprint in both its optical and electrical behavior. Further Spectroscopic ellipsometry (SE) is known to be very sensitive to interfaces of a few nm and hence thin films and multi-layer systems are favorable specimen.

2.5.3.1 Spectroscopic ellipsometry (SE)

UV-light from a Xenon lamp is emitted and polarized linearly by passing through a polarizer in the *ps*-plane of E_i, as illustrated in **Fig. 2.5.3**. Linear polarization of light occurs when the electric and magnetic field vectors are divided in parallel (p) and perpendicular (s) propagation directions orthogonal to each other ($p \perp s$) with no difference in phase.

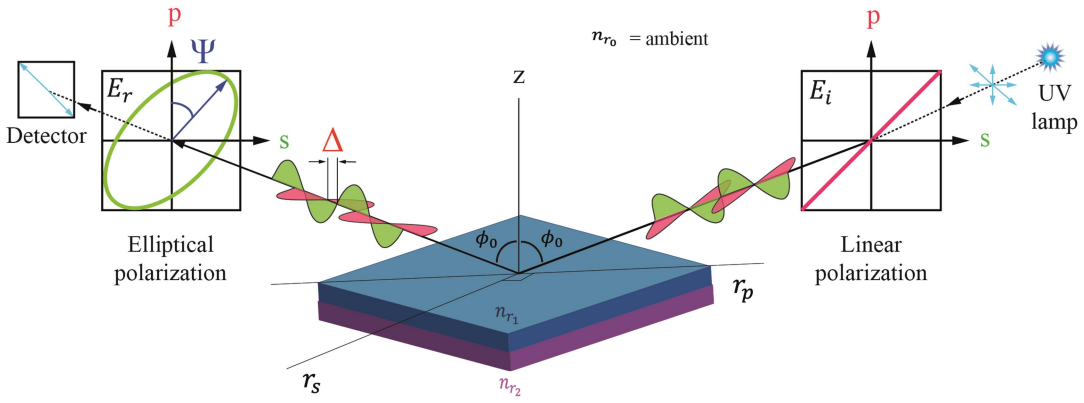

Fig. 2.5.3: Typical geometries in spectroscopic ellipsometry for the polarizer-sample-analyzer configuration, depicted for a multi-layer in ambient with different refractive indices n_r changing the polarization direction of the incident beam (i) from linear to elliptical in the reflected beam (r).

As result a transversal electromagnetic wave propagates with linear oscillation perpendicular to p and s towards the specimen surface. The incident beam angle is fixed to $\phi_0 = \phi_B = 70°$, known as the (pseudo[§]) Brewster angle typical for

[§] Pseudo-Brewster angle for s-polarization direction, as the extinction coefficient k in p-direction is unequal to zero, hence the material is not fully transparent and some attenuation of the incoming beam is expected.[85]

semiconductors, where the reflected beam will exhibit the maximum difference in the wave amplitude of *E* for its *p* and *s* field components upon interaction with the specimen, divisible in the Fresnel reflection coefficients as shown in **Eq. 2.5.10**.[85]

$$r_p = \frac{E_{rp}}{E_{ip}} \quad , \quad r_s = \frac{E_{rs}}{E_{is}} \qquad \text{(Eq. 2.5.10)}$$

Upon interaction of the incident beam with matter, a difference in phase shift Δ and amplitude ratio Ψ of the wave arises. The reflected beam is passing through a phase modulator and analyzer (second polarizer), restoring linearity and enabling the detection of the complex reflectance ratio ρ as a ratio of the Fresnel reflectivity amplitudes and is described by **Eq. 2.5.11**, also known as the fundamental equation of ellipsometry.

$$\rho = \frac{r_p}{r_s} = \tan\psi \cdot e^{i\Delta} \qquad \text{(Eq. 2.5.11)}$$

The complex dielectric function with ε as the permittivity (a measure for electric polarizability of a dielectric medium) can be directly connected to the polarized waves for **Eq. 2.5.12 (a)** and **(b)**, giving information on the refractive index n_r and the extinction coefficient *k*, with N as the complex refractive index.

$$\varepsilon = sin^2\phi_0 + sin^2\phi_0 tan^2\phi_0 \left[\frac{1-\rho}{1+\rho}\right]^2 \qquad \text{(Eq. 2.5.12a)}$$

$$\varepsilon = \varepsilon_r + i\varepsilon_i = (n_r + ik)^2 = N^2 \qquad \text{(Eq. 2.5.12b)}$$

Hence the optical dispersion and absorption are extracted as the real and imaginary part of the permittivity ε, respectively. Under determination of the extinction coefficient *k* the direct observation of absorption energies follows **Eq. 2.5.13** and concludes the condition for certain valence band electronic states through their band gap energy E_g.

$$\beta_a = \frac{4\pi k}{\lambda} \qquad \text{(Eq. 2.5.13)}$$

High sensitivities can be achieved by measuring the relative values of Δ and Ψ as the two signal intensities *Is* and *Ic* collected over a broad range of λ in the UV spectrum, especially sensitive to small changes in thin films and interfaces.[86] In order to deconvolute the information obtained from the relative intensities, the spectra have to be first modeled, as explained in detail for **Section 2.5.3.2**, under a

series of Lorentz oscillators describing the signal of Δ and Ψ as a function of the photon energy[§]. Hence not only optical constants can be calculated, but also the thickness and roughness of the probe for single or multi-layer systems.

In this thesis, spectra were collected in the UVISEL Plus ellipsometry equipment by Horiba Scientific (see **Fig. 2.6.1**), fit with a UV Xenon lamp, a linear polarizer, a phase modulator at 0º and analyzer at 45º fixed, as well as a monochromator infront of the detector, splitting the wavelengths with the iHR320 (Horiba Scientific) monochromator for the detection by a connected CCD (HORIBA syncerity CCD, 1024 x 256, pixel size 26 µm x 26 µm) camera. Acquisition is limited to a spectral range of 0.6 – 5.3 eV. The incident beam angle was fixed to 70º and a spot size of 2 mm^2 on the sample surface. The monochromator enables the detection of individual steps as fraction of a few nm, collecting spectral points on a time scale. Another acquisition mode is enabled by a multi-wavelength (MWL) setup with predefined spectrometric channels, exhibiting a slightly reduced range of 1.5 – 4.9 eV and a less detailed detection of in average every 0.106 eV, with higher resolution towards the mid-UV and visible light and less in the NIR. Acquisition is performed simultaneously in time for all selected wavelengths. The MWL dynamic measurements and some time-resolved triggering during monochromator acquisitions are further elaborated in **Section 2.6.2** for monitoring the operando performance of LMO and LMNO cathodes in **Section 5**. Static spectra of time-invariant samples were collected and analyzed for the thin film anode materials composed of LTO in **Section 4**.

2.5.3.2 Modelling optical absorption

To derive the optical properties of a material mathematically, the complex dielectric function from **Eq. 2.5.12 (b)** can be described by a series of damped harmonic oscillators modeling the frequency dependence of the electron excitation through an external electromagnetic field. As there is a multitude of models describing e.g. metals (Drude) or semiconductors (Lorentz), the focus herein is placed on the Tauc-Lorentz model as a good fit for amorphous and nano-/microcrystalline materials with absorption in the FUV and visible light.[85,87] The model consists of the Tauc dielectric function for the description of inter-band transitions of photon energies E

[§] Photon energy[85] with $\hbar\omega\ [eV] = 1.23985 \cdot \lambda^{-1}[nm]$

above the band gap E_g in combination with the common Lorentz oscillator. Their product results in the material optical absorption as the imaginary part ε_i defined in **Eq. 2.5.14**, for the combination of multiple oscillators described by A_n as the amplitude, E_n the energy position and C_n the damping coefficient or broadening term of the n^{th} absorption peak.[88]

$$\varepsilon_i = \begin{cases} \sum_{n=1}^{N} \frac{1}{E} \cdot \frac{A_n E_n C_n (E - E_g)^2}{(E^2 - E_n^2)^2 + C_n^2 E^2} & \text{for } E > E_g \\ 0 & \text{for } E \leq E_g \end{cases} \qquad \text{(Eq. 2.5.14)}$$

The Tauc-Lorentz dispersion formula of the real part can be derived from **Eq. 2.5.14** under application of the Kramers-Kronig integration.[89] As the dispersion formula does not pay attention to energies below the band gap, further improvement of the Tauc-Lorentz model can be obtained in combination with independent Lorentz/Gaussian oscillators for modeling optical transitions below E_g, as described in detail by *Likhachev et al.*[90]

In this thesis, spectroscopic data is modeled with the DeltaPsi2® software provided by Horiba France SAS. The refractive index of ambient air at standard conditions of temperature and pressure is $n_{r_0} \approx 1$. Hence its influence on the model for the optical properties of the probe is negligible. As shown in **Fig. 2.5.4 (a)** as insert, the applied model is a construct of three averaged layers built from a substrate (ideally metals as fully transparent layers) and the thin film divided in two sublayers of different density, ranging from bulk (100 %) to a mixed layer of voids (50 %) and film material (50 %) to simulate the roughness or porosity of the layer surface. This approach is called Bruggeman effective-medium approximation (EMA),[91–93] and is a common approximation of modeling crystalline dielectrica including their surface roughness. The model for the optical constants of the material itself, in the case of spinel $LiMn_2O_4$, consists of four Tauc-Lorentz oscillators, each describing optical constants at different photon energies by the change of oxidation states in Mn due to interband transitions between the O^{2-}(2p) orbital and $Mn^{3+/4+}$ (3d) of LMO, described by its degenerate energy bands t_{2g} and e_g of the d-orbital.[94] The position of each oscillator in the optical absorption and the relation to the density of states calculated for LMO is shown in **Fig. 2.5.4 (b)**.

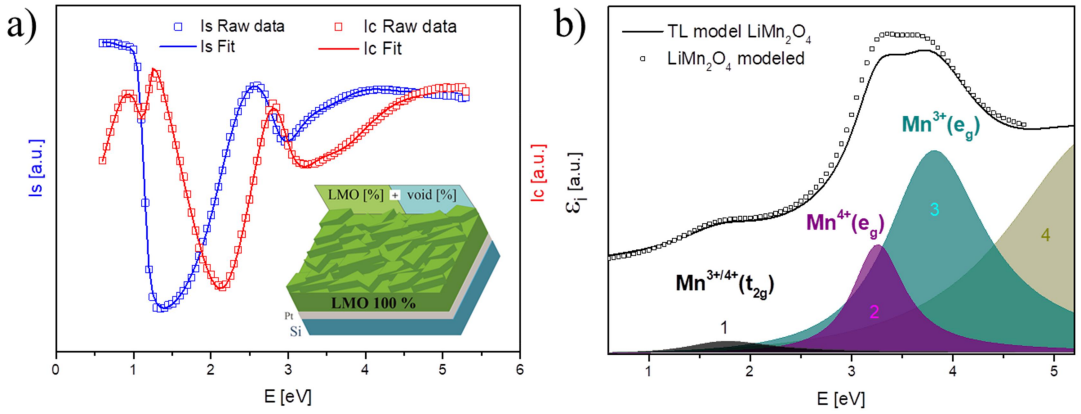

Fig. 2.5.4: Signal of the relative intensities Is and Ic in (a) with the model for the Bruggeman EMA as insert used to perform the fitting of SE data on $LiMn_2O_4$ and (b) the imaginary part of the complex dielectric function to model the optical properties of $LiMn_2O_4$ and its related interband transitions by the sum of four Tauc-Lorentz oscillators.

A comparable model composed of four Tauc-Lorentz oscillators has been applied for LTO thin films in order to conduct their optical properties. For the reflection of the layer roughness and porosity in LTO, the thin film layer has been divided into three sublayers instead of two, with a density decrease of the bulk material from the bottom of 100 % to the top of 50 %. For the fitting of the optical absorption of LATP, only three Tauc-Lorentz oscillators and two sublayers have been included in the model, situated at higher absorption energies due the broader band gap of LTP around 2.4 eV and hence exhibiting a stronger electrically insulating character.[95] Last, models for LMNO thin films were adapted to a mixed multi-oscillator model consisting of 2 Gaussian oscillators and one Tauc-Lorentz oscillator, allowing for the evolution of band transitions below the band gap. The results are presented in **Section 4** for LMO and LTO thin films. In **Section 5** the change of optical absorption is studied for LMO and LMNO while monitoring their electrochemical properties in-situ. The resulting differences and challenges in suitable optical models are explained for operando measurements in **Section 2.6.2**.

2.6 Operando optical characterization techniques

As the previous sections demonstrated, highly surface and interface sensitive techniques are necessary to monitor electrochemical reactions taking place on the interface and bulk of thin films upon operation. Spectroscopic ellipsometry and Raman spectroscopy have proven their sensitivity to structural and microstructural phenomena at the nanoscale, enabling the non-destructive visualization of the

effects in mass and charge transport across thin films in real time. Sample preparation in general is facile for the analysis in Raman or SE and is generally conducted under ambient conditions.

In this thesis, the Raman spectroscopy and SE coupled acquisition stage at the facilities of IREC, as depicted in **Fig. 2.6.1**, is used for operando spectroscopic measurements upon electrochemical performance of LMO and LMNO cathodes.

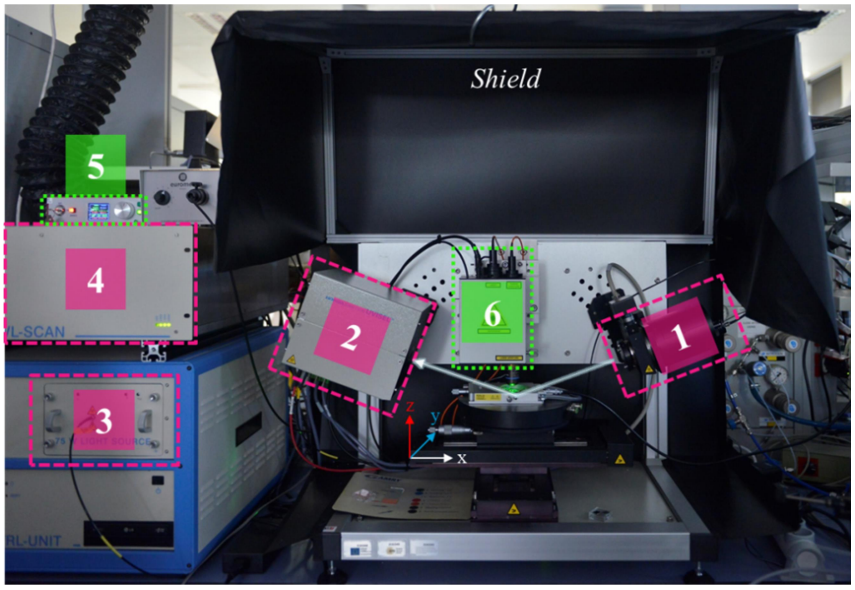

Fig. 2.6.1: Spectroscopic Ellipsometry (red) and Raman (green) setup at IREC facilities. 1) Polarizer, 2) Modulator and Analyzer, 3) Xenon UV 75 W light source, 4) MWL unit, 5) Laser and 6) Raman Laser super-head. Behind the black Raman light shield the spectrometer and CC-detector are placed.

It is complemented by an (air-tight) in-situ chamber, printed at IREC facilities with a Prusa i3® style 3D printer, using photopolymer resin based on methacrylate, shown in **Fig. 2.6.2**. An important aspect of the chamber, besides its capability to block the influence of surrounding air, is the chemical stability of the chamber material towards acid, alkaline and solvent based electrolytes. Further, the windows for enabling light transmittance through the chamber have to be chosen with the same narrative, under additional consideration of UV transparence (for SE) and no detectable activity of Raman vibrational modes in the desired range of observation. The electrochemical setup is chosen based on the electrochemical properties and stability window of LMO as described in **Section 2.5.2.1**. For the electrochemical measurements, the standard three-electrode configuration is kept from conventional measurements in **Section 4**, deciding upon the application of either aqueous or non-aqueous electrolyte systems depending on the practicability and electrochemical

stability requirements. Further all thin film samples are connected through a backside contact of Pt thin film underneath and extended for connection outside the chamber by Al tape and Pt-wires. In order to suppress undesired electrochemical side reactions, the exposure of current collectors towards the electrolyte is prevented under additional sample encapsulation with a chemically highly resistant photocurable resin or multi-component epoxy.

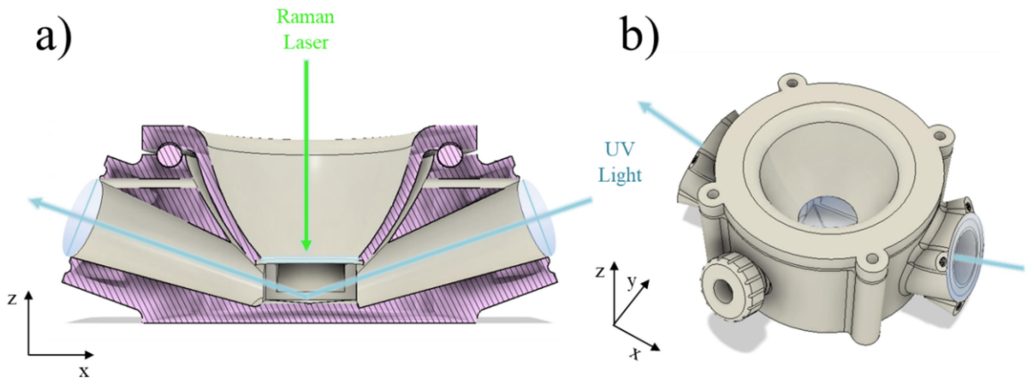

Fig. 2.6.2: In-situ chamber for Raman and Spectroscopic ellipsometry acquisition of air-sensitive measurements in (a) 2D cross-sectional view in line with the SE beam and (b) 3D top-view with the UV beam passing through. Windows consist of UV-transparent CaF and are mounted in 90º angle to the incident and reflected beams. In addition the chamber exhibits an entrance for the reference and/or counter electrode.

2.6.1 Operando Raman spectroscopic acquisition

Raman in-situ measurements are able to reveal the influence of electrode polarization on the local molecule bonds and near order material structure in the bulk, as has been already demonstrated for a variety of electrode materials for the application in Li-ion batteries.[96] Appearing phenomena can be attributed to the change in EDOS at the electrode-electrolyte interface and the charge occupancy inside the layer, hence changing the bond lengths or distorting the lattice. The acquisition speed can be reduced to a few milliseconds in order to follow fast electrochemical phenomena in time.

In this thesis, the change in Raman active vibrational modes between the transition from fully lithiated spinel $LiMn_2O_4$ to delithiated λ-MnO_2 is observed. The acquisition speed is limited to 10 s between each spectrum to secure a reasonable signal-to-noise ratio. Aqueous, light acid-based 1 M Li_2SO_4 electrolyte is applied, as its only observable vibrational mode at the Raman shift of 980 cm^{-1} is not

inhibiting the signal of LMO. Data is collected with EC-Lab® and Labspec 6® simultaneously and further evaluated in **Section 5**.

2.6.2 Operando Spectroscopic ellipsometry acquisition

Spectroscopic ellipsometry can be applied as facile in-situ and in-line monitoring technique for the in-time observation of layer growth and etching mechanisms, as commonly used in CVD and PVD growth techniques, but has only recently been studied for the observation of operando electrochemical reactions.[96,97] Due to its high sensitivity in thin film analysis it can detect changes in optical properties of the bulk and interfaces within nm, e.g. surface layers formed upon electrode operation such as the solid electrolyte interface (SEI) between the electrode and electrolyte. Further the connection of optical properties to the materials electronic band structure can lead in combination with voltammetry and potentiometric techniques to the analysis of the EDOS at solid-solid and solid-liquid interfaces.

In this thesis, an innovative triggering of the monochromator signal has been implemented in order to study operando electrochemical performances of LMO cathode thin films. SE measurements are subjected to certain time limitations imposed by the monochromator. Therefore the ellipsometric signal (i.e. I_s and I_c) is detected at a single photon energy during the desired electrochemical measurements, with 19 different energies being selected between 1.47 to 4.13 eV (sparing the absorbing region of the surrounding Li_2SO_4 aqueous electrolyte) and subsequently studied under repetition of the electrochemical measurements. Sampling rates as high as 10 Hz (1 sample every 100 ms) with the potential reduction of separate frequency intervals above 100 Hz. Limiting conditions are depending on the sample and ambient conditions, such as the signal-to-noise ratio evolving from the materials absorbance or surface roughness, as well as the absorption of the electrolyte or the optical windows of the in-situ optical chamber. Therefore the chamber has been equipped with two optical windows perpendicular to the light beam, made of CaF_2 from Thorlabs, providing a broad transmission window from 18 nm to 8 µm. Further the multi-wavelength (MWL) spectroscopic ellipsometer UVISEL Plus from Horiba is used to study in-time electrochemical reactions taking place upon electrode polarization of LMO and LMNO in the optical range of 250 – 800 nm for every 5.5 nm (1.5 – 4.9 eV). As previously

described in **Section 2.5.3.1**, MWL acquisition enables the detection of multiple wavelengths (photon energies) simultaneously at the same time, with an acquisition speed of 100 ms for each spectrum every 100 ms, enabling an accurate monitoring of fast electrochemical processes. Independent from the acquisition method chosen, the optical models for the analysis in DeltaPsi2® are adapted to the optical constants of the surrounding electrolyte as ambient and further the layer roughness is modeled by substituting the void with the electrolytes optical models. Therefore the optical properties of the surrounding electrolyte have been measured with the liquid enclosed between two planar surfaces, of which one is a prisma, fulfilling the geometrical requirements for SE. The ambient media in the model then is changed from air (n = 1, k= 0) to the optical properties of the surrounding electrolyte, e.g. aqueous Li_2SO_4 (n = 1.34, k = 0)[98,99] or $LiPF_6$ (n = 1.401, k = 0).[100] Changes in the Mn oxidation state can be followed by the shift of absorption in **Fig. 2.5.4 (b)**. The amount of Mn^{3+} decreases upon delithiation and the absorption at the photon energy of Mn^{4+} degenerate E_g energy band is increasing with progressive Li-extraction as the d-orbital occupation changes. Hence the optical properties of the entire layer can be modeled as time-resolved compositional changes in oxidation states between LMO and λ-MnO_2, following the state of charge as percentage in a mixed layer. For the investigation of the spinel $LiMn_2O_4$ at 3 V vs. Li/Li^+, as well as $LiMn_{1.5}Ni_{0.5}O_4$ at high voltages and $Li_4Ti_5O_{12}$ below 1 V vs. Li/Li^+, the optical chamber was prepared inside an argon-filled glove box with oxygen levels around 0.1 ppm and H_2O of 0.0 ppm. After preparation (sample introduction, lithium reference and counter electrode placement, 1 M $LiPF_6$ EC/DMC (1:1) electrolyte fill), the chamber was sealed airtight and transferred to ambient, where it is placed upon the SE stage shown in **Fig. 2.6.1** and connected externally to a Biologic SP-50 potentiostat/galvanostat. Operando SE in combination with electrochemical voltamperometric methods is studied and evaluated in **Section 5** for LMO and LMNO cathode thin films.

2.7 Finite element method (FEM)

The finite element method (FEM) is a mathematical approximation of complex multidimensional systems by dividing the system into smaller parts (finite elements) and solving their partial differential equations (PDE). This is realized under application of a mesh, defining the FE and boundary conditions.[101] The

equation for convection-diffusion limited mass transport phenomena in **Eq. 2.7.1** can be assigned as PDE, including the concentration c of a species, the source element g (here the fixed concentration for a certain boundary) and the diffusion flux J.[102]

$$\frac{\delta c(x,y,z,t)}{\delta t} + \nabla \cdot J = g(c,x,y,z,t) \qquad \text{(Eq. 2.7.1a)}$$

$$J = -D(x,y,z) \cdot \nabla c(x,y,z,t) \qquad \text{(Eq. 2.7.1b)}$$

With D as the diffusion coefficient and ∇ as the Nabla operator for describing a n-dimensional gradient. Under translation into FEM model, it is assumed that any variable can be solved on a basic function Ψ_i for a small indiscriminate domain by their linear combination, as demonstrated in **Eq. 2.7.2** for the concentration c with each single domain j devoted to c_i.[81,101]

$$c \approx \sum_{i=1}^{j} c_i \Psi_i \qquad \text{(Eq. 2.7.2)}$$

The resulting equations are translated into a matrix environment and subsequently solved under application of numerical methods. Time-dependent problems are independently from FEM solved, by using the discretization method.[101]

In this thesis, the lithiation mechanism of LMO thin films was investigated by FEM analysis in respect to the effect of the layers nano-porosity on the intrinsic lithium diffusivity. Therefore COMSOL Multiphysics software was implemented using the *Transport of diluted species* module. 2D axially symmetric grains (see **Fig. 2.7.1**) of various diameters (60 – 100 nm) and a fixed thickness of the film (determined by spectroscopic ellipsometry and TEM analysis) were introduced as the geometrical boundaries of the model. A lateral rectangle controlled by the parameters p an f (p = 2.5 nm and f = 0.8), which are defined in **Fig. 2.7.1 (a)** and **(b)**, served for describing the thin film nano-porosity. A Li concentration of c_{Li} =1 was assumed for the upper and lateral surface domains of the grain as 1D approximation to solve **Eq. 2.7.2**, whereas the bottom surface is assumed as an adiabatic element (diffusion flux equal to zero), as demonstrated in **Fig. 2.7.1 (b)**. Computing the solution in the time dependent mode for a single potential step (initial condition of c_{Li} = 0) resulted in the averaged Li concentration (**Fig. 2.7.1 (d)**) for each domain in time. The top part of the grain rapidly reaches the steady sate concentration of c_{Li} =1, as a

result from the nano-porosity, while the bottom part behaves as a classical 2D diffusion limited front.

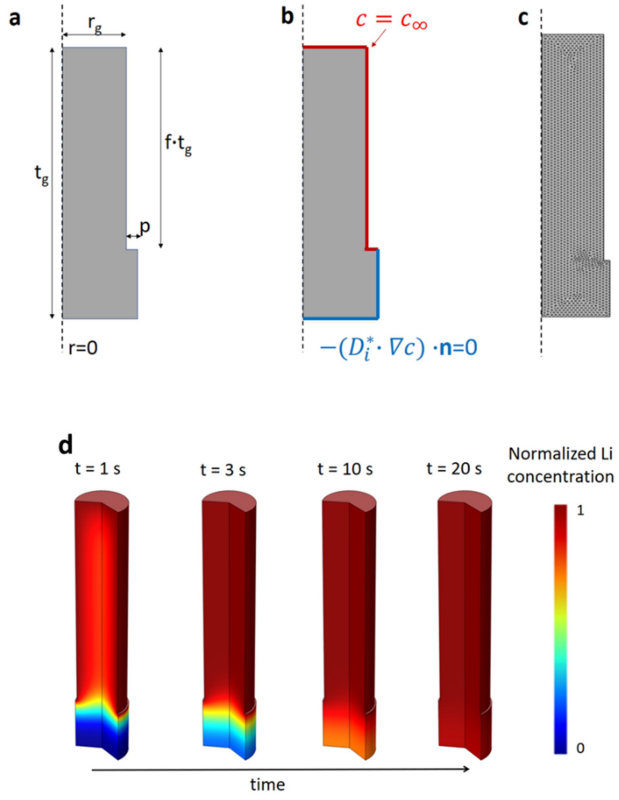

Fig. 2.7.1: Description of the geometric parameters being introduced in the FEM model in (a) and (b). The applied meshing is shown in (c). The resulting time-dependent evolution of the concentration of Li inside the columns upon lithium intercalation is shown in (d).

As shown in **Fig. 2.7.1 (d)**, the simplified approximation to a complex thin film morphology (a variety of grain diameters, shapes, orientations and disorders, etc.) by FEM can be used to obtain the averaged diffusion profiles depending on the Li^+ diffusivity in the layer. Hence, different geometries and diffusivity values have been introduced in the model, compiled and compared with experimental values obtained in **Section 5.3.1.** until a reasonable overlap with experimental data occurred. Results on the FEM modelling for LMO multi-layer thin films during a single potential step are presented in **Section 5.3.1.1** and compared to electrochemical data and operando spectroscopic ellipsometry analysis.

References

(1) Aono, H. Ionic Conductivity of Solid Electrolytes Based on Lithium Titanium Phosphate. *J. Electrochem. Soc.* **1990**, *137* (4), 1023. https://doi.org/10.1149/1.2086597.

(2) Arbi, K.; Bucheli, W.; Jiménez, R.; Sanz, J. High Lithium Ion Conducting Solid Electrolytes Based on NASICON Li1+x Alx M2-x (P O4)3 Materials (M= Ti, Ge and 0≤ X≤ 0.5). *J. Eur. Ceram. Soc.* **2015**, *35* (5), 1477–1484.

(3) Hupfer, T.; Bucharsky, E. C.; Schell, K. G.; Senyshyn, A.; Monchak, M.; Hoffmann, M. J.; Ehrenberg, H. Evolution of Microstructure and Its Relation to Ionic Conductivity in Li1+x Alx Ti2-x (P O4)3. *Solid State Ionics* **2016**, *288*, 235–239. https://doi.org/10.1016/j.ssi.2016.01.036.

(4) Chen, H.; Tao, H.; Zhao, X.; Wu, Q. Fabrication and Ionic Conductivity of Amorphous Li-Al-Ti-P-O Thin Film. *J. Non. Cryst. Solids* **2011**, *357* (16–17), 3267–3271. https://doi.org/10.1016/j.jnoncrysol.2011.05.023.

(5) Tan, G.; Wu, F.; Li, L.; Liu, Y.; Chen, R. Magnetron Sputtering Preparation of Nitrogen-Incorporated Lithium--Aluminum--Titanium Phosphate Based Thin Film Electrolytes for All-Solid-State Lithium Ion Batteries. *J. Phys. Chem. C* **2012**, *116* (5), 3817–3826.

(6) Hofmann, P.; Walther, F.; Rohnke, M.; Sann, J.; Zeier, W. G.; Janek, J. LATP and LiCoPO4 Thin Film Preparation – Illustrating Interfacial Issues on the Way to All-Phosphate SSBs. *Solid State Ionics* **2019**, *342* (August). https://doi.org/10.1016/j.ssi.2019.115054.

(7) Pascal Granger, P.; Parvulescu, V. I.; Kaliaguine, S.; Wilfrid Prellier. *Perovskites and Related Mixed Oxides: Concepts and Applications*; John Wiley & Sons: Weinheim, 2015.

(8) Arbi, K.; Lazarraga, M. G.; Ben Hassen Chehimi, D.; Ayadi-Trabelsi, M.; Rojo, J. M.; Sanz, J. Lithium Mobility in Li1.2 Ti1.8 R0.2 (P O4)3 Compounds (R = Al, Ga, Sc, In) as Followed by NMR and Impedance Spectroscopy. *Chem. Mater.* **2004**, *16* (2), 255–262. https://doi.org/10.1021/cm030422i.

(9) Fu, J. Fast Li+ Ion Conduction in Li2O-Al2O3-TiO2-SiO2-P2O2 Glass-Ceramics. *J. Am. Ceram. Soc.* **2005**, *80* (7), 1901–1903. https://doi.org/10.1111/j.1151-2916.1997.tb03070.x.

(10) Morimoto, H.; Awano, H.; Terashima, J.; Shindo, Y.; Nakanishi, S.; Ito, N.; Ishikawa, K.; Tobishima, S. I. Preparation of Lithium Ion Conducting Solid Electrolyte of

NASICON-Type Li1+xAlxTi2-x(PO4)3 (x = 0.3) Obtained by Using the Mechanochemical Method and Its Application as Surface Modification Materials of LiCoO2 Cathode for Lithium Cell. *J. Power Sources* **2013**, *240*, 636–643. https://doi.org/10.1016/j.jpowsour.2013.05.039.

(11) Bai, H.; Hu, J.; Li, X.; Duan, Y.; Shao, F.; Kozawa, T.; Naito, M.; Zhang, J. Influence of LiBO 2 Addition on the Microstructure and Lithium-Ion Conductivity of Li1+x Alx Ti2-x (P O4)3 (X= 0.3) Ceramic Electrolyte. *Ceram. Int.* **2018**.

(12) Hallopeau, L.; Bregiroux, D.; Rousse, G.; Portehault, D.; Stevens, P.; Toussaint, G.; Laberty-Robert, C. Microwave-Assisted Reactive Sintering and Lithium Ion Conductivity of Li1.3 Al0.3 Ti1.7 (P O4)3 Solid Electrolyte. *J. Power Sources* **2018**, *378*, 48–52.

(13) Waetzig, K.; Rost, A.; Langklotz, U.; Matthey, B.; Schilm, J. An Explanation of the Microcrack Formation in Li1.3Al0.3Ti1.7(PO4)3 Ceramics. *J. Eur. Ceram. Soc.* **2016**, *36* (8), 1995–2001. https://doi.org/10.1016/j.jeurceramsoc.2016.02.042.

(14) Key, B.; Schroeder, D. J.; Ingram, B. J.; Vaughey, J. T. Solution-Based Synthesis and Characterization of Lithium-Ion Conducting Phosphate Ceramics for Lithium Metal Batteries. *Chem. Mater.* **2012**, *24* (2), 287–293. https://doi.org/10.1021/cm202773d.

(15) Wold, A.; Dwight, K. *Solid State Chemistry : Synthesis, Structure, and Properties of Selected Oxides and Sulfides*; Springer Netherlands, 1993.

(16) Julien, C. Electrochemical Performances of Layered Li M1-y M'y O2 (M=Ni, Co; M'=Mg, Al, B) Oxides in Lithium Batteries. *Solid State Ionics* **2000**, *135* (1–4), 121–130. https://doi.org/10.1016/S0167-2738(00)00290-3.

(17) Schell, K. G.; Bucharsky, E. C.; Lemke, F.; Hoffmann, M. J. Effect of Calcination Conditions on Lithium Conductivity in Li1.3 Ti1.7 Al0.3 (P O4)3 Prepared by Sol-Gel Route. *Ionics (Kiel).* **2017**, *23* (4), 821–827.

(18) Eason, R. *Pulsed Laser Deposition of Thin Films: Applications-Led Growth of Functional Materials*; John Wiley & Sons, 2007.

(19) Smith, H. M.; Turner, A. F. Vacuum Deposited Thin Films Using a Ruby Laser. *Appl. Opt.* **1965**, *4* (1), 147. https://doi.org/10.1364/ao.4.000147.

(20) Hass, G.; Ramsey, J. B. Vacuum Deposition of Dielectric and Semiconductor Films by a C O2 Laser. *Appl. Opt.* **1969**, *8* (6), 1115. https://doi.org/10.1364/ao.8.001115.

(21) Venkatesan, T.; Wu, X. D.; Inam, A.; Wachtman, J. B. Observation of Two Distinct

Components during Pulsed Laser Deposition of High Tc Superconducting Films. *Appl. Phys. Lett.* **1988**, *52* (14), 1193–1195. https://doi.org/10.1063/1.99673.

(22) Ford, P. J.; Saunders, G. A. *The Rise of the Superconductors*; CRC Press, 2004. https://doi.org/10.1201/9780203646311.

(23) Greer, J. A.; Tabat, M. D. Large-Area Pulsed Laser Deposition: Techniques and Applications. *J. Vac. Sci. Technol. A Vacuum, Surfaces, Film.* **1995**, *13* (3), 1175–1181. https://doi.org/10.1116/1.579857.

(24) Xia, H.; Wang, H. L.; Xiao, W.; Lai, M. O.; Lu, L. Thin Film Li Electrolytes for All-Solid-State Micro-Batteries. *Int. J. Surf. Sci. Eng.* **2009**, *3* (1–2), 23–43.

(25) Julien, C. M.; Mauger, A. Pulsed Laser Deposited Films for Microbatteries. *Coatings* **2019**, *9* (6), 386. https://doi.org/10.3390/coatings9060386.

(26) Stafe, M.; Marcu, A.; Puscas, N. N. *Pulsed Laser Ablation of Solids: Basics, Theory and Applications*, Springer S.; Springer Science & Business Media, 2014. https://doi.org/10.1007/978-3-642-40978-3.

(27) Amoruso, S. *Plume Characterization in Pulsed Laser Deposition of Metal Oxide Thin Films*; Elsevier Inc., 2018. https://doi.org/10.1016/b978-0-12-811166-6.00006-6.

(28) Delmdahl, R.; Pätzel, R. Pulsed Laser Deposition-UV Laser Sources and Applications. *Appl. Phys. A Mater. Sci. Process.* **2008**, *93* (3), 611–615. https://doi.org/10.1007/s00339-008-4716-7.

(29) Schou, J. Applied Surface Science Physical Aspects of the Pulsed Laser Deposition Technique : The Stoichiometric Transfer of Material from Target to Film. **2009**, *255*, 5191–5198. https://doi.org/10.1016/j.apsusc.2008.10.101.

(30) Pauleau, Y.; European Materials Research Society. *Materials Surface Processing by Directed Energy Techniques*; Elsevier, 2006.

(31) Sambri, A.; Amoruso, S.; Wang, X.; Granozio, F. M.; Bruzzese, R. Plume Propagation Dynamics of Complex Oxides in Oxygen. *J. Appl. Phys.* **2008**, *104* (5). https://doi.org/10.1063/1.2975363.

(32) Predtechensky, M. R.; Mayorov, A. P. Expansion of Laser Plasma in Oxygen at Laser Deposition of HTSC Films:Theoretical Model. *Appl. Supercond.* **1993**, *1* (10–12), 2011–2017. https://doi.org/10.1016/0964-1807(93)90349-7.

(33) Anisimov, S. I.; Bäuerle, D.; Luk'yanchuk, B. S. Gas Dynamics and Film Profiles in Pulsed-Laser Deposition of Materials. *Phys. Rev. B* **1993**, *48* (16), 76–81.

https://doi.org/10.1103/PhysRevB.48.12076.

(34) Canulescu, S.; Papadopoulou, E. L.; Anglos, D.; Lippert, T.; Schneider, C. W.; Wokaun, A. Mechanisms of the Laser Plume Expansion during the Ablation of LiMn 2O4. *J. Appl. Phys.* **2009**, *105* (6). https://doi.org/10.1063/1.3095687.

(35) Packwood, D. M.; Shiraki, S.; Hitosugi, T. Effects of Atomic Collisions on the Stoichiometry of Thin Films Prepared by Pulsed Laser Deposition. *Phys. Rev. Lett.* **2013**, *111* (3), 1–5. https://doi.org/10.1103/PhysRevLett.111.036101.

(36) Rashidian Vaziri, M. R.; Hajiesmaeilbaigi, F.; Maleki, M. H. Monte Carlo Simulation of the Subsurface Growth Mode during Pulsed Laser Deposition. *J. Appl. Phys.* **2011**, *110* (4). https://doi.org/10.1063/1.3624768.

(37) Scharf, T.; Krepbs, H. U. Influence of Inert Gas Pressure on Deposition Rate during Pulsed Laser Deposition. *Appl. Phys. A Mater. Sci. Process.* **2002**, *554*, 551–554. https://doi.org/10.1007/s00339-002-1442-4.

(38) Ojeda-G-P, A.; Schneider, C. W.; Döbeli, M.; Lippert, T.; Wokaun, A. The Importance of Pressure and Mass Ratios When Depositing Multi-Element Oxide Thin Films by Pulsed Laser Deposition. *Appl. Surf. Sci.* **2016**, *389*, 126–134. https://doi.org/10.1016/j.apsusc.2016.07.003.

(39) Wicklein, S.; Sambri, A.; Amoruso, S.; Wang, X.; Bruzzese, R.; Koehl, A.; Dittmann, R. Pulsed Laser Ablation of Complex Oxides: The Role of Congruent Ablation and Preferential Scattering for the Film Stoichiometry. *Appl. Phys. Lett.* **2012**, *101* (13). https://doi.org/10.1063/1.4754112.

(40) Sauvage, F.; Baudrin, E.; Morcrette, M.; Tarascon, J.-M. Pulsed Laser Deposition and Electrochemical Properties of Li Fe P O4 Thin Films. *Electrochem. solid-state Lett.* **2004**, *7* (1), A15--A18.

(41) Sun, J.; Tang, K.; Yu, X.; Li, H.; Huang, X. Needle-like Li Fe P O4 Thin Films Prepared by an off-Axis Pulsed Laser Deposition Technique. *Thin Solid Films* **2009**, *517* (8), 2618–2622.

(42) Simmen, F.; Lippert, T.; Novák, P.; Neuenschwander, B.; Döbeli, M.; Mallepell, M.; Wokaun, A. The Influence of Lithium Excess in the Target on the Properties and Compositions of Li1+x Mn2 O4-δ Thin Films Prepared by PLD. *Appl. Phys. A* **2008**, *93* (3), 711–716. https://doi.org/10.1007/s00339-008-4701-1.

(43) Fehse, M.; Trócoli, R.; Ventosa, E.; Hernández, E.; Sepúlveda, A.; Morata, A.; Tarancón, A. Ultrafast Dischargeable LiMn2O4 Thin-Film Electrodes with

Pseudocapacitive Properties for Microbatteries. *ACS Appl. Mater. Interfaces* **2017**, *9* (6), 5295–5301.

(44) Trócoli, R.; Morata, A.; Fehse, M.; Stchakovsky, M.; Sepúlveda, A.; Tarancón, A. High Specific Power Dual-Metal-Ion Rechargeable Microbatteries Based on Li Mn2 O4 and Zinc for Miniaturized Applications. *ACS Appl. Mater. Interfaces* **2017**, *9* (38), 32713–32719. https://doi.org/10.1021/acsami.7b08883.

(45) Fehse, M.; Trócoli, R.; Hernández, E.; Ventosa, E.; Sepúlveda, A.; Morata, A.; Tarancón, A. An Innovative Multi-Layer Pulsed Laser Deposition Approach for LiMn2O4 Thin Film Cathodes. *Thin Solid Films* **2018**, *648*, 108–112. https://doi.org/10.1016/j.tsf.2018.01.015.

(46) Franssila, S. *Introduction to Microfabrication*; Wiley-Blackwell, 2010.

(47) Herman, M. A.; Richter, W.; Sitter, H. *Epitaxy : Physical Principles and Technical Implementation*; Springer Berlin Heidelberg, 2004.

(48) Groza, J. R.; Shacklefold, J. F. *Materials Processing Handbook*; CRC Press, 2007.

(49) Kajikawa, Y. Analysing Surface Roughness Evolution in Thin Films. *Thin Film Growth* **2011**, 60–82. https://doi.org/10.1533/9780857093295.1.60.

(50) Martin, L. W.; Chu, Y. H.; Ramesh, R. Advances in the Growth and Characterization of Magnetic, Ferroelectric, and Multiferroic Oxide Thin Films. *Mater. Sci. Eng. R Reports* **2010**, *68* (4–6), 89–133. https://doi.org/10.1016/j.mser.2010.03.001.

(51) Liu, C.; Neale, Z. G.; Cao, G. Understanding Electrochemical Potentials of Cathode Materials in Rechargeable Batteries. *Mater. Today* **2016**, *19* (2), 109–123. https://doi.org/10.1016/j.mattod.2015.10.009.

(52) Que, L.; Yu, F.; Sui, X.; Zhao, L.; Zhou, J.; Gu, D.; Wang, Z. Nano Energy Thermal-Induced Interlayer Defect Engineering toward Super High- Performance Sodium Ion Capacitors. **2019**, *59* (November 2018), 17–25. https://doi.org/10.1016/j.nanoen.2019.02.030.

(53) Yildiz, B. " Stretching " the Energy Landscape of Oxides — Effects on Electrocatalysis and Diffusion. **2014**, *39* (February), 147–156. https://doi.org/10.1557/mrs.2014.8.

(54) Ohnishi, T.; Takada, K. Epitaxial Thin-Film Growth of SrRuO3, Sr3Ru 2O7, and Sr2RuO4 from a SrRuO 3 Target by Pulsed Laser Deposition. *Appl. Phys. Express* **2011**, *4* (2), 2–5. https://doi.org/10.1143/APEX.4.025501.

(55) Arbi, K.; Hoelzel, M.; Kuhn, A.; García-Alvarado, F.; Sanz, J. Local Structure and

Lithium Mobility in Intercalated Li3 Alx Ti2-x (P O4)3 NASICON Type Materials: A Combined Neutron Diffraction and NMR Study. *Phys. Chem. Chem. Phys.* **2014**, *16* (34), 18397–18405. https://doi.org/10.1039/c4cp02938k.

(56) Hu, X.; Shao, C.; Wang, J.; Wang, H. Characterization and High-Temperature Degradation Mechanism of Continuous Silicon Nitride Fibers. *J. Mater. Sci.* **2017**, *52* (12), 7555–7566. https://doi.org/10.1007/s10853-017-0988-7.

(57) Seifert, M.; Lattner, E.; Menzel, S. B.; Oswald, S.; Gemming, T. Very Thin Co-Sputtered Ti-Al and Multilayered Ti / Al Films on Thermally Oxidized Si Substrates. *Materials (Basel).* **2020**, *13* (2039), 1–11. https://doi.org/10.3390/ma13092039.

(58) Nalwa, H. S. *Handbook of Thin Film Materials*, 5th ed.; Elsevier, 2001.

(59) Put, B.; Vereecken, P. M.; Labyedh, N.; Sepulveda, A.; Huyghebaert, C.; Radu, I. P.; Stesmans, A. High Cycling Stability and Extreme Rate Performance in Nanoscaled LiMn2O4 Thin Films. *ACS Appl. Mater. Interfaces* **2015**, *7* (40), 22413–22420. https://doi.org/10.1021/acsami.5b06386.

(60) Greiner, W. *Quantum Mechanics: An Introduction*, 4th editio.; Springer Science & Business Media, 2011.

(61) Williams, D. B.; Carter, C. B. Transmission Electron Microscopy: A Textbook for Materials Science. Springer.

(62) Erdman, N.; Bell, D. C.; Reichelt, R. *Scanning Electron Microscopy*; 2019.

(63) Goldstein, J.; Newbury, D. E.; Michael, J. R.; Ritchie, N. W. M.; Scott, J. H. J.; Joy, D. C. *Scanning Electron Microscopy and X-Ray Microanalysis*.

(64) Kuisma-Kursula, P. Accuracy, Precision and Detection Limits of SEM-WDS, SEM-EDS and PIXE in the Multi-Elemental Analysis of Medieval Glass. *X-Ray Spectrom.* **2000**, *29* (1), 111–118. https://doi.org/10.1002/(SICI)1097-4539(200001/02)29:1<111::AID-XRS408>3.0.CO;2-W.

(65) KRUMEICH, F. Properties of Electrons, their Interactions with Matter and Applications in Electron Microscopy.

(66) Edington, J. W. *Electron Diffraction in the Electron Microscope*, 2nd ed.; The Macmillan Press LTD: London, 1975.

(67) Amelinckx, S. *Electron Microscopy : Principles and Fundamentals*; VCH, 1997.

(68) Walls, M.; Tence, M.; Arenal, R.; Pen, F. De. Ultramicroscopy Extending the Analysis

of EELS Spectrum-Imaging Data , from Elemental to Bond Mapping in Complex Nanostructures. **2008**, *109*, 32–38. https://doi.org/10.1016/j.ultramic.2008.07.005.

(69) Williamson, G. K.; Hall, W. H. X-Ray Line Broadening from Filed Aluminium and Wolfram. *Acta Metall.* **1953**, *1*, 22–31.

(70) Ferraro, J. R.; Nakamoto, K.; Brown, C. W. *Introductory Raman Spectroscopy*, 2nd ed.; Academic Press: Amsterdam and Boston, 2003.

(71) Cantarero, A. Raman Scattering Applied to Materials Science. *Procedia Mater. Sci.* **2015**, *9*, 113–122. https://doi.org/10.1016/j.mspro.2015.04.014.

(72) Fateley, W. G.; McDevitt, N. T.; Bentley, F. F. Infrared and Raman Selection Rules for Lattice Vibrations: The Correlation Method. *Appl. Spectrosc.* **2016**, *25* (2), 155–173. https://doi.org/10.1366/000370271779948600.

(73) Bovey, F. A.; Mirau, P. A.; Gutowsky, H. S. *Nuclear Magnetic Resonance Spectroscopy*; Elsevier, 1988.

(74) Antzutkin, O. N. *New Techniques in Solid-State NMR*; Springer Science & Business Media, 2005.

(75) Field, L.D.; Sternhell, S.; Kalman, J. R. *Organic Structures from Spectra*; Wiley, 2013; Vol. 79.

(76) Coats, W. A.; Redfern, J. P. Thermogravimetric Analysis. *Analyst* **1963**, *1* (906), 87–118. https://doi.org/10.1002/9780470697702.ch3.

(77) Kolasinski, K. W. *Surface Science : Foundations of Catalysis and Nanoscience*; Wiley, 2012.

(78) Giessibl, F. J. Advances in Atomic Force Microscopy. *Rev. Mod. Phys.* **2003**, *75* (3), 949–983. https://doi.org/10.1103/RevModPhys.75.949.

(79) Barsoukov, E.; Macdonald, J. R. *Impedance Spectroscopy-Theory , Experiment , And*, 2nd ed.; John Wiley & Sons: Hoboken, 2005; Vol. 125.

(80) Cottis, R.; Turgoose, S. Analysis of Electrochemical Impedance Spectroscopy Data. In *Electrochemical Impedance and Noise*; NACE International, Ed.; United states of America, 1999; pp 35–49.

(81) Chiabrera, F. M. Interface Engineering in Mixed Ionic Electronic Conductor Thin Films for Solid State Devices, 2019.

(82) Zoski, C. G. *Handbook of Electrochemistry*; 2007. https://doi.org/10.1016/B978-0-444-

51958-0.X5000-9.

(83) Zheng, J.; Tan, G.; Shan, P.; Liu, T.; Hu, J.; Feng, Y.; Yang, L.; Zhang, M.; Chen, Z.; Lin, Y.; Lu, J.; Neuefeind, J. C.; Ren, Y.; Amine, K.; Wang, L. W.; Xu, K.; Pan, F. Understanding Thermodynamic and Kinetic Contributions in Expanding the Stability Window of Aqueous Electrolytes. *Chem* **2018**, *4* (12), 2872–2882. https://doi.org/10.1016/j.chempr.2018.09.004.

(84) Xu, K.; Wang, C. Batteries: Widening Voltage Windows. *Nat. Energy* **2016**, *1* (10), 1–2. https://doi.org/10.1038/nenergy.2016.161.

(85) Tompkins, H. G.; Irene, E. A. *Handbook of Ellipsometry*; William Andrew, 2005.

(86) Losurdo, M.; Bergmair, M.; Bruno, G.; Cattelan, D.; Cobet, C.; de Martino, A.; Fleischer, K.; Dohcevic-Mitrovic, Z.; Esser, N.; Galliet, M.; others. Spectroscopic Ellipsometry and Polarimetry for Materials and Systems Analysis at the Nanometer Scale: State-of-the-Art, Potential, and Perspectives. *J. Nanoparticle Res.* **2009**, *11* (7), 1521–1554.

(87) Jellison, G. E.; Modine, F. A. Parameterization of the Optical Functions of Amorphous Materials in the Interband Region. *Appl. Phys. Lett.* **1996**, *69*, 371–373.

(88) Chen, W.; Shen, W. Z. Perspectives in the Characteristics and Applications of Tauc-Lorentz Dielectric Function Model. *Eur. Phys. J. B - Condens. Matter Complex Syst.* **2005**, *43*, 503–507.

(89) Ferlauto, A. S.; Ferreira, G. M.; Pearce, J. M.; Wronski, C. R.; Collins, R. W. Analytical Model for the Optical Functions of Amorphous Semiconductors from the Near-Infrared to Ultraviolet: Applications in Thin Film Photovoltaics. *J. Appl. Phys.* **2002**, *92* (2424).

(90) Likhachev, D. V; Malkova, N.; Poslavsky, L. Modified Tauc – Lorentz Dispersion Model Leading to a More Accurate Representation of Absorption Features below the Bandgap. *Thin Solid Films* **2015**, *589*, 844–851. https://doi.org/10.1016/j.tsf.2015.07.035.

(91) Hao, M. I. Z.; Ian, J. I. E. L.; Ia, Y. A. J.; In, K. U. I. J.; Iping, L. X. U.; Higao, Z.; Ang, X. I. Y.; Ang, S. H. K. Investigation of the Optical Properties of LiTi 2 O 4 and Li 4 Ti 5 O 12 Spinel Films by Spectroscopic Ellipsometry. *Opt. Mater. Express* **2016**, *6* (10), 3366–3374.

(92) Bruggeman, D. A. G. Berechnung Verschiedener Physikalischer Konstanten von Heterogenen Substanzen. *Ann. Phys.* **1935**, *5* (24), 636–664.

(93) Aspens, D. E.; Theeten, J. B. Investigation of Effective-Medium Models of Microscopic Surface Roughness by Spectroscopic Ellipsometry. *Phys. Rev. B* **1979**, *20* (8), 3292–3302.

(94) Ouyang, C. Y.; Shi, S. Q.; Lei, M. S. Jahn-Teller Distortion and Electronic Structure of LiMn2O4. *J. Alloys Compd.* **2009**, *474* (1–2), 370–374. https://doi.org/10.1016/j.jallcom.2008.06.123.

(95) Persson, K. Materials Data on LiTi2(PO4)3 (SG:167) by Materials Project https://www.materialsproject.org/materials/mp-18640/ (accessed Apr 21, 2020). https://doi.org/10.17188/1193306.

(96) Liu, D.; Shadike, Z.; Lin, R.; Qian, K.; Li, H.; Li, K.; Wang, S.; Yu, Q.; Liu, M.; Ganapathy, S.; others; Qin, X.; Yang, Q.-H.; Wagemaker, M.; Kang, F.; Yang, X.-Q.; Li, B. Review of Recent Development of In Situ/Operando Characterization Techniques for Lithium Battery Research. *Adv. Mater.* **2019**, *31* (28), 1806620. https://doi.org/10.1002/adma.201806620.

(97) Morata, A.; Siller, V.; Chiabrera, F.; Nuñez, M.; Trocoli, R.; Stchakovsky, M.; Tarancon, A. Operando Probing of Li-Insertion into LiMn2O4 Cathodes by Spectroscopic Ellipsometry. *J. Mater. Chem. A* **2020**, 1–7.

(98) Guo, Y.; Li, L.; Cao, L.; Yu, X.; Wang, S.; Deng, T. Solubilities, Densities and Refractive Indices in the Aqueous Quaternary System of Lithium Sulfate, Lithium Metaborate, and Lithium Carbonate at 288.15, 298.15, 308.15 K and 0.1 MPa. *J. Chem. Eng. Data* **2016**. https://doi.org/10.1021/acs.jced.6b00777.

(99) Webster, R. D.; Beaglehole, D. In Situ Electrochemical-Ellipsometry Studeis of Charge-Transfer Processes at the Liquid/Liquid Interface. *Phys. Chem. Chem. Phys.* **2000**, *2*, 5660–5666.

(100) Lei, J.; Li, L.; Kostecki, R.; Muller, R.; McLarnon, F. Characterization of SEI Layers on LiMn2O4 Cathodes with In Situ Spectroscopic Ellipsometry. *J. Electrochem. Soc.* **2005**, *152* (4), A774–A777. https://doi.org/10.1149/1.1867652.

(101) Mats G. Larson; Fredrik Bengzon. *The Finite Element Method: Theory, Implementation, and Applications*; Springer Science & Business Media, 2013.

(102) Crank, J. *The Mathematics of Diffusion*; Oxford University Pess, 1979.

3. LATP thin film solid electrolytes fabricated by PLD

3.1 Introduction

Solid electrolytes for the application in all-solid-state batteries are defined by their good ionic conductivity and negligible electronic conduction, a broad electrochemical stability window, high chemical compatibility at the electrode-electrolyte interface and mechanical resistance against deformation, as well as a desirable stability towards air and moisture for the facilitated handling during device processing and operation.[1] NASICON-like LATP superionic conducting solid electrolytes derive from $LiTi_2(PO_4)_3$ under partial replacement of Ti^{4+} with Al^{3+}. This leads to a notable increase in ionic conductivity up to 10^{-4} S cm^{-1} and electronic conductivities as low as 10^{-10} S cm^{-1} at room temperature, defining $Li_{1+x}Al_xTi_{2-x}(PO_4)_3$ as feasible solid electrolyte in all-solid state batteries, especially in thin film form.[2,3]

In the following sections, solid-state synthesis of LATP is investigated and different calcination and sintering conditions examined are briefly summarized in **Section 3.2.1**. The synthesis of a feasible target for the deposition of LATP thin films in the large-area (LA) Pulsed Laser Deposition (PLD) is accompanied in several steps of analysis, concerning mainly its structure and microstructure, but also the electronic properties presented in **Section 3.2.2**. The fabrication of first LATP thin films is demonstrated in **Section 3.3.1** under variation of the partial oxygen pressure during target ablation, which is crucial for mass transport limiting deposition conditions . After optimization of thin film deposition conditions, the effect of post-deposition heat treatments (annealing) on the structure, microstructure and functional thin film properties is investigated in **Section 3.3.2** and presented as a possibility to engineer the electrochemical performance of LATP thin films.

3.2 LATP bulk synthesis and target optimization

The fabrication of LATP bulk materials has seen a broad variation of different synthesis routines, of which solution-based and solid-state reactions can be considered as the most explored. As emphasized earlier in **Section 2.2.1**, solution-based (also called soft chemistry) routines such as sol-gel reactions offer a better contact between precursors and more gentle synthesis temperatures to preserve the desired lithium content. Solid-state synthesis on the other hand (also referred to as

ceramic method) exhibits poor contact between its precursors, even though the specific surface area *SSA* (as explained in **Section 2.2.2**) can be increased by refining the particle size. Nonetheless, higher sintering temperatures to achieve maximum densities for sufficiently good ionic conductivities are required, but may also cause a certain loss of lithium by volatilization.[4–7]

As for this thesis a target of suitable dimensions is required for the deposition of thin films by LA-PLD (see **Section 2.2.2**), the amount of powders reproducible by the same synthesis routine has to be fairly large. For this reason, solid-state synthesis is the route of choice. In literature, extensive efforts were made on the understanding of calcination and sintering conditions of LATP bulk powders and pellets of different synthesis routines with their resulting effects on the phase purity, crystallinity and ionic conductivities.[6,8–10] Those studies are applied in the following for the synthesis of powders and pellets as first approach for a suitable target in the PLD.

3.2.1 Solid-state synthesis of LATP powders

Conventional precursors in the solid-state synthesis of LATP are based on organic compounds containing the cationic sources in carbonates (Li_2CO_3), oxides (TiO_2, Al_2O_3) and hydroxides ($Al(OH)_3$), as well as the anionic source, typically provided by phosphates ($NH_4H_2PO_4$). As shown in **Fig. 3.2.1 (a)** by TGA measurements for combined LATP reagents (x~ 0.5), the greatest loss in weight up to -25 % is monitored between 35 – 440 ºC, which is defined by the evaporation of water, carbon and nitrogen oxides, as well as ammonia gases. This so-called calcination (pyrolysis) can be an important reaction step before sintering, in order to improve phase purity and reaction kinetics. Usually a regrinding is performed after evaporating undesired organic compounds, with the purpose of reducing reaction pathways between remaining, non-reacted compounds. For LATP typical calcination temperatures range between 400 – 900 ºC, dependent on the precursors and reaction path chosen.[2,8,9]

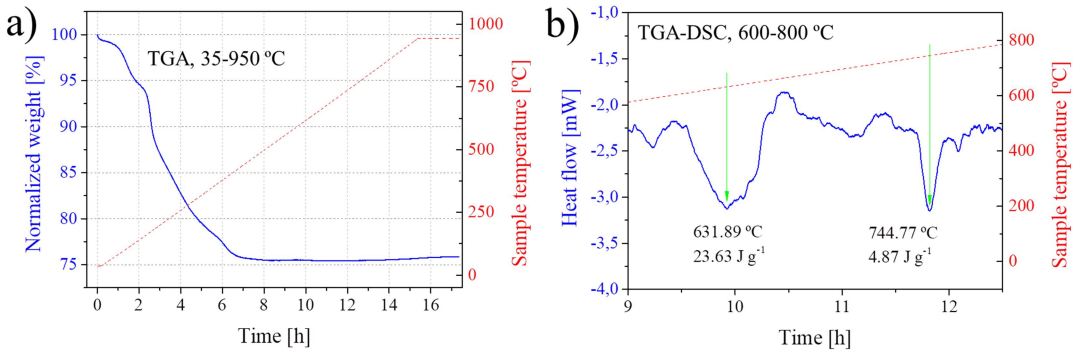

Fig. 3.2.1: LATP precursors are mixed and reacted from 35 – 950 °C in (a) and the weight loss monitored by TGA. In (b) LATP powders pre-reacted at 600 °C are heated between 600 – 800 °C in order to monitor changes in the heat flow by TGA-DSC. Ramping was kept equal for both techniques at 1 °C min^{-1}.

Independent from the synthesis routine selected, according to literature the crystalline NASICON phase of LATP is first formed above 526 °C and no further chemical reactions of noteworthy impact on weight changes have been observed above 700 °C.[9] Only a small decrease in mass has been reported above 500 °C, which can be attributed to the evaporation of volatile LiO_2.[5] In comparison to the weight changes monitored in **Fig. 3.2.1 (a)** above 440 °C, the normalized weight remains stable until~ 830 °C and afterwards slightly increases with increasing temperature. This may be the result of secondary phases forming typically above 800°C, possibly of higher densities than LATP (ρ~2.92 g cm^{-3}).[5,11,12] All secondary phases formed for T > 800 °C are related to the loss of lithium in the NASICON lattice, leading to the necessity of balancing the charge imbalance, which is usually stabilized by the formation of $AlPO_4$, TiO_2 and various pyrophosphates. Phase transitions or crystallization, which do not necessarily come along with a notable change in weight, were monitored using TGA-DSC in **Fig. 3.2.1 (b)** by following the heat flow between 600 – 800 °C of LATP powders (x~0.5) pre-reacted at 600 °C. Herein two clear endothermic peaks are visible. The broader peak with its minimum at ~632 °C and a thermal heat capacity of 23.63 J g^{-1} may be assigned to the melting range of the Li_2CO_3 precursor, which is initiated around 618 °C.[13] The sharp endothermic peak at ~745 °C with a thermal heat capacity of 4.87 J g^{-1} may be caused by the transition or crystallization of a phase, which could not be identified unambiguously by means of TGA techniques. In order to improve the assignment, a series of different LATP compositions under the variation of the Al-dopant content x is studied, using temperature dependent in-situ XRD in **Fig. 3.2.2**.

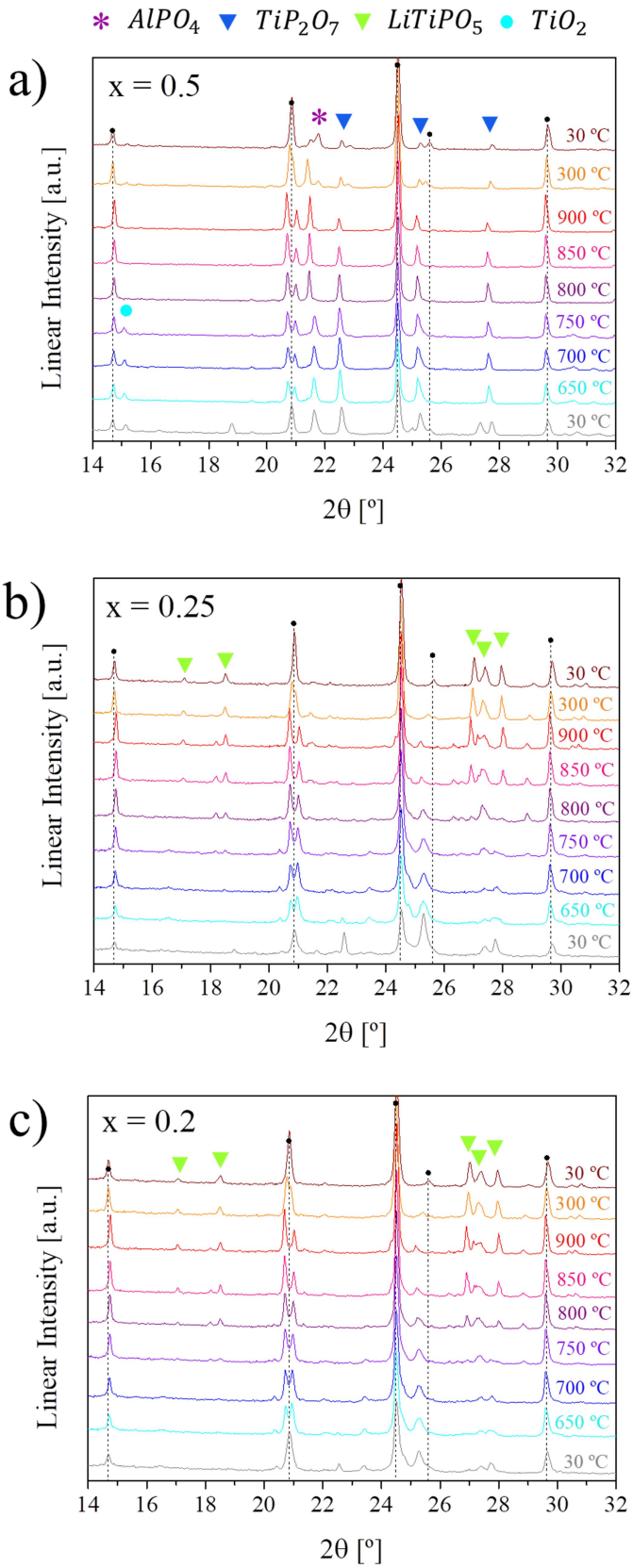

Fig. 3.2.2: In-situ XRD in dependence of the annealing temperatures applied on LATP powders pre-reacted at 650 ºC of different compositions in $Li_{1+x}Al_xTi_{2-x}(PO_4)_3$ with x between 0.5 (a), 0.25 (b) and 0.2 (c). All traces are vertically shifted. The main phase of LATP is referenced by NASICON $LiTi_2(PO_4)_3$ corresponding to JCPDS 00-035-0754

(black circles and vertical dotted lines). Secondary phases correspond to $AlPO_4$ (violet*, JCPDS 00-011-0500), TiP_2O_7 (blue triangles, JCPDS 00-038-1468), $LiTiPO_5$ (green triangles, JCPDS 00-044-0083) and TiO_2 (turquoise circle, JCPDS 00-046-1237).

In **Fig. 3.2.2** the X-ray diffractograms collected at different temperatures is displayed, for compositions of $Li_{1+x}Al_xTi_{2-x}(PO_4)_3$ desired to be at 0.2, 0.25 or 0.5 for x. Al samples show the NASICON structure of LTP with a slight shift to higher angles due to Al-dopant intercalation. A certain peak split can be observed at 20.86º for higher temperatures, as the reflections of (114) and (120) lattice planes usually overlap at room temperature.[14]As in-situ obtained diffractograms (not shown) of pre-reacted powders between 600 ºC and 650 ºC could not give evidence of any structural changes, the calcination temperature of LATP reagents was fixed at 650 ºC, in order to pre-react all involved compounds and to minimize the amount of the subsequent re-grinding and milling steps. Possible secondary phases occurring in the Li_2O-TiO_2-P_2O_5 material system can be derived from ternary phase diagrams, predicting mostly pyrophosphates and titania to occur under Li-evaporation.[15] Therefore the formation of $LiTiPO_5$ does not surprise when analyzing **Fig. 3.2.2 (b,c)**, as a result of annealing above 800 ºC and especially evident for lower Al-dopant concentrations between 0.2 – 0.25. For the molar ratio of x = 0.5 in **Fig. 3.2.2 (a)** the predominant secondary phases are $AlPO_4$ and TiP_2O_7, with an increased presence in the pre-reacted powders and a decrease upon annealing. This may have different reasons than only possible Li-loss as explanation for impurities. As the Al-concentration appears to be close to the maximum, its intercalation inside the NASICON structure may result in a saturation of the lattice, complicating further intercalation of surplus dopant cations, which as a result leads to their segregation as secondary phases.[2] Further the peak appearing below 800 ºC at 15.09º is attributed to titania in the monoclinic crystallographic system (see blue circle in **Fig. 3.2.2 (a)**), although the assignment is not unambiguous, as additional reflections of the same phase could not be identified. Difficulties resulted from the lack of a high-temperature data base in XRD references. As this phase seems to disappear above 750 ºC, it may be related to the endothermic peak in **Fig. 3.2.1 (b)** at ~ 745 ºC, given the tolerances of different equipment used for heating, different but comparable amounts of material reacted and certain variations in the material composition are possible.

3.2.2 Sintering of pellets

As the goal is to fabricate a suitable LATP target applicable in LA-PLD, despite the higher amount of secondary phases predictable for x = 0.5 from in-situ XRD in **Fig. 3.2.2 (a)**, the composition with the maximum Al-dopant concentration acceptable by the LATP lattice was chosen to better compensate possible material losses in the PLD (see **Section 2.3.3** for further details).[2] This is most likely the case for lithium, which is assumed in this work to be counteracted by a higher Al-amount, simultaneously intercalating more lithium inside the LATP lattice per formula unit. Ex-situ X-ray diffractograms of powders calcined at 650 ºC and sintered into 1" pellets at 950 ºC are displayed in **Fig. 3.2.3 (a)** with the corresponding Raman spectra of the pellets in **(b)**.

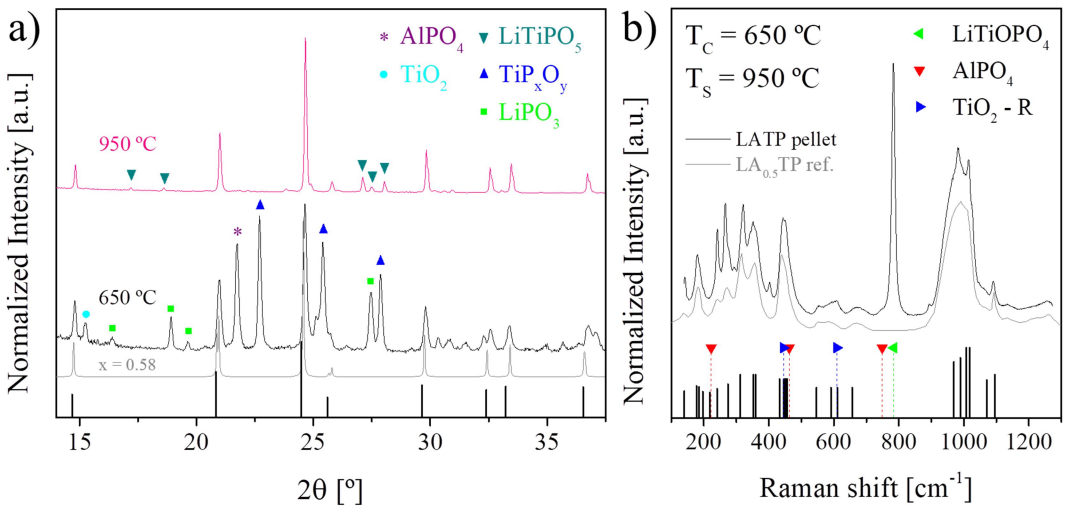

Fig. 3.2.2: Ex-situ XRD of LATP powder calcined (index C) at 650 ºC, reground and sintered (index S) as 1" pellet at 950 ºC in (a) is compared to the diffractogram of LATP with x = 0.58 (grey line) from *Dashjav et al.*[12] All intensities are normalized and horizontally shifted. The main phase of LATP is referenced as NASICON $LiTi_2(PO_4)_3$ (black vertical lines, JCPDS 00-035-0754). Secondary phases correspond to JCPDS data files of $AlPO_4$ (00-011-0500), $Ti(PO_3)_3$ and TiP_2O_7 (01-082-1178/00-038-1468), $LiPO_3$ (01-070-0274), β-$LiTiOPO_4$ as $LiTiPO_5$ (00-044-0083) and TiO_2 (00-046-1237). Corresponding Raman spectra are shown in (b) with vibrational modes for LTP indicated as black vertical lines.[16–18] Again reference is made to literature on LATP with x = 0.5 (grey line).[19] Secondary phases are indicated for Rutile (blue),[16] $AlPO_4$ (red)[20,21] and β-$LiTiOPO_4$ or $LiTiPO_5$ (green).[22]

Similar secondary phases are present as previously assigned in **Fig. 3.2.2 (a)** also in **Fig. 3.2.3 (a)** for powders after calcination at 650 ºC. After a repeated milling of the pre-reacted powders, small pellets of 1" diameter were isostatically pressed and sintered. According to literature and preliminary studies on the optimum

conditions, the best sintering temperature (T_S) was determined to be 950 ºC, as a good compromise between phase purity and density.[23] Acceptable phase purity of LATP has been achieved with minor amounts of secondary phases mainly attributed to $LiTiPO_5$, which coincides with β-$LiTiOPO_4$ at a Raman shift of 785 cm^{-1} as shown in **Fig. 3.2.3 (b)** and is believed to act as sintering aid in the densification of the LATP lattice, being one of the main reasons for good overall ionic conductivities.[7,22] Raman spectra hence complement the information from XRD analysis, giving not only details on possible secondary phases, but also valuable insight into different dopant amounts, as in **Fig. 3.2.3 (b)** the reference of *Dashjav et al.*[19] suggests the Al concentration to be about 0.5 per unit formula. Therefore an increase in the sintering temperature is not necessary and annealing periods are kept short (2 h), as the risk of excessive lithium loss and the formation of less desirable phases is big with higher dopant concentrations.

3.2.3 LATP target for PLD

The previously determined synthesis conditions are transferred in the following section in order to fabricate a target, suitable for the deposition in LA-PLD. Greater amounts of powder necessary need to be processed simultaneously for the enlarged lateral target dimensions of 3”. Resulting X-ray diffractograms and Raman spectra are shown in **Fig. 3.2.4**.

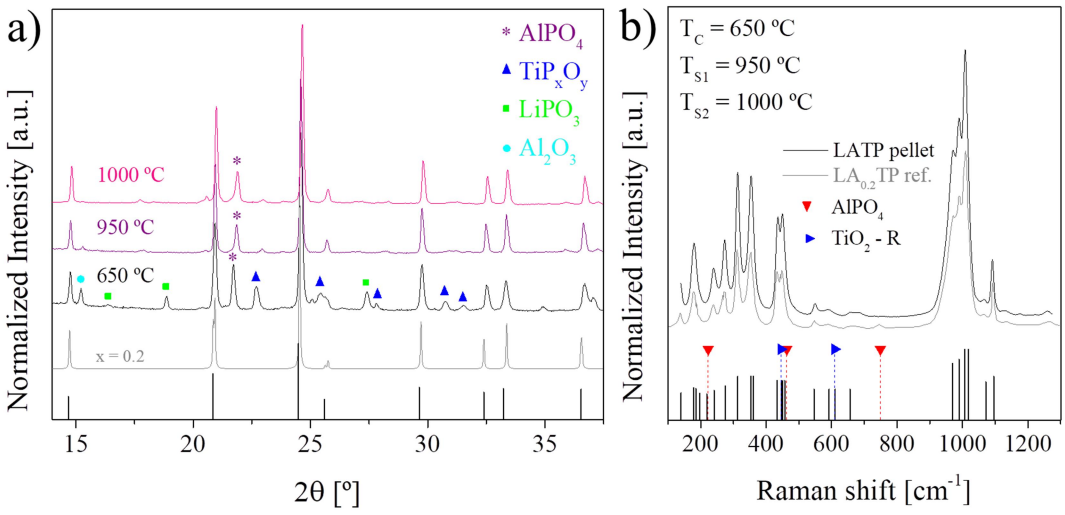

Fig. 3.2.3: Ex-situ XRD of LATP powder calcined (index C) at 650 ºC, reground and sintered (index S) as pellet at 950 ºC and again as 3” pellet at 1000 ºC in (a). As comparison the diffractogram of LATP with x = 0.2 (grey line) is shown from *Dashjav et al.*[12] All intensities are normalized and horizontally shifted. The main phase of LATP is referenced as NASICON $LiTi_2(PO_4)_3$ (black vertical lines, JCPDS 00-035-0754).

Secondary phases correspond to JCPDS data files of $AlPO_4$ (00-011-0500), $Ti(PO_3)_3$ and TiP_2O_7 (01-082-1178/00-038-1468), $LiPO_3$ (01-070-0274) and TiO_2 (00-046-1237). Corresponding Raman spectra are shown in (b) with vibrational modes for LTP indicated as black vertical lines.[16–18] Again reference is made to literature on LATP with x = 0.2 (grey line).[19] Secondary phases are indicated for Rutile (blue)[16] and $AlPO_4$ (red).[20,21]

A difference in weight for 1" and 3" pellets is causing a notable effect on the amount and nature of secondary phases, although exposed to the same pre-heating, calcination treatment and reacted in the same platinum crucible. It becomes evident how sensitive solid-state reactions can be when comparing **Fig. 3.2.3** to **Fig. 3.2.4**, even to the slightest change in conditions. To obtain a high purity of the desired phase, the length of reaction paths is crucial. Therefore smaller amounts of material ensure low impurities, because they facilitate a thorough mixture of the precursors, reduce the length of reaction paths and therefore greatly influence the appearance of secondary phases. Annealing at 950 ºC improved crystallinity and phase purity of the calcined powders in **Fig. 3.2.4 (a)**, but also formed $AlPO_4$ as predominant secondary phase for increased quantities (3" target). Therefore a subsequent milling, repeated target pressing and sintering at increased T_S for the densification of the final 3" target for PLD depositions appeared necessary, as the density of the target has priority above the phase purity, in order to ensure optimized ablation conditions and a minimized particle ejection. Sintering was repeated at a slightly increased temperature of 1000 ºC, which has been reported to approach good densities and low open porosities, but on the contrary is known to have comparably low ionic conductivities due to unfavorable $AlPO_4$ bulk formation and phase transformation.[23] No further increase in sintering temperatures above 1000 ºC is considered in order to delimit the lithium loss, although better ionic conductivities are expectable.[5,23] In **Fig. 3.2.4 (b)** the Raman signal of the 3" pellet sintered at 1000 ºC does not show any secondary phase, which according to XRD should give vibrational modes correlated to $AlPO_4$. As those are overlapping with most LATP lattice vibrations and also aluminium phosphates can exhibit many different crystallographic lattices, it was not possible to assign any signal with certainty to $AlPO_4$. Only the peak appearing at 749 cm^{-1} may eventually give some indication about the $AlPO_4$ presence, as LATP does not show any Raman signal in the surrounding optical range.[20] Referring to XRD analysis in **Fig. 3.2.4 (a)**, as there is clear evidence of $AlPO_4$, the amount of Al intercalated in the LATP lattice may differ from the expectation of Al-dopant by EDS, resulting in x = 0.56, under the

assumption of phase pure LATP. Especially Raman spectra support the hypothesis that great amounts of aluminium in the pellet sintered at 1000 ºC are placed outside the NASICON lattice, when comparing to the Raman signal of LATP with x = 0.2 from literature to the one obtained in **Fig. 3.2.4 (b)**.[19]

SEM images of the pellets analyzed by XRD and Raman are shown in **Fig. 3.2.5**, with the microstructure of 1" pellets sintered at 950 ºC being composed of common cubic clusters for LATP crystallites in **(a)**,[23] and a good contact between grains of an average size of 2.9 µm and relatively low amounts of micro-cracks. On the contrary, the surface of the 3" pellet sintered at 1000 ºC in **Fig. 3.2.5 (b)** exhibits a rough surface covered in micro-sized, shapeless particles with separated cubic clusters between them. The determination of the average grain size is difficult and can only be approximated with **Fig. 3.2.5 (c)** to range between 2 – 3 µm. The crystallite contact appears less, the porosity higher and the density lower.

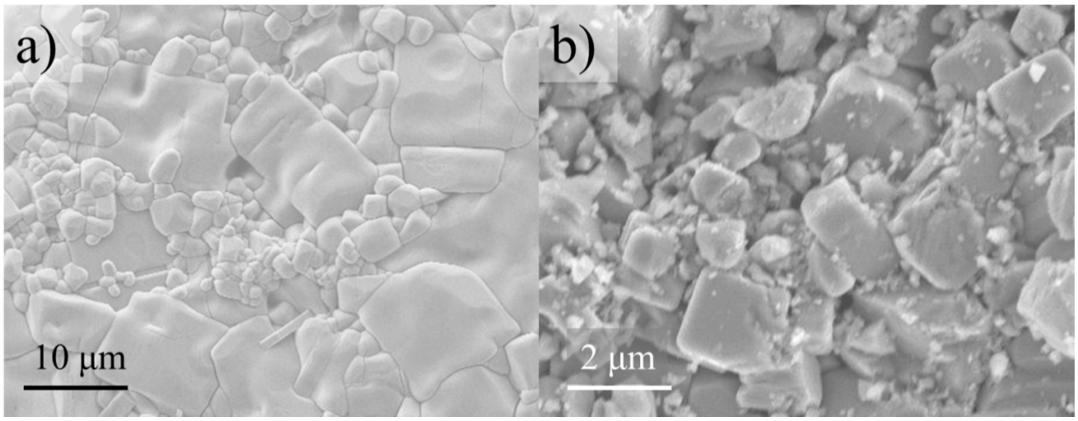

Fig. 3.2.4: SEM images of the LATP pellet calcined at 650 ºC and sintered at 950 ºC in (a) and of the 3" target sintered at 1000 ºC in (b).

As a result a 3" target was successfully synthesized for the deposition of LATP thin films by PLD, and although lacking Al-dopant inside the NASICON lattice, EDS measurements could proof the stoichiometric ratio (*z*) of (Al+Ti)/P ≈ 0.65, which compared to the stoichiometric $LiTi_2(PO_4)_3$ host lattice should be around Ti/P ≈ 0.67. Concluding calculations for the average Al-content revealed x ≈ 0.56 (assumption of LATP single phase target). Only minor secondary phases are present, mainly dominated by $AlPO_4$ as shown in **Fig. 3.2.3**. The density of the target calculated after annealing at 1000 ºC is around 76 % of the theoretical density, when assuming pure LATP phase with $\rho \sim 2.92$ g cm^{-3},[24] being sufficient (although not excellent) for a qualitatively high deposition by PLD.

3.2.4 Ionic mass transport properties

All the structural and microstructural results on the targets previously described in **Section 3.2.1** are having a great impact on the electrochemical performance of the pellets. In order to evaluate the effect especially on the ionic conductivity, electrochemical impedance spectra were collected on vertically aligned, parallel gold electrodes. An impedance spectrum measured at 250 ºC across-plane is shown in the Nyquist plot in **Fig. 3.2.6 (a)**, with the corresponding Bode plot in **(b,c)** for a 1" pellet of the same pre-reacted powder at 950 ºC and sintered at 1000 ºC, hence comparable to the expectable electrical properties of the 3" target.

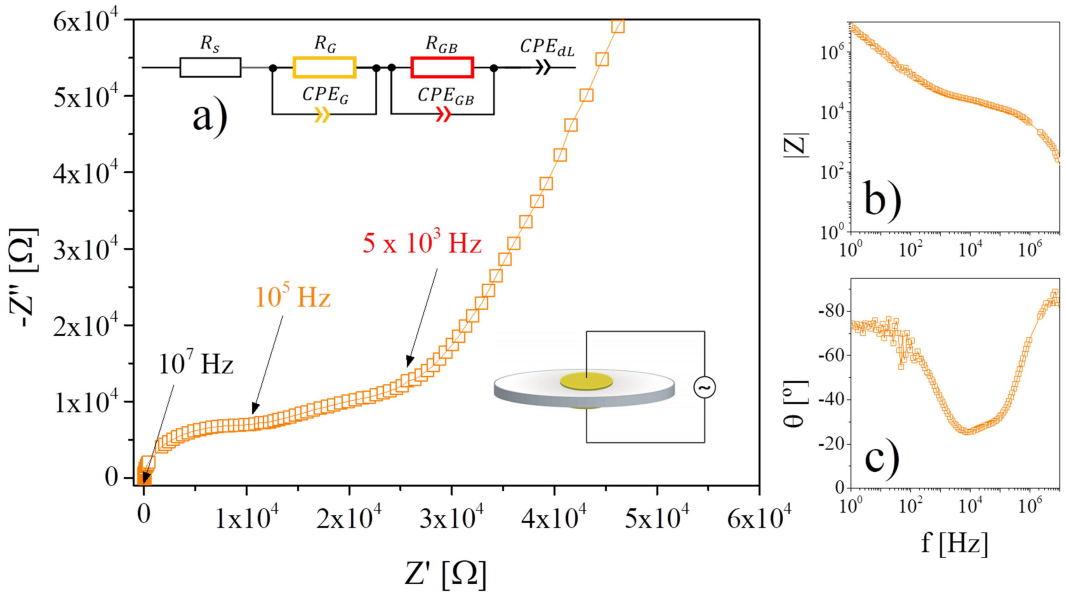

Fig. 3.2.5: Nyquist plot of an 1" pellet calcined at 650 ºC, annealed at 950 ºC and sintered at 1000 ºC in (a) and the Bode plot in (b) and (c). Raw data (squares) is shown for a spectrum taken at 250 ºC in air and fitted (lines) with the model described in (a) by the equivalent circuit (top left). In addition the AC measurement setup across-plane (lower right) is presented on sputtered gold electrodes as current collectors of 7.5 mm^2 surface area.

The equivalent circuit included in **Fig. 3.2.6 (a)** as inset (top left) shows two electrolyte contributions, both clearly visible in the Nyquist and Bode plot and attributed to the grain (G) and grain boundary (GB) resistance of the LATP pellet. Those two semicircles are described with two R-CPEs in series with a prefixed serial resistance R_S for the current collection and a final CPE in series for the description of ion blocking processes at the gold electrode – electrolyte interface at frequencies above $0.5 \cdot 10^2$ Hz (see detailed explanation of elements in the equivalent circuits in **Section 2.5.1.2**).

The Arrhenius plot in **Fig. 3.2.7** is achieved by calculating the ionic conductivity σ derived from the specific resistance of the electrolyte grains and grain boundaries after fitting the equivalent circuit (see **Eq. 2.5.3**) and plotting log(σ) over T^{-1}. A linear Arrhenius like relation is achieved, in which the slope represents the energy of activation E_A and the y-intercept the pre-exponential factor σ_0, as can be deduced by **Eq. 3.2.1** in its exponential shape.

$$\sigma = \sigma_0 \cdot e^{\frac{-E_A}{k_B \cdot T}} \qquad \text{(Eq. 3.2.1)}$$

Including k_B as Boltzmann-constant and T as the temperature.

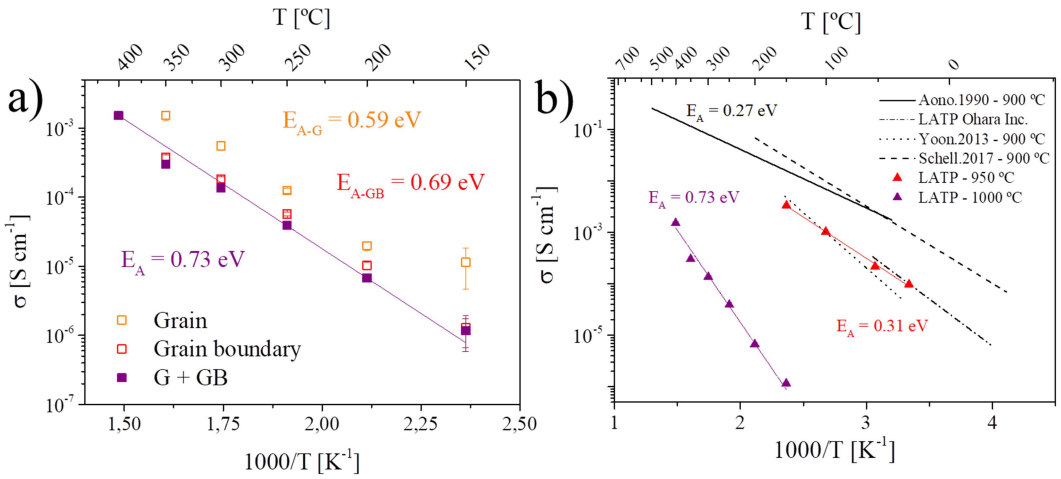

Fig. 3.2.6: Arrhenius plot of the 1" pellet sintered at 1000 °C is shown in (a) with corresponding contributions of grains (G) and grain boundaries (GB). In (b) both pellets investigated, with a final sintering at 950 °C or 1000 °C, are presented in respect to the ionic conductivities of similar LATP bulk materials reported in literature.[2,8,9,25]

The Arrhenius plot of the pellet sintered at 1000 °C is shown in **Fig. 3.2.7 (a)** with its grain (G) and grain boundary (GB) contributions deduced from the model of equivalent circuits, and their sum (G+GB) as overall ionic conductivity. The ionic conductivity and activation energy of the grains and grain boundaries differ, indicating the grain boundaries as the transport limiting obstacles with lower σ and higher $E_{A\text{-}GB}$ in respect to the grains $E_{A\text{-}G}$.[9,26] Comparing the pellets sintered at 1000 °C and 950 °C (both previously calcinated at 650 °C and annealed at 950 °C) to each other and to literature, the pellet sintered at lower temperatures and pre-reacted with smaller amounts of precursors exhibits the better ionic conductivity and a suitable E_A of ~0.31 eV for LATP bulk materials.[2,8,9,25] This clearly results from the high phase purity, good Al-dopant intercalation and therefore increased lithium content, as well as the closely packed microstructure and reduced amounts of grain

boundaries. In contrast, the pellet sintered at 1000 ºC (representative for the 3" target used for LA-PLD) exhibits very low ionic conductivities and a quite high overall energy of activation of ~ 0.73 eV, possibly resulting from the high amount of $AlPO_4$ leading to the segregation of Al outside the NASICON structure and a correlated detachment of the particle contacts.[5] Therefore grain boundaries have an increased impact on the ionic conductivity as usual, but also bulk ionic conductivities are low and their activation energies high, due to the lack of lithium content inside the LATP lattice. Nonetheless, a suitable target for the deposition of LATP thin films by LA-PLD has been fabricated using solid-state synthesis and the resulting layers are studied in the following sections with the aim to fabricate solid electrolyte thin films applicable in lithium ion microbatteries.

3.3 Fabrication of LATP thin films

The implementation of all-solid-state lithium-ion batteries to replace common button batteries with liquid electrolytes is still pending on the development of feasible solid electrolyte materials of high ionic conductivity (10^{-5} – 10^{-3} S cm^{-1}) at room temperature.[27] LiPON usually is the material of choice in thin film solid electrolytes. Although it lacks of fast ionic transportation at room temperature (10^{-6} S cm^{-1}) in comparison to other materials, as a thin film (of less than 1 μm in thickness) it can reach remarkably low area specific resistances (ASR) of 10 Ω cm^2 and below.[28,29] However, in order to reach such levels of conductivity, LiPON needs to remain amorphous, which limits its application in high temperature devices or the implementation of additional processing steps involving high temperature.[30,31] For this reason, there is great interest on developing crystalline electrolytes, which can resist much higher temperatures.[28]

Importantly, in contribution to the ionic conductivity of the electrolytes, other issues have to be faced, such as multiple interfacial contact resistances in boundaries between grains and electrodes.[32,33] In respect to this, physical vapor deposition techniques can offer a good control of the layer properties, while still providing industrial up-scaling capabilities. Among these, Pulsed Laser Deposition (PLD) has become a popular choice to produce dense and possibly oriented thin layers of high quality, uniformity and smooth surfaces, offering good stoichiometric transfer from a wide range of different applicable target

materials.[34,35] Due to its high potential to resolve interfacial issues at the electrode-electrolyte interface, PLD has been predicted as a relevant technology in commercialized thin film microbattery fabrication for more than a decade,[36] and to this moment a vast selection of various materials has already been implemented in the pulsed laser ablation.[37] NASICON-type $A_xM_2(XO_4)_3$ glass-ceramics for the deposition in PLD have been first realized for sodium rechargeable battery systems with Na^+ occupied A-sites.[38] After a rare series of the related Li-stabilized compounds as thin films,[39–42] finally first layers of $Li_{1+x}Al_xTi_{2-x}(PO_4)_3$ (LATP) were recently fabricated by PLD. However, whilst a complete structural characterization was conducted in that work, results on electrochemical performance of thin films were never presented.[43]

Hence it is of major interest to present an electrochemical characterization and to further study the role of microstructure and grain boundaries in the charge transfer mechanisms of LATP thin film electrolytes deposited by PLD, which has not been reported so far. In this section we present the first large-area (LA) PLD thin film of $Li_{1+x}Al_xTi_{2-x}(PO_4)_3$, showing their performance and discussing their potential application as highly ion conductive solid electrolyte for all-solid-state lithium-ion batteries.

3.3.1 Optimization of the LA-PLD deposition process

Using the target of LATP synthesized as described previously in **Section 3.2**, thin films have been deposited by LA-PLD for the first time onto various kinds of substrates with a conductive or insulating, amorphous or crystalline nature. In order to achieve suitable layer stoichiometry and morphology leading to appropriate electrochemical performance, the impact of oxygen background gas pressure (pO_2) during deposition is studied in a large range of 20 – 200 mT. Other parameters like laser energy and deposition temperature have been maintained constant. The resulting layers are characterized both in as-deposited state and after an annealing process at 900ºC. This last post-processing is a common practice conducted with the aim to improve the crystallinity, restructure and re-oxidize layers. The following sections are concentrated on the general effect of the variation in pO_2 and structural, microstructural and electrochemical changes due to the post-annealing.

3.3.1.1 Thin film composition

The thin film composition as a function of pO_2 was probed by energy and wavelength dispersive spectroscopy (EDS/WDS) and the cation ratio z = (Al+Ti)/P was calculated. As shown in **Fig. 3.3.1 (a)** the correlation between z and the applied pO_2 for depositions at 700 °C follows an exponential decay function, clearly related to a deficiency in phosphorus at first, which can be counteracted with an increase in the oxygen partial pressure. A certain P-deficiency was also observed for the target (data not shown) after multiple depositions, differing from its initial optimum stoichiometric composition at z*.

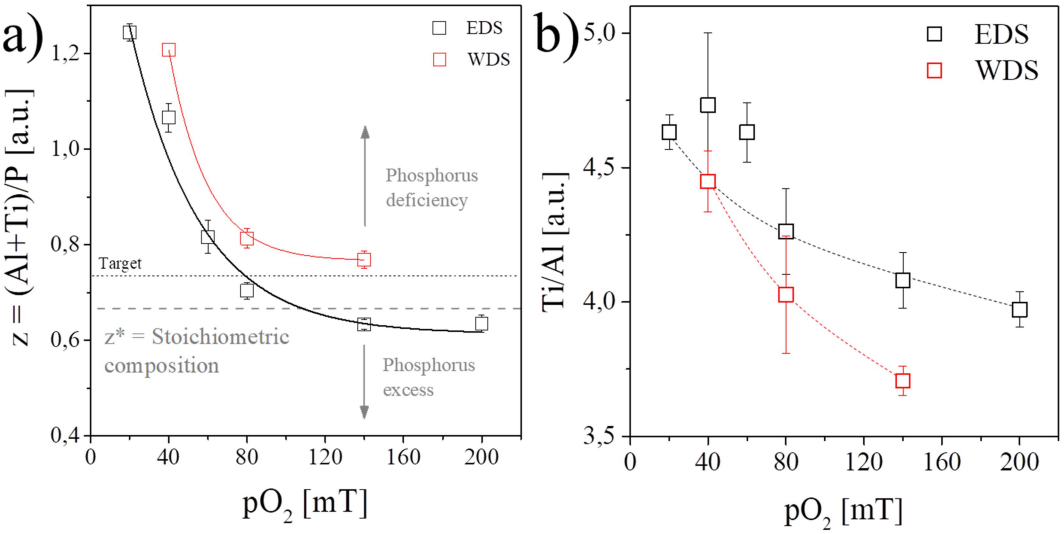

Fig. 3.3.1: EDS and WDS measurements of the as-deposited LATP thin films at different pO_2 during deposition in the PLD with respect to the stoichiometric composition z* (grey dotted line) for LATP and the target composition after multiple depositions (black dotted line).

The overall cation ratio z between heavy (H) and light (L) elements and the Ti/Al ratio in particular are shown in **Fig 3.3.1**. Both decrease with higher pO_2 exponentially and especially z is approaching some kind of plateau above 80 mT around the optimum stoichiometric composition z* to form $Li_{1+x}Al_xTi_{2-x}(PO_4)_3$. Hence, when increasing the pO_2 the H/L ratio decreases with the lighter element being better transferred, which is in agreement with the reported dependence of cation ratios for background gas pressure between 10^{-2} – $3 \cdot 10^{-1}$ mbar (~ 10 – 200 mT) in literature (see **Section 2.3.3** for details).[44] As the oxygen molecule is heavier than lithium, aluminium and phosphorus cations, those are more likely to be scattered on their way from the target to the substrate, while the heavier titanium is

less affected.[45] Therefore changes in the background gas pressure create different plume kinetics and sizes, deposition rates and film compositions. Note that EDS analysis is only reliable to state the overall distribution of elements in the analyzed area as an approximation of the Al-dopant amount within the thin films, which is ranging between $0.35 \leq x \leq 0.40$ under progressive increase with higher oxygen partial pressures. WDS analysis exhibits a similar trend as EDS for the same layers deposited at different pO_2, but is defined in general by a greater P-deficiency. This difference clearly is a result from the techniques sensitivity and peak resolution in the evaluated spectra, whereas WDS appears to be more unambiguous. Hence the obtained quantifications are unsuitable to determine the exact material composition, especially the amount of lithium and aluminium finally intercalated inside the lattice or segregated as possible secondary phase. In comparison to the target composition determined by EDS before ablation with $x = 0.56$ and afterwards with $x = 0.62$, the loss of aluminium between the target and substrate surface seems clear for all thin films deposited in the PLD. Additional phosphorus deficiency for all thin films (as can be assumed from WDS results) and the target itself after ablation, may suppress the formation of ion blocking, phosphatic secondary phases such as $AlPO_4$.

3.3.1.2 Structural characterization

X-ray diffractograms conducted from thin films are presented in **Fig. 3.3.2 (a)**. A broadening in peaks and background signal reveal the presence of nanometric crystallites and amorphous material. In general, the layers presented a reduced amount of secondary phases in comparison to the target. Raman spectra of the same samples were collected in order to give complementing information on the phase purity and help in the assignment of secondary phases (**Fig. 3.3.2 (b)**). Crystallization at 900 ºC leads to intensified and sharpened reflections, but also the amount of secondary phases increases, which is more severely occurring in the low and high pO_2 ranges. The secondary phases mainly consist of $AlPO_4$, Rutile TiO_2, $LiTiOPO_4$ and Li_2TiO_3 and can be associated to signals appearing for XRD and Raman analysis in **Fig. 3.3.2**, as particularly well resolved in the Raman spectra with peaks of a Raman shift at 605 cm^{-1}, 749 cm^{-1} and 780 cm^{-1}.[16,17,21]

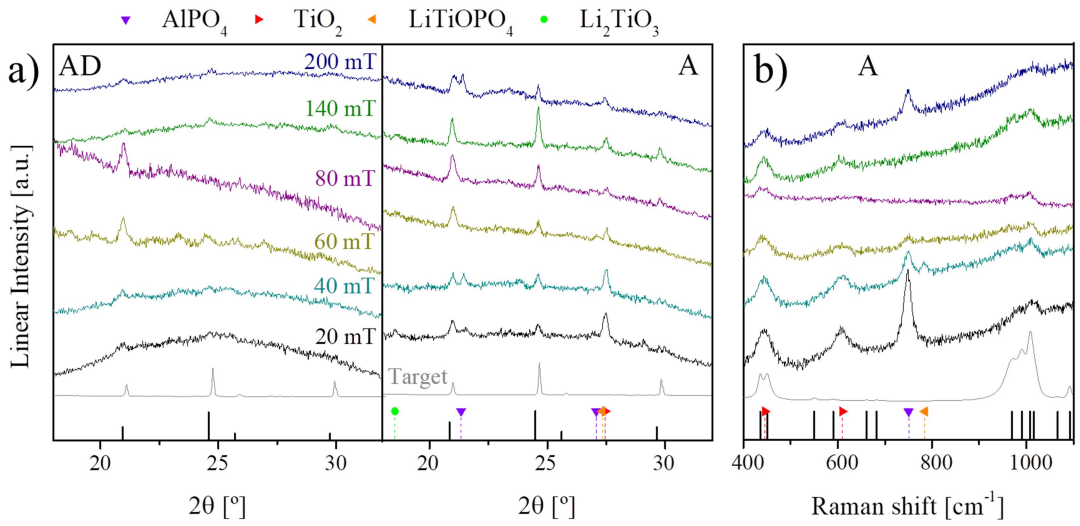

Fig. 3.3.2: X-Ray diffractograms (a) of LATP thin films deposited at different partial oxygen pressures pO_2 in the LA-PLD for as-deposited (AD) and annealed (A) layers on amorphous Si_3N_4 substrates. Corresponding Raman spectra are depicted for the layers annealed at 900 °C (b). Grey lines relate to the response of the target used for laser ablation. Black vertical lines refer to the undoped $\mathbf{LiTi_2(PO_4)_3}$ phase in JCPDS 00-035-0754 for XRD and in *Giarola et al.* for Raman.[17] Secondary phases are assigned to $\mathbf{AlPO_4}$(violet), Rutile $\mathbf{TiO_2}$(red), $\mathbf{LiTiOPO_4}$(orange) and $\mathbf{Li_2TiO_3}$(green).[16,21]

As previously examined in **Section 3.2**, especially $AlPO_4$ is known to be an impediment at a certain amount, as it is not a lithium-ion conductor and acts as blockade for the charge transport.[46] This impurity derives from a lithium deficiency, which leads to an imbalance of the tetravalent titanium vacancies in the NASICON lattice. Therefore excess trivalent aluminium is not intercalated as dopant and is forming instead a secondary phase with phosphate ions. This is expectable, as lithium deficiency is a common issue in PLD depositions due to the high volatility of lithium.[47] When correlating X-ray diffractograms and Raman spectra to the elemental analysis obtained from EDS and WDS in **Fig. 3.3.1**, the presence of $AlPO_4$ may be explained at lower pO_2 with a high off-stoichiometry for the formation of LATP and difficulties placing Al-dopant inside the NASCION lattice. For higher pO_2 an increased transference of Al and P from the target occurs over other elements, again in favor of the $AlPO_4$ formation. For all samples analyzed between 20 – 200 mT, the thin film deposited at 80 mT exhibited the smallest amount of secondary phases after annealing.

3.3.1.3 Thin film microstructure

SEM images in **Fig. 3.3.3** reveal the microstructure for as-deposited and annealed thin films as a function of different pO_2 applied during deposition in the LA-PLD,

ranging from 20 – 200 mT. Layers deposited at lower pO_2 tend to consist of smaller particles (a,b) as in comparison to higher pO_2 (e,f) with the more likely event of greater particle ejection from the target and the formation of agglomerates in the generated plasma plume (see **Section 2.3** for detailed description of the PLD and the influence of the background gas pressure).

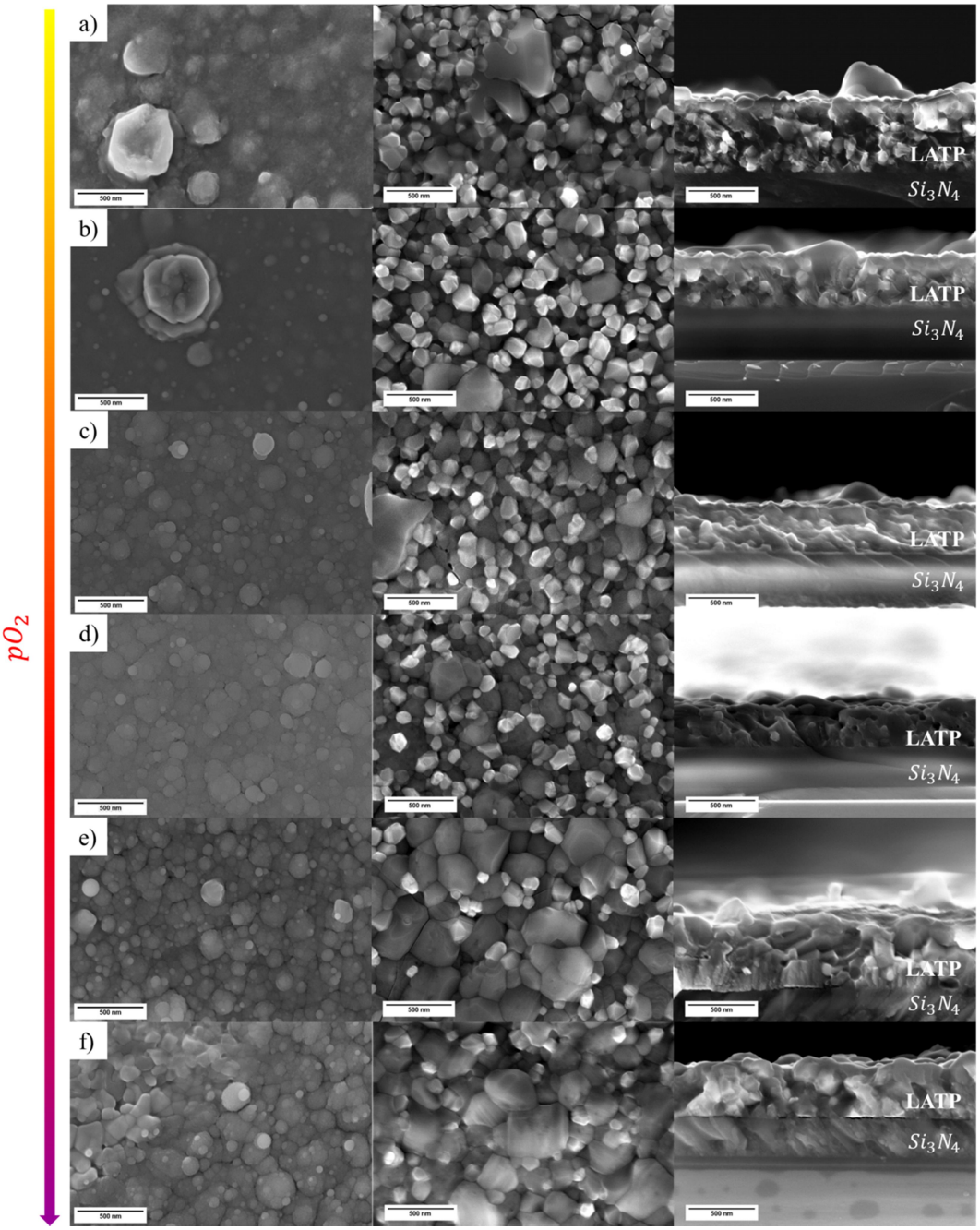

Fig. 3.3.3: Scanning electron images of LATP layers on $\boldsymbol{Si_3N_4|SiO_2|Si_{(100)}}$ chips of different morphologies as-deposited (left column) and after annealing at 900 °C shown in-plane (center column) and across-plane (right column). Depositions were performed at different pO_2, increasing with a) 20m T, b) 40 mT, c) 60 mT, d) 80 mT, e) 140 mT to f) 200 mT. Scale bars correspond to 500 nm.

The growth mechanism observable on the amorphous substrates consisting of $Si_3N_4|SiO_2|Si_{(100)}$ chips leads to the preferential formation of islands. Hence singular nano-crystallites ejected from the target form a “cauliflower-like” morphology due to limited surface diffusion energy available.[48] Annealing increases the crystallite size of the thin films with higher partial oxygen pressure during layer deposition. A more inhomogeneous distribution of the size is observed between grains of different mass contrasts. This leads to the accumulation of smaller grains, the preferential growth of bigger crystallites and a higher homogeneity in the overall composition. A balanced ratio between crystallites of different sizes and contrast is observed for layers deposited at 80 mT.

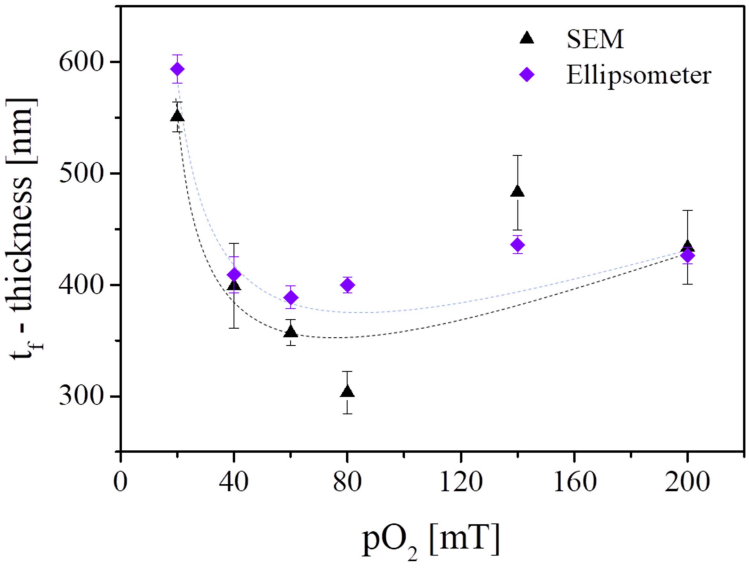

Fig. 3.3.4: Thickness determination by SEM and spectroscopic ellipsometry for the thin films t_f is shown, with trends indicated as dotted lines as guide for the eyes.

When comparing the layer thicknesses obtained from SEM and spectroscopic ellipsometry in **Fig. 3.3.4**, pressures of 40 - 80 mT provide the thinner layers. At higher oxygen partial pressures above 80 mT, film thicknesses increase again.

3.3.1.4 Electrochemical characterization

The suitability of the fabricated layers as solid electrolyte depends on its ionic conductivity. In-plane conductivity of the layers was measured in EIS measurements. **Fig. 3.3.5 (a)** shows an example of the equivalent circuit applied in the following for the evaluation of EIS data.

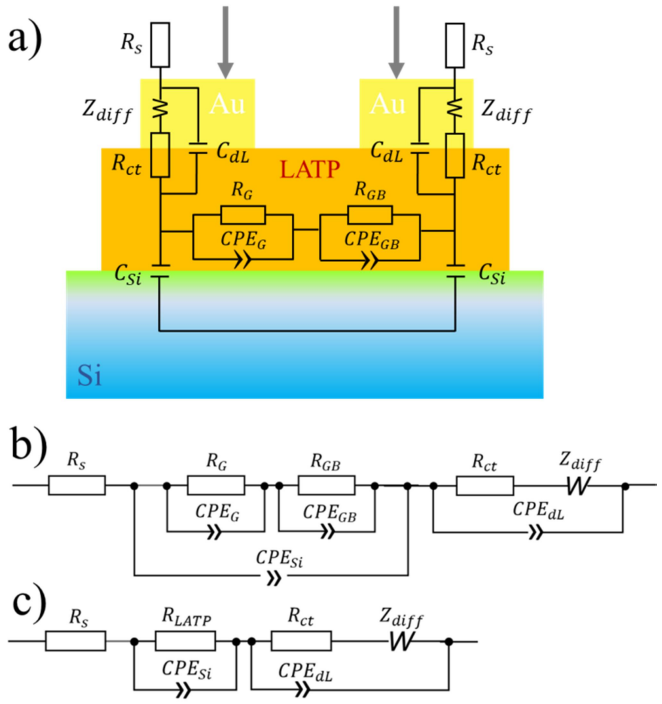

Fig. 3.3.5: Schematic illustration of the EIS measurements conducted in-plane on LATP thin films deposited on Si_3N_4 substrates and connected with sputtered gold electrodes, with the corresponding equivalent circuit in (a), which can be summarized as depicted in (b). Further simplification is conducted in (c) as $CPE_{Si} >> CPE_G + CPE_{GB}$.

The obtained Nyquist plot is shown in **Fig. 3.3.6 (a)** for the thin film deposited at 80 mT and measured at 300 ºC, with a sketch of the equivalent circuit from **Fig. 3.3.5 (c)** and the in-plane measurement setup as inset. First, it is important to remark that, opposite to the LATP pellet measurements, the contributions of grain and GBs are not distinguishable in this case due to the presence of a masking high capacitance associated to the Si_3N_4 in the Silicon substrate. Taking this into consideration, the first arc is related to the overlapped contribution of grain and GB, i.e. $R_{LATP}=R_G+R_{GB}$, in parallel with the previously mentioned Si_3N_4 dominant capacity (CPE_{Si}). In series with this ($R_{LATP}CPE_{Si}$) element, there is an additional serial resistance R_s from the electronic contacts. This value appears with a very small contribution, as the impedance measurements were conducted in a pseudo-4-wire measurement setup described in **Section 2.5.1.1**. The second arc appears with a stronger depression angle of the CPE_{dL} element and further forms a unit with the inclined spike starting at 100 Hz referring to a Warburg element Z_{ct} describing diffusive processes during the charge-transfer (ct). The model for the second arc therefore results in a so-called Randles equivalent circuit, summarizing the

electrode-electrolyte or electrolyte-substrate interface ion-blocking processes, which can potentially result in an inter-diffusive lithium intercalation layer.[49–51]

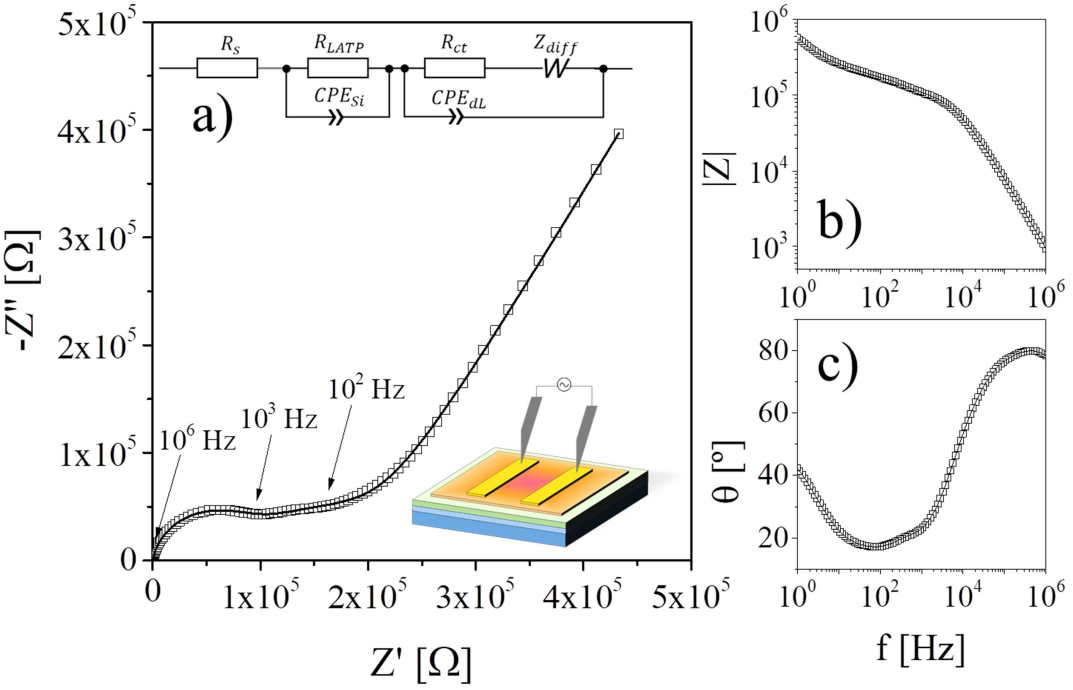

Fig. 3.3.6: Nyquist plot in (a) with the schematic measurement setup (bottom) and equivalent circuit as insert (top) and (b-c) the Bode plot at 300 °C in air from the sample deposited at 80 mT exemplary for all impedance measurements collected.

To compare different assignments in the frequencies and for qualitative comparison of the fitting towards the measurements, the Bode plot is observed in **Fig. 3.3.6 (b)** and **(c)** as support to deduce a physical meaningful equivalent circuit by splitting contributions of different time constants in dependence on their frequency.

Complementary deposition of LATP layers on Si_3N_4 were carried out by varying the pO_2. After fitting the EIS measurements similar to **Fig. 3.3.6** at all the temperatures with the previously discussed equivalent circuit and applying the right geometry (see **Fig. 2.5.2 (b)**), it was possible to plot the Arrhenius relation of the conductivity for the LATP layer on Si_3N_4 before and after annealing, under application of **Eq. 3.2.1**. The ionic conductivity σ_i of these thin film layer are represented in **Fig. 3.3.7**, resulting all in a linear Arrhenius-like behavior. The increase in partial oxygen pressure greatly enhances the ionic conductivity until it saturates at pressures above 80 mT with no further major increase. This may result from the huge compositional similarity between samples deposited at 80 – 200 mT, as it can be deduced from previously discussed XRD data in **Fig. 3.3.2 (a)**.

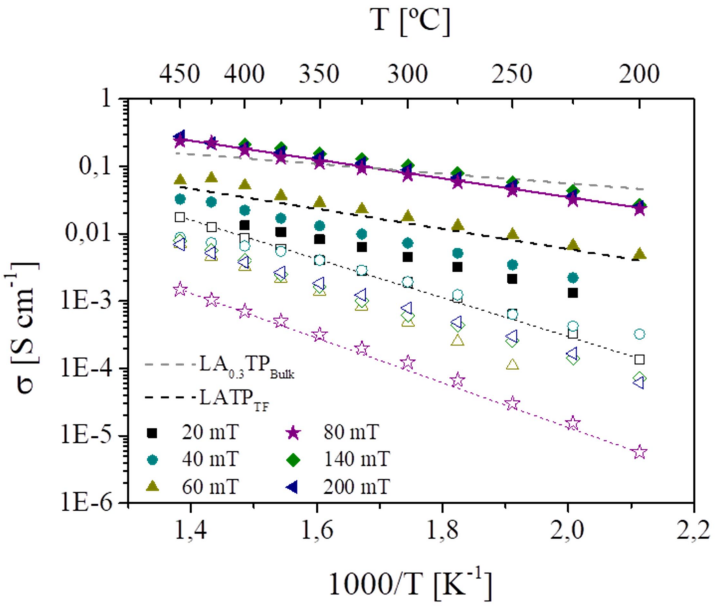

Fig. 3.3.7: Arrhenius plot of the overall conductivities of the thin films as-deposited at various oxygen partial pressures (empty symbols) and after annealing (full symbols) in comparison to a polycrystalline, bulky sample of $LA_{0.3}TP_{Bulk}$ (x = 0.3)[2] and an amorphous thin film $LATP_{TF}$ produced by RF magnetron sputtering.[40]

Fitting the slopes in **Fig. 3.3.7** it is possible to extrapolate the ionic conductivity at room temperature and to determine the energy of activation E_A for the overall ionic conductivity by using the Arrhenius relation described in **Eq. 3.2.1**. Ionic conductivities predicted for films deposited at higher pO_2 range between 0.1 to 0.3 mS cm^{-1} after annealing at 900 ºC. The energy of activation E_A for the overall in-plane ionic conductivity in the thin films and the pre-exponential factor σ_0 are plotted in **Fig. 3.3.8** dependent on the layer composition calculated from EDS measurements. The activation energy for lower z values (and therefore higher partial oxygen pressures applied) ranges between 0.32 – 0.34 eV and is comparable to E_A values of other LATP thin films deposited utilizing RF magnetron sputtering (0.32 eV)[40] and close to the characteristic values of the bulk material (0.27 eV).[2] As demonstrated, the amounts of aluminium and phosphorus play a crucial role in obtaining the right phase and enhancing the mobility of charge carriers. With the simultaneous introduction of aluminium and lithium in the lattice the ionic conductivity profits from two phenomena, as can be noticed form the high pre-exponential factor σ_0, representing a parameter directly correlating to the amount of mobile charge carriers available in the lattice. Its value greatly increases with annealing after deposition (see changes of y-intercept in **Fig. 3.3.7**) just like the overall ionic conductivity as a result of the enhanced ionic mobility in the thin

films, underlining the necessity of the lattice reconstruction after deposition to form more of the active electrolyte material. But not only more mobile charge carriers are available in the NASICON structure, also the bottlenecks for ion transportation become wider between the lithium occupation sites due the Al-dopant intercalation, leading to a facilitated ion hopping throughout the lattice.[24] The additional grain growth, as visible in **Fig. 3.3.3**, possibly leads to lower amounts of grain boundaries, which are potential obstacles for the ion hopping process and can therefore cause an increase in the activation energy.

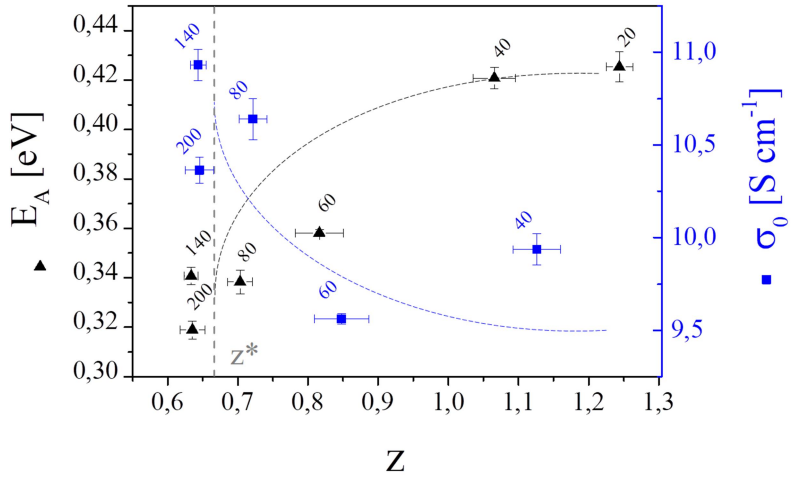

Fig. 3.3.8: Relation of the energy of activation E_A (black) and the pre-exponential factor σ_0 (blue) towards the films cation ratio z (analyzed by EDS) in respect to the stoichiometric composition *z**. The dotted lines serve as guide for the eyes.

3.3.2 Thermal grain and grain boundary engineering

The previous studies demonstrate a strong increase in ionic conductivity after annealing and require further investigation. The following section concentrates on the clarification of LATP thin film properties before and after an additional heat treatment with the aim of understanding the reasons behind this improvement. A thorough investigation on the evolution of the composition, microstructure and molecular environment is carried out.

3.3.2.1 Impact on microstructure and roughness

Thin films deposited at a pO_2 of 80 mT have been studied as-deposited (AD) at 700 ºC and annealed (A) at 800 ºC for 5h in ambient air, using Silicon single-crystalline chips with Si_3N_4 as amorphous top layer, glassy SiO_2 or crystalline Pt thin films as substrates, with a great stability at elevated temperatures and no reaction between

LATP and the substrate material (see experimental details in **Section 2.3.4** and **2.3.5**). To further investigate the microstructure, layers deposited on Si_3N_4 were prepared with a Ga-ion FIB to produce thin lamellas of AD and A to study in the STEM and are compared with images collected in the SEM in **Fig. 3.3.9**.

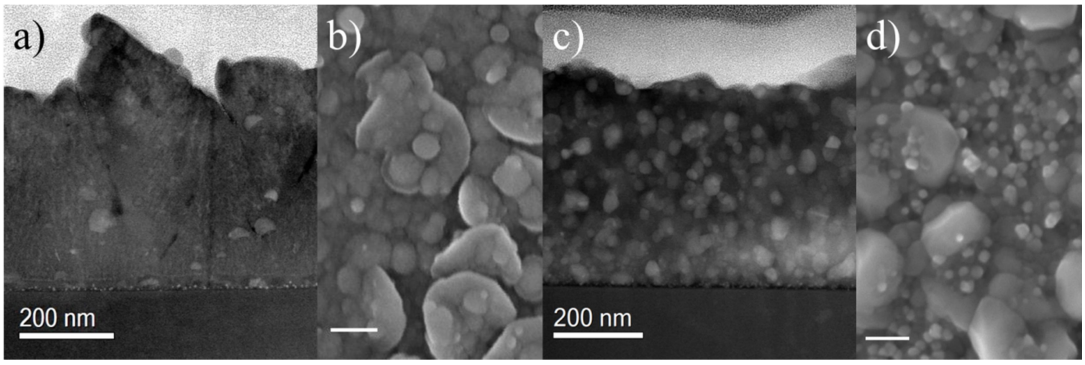

Fig. 3.3.9: STEM dark field images collected for as-deposited (a) and annealed (c) thin films in cross-section of the layers with a thickness around 445 nm. SEM images of the same layers surface AD (b) and A in (d). The length of the bar in the bottom lower-left is equal to 200 nm.

The microstructure for the AD layer appears rugged but locally compact, consisting of very fine nano-crystallites embedded in greater particles slightly spaced from each other (in **Fig. 3.3.9 (a-b)**) with an root mean squared roughness Rq ~ 27 nm as shown for the corresponding AFM image in **Fig. 3.3.10 (a)**. After annealing small particles are homogeneously distributed within a dense matrix (see **Fig. 3.3.9 (c-d)**) and the surface slightly smoothened to Rq ~ 21 nm (**Fig. 3.3.10 (b)**). The particles or grains visible in **Fig. 3.3.9** exhibit different intensities towards each other, which may result from possible changes in the composition. The nature of the grains and the surrounding material matrix is further evaluated in respect to their structure in **Section 3.3.2.2** and their composition in **Section 3.3.2.3**.

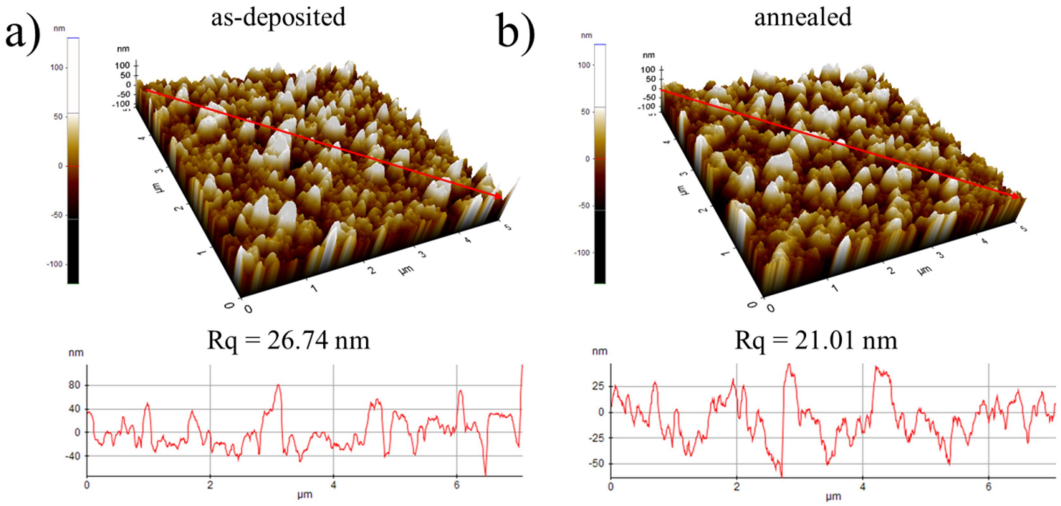

Fig. 3.3.10: AFM images of as-deposited (a) and annealed (b) thin films on Si_3N_4 and corresponding line scan profiles (red arrow) below, indicating their root mean squared surface roughness Rq.

3.3.2.2 Structural changes upon annealing

The structure of both as-deposited (80 mT) and annealed thin films is confirmed to be LATP with only minor amounts of secondary phases after annealing visible by means of XRD and Raman, as shown in **Fig. 3.3.11**.

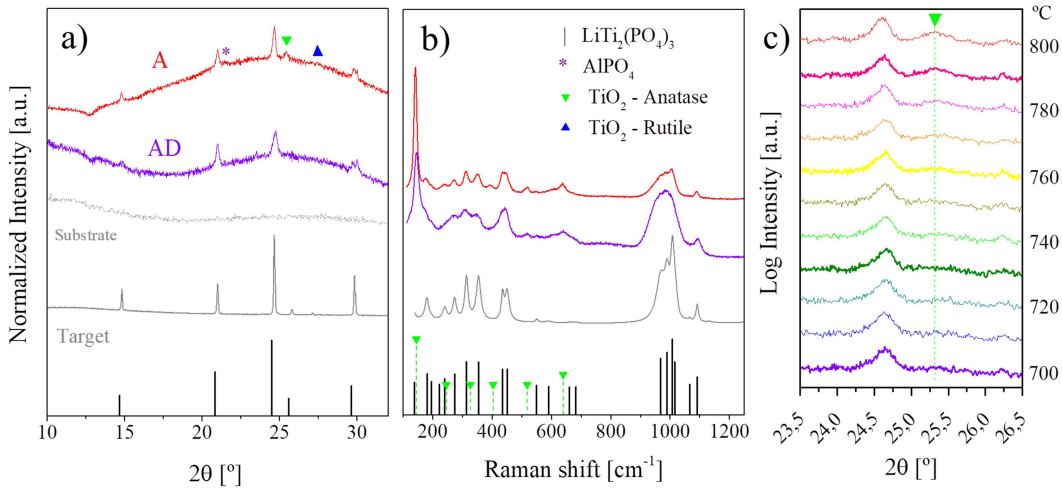

Fig. 3.3.11: Structural analysis of LATP for AD and A thin films in respect to the target in (a) by XRD, (b) Raman spectroscopy and (c) temperature dependent in-situ XRD. References for XRD correspond to $Li_2Ti(PO_4)_3$ (JCPDS 00-035-0754) and Anatase (JCPDS 01-073-1764) and Rutile (JCPDS 01-078-1510), as well as in Raman spectra with corresponding LTP[17] and Anatase[52] in (b) for equivalent layers deposited on Pt.

The broad scattering hump present in the background signal of the X-ray diffractograms in **Fig. 3.3.11 (a)** results from the amorphous Si_3N_4 substrates, as has been clarified by diffraction experiments conducted in GI-XRD (not shown)

where the substrate influence is excluded. Upon annealing, diffraction peaks become sharper, indicating a growth of crystallites present in the layer which is further supported by images taken in the AFM (compare **Fig. 3.3.10**). Small amounts of impurities appear to be present especially after annealing, as shown in the peak at 25.4º for Anatase TiO_2 and crystalline $AlPO_4$ at 21.6º. As the in-situ X-ray diffractograms of LATP thin film on Si_3N_4 in **Fig. 3.3.11 (c)** reveal, the Anatase peak intensifies upon annealing notably after 790 ºC. In **Fig. 3.3.11 (b)** Raman spectra clearly indicate the presence of Anatase phase (mainly visible in the vibrational mode at 140 cm^{-1}), for both as-deposited and annealed samples, with a notable increase in the relative intensity for the latter.

Similar conclusions can be drawn from HAADF-HRSTEM images collected on thin film lamellas in **Fig. 3.3.12** of AD **(a)** and A **(b)** for LATP deposited on amorphous Si_3N_4. The presence of TiO_2 as particles embedded in the as-deposited layers of LATP is shown in **(a)**. A clear structural difference before and after annealing at 800 ºC is observable, as FFTs of HR-STEM images verify the character of particles and their environment to strongly differ between AD and A. Whereas AD indicates a nano-crystralline layer consisting of LATP predominantly, the amount of amorphous material dominates the signal in the FFT of **Fig. 3.3.12 (b)** for A, disclosing the glassy nature of the intergranular matrix in which crystalline particles are embedded (colored regions) with reflections in the FFT corresponding to interplanar distances for LATP nano-crystals.

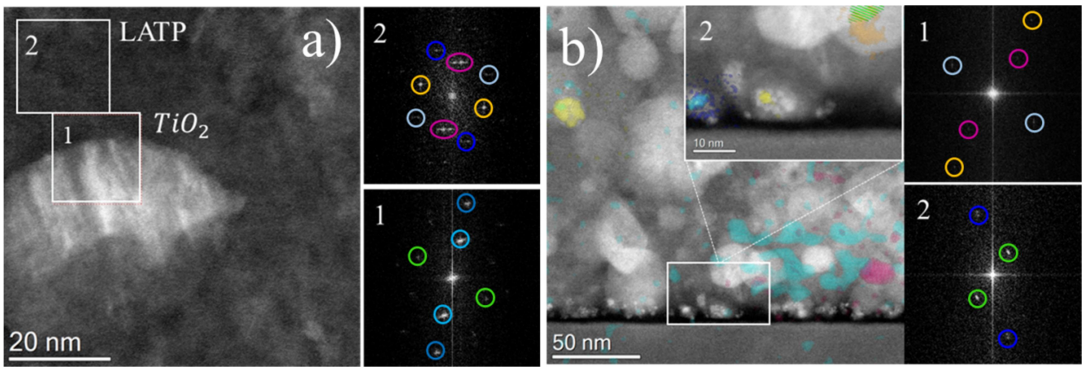

Fig. 3.3.12: The HAADF-HRSTEM image is shown for a crystalline TiO_2 particle embedded in the polycrystalline LATP matrix for AD in (a) with corresponding FFTs for the regions-of-interest (1,2). In (b) crystalline particles embedded in an amorphous matrix are visible after annealing with corresponding FFT of (1) the full frame image and (2) the magnification of the marked area of interest at the bottom of the layer. Crystalline signals of similar crystalline orientations appearing in the FFT are colored correspondingly in the displayed HAADF-HRSTEM images.

The results are in concordance with literature in which the formation of TiO_2 as a result of lithium loss during the annealing at elevated temperatures above 750 ºC was reported.[43] Also, lattice transformation of the rhombohedral LATP to the orthorhombic $AlPO_4$ upon the suspension of Ti appears for all temperatures above 500 ºC with an increasing fraction for higher and longer temperature treatments.[5,53] As depositions in the PLD are generally affected by a certain loss of lithium,[47] the presence of TiO_2 in both AD and A can be considered expectable. However, the appearance of TiO_2 due to Li loss is linked to the formation of $AlPO_4$. For a better understanding of which character grains and glassy phases are, the analysis of their composition and local atomic environment is required, as diffraction and scattering events are unable to disclose the nature of amorphous materials.

3.3.2.3 Modifications in composition and atomic environments

To further complement the understanding of the local environment concerning Li- and Al-sites occupation and their coordination in the lattice, solid state NMR was performed on glassy SiO_2 substrates for as-deposited and annealed thin films and is shown in **Fig. 3.3.13** for ^{7}Li in **(a)** and ^{27}Al chemical shifts in **(b)**. According to the ^{7}Li spectrum before annealing in **Fig. 3.3.13 (a)**, the main peak at $\delta \approx -2.5$ ppm can be attributed to the preferable occupation of Li-ions at the six-fold coordinated Li1 interstitial sites in the NASICON structure of LTP.[6] The sharp line width indicates a good Li-ion mobility with a slight broadening in the ^{7}Li signal due to increased amorphization and lithium displacement in phases different from NASICON compounds.[6,10,54] A second ^{7}Li signal at $\delta \approx 0$ ppm appears related to the occupation of Li3 sites due to the incorporation of Al in the LATP structure.[55,56] Li3 sites are four-fold interstitials near Li2 sites, located between three-oxygen faces surrounding Li2 cavities (see **Section 1.3.2** for more details). As the occupation of Li3 sites reduces the electrostatic repulsion towards Li1, the mobility of lithium ions is enhanced along the conduction pathways upon Al intercalation into the lattice.[55]

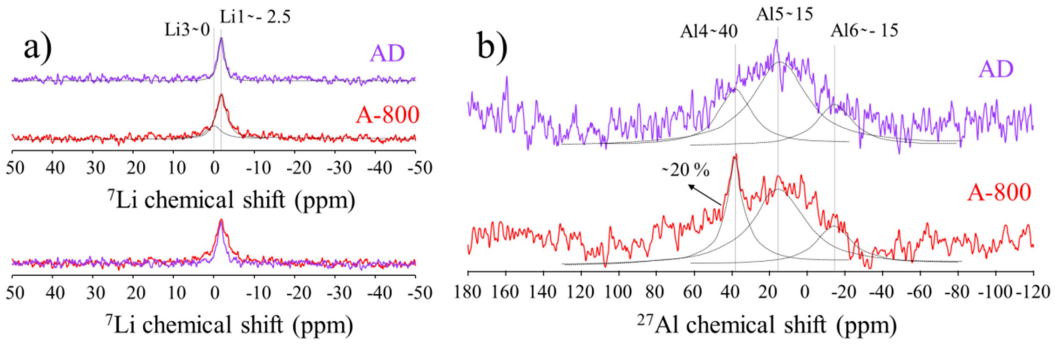

Fig. 3.3.13: Solid state NMR spectra from as-deposited and annealed thin films on SiO_2 substrates with the chemical shifts observed for a) ^{7}Li-MAS-NMR and b) ^{27}Al-MAS-NMR. Possible assignments are fit considering Gaussian distributions (black lines) and are displayed for the purpose of illustration.

The spectrum of ^{27}Al-MAS-NMR recorded for the as-deposited layers in **Fig. 3.3.13 (b)** consists of a non-resolved broad contribution in the range of $\delta \approx$ - 40 to 60 ppm, in accordance with previously reported coordination environments of AlOy in literature.[57] As common for LATP in the NASICON structure, one would expect the chemical shift δ at −15 ppm to appear for Aluminum in the octahedral coordination forming AlO_6, but instead the predominant chemical shift for AD appears at $\delta \approx$ 15 ppm, ascribed to five-coordinated AlO_5 and related to an amorphous environment.[10,54,56,58] In addition the signal resolved at $\delta \approx$ 40 ppm can be ascribed to the tetrahedral coordination of AlO_4 common for the formation of $AlPO_4$ secondary phase, which exhibits a strong increase after annealing with a proportion of ~ 20 % in the layer, matching previous observations from X-ray diffractograms (**Fig. 3.3.11 (a)**). A crystalline phase of $AlPO_4$ is a common result of lithium loss upon annealing and may inhibit the intercalation of Al-dopant in the LATP lattice.[2] The here observed ^{27}Al chemical shift at $\delta \approx$ 40 ppm is believed to correlate to an amorphous configuration of $AlPO_4$.[5] Finally the chemical shift is fit with Gaussian contributions and the area underneath the curve for the octahedral AlO_6 environment shows as small increase as a result of the annealing, hence supporting the conclusion from the ^{7}Li spectra to intercalate more active charge carriers in the lattice in the presence of elevated temperatures.

In **Fig. 3.3.14** the previous overall dominating homogeneous distribution of elements of as-deposited layers in **(a)** changed for annealed layers in **(b)** significantly. EELS spectra for the AD sample support the assignment of particles to titania previously made by XRD and Raman analysis in **Fig. 3.3.11**. The

rearrangement in elemental distribution upon annealing becomes evident in **Fig. 3.3.14 (b)**, showing a separation between particles and their surrounding intergranular matrix. Different mechanisms appear to dominate the redistribution. First the Al-rich areas do not necessarily correlate with the Li-, P- and O-content, but appear to be proportionate with the Ti intensities for the majority of the observable area. A clear enrichment of Li outside the crystalline particles and a respectively high concentration of Ti and Al inside the particles can be assigned to the sufficient intercalation of Al-dopant inside the NASICON lattice. No further Li-uptake from the surrounding matrix was favorable under elevated temperatures, which ensured its presence at the intergranular domains.

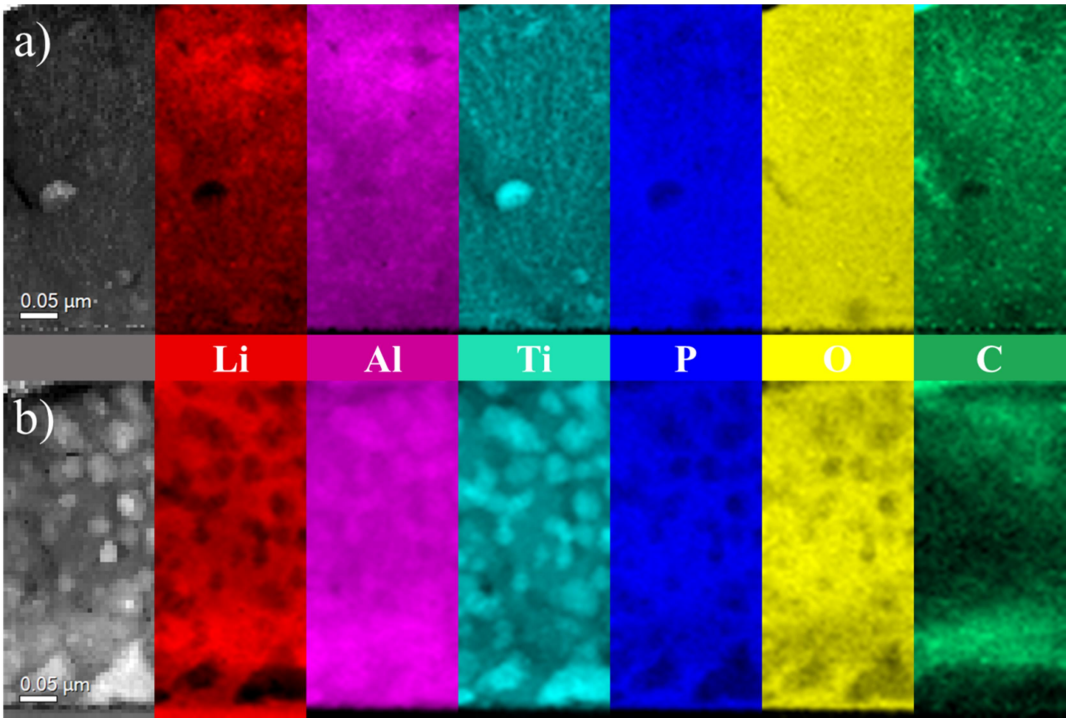

Fig. 3.3.14: STEM dark field images of the thin films a) AD and b) A, with the corresponding EELS elemental maps for Li, Al, Ti, P, O and C.

Consequently **Fig. 3.3.12 (b)** and **3.3.14 (b)** conclude the grains to primarily consist of LATP in a crystalline phase, with smaller amounts of only LTP possible and an intergranular glassy phase present, enriched in Li, P and O. The compositional character of the amorphous matrix has been previously investigated in bulk materials, assuming excess in phosphorus to lead to the formation of Li_3PO_4 and P_2O_5, or even $LiTiPO_5$, acting as a kind of sintering aid, hence improving densification and the contact area between domains of different orientation.[59,60] With the clear signal of Al also in the glassy phase, even amorphous $AlPO_4$ may be

partly present.[5] The appearance of glassy phases around crystallites has been reported already early on with the first studies on the replacement of Ti^{4+} with trivalent M^{3+} cations in the $Li_{1+x}M_xTi_{2-x}(PO_4)_3$ matrix by *Aono et al.*, demonstrating the likelihood of cation replacement depending on how closely related the cationic radii are.[2,61] The more different the cation size, the less likely the full replacement of tetravalent by trivalent cations, hence a secondary phase segregates near the grain boundary of surplus elements, leading to a better densification of the material and an improved ionic conductivity. This mechanism is frequently observed in bulk materials, but has not been reported to this extend in thin films.

3.3.2.4 Ionic transport mechanisms

To further examine the effect of stoichiometry, structure and microstructure on the overall ionic conductivity and feasibility of the LATP thin films deposited by PLD as solid electrolyte, **Fig. 3.3.15** shows the Nyquist plot **(a)** collected in-plane for a layer as-deposited and annealed, with the corresponding Arrhenius plot for in-plane and across-plane conductivity measurements in **(b)**. The inserts in **(a)** show the equivalent circuit (top insert, see **Section 2.5.1.2** and **Section 3.3.1.4** for detailed explanation) as a model to the fitting procedure and the corresponding measurement setup (central insert below, see **Fig. 2.5.2 (b)** for further description).

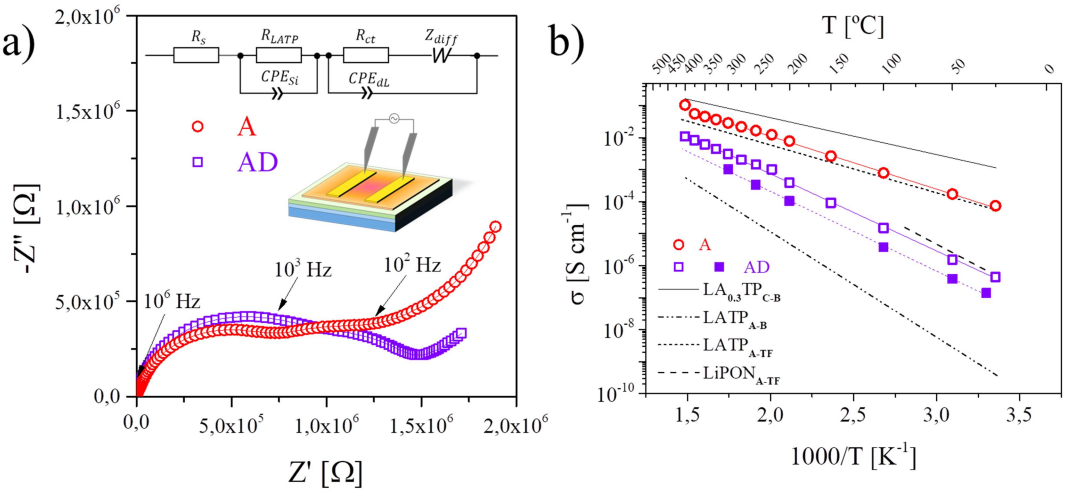

Fig. 3.3.15: Data (symbols) and fitting (lines) of representative Nyquist plots are shown in (a) with the schematic in-plane measurement setup (center) and equivalent circuit as inset (top) for the as-deposited sample (measured at 400 ºC) and the annealed sample (measured at 150ºC) in air. The resulting Arrhenius plot of the overall conductivities of the AD and A thin films are compared for in-plane (empty symbols) and cross-plane (filled symbols) in (b) to a polycrystalline (C), bulk (B) sample of $LA_{0.3}TP_{C-B}$ (x = 0.3)[61] including overall

grain and grain boundary contributions, an amorphous bulk sample $LATP_{A-B}$[10] and a thin film (TF) of amorphous character produced by RF magnetron sputtering $LATP_{A-TF}$.[40] Additional reference is made to $LiPON_{A-TF}$ amorphous thin films deposited by RF sputtering.[62]

The profile of the Nyquist plots collected before and after annealing in **Fig. 3.3.15 (a)** has been reported previously in connection with amorphous materials of similar stoichiometry to LATP, with stronger similarity to $Li_2O - Al_2O_3 - TiO_2 - P_2O_5$ glass after annealing.[10] Hence, the equivalent circuit indicates with the first R-CPE element the resistance of the LATP crystalline phase and its grain boundaries, whereas the second contribution in series, the so-called Randles circuit usually is attributed to diffusive processes at ion-blocking domains,[63] which appears to be mainly present for Si_3N_4 (see **Fig. 3.3.5 (a-c)**). Nevertheless, the first arc is attributed to LATP and the corresponding ionic conductivity σ calculated as described in **Eq. 2.5.3**. The Arrhenius plot shown in **Fig. 3.3.15 (b)** demonstrates the annealing to greatly enhance the overall ionic conductivity in-plane from as-deposited thin films. Li-ion conductivities of as-deposited layers around room temperature range between 10^{-7} and 10^{-6} S cm^{-1}, for cross-plane and in-plane measurements respectively, while annealed LATP films present an increase of orders in magnitude, reaching values of 10^{-4} S cm^{-1} in-plane under ambient.

In a preliminary study lined out in **Section 3.3.1** it was possible to evaluate this effect on the ionic conduction to be the strongest for samples deposited at 80 mT, as shown in the Arrhenius plot in **Fig. 3.3.7**. Concerning all thin films deposited, the activation energy E_A calculated from the Arrhenius equation **Eq. 3.2.1** for the Li-ion hopping mechanisms greatly improves upon annealing, from a charge transfer believed to be dominated by the grain boundary with 0.52 eV in polycrystalline AD samples, to values approaching characteristic activation energies for bulk LATP of 0.37 eV in-plane for annealed layers.[26] To compare with ionic conductivities of similar physical vapour deposition techniques previously tried on LATP, reference is made in **Fig. 3.3.15 (b)** to a study on amorphous layers of Li-Al-Ti-P-O deposited through RF magnetron sputtering by *Chen et al.*[40] Values for E_A around 0.32 eV and ionic conductivities about 10^{-4} S cm^{-1} were obtained across-plane at 25 ºC, being comparable to the in-plane ionic conduction mechanisms lined out in this work.

The performance of annealed LATP layers when measured across-plane was difficult to evaluate so far (see the comparison of EIS data for as-deposited layers and annealed layers in **Fig. 3.3.16)**. Whilst the electrolyte contribution at high frequencies for cross-plane EIS measurements of as-deposited LATP thin films is clearly resolved in the Nyquist plot (**Fig. 3.3.16 (a))**, the impedance spectra of the annealed layers presents a major contribution from the ion blocking electrodes. This large contribution hides the one from the solid electrolyte, inducing a large error in the fitting. Therefore, it is not possible to obtain the conductivity values for annealed samples. Despite this, it is important to remark that the Nyquist plot of the annealed thin film (**Fig. 3.3.16 (b)** at room temperature) does not show short circuits and hence there is no indication for electronic transport between the metallic contacts, i.e. this confirms that the LATP layer acts as an electrolyte.

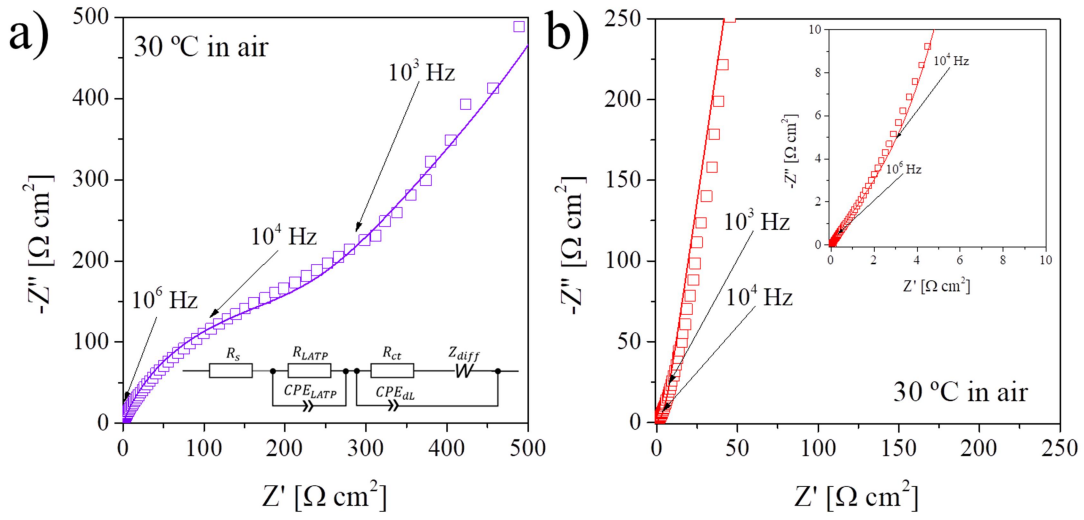

Figure 3.3.16: Cross-plane EIS measurements for as-deposited (a) and annealed (b) LATP thin films. Squares indicate the data points collected at different frequencies, lines indicate the corresponding fit with equivalent circuits (see inset in (a)).

Nonetheless, the improvement from glassy bulk samples to amorphous thin films is enormous comparing their ionic conductivities (σ_B ~ 10^{-9} S cm^{-1} and σ_{TF} ~ 10^{-4} S cm^{-1}) at room temperature in **Fig. 3.3.15 (b)**. Partial crystallization of the LATP bulk up to 850 °C provides comparable results as the partially crystalline LATP thin films presented in this work, with in-plane activation energies of 0.33 eV, excellent ionic in-plane conductivities of ~ 10^{-4} S cm^{-1} for annealed layers and comparable ASR to LiPON for as-deposited thin films with thicknesses around 500 nm, all together being considered appropriate properties for feasible solid electrolytes in literature.[10,27,29,64]

3.4 Conclusions

Solid-state synthesis of $Li_{1+x}Al_xTi_{2-x}(PO_4)_3$ powders has been realized for different Al-dopant concentrations (x) of 0.2, 0.25 and 0.5. For the fabrication of first pellets, the LATP composition with the maximum acceptable Al amount of x = 0.5 was chosen. Material properties of sintered 1" pellets of x ~ 0.5 were optimized, reaching values of ionic conductivities at room temperature of $1 \cdot 10^{-4}$ S cm^{-1} and activation energies of 0.31 eV, demonstrating good mass transport properties in comparison to literature.[2,8,9,25] For the calcination and sintering of the 3" target for laser ablation, the process was up scaled to larger badges. Hence the amount of secondary phases, especially the ion blocking $AlPO_4$, was much higher and therefore inhibited the grain growth and material densification. Mass transport mechanisms are disturbed and a comparable target of 1" exhibited low ionic conductivities of ~$2 \cdot 10^{-9}$ S cm^{-1} estimated at room temperature and high activation energies of 0.57 eV. Nonetheless the target exhibited a suitable density and phase purity for the application in laser ablation and first thin films of LATP were deposited by large-area PLD, with the focus on optimizing deposition parameters and balancing disadvantageous secondary phases evolving from the target.

LA-PLD has been demonstrated to be a well suited technique to successfully deposit and engineer a dense thin film of LATP as solid electrolyte with application in all-solid state lithium-ion batteries of industrial extent. As part of the kinetics in the PLD it greatly supports the precise stoichiometric control and the suppression of secondary phases coming from the target (such as $AlPO_4$) due to more backscattering events of lighter elements (such as Al and P), if deposition parameters are customized accordingly. A dense and homogeneous thin film is achieved after optimization of the oxygen partial pressure in **Section 3.3.1** for the range of 20 – 200 mT and substrate temperatures of 700 ºC. As a result, the composition, structure and microstructure, as well as the electrochemical properties could be improved. As-deposited thin films, against all expectations from EDS elemental studies and structural analysis by XRD, could reach good ionic conductivities at room temperature of ~10^{-6} S cm^{-1} with a relatively high activation energy of 0.58 eV. In a broader evaluation of desired thin film properties of the LATP solid electrolyte, optimum overall performance was achieved with depositions at 80 mT, consisting of a cationic ratio close to the desired optimum

stoichiometry with x = 0.5, reduced secondary phases and a homogeneous microstructure. Ionic conductivities at room temperature for as-deposited samples of LATP are generally in the range of 10^{-7} to 10^{-6} S cm^{-1}, which is comparable to current state-of-the-art thin film electrolytes (i.e. LiPON). According to the microstructure discussed in **Section 3.3.2**, higher values of conductivity are probably hindered by the presence of spaced grain boundaries (slightly disconnected particles). After subjecting the layers to an annealing process between 800 – 900 ºC, the ionic conductivity raised up to excellent values as high as 10^{-4} S cm^{-1} at room temperature. This enhancement is likely due to the strong advantage of lattice reformation during the annealing that resulted in an improved contact across interfacial domains of different orientations (through the formation of amorphous phases at the grain boundary). The preferred segregation of secondary phases to an intergranular matrix upon heat treatment is likely driven by the inhibited acceptance of Li and Al inside the NASICON lattice, which presented Al-contents of $0.35 \leq x \leq 0.4$ for as-deposited thin films. As result the exact compositional character of the glassy phase appears variable for different stoichiometries of the host material being reported in literature.[59,60,65] In the synthesized layers $AlPO_4$ appears partly as glassy material, likely to inhibit the ionic transport just as in its crystalline form,[5,65,66] but in addition has been reported to improve the performance for anode and cathode materials.[67,68] Therefore it is crucial in the electrochemical material performance to concentrate on the stabilization of the amorphous intergranular phase at high temperatures and to delimit the excessive segregation of aluminium outside the NASICON lattice. This is achieved especially by controlling annealing temperatures and dopant concentrations.[23,69] Overall, the deposition of highly dense and homogenous LATP layers with excellent ionic conductivity properties (as-synthesized and after annealing) demonstrates the potential of NASICON-type thin film electrolytes for future all-solid-state microbatteries.

References

(1) Lee, S.-D.; Jung, K.-N.; Kim, H.; Shin, H.-S.; Song, S.-W.; Park, M.-S.; Lee, J.-W. Composite Electrolyte for All-Solid-State Lithium Batteries: Low-Temperature Fabrication and Conductivity Enhancement. *ChemSusChem* **2017**, *10* (10), 2175–2181. https://doi.org/10.1002/cssc.201700104.

(2) Aono, H. Ionic Conductivity of Solid Electrolytes Based on Lithium Titanium Phosphate. *J. Electrochem. Soc.* **1990**, *137* (4), 1023. https://doi.org/10.1149/1.2086597.

(3) Popovici, D.; Nagai, H.; Fujishima, S.; Akedo, J. Preparation of Lithium Aluminum Titanium Phosphate Electrolytes Thick Films by Aerosol Deposition Method. *J. Am. Ceram. Soc.* **2011**, *94* (11), 3847–3850. https://doi.org/10.1111/j.1551-2916.2011.04551.x.

(4) Pascal Granger, P.; Parvulescu, V. I.; Kaliaguine, S.; Wilfrid Prellier. *Perovskites and Related Mixed Oxides: Concepts and Applications*; John Wiley & Sons: Weinheim, 2015.

(5) Key, B.; Schroeder, D. J.; Ingram, B. J.; Vaughey, J. T. Solution-Based Synthesis and Characterization of Lithium-Ion Conducting Phosphate Ceramics for Lithium Metal Batteries. *Chem. Mater.* **2012**, *24* (2), 287–293. https://doi.org/10.1021/cm202773d.

(6) Arbi, K.; Mandal, S.; Rojo, J. M.; Sanz, J.; Kumar, B.; Aono, H. Dependence of Ionic Conductivity on Composition of Fast Ionic Conductors Li1+x Ti2-x Alx (P O4)3 , $0 \leq x \leq 0.7$. A Parallel NMR and Electric Impedance Study. *Chem. Mater.* **2002**, *14* (3), 1091–1097. https://doi.org/10.1149/1.2086597.

(7) Hupfer, T.; Bucharsky, E. C.; Schell, K. G.; Hoffmann, M. J. Influence of the Secondary Phase LiTiOPO 4 on the Properties of Li1+x Alx Ti2-x (P O4)3 (x = 0; 0.3). *Solid State Ionics* **2017**, *302*, 49–53. https://doi.org/10.1016/j.ssi.2016.10.008.

(8) Schell, K. G.; Bucharsky, E. C.; Lemke, F.; Hoffmann, M. J. Effect of Calcination Conditions on Lithium Conductivity in Li1.3 Ti1.7 Al0.3 (P O4)3 Prepared by Sol-Gel Route. *Ionics (Kiel).* **2017**, *23* (4), 821–827.

(9) Yoon, Y.; Kim, J.; Park, C.; Shin, D. The Relationship of Structural and Electrochemical Properties of NASICON Structure Li1.3 Al0.3 Ti1.7 (P O4)3 Electrolytes by a Sol-Gel Method. *J. Ceram. Process. Res.* **2013**, *14* (4), 563–566.

(10) Soman, S.; Iwai, Y.; Kawamura, J.; Kulkarni, A. Crystalline Phase Content and Ionic Conductivity Correlation in LATP Glass-Ceramic. *J. Solid State Electrochem.* **2012**, *16*

(5), 1761–1766. https://doi.org/10.1007/s10008-011-1592-4.

(11) Pérez-Estébanez, M.; Isasi-Marín, J.; Többens, D. M.; Rivera-Calzada, A.; León, C. A Systematic Study of Nasicon-Type Li1+x Mx Ti2-x (P O4)3 (M: Cr, Al, Fe) by Neutron Diffraction and Impedance Spectroscopy. *Solid State Ionics* **2014**, *266*, 1–8. https://doi.org/10.1016/j.ssi.2014.07.018.

(12) Dashjav, E.; Tietz, F. Neutron Diffraction Analysis of NASICON-Type Li1+x Alx Ti2-x P3 O12. *Zeitschrift für Anorg. und Allg. Chemie* **2014**, *640* (15), 3070–3073. https://doi.org/10.1002/zaac.201400195.

(13) Sigma-Aldrich. Lithium carbonate [Material Safety Data Sheet] https://www.sigmaaldrich.com/MSDS/MSDS/DisplayMSDSPage.do?country=DE&language=EN-generic&productNumber=431559&brand=ALDRICH&PageToGoToURL=https%3A%2F%2Fwww.sigmaaldrich.com%2Fcatalog%2Fsearch%3Fterm%3DLi2CO3%26interface%3DAll%26N%3D0%26mode%3Dmatch%2520pa (accessed Sep 5, 2020).

(14) Hupfer, T.; Bucharsky, E. C.; Schell, K. G.; Senyshyn, A.; Monchak, M.; Hoffmann, M. J.; Ehrenberg, H. Evolution of Microstructure and Its Relation to Ionic Conductivity in Li1+x Alx Ti2-x (P O4)3. *Solid State Ionics* **2016**, *288*, 235–239. https://doi.org/10.1016/j.ssi.2016.01.036.

(15) Robertson, A.; Fletcher, J. G.; Skakle, J. M. S.; West, A. R. Synthesis of Li Ti P O5 and Li Ti As O5 with the α-Fe2 P O5 Structure. *J. Solid State Chem.* **1994**, *109* (1), 53–59. https://doi.org/10.1006/jssc.1994.1070.

(16) Eddahaoui, K.; Benmokhtar, S.; Manoun, B.; Belaaouad, S.; Lazor, P. Vibrational Spectra and Factor Group Analysis of M0.50 Ti O P O4 Oxyphosphates (M=Mg, Zn, Ni, Co, Fe and Cu). *Spectrochim. Acta. A. Mol. Biomol. Spectrosc.* **2012**, *99*, 81–89. https://doi.org/10.1016/j.saa.2012.08.033.

(17) Giarola, M.; Sanson, A.; Tietz, F.; Pristat, S.; Dashjav, E.; Rettenwander, D.; Redhammer, G. J.; Mariotto, G. Structure and Vibrational Dynamics of NASICON-Type Li Ti2 (P O4)3. *J. Phys. Chem. C* **2017**, *121* (7), 3697–3706.

(18) BURBA, C.; FRECH, R. Vibrational Spectroscopic Study of Lithium Intercalation into Li Ti2 (P O4)3. *Solid State Ionics* **2006**, *177* (17–18), 1489–1494. https://doi.org/10.1016/j.ssi.2006.07.015.

(19) Dashjav, E.; Ma, Q.; Xu, Q.; Tsai, C.-L.; Giarola, M.; Mariotto, G.; Tietz, F. The Influence of Water on the Electrical Conductivity of Aluminum-Substituted Lithium

Titanium Phosphates. *Solid State Ionics* **2018**, *321*, 83–90. https://doi.org/10.1016/j.ssi.2018.04.010.

(20) Ouillon, R.; Pinan-Lucarre, J.-P.; Ranson, P. Anharmonicity of Zone-Centre Optical Phonons: Raman Spectra of the Isomorphous α-Quartz, Berlinite and Gallium Phosphate in the Temperature Range 8-300 K. *J. Raman Spectrosc.* **2000**, *31* (7), 605–613. https://doi.org/10.1002/1097-4555(200007)31:7<605::AID-JRS583>3.0.CO;2-C.

(21) Cîntă Pînzaru, S.; Onac, B. P.; Pînzaru, S. C.; Onac, B. P. Raman Study of Natural Berlinite from a Geological Phosphate Deposit. *Vib. Spectrosc.* **2009**, *49* (2), 97–100. https://doi.org/10.1016/j.vibspec.2008.05.003.

(22) Butt, G.; Sammes, N.; Tompsett, G.; Smirnova, A.; Yamamoto, O. Raman Spectroscopy of Superionic Ti-Doped Li3 Fe2 (P O4)3 and Li Ni P O4 Structures. *J. Power Sources* **2004**, *134* (1), 72–79. https://doi.org/10.1016/j.jpowsour.2004.01.053.

(23) Yu, S.; Mertens, A.; Gao, X.; Gunduz, D. C.; Schierholz, R.; Benning, S.; Hausen, F.; Mertens, J.; Kungl, H.; Tempel, H.; Eichel, R.-A. Influence of Microstructure and AlPO 4 Secondary-Phase on the Ionic Conductivity of Li1.3 Al0.3 Ti1.7 (P O4)3 Solid-State Electrolyte. *Funct. Mater. Lett.* **2016**, *09* (05), 1650066. https://doi.org/10.1142/S1793604716500661.

(24) Arbi, K.; Hoelzel, M.; Kuhn, A.; García-Alvarado, F.; Sanz, J. Structural Factors That Enhance Lithium Mobility in Fast-Ion Li1+x Ti2-x Alx (P O4)3 ($0 \leq x \leq 0.4$) Conductors Investigated by Neutron Diffraction in the Temperature Range 100-500 K. *Inorg. Chem.* **2013**, *52* (16), 9290–9296. https://doi.org/10.1021/ic400577v.

(25) Mariappan, C. R.; Gellert, M.; Yada, C.; Rosciano, F.; Roling, B. Grain Boundary Resistance of Fast Lithium Ion Conductors: Comparison between a Lithium-Ion Conductive Li-Al-Ti-P-O-Type Glass Ceramic and a Li1.5 Al0.5 Ge1.5 P3 O12 Ceramic. *Electrochem. commun.* **2012**, *14* (1), 25–28.

(26) Breuer, S.; Prutsch, D.; Ma, Q.; Epp, V.; Preishuber-Pflügl, F.; Tietz, F.; Wilkening, M. Separating Bulk from Grain Boundary Li Ion Conductivity in the Sol-Gel Prepared Solid Electrolyte Li1.5 Al0.5 Ti1.5 (P O4)3. *J. Mater. Chem. A* **2015**, *3* (42), 21343–21350.

(27) Sun, C.; Liu, J.; Gong, Y.; Wilkinson, D. P.; Zhang, J. Recent Advances in All-Solid-State Rechargeable Lithium Batteries. *Nano Energy* **2017**, *33*, 363–386. https://doi.org/10.1016/j.nanoen.2017.01.028.

(28) Liang, X.; Tan, F.; Wei, F.; Du, J. Research Progress of All Solid-State Thin Film Lithium Battery. *IOP Conf. Ser. Earth Environ. Sci.* **2019**, *218* (1), 12138.

https://doi.org/10.1088/1755-1315/218/1/012138.

(29) Jiang, Z.; Han, Q.; Wang, S.; Wang, H. Reducing the Interfacial Resistance in All-Solid-State Lithium Batteries Based on Oxide Ceramic Electrolytes. *ChemElectroChem* **2019**, *6* (12), 2970–2983. https://doi.org/10.1002/celc.201801898.

(30) Nazri, G. A.; Pistoia, G. *Lithium Batteries: Science and Technology*; Springer US, 2008.

(31) Li, D.; Ma, Z.; Xu, J.; Li, Y.; Xie, K. High Temperature Property of All-Solid-State Thin Film Lithium Battery Using LiPON Electrolyte. *Mater. Lett.* **2014**, *134*, 237–239. https://doi.org/10.1016/j.matlet.2014.07.092.

(32) Bai, L.; Xue, W.; Li, Y. Y.; Liu, X.; Li, Y. Y.; Sun, J. The Interfacial Behaviours of All-Solid-State Lithium Ion Batteries. *Ceram. Int.* **2018**, *44* (7), 7319–7328. https://doi.org/10.1016/j.ceramint.2018.01.190.

(33) Maier, J. Size Effects on Mass Transport and Storage in Lithium Batteries. *J. Power Sources* **2007**, *174* (2), 569–574. https://doi.org/10.1016/j.jpowsour.2007.06.246.

(34) Schaaf, P. *Laser Processing of Materials: Fundamentals, Applications and Developments*; Springer series in materials science, 0933-033X; Springer: Berlin and London, 2010; Vol. 139.

(35) Greer, J. A.; Tabat, M. D. Large-Area Pulsed Laser Deposition: Techniques and Applications. *J. Vac. Sci. Technol. A Vacuum, Surfaces, Film.* **1995**, *13* (3), 1175–1181. https://doi.org/10.1116/1.579857.

(36) Xia, H.; Wang, H. L.; Xiao, W.; Lai, M. O.; Lu, L. Thin Film Li Electrolytes for All-Solid-State Micro-Batteries. *Int. J. Surf. Sci. Eng.* **2009**, *3* (1–2), 23–43.

(37) Julien, C. M.; Mauger, A. Pulsed Laser Deposited Films for Microbatteries. *Coatings* **2019**, *9* (6), 386. https://doi.org/10.3390/coatings9060386.

(38) Eason, R. *Pulsed Laser Deposition of Thin Films: Applications-Led Growth of Functional Materials*; John Wiley & Sons, 2007.

(39) Wu, X. M.; Li, X. H.; Wang, S. W.; Wang, Z.; Zhang, Y. H.; Xu, M. F.; He, Z. Q. Preparation and Characterization of Lithium-Ion-Conductive Li1.3 Al0.3 Ti1.7 (P O4)3 Thin Films by the Solution Deposition. *Thin Solid Films* **2003**, *425* (1–2), 103–107. https://doi.org/10.1016/S0040-6090(02)01094-5.

(40) Chen, H.; Tao, H.; Zhao, X.; Wu, Q. Fabrication and Ionic Conductivity of Amorphous Li-Al-Ti-P-O Thin Film. *J. Non. Cryst. Solids* **2011**, *357* (16–17), 3267–3271. https://doi.org/10.1016/j.jnoncrysol.2011.05.023.

(41) Tan, G.; Wu, F.; Li, L.; Liu, Y.; Chen, R. Magnetron Sputtering Preparation of Nitrogen-Incorporated Lithium--Aluminum--Titanium Phosphate Based Thin Film Electrolytes for All-Solid-State Lithium Ion Batteries. *J. Phys. Chem. C* **2012**, *116* (5), 3817–3826.

(42) Liang, Y.; Peng, C.; Kamiike, Y.; Kuroda, K.; Okido, M. Gallium Doped NASICON Type Li Ti2 (P O4)3 Thin-Film Grown on Graphite Anode as Solid Electrolyte for All Solid State Lithium Batteries. *J. Alloys Compd.* **2019**, *775*, 1147–1155.

(43) Hofmann, P.; Walther, F.; Rohnke, M.; Sann, J.; Zeier, W. G.; Janek, J. LATP and LiCoPO4 Thin Film Preparation – Illustrating Interfacial Issues on the Way to All-Phosphate SSBs. *Solid State Ionics* **2019**, *342* (August). https://doi.org/10.1016/j.ssi.2019.115054.

(44) Amoruso, S. *Plume Characterization in Pulsed Laser Deposition of Metal Oxide Thin Films*; Elsevier Inc., 2018. https://doi.org/10.1016/b978-0-12-811166-6.00006-6.

(45) Korotcenkov, G. *Metal Oxide-Based Thin Film Structures: Formation, Characterization and Application of Interface-Based Phenomena*; Elsevier, 2017.

(46) Arbi, K.; Bucheli, W.; Jiménez, R.; Sanz, J. High Lithium Ion Conducting Solid Electrolytes Based on NASICON Li1+x Alx M2-x (P O4)3 Materials (M= Ti, Ge and 0≤ X≤ 0.5). *J. Eur. Ceram. Soc.* **2015**, *35* (5), 1477–1484.

(47) Simmen, F.; Lippert, T.; Novák, P.; Neuenschwander, B.; Döbeli, M.; Mallepell, M.; Wokaun, A. The Influence of Lithium Excess in the Target on the Properties and Compositions of Li1+x Mn2 O4-δ Thin Films Prepared by PLD. *Appl. Phys. A* **2008**, *93* (3), 711–716. https://doi.org/10.1007/s00339-008-4701-1.

(48) Sauvage, F.; Baudrin, E.; Morcrette, M.; Tarascon, J.-M. Pulsed Laser Deposition and Electrochemical Properties of Li Fe P O4 Thin Films. *Electrochem. solid-state Lett.* **2004**, *7* (1), A15--A18.

(49) Mariappan, C. R.; Yada, C.; Rosciano, F.; Roling, B. Correlation between Micro-Structural Properties and Ionic Conductivity of Li1.5 Al0.5 Ge1.5 (P O4)3 Ceramics. *J. Power Sources* **2011**, *196* (15), 6456–6464. https://doi.org/10.1016/j.jpowsour.2011.03.065.

(50) Barsoukov, E.; Macdonald, J. R. *Impedance Spectroscopy-Theory , Experiment , And*, 2nd ed.; John Wiley & Sons: Hoboken, 2005; Vol. 125.

(51) Iriyama, Y.; Yada, C.; Abe, T.; Ogumi, Z.; Kikuchi, K. A New Kind of All-Solid-State Thin-Film-Type Lithium-Ion Battery Developed by Applying a DC High Voltage. *Electrochem. commun.* **2006**, *8* (8), 1287–1291.

https://doi.org/10.1016/j.elecom.2006.03.003.

(52) Lakshmi-Narayana, A.; Hussain, O. M.; Mauger, A.; Julien, C. Transport Properties of Nanostructured Li2 Ti O3 Anode Material Synthesized by Hydrothermal Method. *Sci* **2019**, *1* (39), 1–16.

(53) Waetzig, K.; Rost, A.; Langklotz, U.; Matthey, B.; Schilm, J. An Explanation of the Microcrack Formation in Li1.3Al0.3Ti1.7(PO4)3 Ceramics. *J. Eur. Ceram. Soc.* **2016**, *36* (8), 1995–2001. https://doi.org/10.1016/j.jeurceramsoc.2016.02.042.

(54) Liu, Z.; Venkatachalam, S.; Kirchhain, H.; van Wüllen, L. Study of the Glass-to-Crystal Transformation of the NASICON-Type Solid Electrolyte Li1 + XAlxGe2 − x(PO4)3. *Solid State Ionics* **2016**, *295*, 32–40. https://doi.org/10.1016/j.ssi.2016.07.006.

(55) Arbi, K.; Hoelzel, M.; Kuhn, A.; García-Alvarado, F.; Sanz, J. Local Structure and Lithium Mobility in Intercalated Li3 Alx Ti2-x (P O4)3 NASICON Type Materials: A Combined Neutron Diffraction and NMR Study. *Phys. Chem. Chem. Phys.* **2014**, *16* (34), 18397–18405. https://doi.org/10.1039/c4cp02938k.

(56) Kwatek, K.; Slubowska, W.; Trebosc, J.; Lafon, O.; Nowinski, J. L. Structural and Electrical Properties of Ceramic Li-Ion Condcutors Based on Li 1.3 Al 0.3 Ti 1.7 (PO4)3- LiF. *J. Eur. Ceram. Soc.* **2020**, *40* (1), 85–93.

(57) Edén, M. Annual Reports on NMR Spectroscopy - 27 Al NMR Studies of Aluminosilicate Glasses. **2015**, *86*, 237–331. https://doi.org/10.1016/bs.arnmr.2015.04.004.

(58) Lee, S. K.; Lee, S. B.; Park, S. Y.; Yi, Y. S.; Ahn, C. W. Structure of Amorphous Aluminum Oxide Structure of Amorphous Aluminum Oxide. *Phys. Rev. Lett.* **2009**, 3–7. https://doi.org/10.1103/PhysRevLett.103.095501.

(59) Forsyth, M.; Wong, S.; Nairn, K. M.; Best, A. S.; Newman, P. J.; MacFarlane, D. R. NMR Studies of Modified Nasicon-like, Lithium Conducting Solid Electrolytes. *Solid State Ionics* **1999**, *124* (3–4), 213–219. https://doi.org/10.1016/S0167-2738(99)00213-1.

(60) Robertson, A. D.; West, A. R.; Ritchie, A. G. Review of Crystalline Lithium-Ion Conductors Suitable for High Temperature Battery Applications. *Solid State Ionics* **1997**, *104* (1–2), 1–11.

(61) Aono, H.; Sugimoto, E.; Sadaoka, Y.; Imanaka, N.; Adachi, G. ya. Electrical Properties and Crystal Structure of Solid Electrolyte Based on Lithium Hafnium Phosphate LiHf2(PO4)3. *Solid State Ionics* **1993**, *62* (3–4), 309–316. https://doi.org/10.1016/0167-2738(93)90387-I.

(62) Van-jodin, L. Le; Ducroquet, F.; Sabary, F.; Chevalier, I. Dielectric Properties , Conductivity and Li+ Ion Motion in LiPON Thin Films. *Solid State Ionics* **2013**, *253*, 151–156. https://doi.org/10.1016/j.ssi.2013.09.031.

(63) Thomas, M. G. S. R. AC Impedance Analysis of Polycrystalline Insertion Electrodes: Application to Li1−x Co O2. *J. Electrochem. Soc.* **1985**, *132* (7), 1521. https://doi.org/10.1149/1.2114158.

(64) Pasta, M.; Armstrong, D.; Brown, Z. L.; Bu, J.; Castell, M. R.; Chen, P.; Cocks, A.; Corr, S. A.; Gussen, E. J.; Darnbrough, E.; Deshpande, V.; Doerrer, C.; Dyer, M. S.; El-Shinawi, H.; Fleck, N.; Grant, P.; Gregory, G. L.; Grovenor, C.; Hardwick, L. J.; Irvine, J. T. S.; Lee, H. J.; Li, G.; Liberti, E.; Mcclelland, I.; Monroe, C.; Nellist, P. D.; Shearing, P. R.; Shoko, E.; Song, W.; Jolly, D. S.; Thomas, C. I.; Turrell, S. J.; Vestli, M.; Williams, C. K.; Zhou, Y.; Bruce, P. G. 2020 Roadmap on Solid-State Batteries. *J. Phys. Energy* **2020**, *2* (3).

(65) Jiménez, R.; Del Campo, A.; Calzada, M. L.; Sanz, J.; Kobylianska, S. D.; Solopan, S. O.; Belous, A. G. Lithium La0.57 Li0.33 TiO3 Perovskite and Li1.3 Al0.3 Ti1.7 (P O4)3 Li-NASICON Supported Thick Films Electrolytes Prepared by Tape Casting Method. *J. Electrochem. Soc.* **2016**, *163* (8), A1653--A1659.

(66) Gunduz, Deniz Cihan; Schierholz, Roland; Yu, Shicheng; Tempel, Hermann; Kungl, Hans; Eichel, R.-A. Combined Quantitative Microscopy on the Microstructure and Phase Evolution of Li1.3 Al0.3 Ti1.7 (PO4)3 Ceramics. *J. Adv. Ceram.* **2020**, *9* (2), 149–161.

(67) Hu, B.; Wang, X.; Shu, H.; Yang, X.; Liu, L.; Song, Y.; Wei, Q.; Hu, H.; Wu, H.; Jiang, L.; Liu, X. Improved Electrochemical Properties of BiF 3 / C Cathode via Adding Amorphous AlPO 4 for Lithium-Ion Batteries. **2013**, *102*, 8–18. https://doi.org/10.1016/j.electacta.2013.03.168.

(68) Venkateswara Rao, C.; Soler, J.; Katiyar, R.; Shojan, J.; West, W. C.; Katiyar, R. S. Investigations on Electrochemical Behavior and Structural Stability of Li1.2 Mn0.54 Ni0.13 Co0.13 O2 Lithium-Ion Cathodes via in-Situ and Ex-Situ Raman Spectroscopy. *J. Phys. Chem. C* **2014**, *118* (26), 14133–14141. https://doi.org/10.1021/jp501777v.

(69) Liu, Z.; Venkatachalam, S.; Kirchhain, H.; van Wüllen, L. Study of the Glass-to-Crystal Transformation of the NASICON-Type Solid Electrolyte Li1 + XAlxGe2 − x(PO4)3. *Solid State Ionics* **2016**, *295*, 32–40. https://doi.org/10.1016/j.ssi.2016.07.006.

4. Spinel thin film electrodes by PLD

4.1 Introduction

The selection of electrode materials is crucial when aiming for high specific energies, capacities and long term stability in all-solid-state battery devices. The development of lithium transition metal oxides as suitable Li intercalation electrodes has brought a huge advantage to the fabrication and applicability of lithium-ion batteries in terms of safety, specific energy and power, life cycle stability, cost effectiveness and environmental friendliness.[1]

The strong advantages of using spinel type intercalation materials as electrodes in lithium ion batteries have been pointed out in **Section 1.4**, and can be summarized in their high rate capability and long cycle lifetime, with good capacity retention reproducing high specific capacities, as well as their high natural abundance leading to low costs and an acceptable environmental impact.[2,3] On the other hand, while a main concern for the application of intercalation materials in all-solid-state batteries especially in thin film form counts the volumetric expansion upon lithium (de-) intercalation in the lattice, $LiMn_2O_4$ and $Li_4Ti_5O_{12}$ are known for their low lattice volume changes resulting in very low (less than 5 %) or "zero-strain" effects during battery operation.[4–6] Further, they allow the use of a broader range of electrolyte materials, including those which are not stable towards metallic lithium, as it is the case for LATP with the reduction of Ti^{4+} against Li metal.[7]

Especially, the application of thin films has opened new possibilities in terms of material stability and cycle life, as the introduction of nano-shapes in the microstructure can greatly improve certain obstacles in ionic mass transport phenomena.[4,5,8,9] The fabrication of such nanostructures in the form of thin films usually involve high vacuum deposition techniques like sputtering, Atomic Layer Deposition (ALD) or PLD.[10] As an emerging technique in the fabrication of Li-ion thin film microbatteries,[11] pulsed laser deposition can be applied in a multi-layer approach of alternating layers in order to compensate for certain material losses of volatile lithium.[12,13]

Following this strategy, the next sections deal with nano-crystalline thin films deposited by a multi-layer approach in a LA-PLD under the use of alternating targets of LMO or LTO with Li_2O, whereas the latter serves for the compensation of lithium. The structural and microstructural evolution upon excess lithium is

studied for both and the resulting electrochemical properties have been evaluated in liquid electrolyte solutions with aqueous and non-aqueous systems. As multi-layer LA-PLD thin films of LMO have already shown exceptionally good performances in aqueous solutions, demonstrated in previous works from the group for the 4 V region[12,13] versus lithium, comparable LMO layers are studied in aprotic electrolyte solutions for the intercalation of two Li^+ around the 3 V region (work within **Section 4.2**). Based on the experience with the cathodic thin films, LTO layers as anode materials are deposited for the first time by multi-layer LA-PLD in **Section 4.3**. Their structural, microstructural, optical and electrochemical properties are studied upon increasing Li_2O addition in the material composition.

4.2 Development of $LiMn_2O_4$ thin film cathodes

A common metal-oxide operating as a cathode in lithium-ion batteries is $LiMn_2O_4$ in the cubic crystallographic system (spinel). Due to its low cost, high safety and a good cycling stability, it has been studied in various applications for bulk or thin film batteries being a promising candidate. This is due to its high specific capacity of 595 mAh cm^{-3} (ρ = 4.02 g cm^{-3}) under exchange of one electron intercalating Li^+ when changing the oxidation number of Mn^{4+} to a mixed-valent state of $Mn^{3+/4+}$ (4 V plateau). Moreover, LMO can theoretically reach values of 1240 mAh cm^{-3} (ρ = 4.19 g cm^{-3}) when operating at lower voltages ~3V vs. lithium (3 V plateau) under the exchange of an additional electron for transforming the manganese oxidation state fully to +III.[5] Mn-dissolution and an unfavorable lattice expansion (greater than 5 %) due to the Jahn-Teller distortion onset, occurring when more than half of the manganese is transformed to Mn^{3+}, have been limiting the exploration of the 3 V plateau (2 – 3.5 V vs. Li/Li^+) beyond the recommended voltage range of the 4 V plateau (3.5 - 4.5 V vs. Li/Li^+) for LMO in battery applications.[14] As previous studies reported on the increased stability of nano-shaped materials in terms of cycling stability,[4] is has been a controversial discussion if the so-called overdischarge at the 3 V plateau of LMO is acceptable for nano-sized samples or not. Whereas *Kosilov et al.*[14] predicted better stabilities in micro-sized materials, *Put et al.*[5] on the contrary produced RF-sputtered LMO layers of 25 nm thickness and could demonstrate good cycling stability of 80 % capacity retention at 50 C for high theoretical capacities of 1240 mAh cm^{-3}.

In the following, a refinement of alternating ablation steps and its influence in phase purity of the resulting LMO multi-layer is conducted in **Section. 4.2.1**, as well as the thickness dependence of structure and microstructure of the thin films evaluated. Further electrochemical measurements in aqueous electrolyte are conducted in **Section 4.2.2** and investigated upon the material changes previously introduced by thickness variations. A final layer deposited under optimized conditions in the PLD of LMO and Li_2O multi-layers is studied in the full electrochemical stability window of LMO under exploration of the 3 V plateau versus lithium in a non-aqueous electrolyte in **Section 4.2.3**.

4.2.1 Deposition of $LiMn_2O_4$ multi-layer thin films

In this section, the group's state-of-the-art $LiMn_2O_4$ deposition procedures have been further optimized through multi-layering by improving the composition and microstructure of LMO films. Also, the impact of the film thickness on its quality, which is crucial for the development of final devices, has been studied.

In the group's seminal work, *Fehse et al.*[12] conducted preliminary studies on LMO multi-layered thin films deposited by PLD under alternation of targets every 1000 counts to reach an ablation ratio between LMO and Li_2O of 2:1 respectively. Although the multi-layer approach was successfully proved, secondary phases including manganese oxide were present in the final films. In this work, the multi-layering process has been refined with less pulses on each target for each ablation cycle, resulting in more alternations and more cycles in total in order to obtain a better "mixing" and the impact of the relative number of pulses between $LiMn_2O_4$ and Li_2O has been studied. More specifically, the alternation of LMO and Li_2O target ablation was done every 400 to 800 counts and the content of Li_2O increased to a pulse ratio of 4:3. A minimum of secondary phases such as Mn_3O_4 could be reached, as shown by XRD analysis in **Fig. 4.2.1 (a)**.

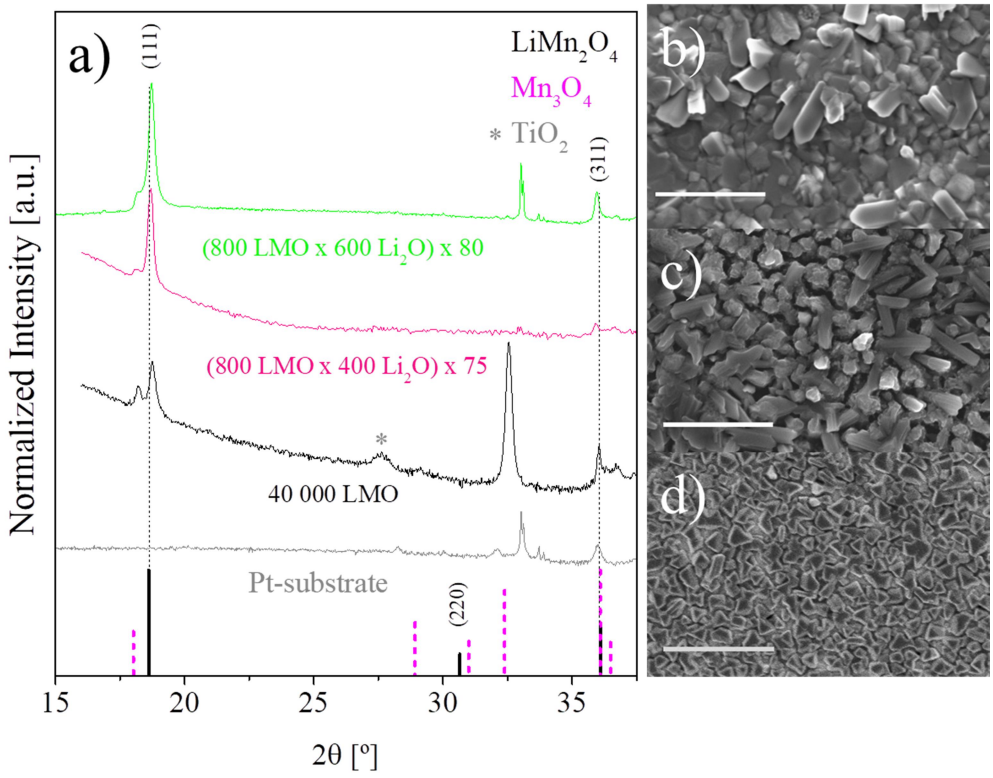

Fig. 4.2.1: X-ray diffractograms of polycrystalline LMO and Li_2O multi-layers on Pt-substrates are shown for a variety of lithium contents in (a), with the signal from the plain Pt-substrate for comparison (grey line). Laser fluence was fixed between 500 - 550 mJ cm^{-2} (spot size 0.39 cm^2). Thin film deposition conditions are indicated as (pulses on $LiMn_2O_4$ x pulses on Li_2O) x number of cycle repetitions, respectively. JCPDS reference is made to $LiMn_2O_4$ (00-035-0782), Mn_3O_4 (01-080-0382) and TiO_2 (01-088-1172). SEM images correspond to the thin films deposited in (a) with pulse ratios of (b) 4:3, (c) 2:1 and (d) 1:0. The white scale bar corresponds to 1 µm.

The diffractograms in **Fig. 4.2.1 (a)** show a clear spinel phase of LMO due to the pronounced (111) plane at 2θ~18.7°, with an increasing relative intensity for higher contents of Li_2O. A strong signal from the electrochemically inactive tetragonal phase of Mn_3O_4 is observable, which is evidenced by a defined peak or shoulder at 18.0° with (101) orientation and a strong signal at 32.5° related to the (103) crystallographic plane especially for layers without additional Li_2O. The presence of Mn_3O_4 is resulting from lithium losses during thin film deposition.[15,16] A further secondary phase indicated corresponds to TiO_2 (grey asterisk) evolving from the substrate due to the titanium adhesive layer for Pt-sputtering. The addition of higher lithium amounts leads to a strong reduction of Mn_3O_4 secondary phases and a stronger spinel peak at 18°, indicating higher phase purity and crystallinity. This observation is supported by SEM images taken for the thin films of different LMO:Li_2O ablation ratios in **Fig. 4.2.1 (b-d)**. The sole ablation of the LMO target

in **(d)** is leading to very small, separated crystallites as there is a great amount of Mn_3O_4 possibly impeding the layer densification and crystal growth. With the addition of Li_2O a strong reduction of tetragonal manganese oxide is leading to a better crystallisation and LMO spinel phase purity, but still the contact between crystallites appears to be low in **(c)** for ablation ratios of 2:1. Therefore a further increase in lithium content is favourable as demonstrated for the ablation ratio of 4:3 for LMO:Li_2O in **Fig. 4.2.1 (b)**, as the crystal growth appears advanced and the contact between separate grains improved, hence resulting in shorter lithium migration paths and possibly better electrochemical kinetics. Nonetheless, LMO thin films deposited by PLD are mostly composed of crystallites at nano-scale, and therefore resulting changes in the material properties in comparison to bulk materials are considered to be favourable in the electrochemical performance, as a result of enhanced surface-to-volume ratio, reduced diffusion path lengths, low volumetric expansion and the special status of the surface area as attraction for electrochemically active sites.[4,17,18]

As previous publications dealing with the electrochemical performance of LMO multi-layers deposited by PLD could prove their exceptionally good electrochemical performance in aqueous media,[13,16] further investigations are concentrated on the better understanding of their mass transport kinetics in relation to layer thickness and crystallization. Moreover, the capacity of a battery is directly related to the thickness of the electrodes, therefore, thick layers are ultimately pursued. Hence, LMO layers of different thicknesses deposited by multi-layer PLD in the 4:3 ablation ratio have been realized and are presented in SEM images shown in **Fig. 4.2.2**.

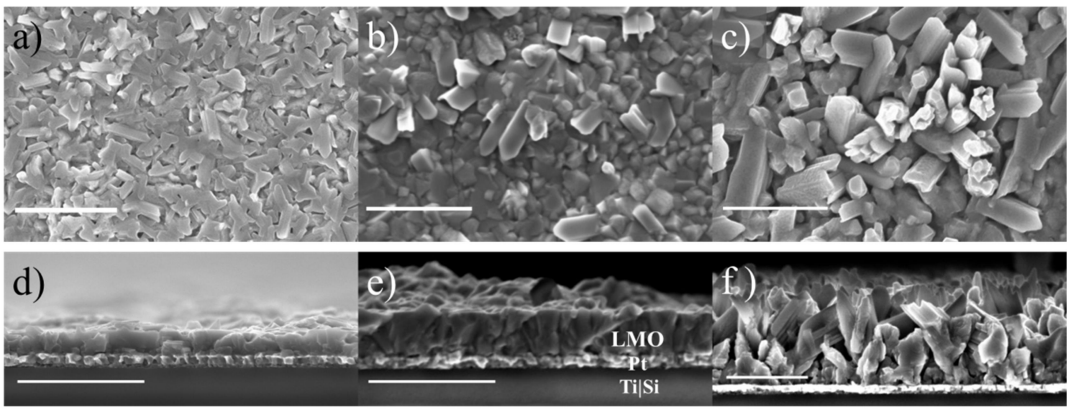

Fig. 4.2.2: SEM images of LMO thin films deposited on Pt-substrates composed of alternating LMO and Li_2O ablation cycles, for (a) 30 cycles, (b) 80 cycles and (c) 130 cycles. SEM cross-sections correspond to LMO-130 (30 cycles with 180 nm thickness) in (d), LMO-340 (80 cycles with 340 nm) in (e) and LMO-1070 (130 cycles with 1070 nm) in (f). The remaining substrate below the 80 nm sputtered Pt-layer consists of a thin titanium adhesive layer (10 nm) on $Si_3N_4|SiO_2|Si$-wafer (top to bottom) which is abbreviated as "Ti|Si". The white bar corresponds to 1 µm.

The samples present increasing crystallization upon raising thicknesses when comparing **Fig. 4.2.2 (a)** to **(c)** for LMO-180 to LMO-1070 respectively. The size of crystallites correlates to the amount of grain boundaries (obstacles in the ionic transport mechanism) as well as their shape and orientation having an impact on the layer densification. Further thin film structural dependence on the layer thickness is studied in **Fig. 4.2.3** by X-ray diffractograms and Raman spectroscopy.

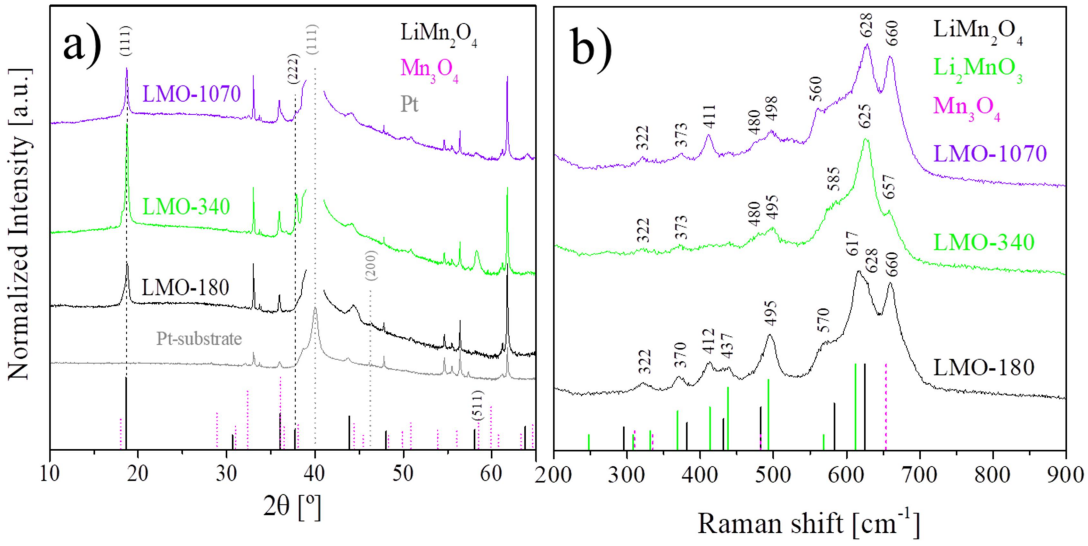

Fig. 4.2.3: Thickness dependent X-ray diffractograms in (a) and Raman spectra in (b) of LMO multi-layers deposited with180 nm, 340 nm and 1070 nm in thickness. The intensities of diffractrograms have been normalized to the peaks resolving from the substrate at 33° and 62°. Reference is made to the JCPDS data base with $LiMn_2O_4$ (00-035-0782), Mn_3O_4 (01-080-0382) and Pt (00-004-0802) for X-ray diffraction. Raman spectra are referenced to literature.[19,20]

As can be observed in **Fig. 4.2.3 (a)** the signal of the (111) plane of spinel phase LMO is the strongest for all layers, with a slight preferential orientation in (111) for LMO-340 as the well pronounced peak at 38º suggests. Again the presence of Mn_3O_4 can be evidenced, as the result of some lithium loss. This secondary phase in particular can be detected with greater certainty by Raman spectra in **Fig. 4.2.3 (b)**, as it exhibits strong Raman activity for the MnO_6 symmetric Mn-O stretching vibration associated to A_{1g} mode between 654 - 661 cm^{-1} typical for Mn_3O_4.[19–22] Further the formation of the lithium-rich, monoclinic (layered) phase Li_2MnO_3 including rock salt stoichiometry appears probable, as the activity of the vibrational modes occurring at 370, 412, 437, 495 and 617 cm^{-1} may indicate, especially for thin layers.[18,19,23,24] Due to its high similarity in X-ray diffraction patterns to spinel $LiMn_2O_4$ phase, it could not be distinguished from X-ray peaks occurring for the spinels in **Fig. 4.2.3 (a)**.[19] Li_2MnO_3 has formerly been believed to be electrochemically inactive, as all octahedral sites necessary for Li^+ ion intercalation are occupied and tetra-valent Mn cannot be further oxidized. On the contrary *Park et al.*[18] demonstrated oxygen-rich Li_2MnO_{3+y} nano-powders to be electrochemically active, *Müller et al.*[25] were able to obtain high capacities for oxygen-deficient $Li_2MnO_{3-\delta}$ and *Amalraj et al.*[23] could provide proof of reversible layered-to-spinel type transition upon electrochemical cycling below 4.5 V. Generally speaking, localized stoichiometric inhomogeneities as the result of mass transport kinetics in the PLD can not only lead to deficiencies in volatile compounds, but also create a slightly varied local stoichiometry as a result of the background gas pressure. Hence lithium-rich and lithium-poor compounds related to LMO can be present simultaneously, depending on the accurate substrate temperature and background gas pressure, substrate-to-target distance and especially the laser fluence during target ablation (see **Section 2.3** for details in the mentioned PLD parameters), all having a great influence on the final layer composition. As result, the layer of LMO-340 presents the lowest amount of secondary phases in XRD and Raman.

4.2.2 Optical characterization of LMO thin films

Optical properties have been monitored by spectroscopic ellipsometry (SE) for different thicknesses of LMO thin films and the resulting spectra were modeled using the approach presented in **Section 2.5.3.2**. Optical models consisted of four Tauc-Lorentz oscillators, representing different optical absorption bands correlated

to certain interband transitions for the O^{2-} (2p) – $Mn^{3+/4+}$ (3d) hybridized orbital. The imaginary part of the complex dielectric function ε_i in **Eq. 2.5.12 (b)** is used to directly observe the materials optical absorption upon various thicknesses in **Fig. 4.2.4**, with the second derivative of the extinction coefficient *k* as inset. The weighted sum of squared deviations for the SE model, also known as χ^2, ranges for the fitting between 0.2 – 10.3, which is acceptable for obtaining reliable results on the materials optical properties.

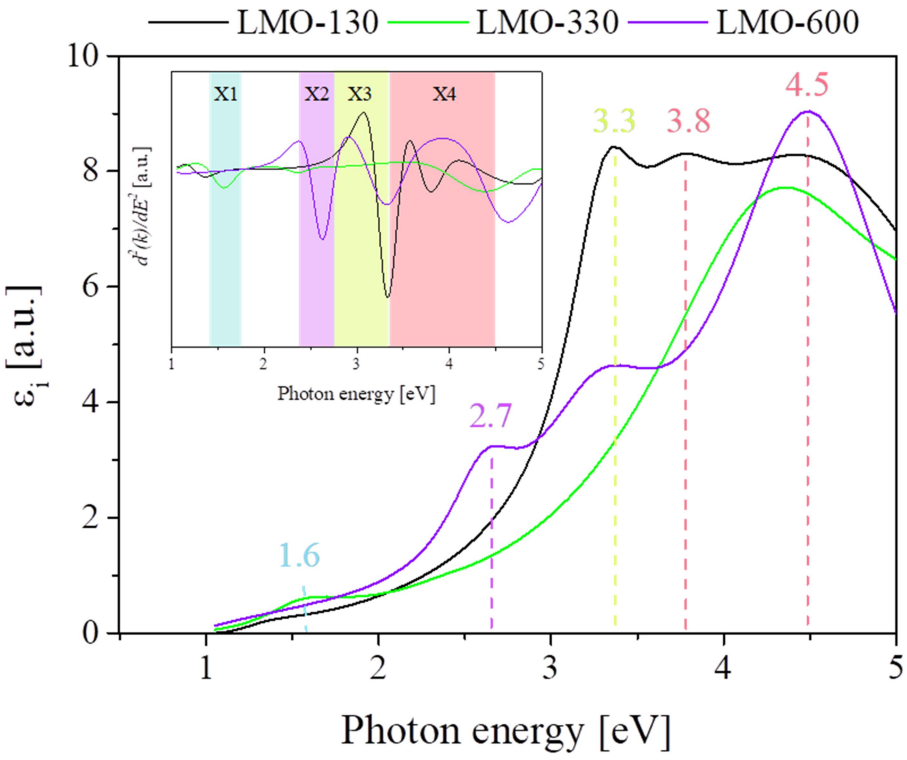

Fig. 4.2.4: Horizontally shifted traces of the imaginary (index i) part of the permittivity ε (optical absorption) over the corresponding photon energy of LMO thin films for different thicknesses of 130 nm (LMO-130), 330 nm (LMO-330) and 600 nm (LMO-600). The second derivative of the extinction coefficient *k* is plotted over the photon energy as inset. The colored areas of X1 - X4 correspond to vertical, dashed lines in ε_i indicating significant changes in the absorption bands.

The optical absorption of the spectra in **Fig. 4.2.4** can be divided into optical bands marked as X1 – X4, which have been compared to the density of states for the electronic bandstructure of LMO (compare **Section 1.4.1**). Transitions at low photon energies around 1.6 eV (X1) may be assigned to crystal-field (CF) transitions of Mn^{3+} ions, especially strong for the presence of Mn_3O_4, which further lacks absorption bands at higher photon energies and is mainly observable due to its transitions at low energies.[26] The absorption band X2 between 2.4 – 2.7 eV can be

assigned to certain charge transfer (CT) intraband transitions between t_{2g} and e_g states of octahedral Mn^{3+} (3d), as it has been observed by *Kim et al.*[26] for Mn_2O_3, but also Mn^{2+} has been reported to locate an absorption band around 2.7 eV.[27–29] The broad absorption band (X3) around 2.8 – 3.3 eV in **Fig. 4.2.4** can be attributed to the CT transitions between O^{2-}(2p) and the Mn^{4+} (e_g) of $LiMn_2O_4$.[30] As the oxidation state of stoichiometric LMO is mixed valent, the absorption bands for X4 possibly correlate to O^{2-}(2p) – Mn^{3+} (e_g) transitions, visible between 3.4 – 4.0 eV.[31,32] The last absorption band reported for X4 in **Fig. 4.2.4** around 4.5 eV can be correlated to the transitions between p(O^{2-}) and s(Mn^{3+}) reported for Mn_2O_3.[26] Therefore optical absorption spectra reveal not only the presence of the mixed-valence of the LMO thin films, additionally different environments of the Mn-O bonds associated with spinel $LiMn_2O_4$ and several manganese oxides could be observed.

In order to determine the changes in the electronic bang gap energy E_g upon increasing thicknesses, the Tauc plot[33] of $(\alpha h\nu)^{1/2}$ over the photon energy ($h\nu$) is shown in **Fig. 4.2.5**, with the absorption coefficient α and the reverse exponential of m = 2 describing indirect band transitions (smallest energy difference between occupied and unoccupied energetic states)[34] as reported for LMO by *Paulraj et al.*[35] The E_g calculated from the intercept of the linear extrapolation (dashed lines) with the x-axis at α = 0 is plotted over the layer thickness and shown as insert.

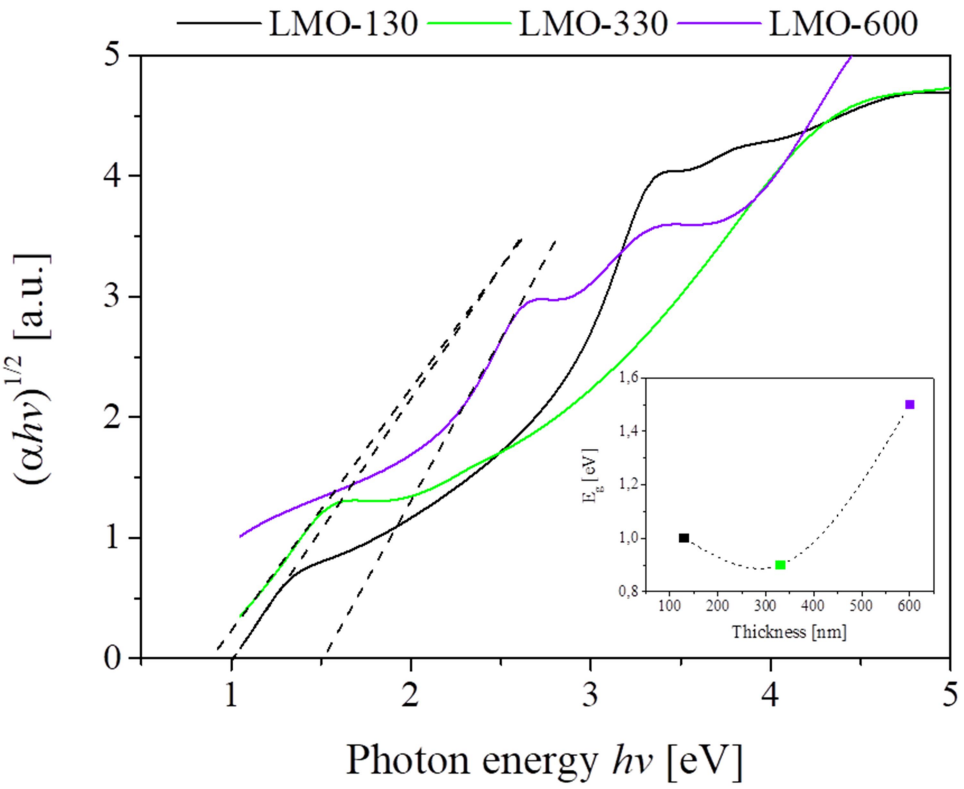

Fig. 4.2.5: Tauc plot for different thicknesses of LMO with 130 nm, 330 nm and 600 nm. The resulting band gap energies are depicted as insert as a function of the film thickness.

The indirect electronic band gaps obtained from the Tauc plot of LMO range between 0.9 – 1.5 eV, which is in good agreement to values reported by *Paulraj et al.*[35] for similar RF-sputtered thin films of LMO. As it can be observed in **Fig. 4.2.5** with increasing thickness from 130 – 600 nm, the indirect band gap overall increases, which can be attributed to a higher degree of crystallization (compare SEM images **Fig. 4.2.2**). Similar behavior has been observed when increasing the annealing temperature for RF-sputtered nano-crystalline LMO thin films and could be correlated to the re-creation of local oxygen stoichiometries incorporated in the defect crystal lattice upon annealing and the resulting crystal growth. Therefore *Paulraj et al.*[35] concludes a possible tuning of the optical band gap by microstructural features, which may have a strong impact on the functional properties of the layers as cathode materials, especially concerning their charge and mass transport kinetics. For LMO thin films deposited by multi-layer PLD a certain variation in the local oxygen stoichiometry is possible and in combination with the increasing crystal growth with thicker layers this may slightly impact the optical band gap and secondary phases. Although the answer about the origin of these changes is out of the scope of this thesis, this optical sensitivity becomes extremely

important to propose new in-situ/operando characterization methods based on optical techniques, as presented in detail in **Section 5**.

4.2.3 Reaction kinetics of multi-layer LMO in aqueous electrolyte

The electrochemical properties of LMO thin films deposited with 80 repeated cycles of alternating LMO:Li_2O targets in 4:3 ablation ratio are evaluated in an aqueous electrolyte of 1 M Li_2SO_4 against platinum as counter electrode (CE) and Ag/AgCl reference electrode (RE) introduced in 3 M KCl solution and sealed with mesoporous glass frit. **Fig. 4.2.6** presents cyclic voltammograms collected for different layer thicknesses at a fixed scan rate of 16 mV s^{-1}.

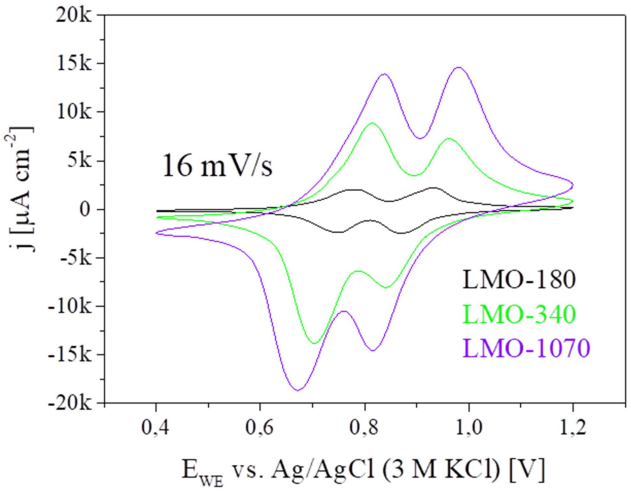

Fig. 4.2.6: Cyclic voltammetry of quasi-triangular voltage steps with a scan rate of 16 mV s^{-1} for LMO-180, LMO-340 and LMO-1070 in aqueous 1 M Li_2SO_4 vs. Ag/AgCl (3 M KCl) reference electrode. Reproduced with permission from *Erinmwingbovo et al.*[36]

The calculated areal capacity from the CV curves of the films increases with film thicknesses from 4.7 µAh cm^{-2} for LMO-180 to 23.4 µAh cm^{-2} for LMO-340 and 69.4 µAh cm^{-2} for LMO-1070, as could be calculated from the cyclic voltammograms. This reveals notable difference to previous studies on thin film electrodes, as the resistance of the insulating LMO layers should cause slower reaction kinetics with increasing layer thickness due to higher charge transfer resistances and therefore lower capacities.[5,37] Explanations for this behaviour have been attributed to the nature of nano-sized particles being present in the layer, which have proven to cause lower capacities with smaller particle sizes due to their increased surface-to-volume ratio.[5,38] As it has been concluded from SEM images in **Fig. 4.2.2**, thicker layers show larger crystallites with less grain boundaries.

Therefore mass transport is suffering lower impediments with higher crystallinity, following a trend of higher diffusion coefficients D_{Li} in bigger crystallites.[39,40] Values of the apparent D_{Li} calculated from DMFA data by *Erinmwingbovo et al.*[36,41] are ascending from 10^{-10} cm^2 s^{-1} for 180 nm to 10^{-8} cm^2 s^{-1} for 1070 nm thick LMO thin films, demonstrating a good agreement towards literature.[42]

To further emphasize on the cycling stability of relatively thick LMO-340 layers, cyclic voltammograms collected at different scan rates between 10 – 50 mV s^{-1} are shown in **Fig. 4.2.7** for a repetition of various subsequent cycles at each scan rate.

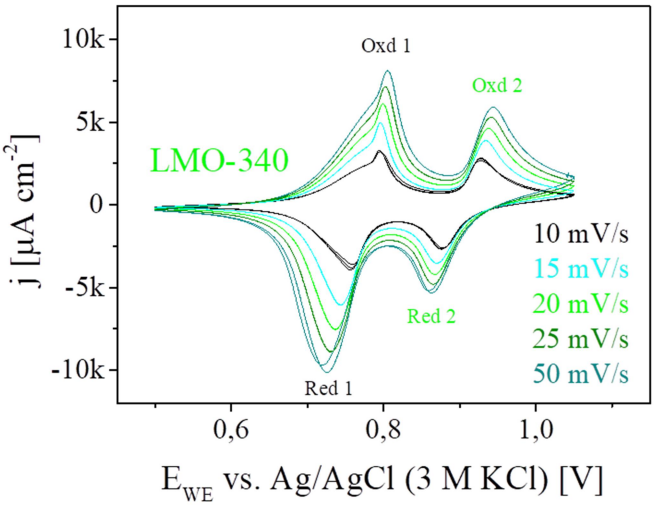

Fig. 4.2.7: Cyclic voltammetry (voltage sweep) in aqueous 1 M Li_2SO_4 vs. Ag/AgCl (3 M KCl) reference electrode in (a) for the thin film with 340 nm thickness for different scan rates between 10 – 50 mV s^{-1}.

Two fully reversible redox-peaks are observable in the CV of **Fig 4.2.7**, corresponding to a two-step lithium (de-) intercalation process described in **Section 1.4.1** for **Eq. 1.4.1**, consisting of (i) Li^+ (de-) solvation and adsorption in the inner Helmholtz plane (IHP), (ii) Li^+ (de-) insertion into $LiMn_2O_4$ and (iii) Li^+ bulk diffusion inside the spinel lattice.[41] With an increase in the scan rate v in **Fig. 4.2.7 (a)**, the peak current densities increase and peak potentials shift, showing good reversibility and stability throughout all cyclic voltammograms collected.

4.2.4 Overdischarge of multi-layer LMO

LMO thin films deposited by multi-layer PLD are studied in the following for the first time exceeding the commonly used operational potential region for battery applications between 3.5 - 4.5 V vs. Li/Li$^+$ (4 V plateau) down to 2.0 V vs. Li/Li$^+$ (3 V plateau). This process is called overdischarge and is typically avoided as it has

shown severe material damages associated to manganese dissolution and Jahn-Teller distortion, amounting to a volume expansion of more than 5 % causing severe material damages limiting the cycling stability for all-solid-state batteries, as described in **Section 1.4.1**.[5,43] However, it has been reported that nano-shapes and thin films can potentially mitigate these detrimental effects.[4,5] For the following electrochemical analysis, multi-layered LMO thin films of 320 nm thickness have been deposited as previously described, keeping the ablation ratio of 4:3 for LMO to Li_2O, respectively. In **Fig. 4.2.8** the structure and microstructure of the as-deposited LMO thin film is characterized by SEM images, showing an increased porosity.

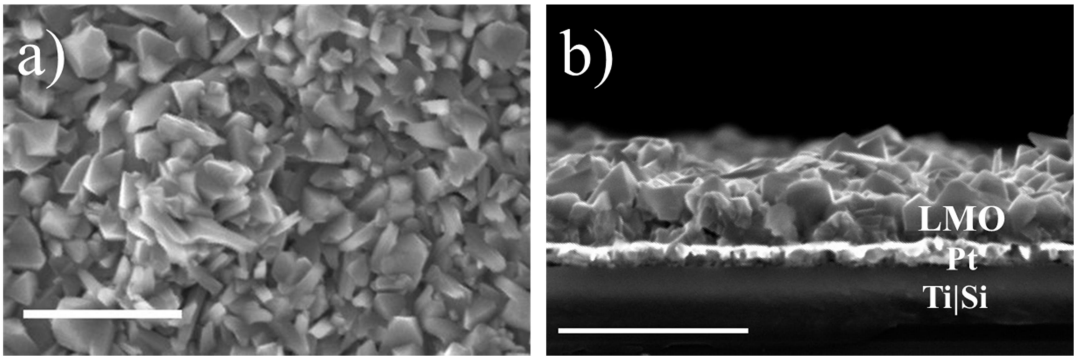

Fig. 4.2.8: SEM images are shown for a porous LMO thin film of 320 nm thickness. The white scale bar corresponds to 1µm.

A relatively rough surface and high porosity appear, as possible result of thermal instabilities coming from the Pt-substrate at elevated deposition temperatures of 650 ºC. The particle size has been determined to range between 100 – 400 nm with an approximated mean particle size of ~ 250 nm. Structural analysis by XRD and Raman are in agreement with the previous results obtained from **Fig. 4.2.3**. First cyclic voltammograms were collected in the usual potential window between 3.5 – 4.5 V vs. Li as CE and RE, using 1 M $LiPF_6$ with EC/DMC (1:1) as electrolyte, in good agreement towards previous measurements in aqueous. The potential window was subsequently extended to the 3 V plateau as can be seen in **Fig 4.2.9 (a)** for a scan rate of 1 mV s^{-1}.

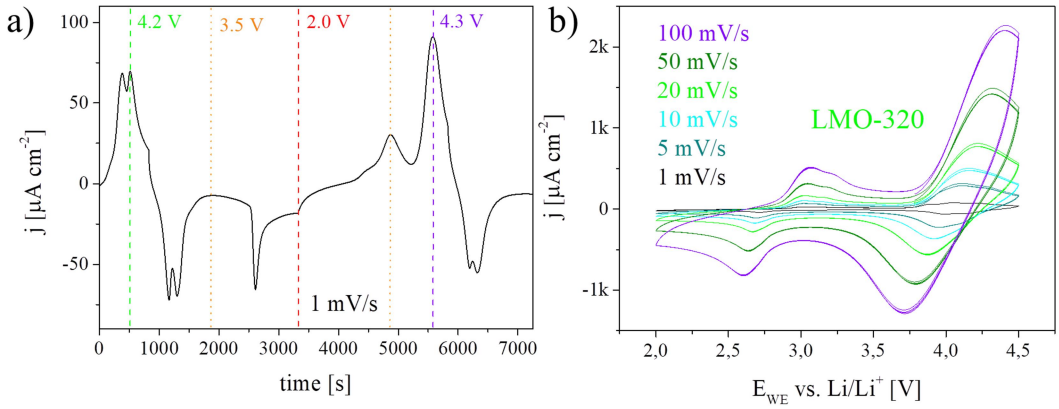

Fig. 4.2.9: Transition between the cyclic voltammogram limited to 4 V plateau towards the extended 3 V plateau in (a) at 1 mV s^{-1} and the corresponding changes in the redox peak potentials marked by vertically dashed lines. Corresponding cyclic voltammograms at different scan rates over the entire theoretical electrochemical stability window are collected in (b). The measurements composed of LMO-320 films as WE in 1 M $LiPF_6$ EC/DMC (1:1) liquid electrolyte and Li as RE and CE in a three-electrode setup in an open cell under protective Ar atmosphere.

The common cathodic and anodic redox peaks for the $Mn^{3+/4+}$ transition under exchange of one Li^+ around 4.2 V vs. Li/Li^+ are well defined (green dashed line) and fully reversible in the 4 V plateau as shown in **Fig. 4.2.9 (a)**. With progressive voltage sweep in the anodic part, a discharge current for the intercalation of an additional Li^+ is applied, under the formation of tetragonal $Li_2Mn_2O_4$. Passing to the 3 V plateau, which corresponds to the current response for everything after 3.5 V (orange dotted line) a strong anodic reduction peak appears at 2.7 V related to the full transition of mixed-valent $Mn^{3+/4+}$ to Mn^{3+}. The scan is reversed at 2 V (red dashed line) with a cathodic current for charging, under the structural transition of tetragonal-to-spinel around 3.5 V. With further potential increase up to 4.5 V, the oxidation peak of $Mn^{3+/4+}$ transition forms one joint redox-peak around 4.3 V instead of separating into the previously well-defined doublet oxidation peaks. For the anodic reduction peak this transition from doublet to single peak takes place initially, but with increasing cycle numbers and scan rates the redox-peaks are symmetric single-peaks for both cathodic and anodic currents as demonstrated in **Fig. 4.2.9 (b)**. A similar behaviour has been reported previously by *Rougier et al.*[44] and was assigned to the lattice distortion in the 3 V plateau taking its tribute also in the 4 V plateau, caused by the additional obstacles to be overcome for lithium (de-) intercalation. Under consideration of the possible co-existence of rock salt structures with spinel LMO, the electrochemical cyclic voltammograms of oxygen-deficient $Li_2MnO_{3-\delta}$ reported by *Müller et al.*[25] are very similar in their peak

positions and broadening when comparing to the CV presented in **Fig. 4.2.9 (b)** for the LMO multi-layers in this work. As it can be seen in **Fig. 4.2.10**, the effect of peak broadening vanishes when restricting again to the typical high voltage region around the 4 V plateau, where redox-peaks become pronounced again.

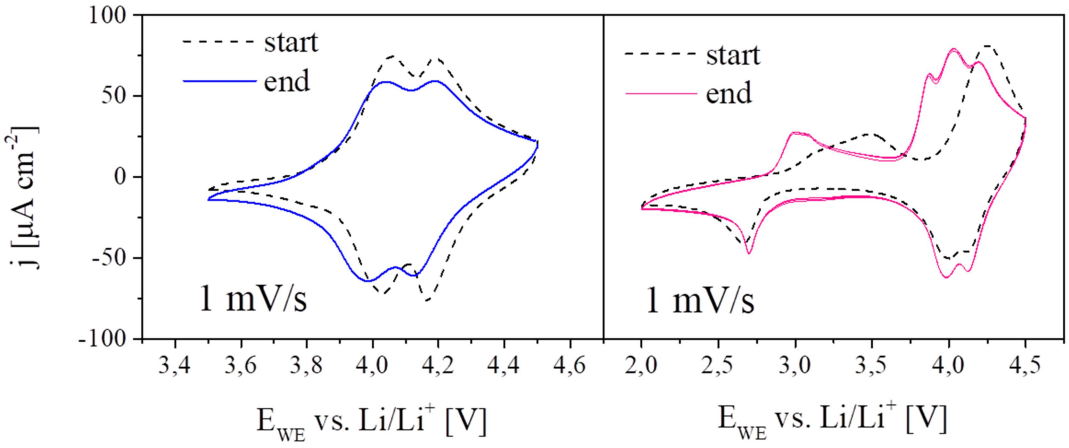

Fig. 4.2.10: Cyclic voltammograms of LMO thin films at 1 mV s^{-1} from the beginning (start – dashed lines) and at the end (bulk lines) after cycling for more than 24 h at different scan rates for the 4 V (left) and 3 V (right) plateau.

While the limited range between 3.5 – 4.5 V vs. Li/Li^+ shows slightly damped redox peaks when comparing the CV from the beginning (start) and end, the voltammogram including also the 3 V plateau shows improved redox peak definition and an additional oxidation peak at 3.8 V. This oxidation peak appears to be irreversible and has formerly been reported in literature[5,45] as a result of the layered rock salt stoichiometry for Li_2MnO_3 taking action in the electrochemical (de-) lithiation reactions. This phase is detected in Raman spectra for pristine layers in **Fig. 4.2.3**, co-existing with the $LiMn_2O_4$ spinel. Additionally, a certain activation process over extended cycling becomes evident in **Fig. 4.2.10 (b)**, which is attributed to the electrochemical activation of layered Li_2MnO_3 at high cut-off voltages around 4.8 V vs. Li/Li^+, revealing stable electrochemical performance under extraction of Li_2O.[25,46,47] Details on the Li_2MnO_3 activation and its layered-to-spinel transformation are described in **Section. 1.4.1**. When comparing to literature, two phenomena have been related to cause the additional oxidation, as either (i) an incomplete extraction of lithium at 3.12 V residing at octahedral sites of the layered rock salt Li_2MnO_3-$LiMnO_2$ (1:1) occurs, which then are de-intercalated at 3.85 V,[24,25,48] or (ii) the irreversible formation of Li_2CO_3 at its standard electrode potential of 3.82 V vs. Li/Li^+ is taking place, due to the loss in

oxygen and its reaction with the carbonaceous electrolyte (which amounts to consume about 13 % on the total charge).[49] In conclusion, both layered rock salt and spinel stoichiometries appear to be present in the PLD thin films, as possible result from the hindered intermixing of Li_2O and $Li_xMn_2O_4$ multi-layers.

In **Fig. 4.2.11** the areal specific capacities obtained at various C-rates are examined from first measurements before and after the additional layer activation.

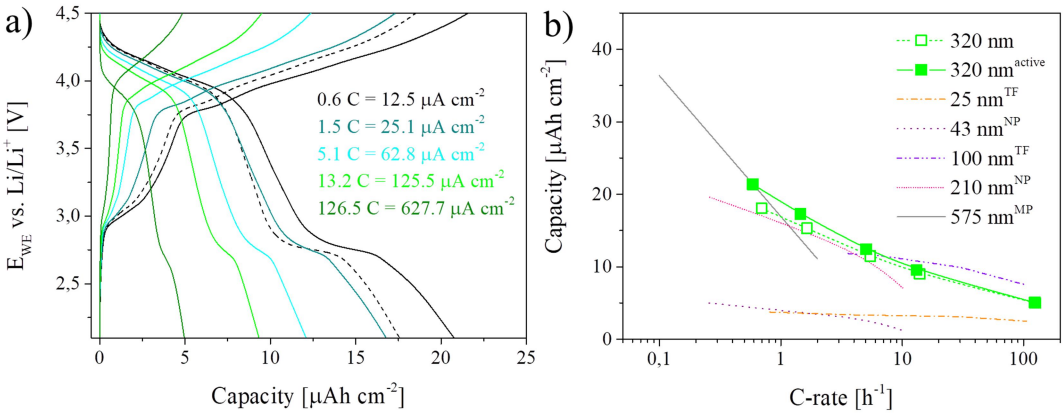

Fig. 4.2.11: Charge/discharge curves of different C-rates of LMO-320 in (a) with the dashed lines corresponding to the areal specific capacity obtained at 12.5 µA cm^{-2} before electrochemical activation. The resulting areal discharge capacities over the C-rate are shown in (b) from before layer activation (empty squares) and after activation (filled squares). Reference is made in (b) to RF-sputtered LMO thin films (TF),[5] LMO Nanoparticles (NP)[38] and Microparticles (MP) in a thick layer.[50]

Due to existing porosity and high layer roughness, capacities are referenced to the exposed thin film surface, as the volumetric determination did not appear reasonable. Discharge curves from 4.5 – 2.0 V vs. Li/Li$^+$ in **Fig. 4.2.11 (a)** show a defined plateau around 2.7 V corresponding to the lithium intercalation into $LiMn_2O_4$ forming $Li_{1+x}Mn_2O_4$ under a certain tetragonal distortion of the lattice. In addition, the layer activation described previously caused a small increase in the resulting areal specific capacity for the same scan rates before (dashed lines) and after (solid lines). This is supporting the hypothesis of Li-rich layered oxides being partially present, increasing their activity and stability upon electrochemical cycling, under introduction of a higher defect abundance in nano-scaled grains.[51] The resulting areal specific capacities increased with lower rates and are highly dependent on the layer thickness and mean particle size, as evidenced in **Fig. 4.2.11 (b)**. For lithiating $Li_{1+x}Mn_2O_4$, bulk materials of LMO tend to react in a "core-shell" manner, forming a Li-rich outer layer around the particles, whereas nano-shapes below 100 nm commence to suppress this layer and rather form solid

solutions.[38] This causes a clear separation of the areal specific capacity in **Fig. 4.2.11 (b)** into thicker layers with greater spatial dimensions in their crystallites, behaving similar to the bulk material, or nano-shapes below 50 nm forming solid solutions. Although very low areal capacities result from small crystallites, extremely high volumetric capacities have been reported approaching the theoretically possible specific capacity of 296 mAh g^{-1} for the intercalation of two lithium.[5] Despite the high surface-to-volume ratio, the formation of the solid solution for Li-rich and poor states eliminates separate domains and hence facilitates the mass transfer and has shown to allow the intercalation of up to 2.5 Li^+ resolving in $Li_{2.5}Mn_2O_4$.[38] PLD multi-layers of LMO-320 exhibit random porosity and hence are experiencing a strong loss in volumetric capacities. Nonetheless, they coincide for their areal specific capacities very much with RF-sputtered LMO layers of 100 nm thickness, which will be used in the following as a reference in the fast charge and discharge of LMO thin films.

As commented before, stability problems due to volume expansion, appearing of cracks, loss of contact with the current collector etc. are dissuading factors for the exploration of LMO in its full potential range. In order to evaluate the stability of the here fabricated thin film LMO, the layer has been subjected to long-term cycling. With this aim, 100 charge-discharge cycles have been repeated in the potential range of 2 – 4.5 V vs. Li/Li^+ at very high C-rates around 167 C. The results are summarized in **Fig. 4.2.12**.

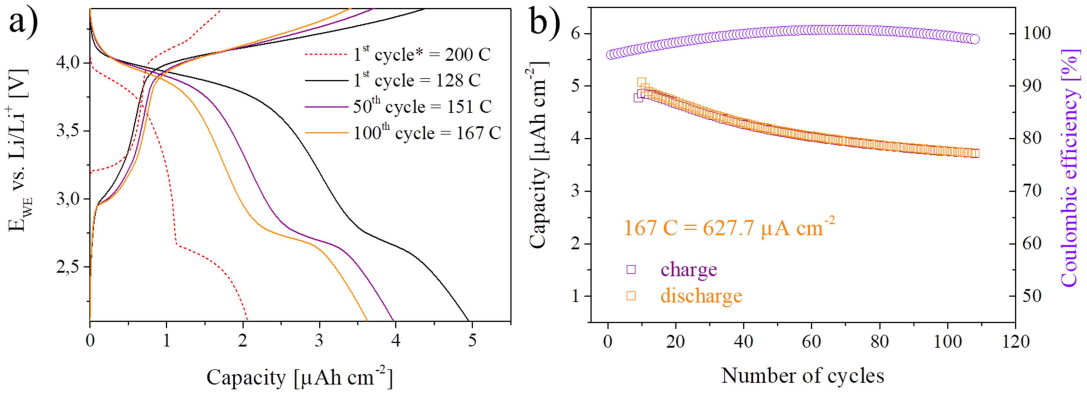

Fig. 4.2.12: Long-term cycling stability for repeated charge/discharge curves between 128 – 167 C over 100 cycles is presented in (a) with a reference (*) to a RF-sputtered thin film of 100 nm thickness studied at 200 C.[5] The resulting capacity retention and coulombic efficiency for LMO-320 is shown in (b). The applied current density was kept constant at 627.7 µA cm^{-2}.

The decrease in discharge capacity from ~4.9 μAh cm^{-2} to ~3.6 μAh cm^{-2} after 100 cycles at 167 C results in a capacity retention of ~70 % with simultaneously high coulombic efficiencies around 99 %. This degradation, while relevant, is still much smaller than the one observed in literature.[5,50] For example, RF-sputtered thin films of LMO exhibit relative similar electrochemical behaviour to PLD thin films, when comparing the charge/discharge curve collected at 200 C for a thin film of 100 nm thickness towards LMO-320 in **Fig. 4.2.12 (a)**. The sputtered layers, between 75 – 100 nm thickness, have been cycled at very slow rates of 1 C in the same potential range as in **Fig. 4.2.12** and their capacity dropped to 50 % of their initial capacity already after 10 cycles. This has been explained with manganese dissolution as the main cause of this degradation, which would show less impact in proportion for thinner films and when additionally protected by a thin layer of LiPON.[5] On the other hand, other factors like volume expansion and the consequent cracks and delamination issues would have a major impact on thicker films like the ones presented here, especially at high cycling rates. Nonetheless, multi-layer PLD enabled the deposition of 320 nm thick LMO thin films, with an extraordinary good cycling stability at very high rates of 167 C over 100 cycles with only 30 % loss in specific capacity due to Mn-dissolution, 20 % less than it has been reported for plain RF-sputtered LMO thin films by *Put et al.*[5]

4.3 Development of $Li_4Ti_5O_{12}$ thin film anodes

The negative intercalation electrode for lithium ion batteries based on spinel $Li_4Ti_5O_{12}$ is widely known for its good reversibility upon electrochemical lithium (de-) intercalation of three Li^+ ions, allowing specific capacities of 634 mAh cm^{-3} (175 mAh g^{-1}) while performing as "zero-strain" material with a very low lattice expansion (0.2 – 0.3 %). Its advanced safety at high rates, good cycling stability, low cost and environmental friendliness make it an ideal choice to replace common carbon intercalation anodes.[3,6,52,53]

Due to the expertise gained in the previous work for PLD depositions of LMO, the spinel anode material $Li_4Ti_5O_{12}$ is studied in the following with the same alternating multi-layer approach by LA-PLD as has been described in **Section 1.4.2**. Using this procedure, samples with different proportions of added Li have been fabricated, and their structure, microstructure and electrochemical

performance have been characterized. Details on the experimental parameters are described in **Section 2.3.3**.

4.3.1 Structure and microstructure

The evolution of the microstructure upon lithium addition is shown in **Fig. 4.3.1**, ranging from the sole ablation of the LTO target in **(a)** to the ablation ratio of 2:1 between LTO and Li_2O in **(b)** and 4:3 in **(c)** under the same deposition conditions as has been previously optimized for LMO, which can be applied due to the similar atomic mass of Mn (55 u) and Ti (48 u) resulting in possibly comparable deposition kinetics in the PLD.

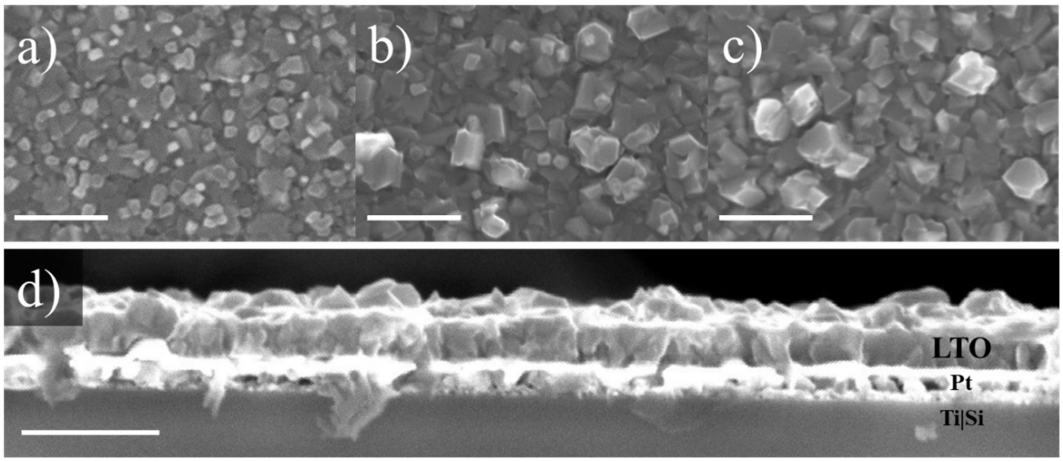

Fig. 4.3.1: SEM images of LTO thin films deposited as alternating multi-layers of $Li_4Ti_5O_{12}$ and Li_2O by LA-PLD. The pulse ratio for LTO : Li_2O is distributed as (a) 1:0, (b) 2:1 and (c) 4:3. In (d) the cross-section for the LTO thin film (2:1) is shown on top of the Pt current collector. The film thickness measured is~145.5 nm and the white scale bar corresponds to 500 nm. The remaining substrate below the 80 nm sputtered Pt-layer consists of a thin titanium adhesive layer (10 nm) on $Si_3N_4|SiO_2|$Si-wafer (top to bottom) which is abbreviated as "Ti|Si".

As the comparison of SEM images in **Fig. 4.3.1 (a – c)** clarifies, the addition of Li_2O increases the crystallite size, with particles in the average of 100 nm for LTO to 150 nm for LTO:Li_2O. This improvement of the thin film crystallization leads to an enhanced microstructure with a reduction in the grain boundaries, as possible hindrance for the ionic mass transport. Additionally, very small particles in the order of 50 nm can be observed in all three layers. Cross-sectional images reveal dense layers of thicknesses around 146 nm, as it is retrieved from **Fig. 4.3.1 (d)** for layers deposited at a pulse ratio of 2:1 for LTO:Li_2O.

In **Fig. 4.3.2** the structural evolution of the $Li_4Ti_5O_{12}$ spinel phase upon a staggered lithium addition in the PLD is monitored by GI-XRD and Raman analysis.

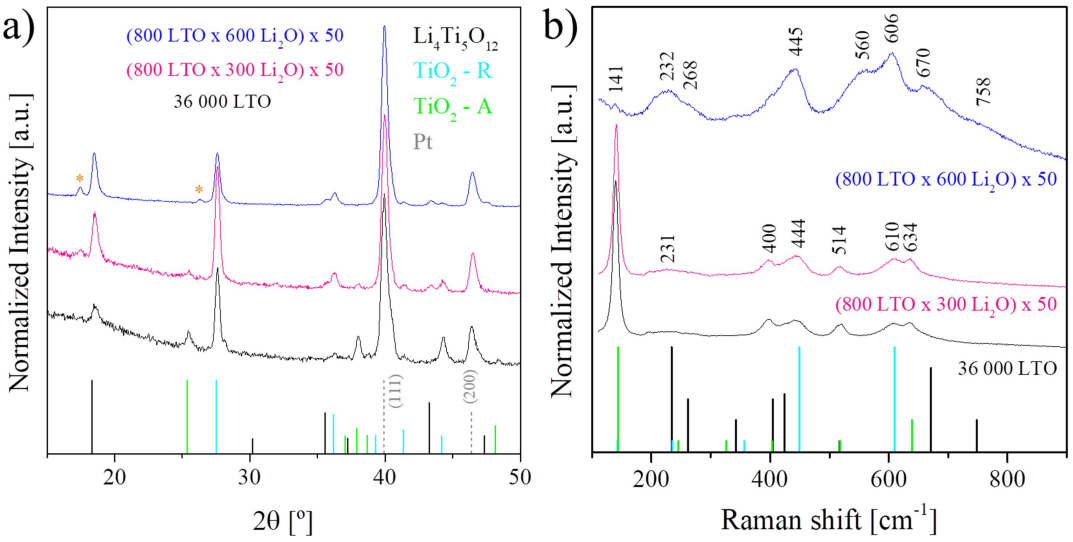

Fig. 4.3.2: GI-XRD of LTO thin films upon different amounts of additional Li_2O in (a) and the corresponding Raman spectra in (b). Thin film deposition conditions are indicated as (pulses on $Li_4Ti_5O_{12}$ x pulses on Li_2O) x number of cycle repetitions, respectively. X-ray patterns are referenced to the JCPDS data base for $Li_4Ti_5O_{12}$ (00-049-0207), Rutile (01-078-1510), Anatase (01-073-1764) and Pt (01-087-0640) as substrate. An additional phase (orange arsterisk) could not be assigned to a specific material pattern with certainty, but may be attributed to some titania occurring upon higher lithium amounts. Raman references are deduced from literature.[9]

As X-ray diffractograms collected in grazing incidence in **Fig. 4.3.2 (a)** reveal a clear response of the thin films, the spinel phase of LTO can be identified by the characteristic peak at 2θ~18.5º, which exhibits an increase in crystallinity with the progressive addition of Li_2O during the layer deposition. Further, peaks corresponding to TiO_2 Rutile and Anatase secondary phases can be assigned. The Rutile phase appears to be present in large amounts in all cases, showing a slight decrease for layers with the higher lithium content. In contrast, Anatase shows an important decrease with higher addition of Li_2O. The appearance of a probable titania secondary phase, which could not be assigned unambiguously to a definite phase (see orange asterisk), occurs when multi-layering with Li_2O target is implemented in the process. Raman spectra in **Fig. 4.3.2 (b)** reveal the presence of mainly Anatase and Rutile phases and no evidence of spinel LTO for lower lithium contents. With increasing Li_2O addition, the Anatase signal vanishes and some vibrational modes of LTO become evident. Rutile appears to be present at any lithium concentration, which is in accordance with the phases identified by GI-

XRD. When comparing to literature on nano-sized materials and their Raman spectra, the vibrational modes recorded for black titania (B-TiO_2) by *Patil et al.*[54] correlate very much with the ones reported in this work, as a combination of shifted Anatase and Rutile Raman bands in **Fig. 4.3.2 (b)**. This may further explain the additional phase appearing in **Fig. 4.3.2 (a)**, as B-TiO_2 is strongly related to the Anatase structure, with some additional disorders evolving from oxygen vacancies.[54,55]

4.3.2 Optical characterization of LTO thin films

Further the electronic band gap energy and optical absorption have been evaluated using spectroscopic ellipsometry (SE) with the modeling approach presented in **Section 2.5.3.2** consisting of four Tauc-Lorentz oscillators. The density of states (DOS) for LTO has been explained previously in **Section 1.4.2** and is used for further understanding of optical spectra. In order to differentiate between different electronic states evolving upon lithium addition in the multi-layer pulsed laser deposition of LTO, the materials optical absorption is obtained from the imaginary part of the complex permittivity ε described in **Eq. 2.5.12 (b)** and the occurring absorption bands allocated at certain energetic states of the O_{2p} and Ti_{3d} orbitals in **Fig. 4.3.3** supported by the second derivative of the extinction coefficient *k* as inset. The weighted sum of squared deviations χ^2 for the fitting ranges between 1.3 – 2.3 and is small enough for obtaining reliable results.

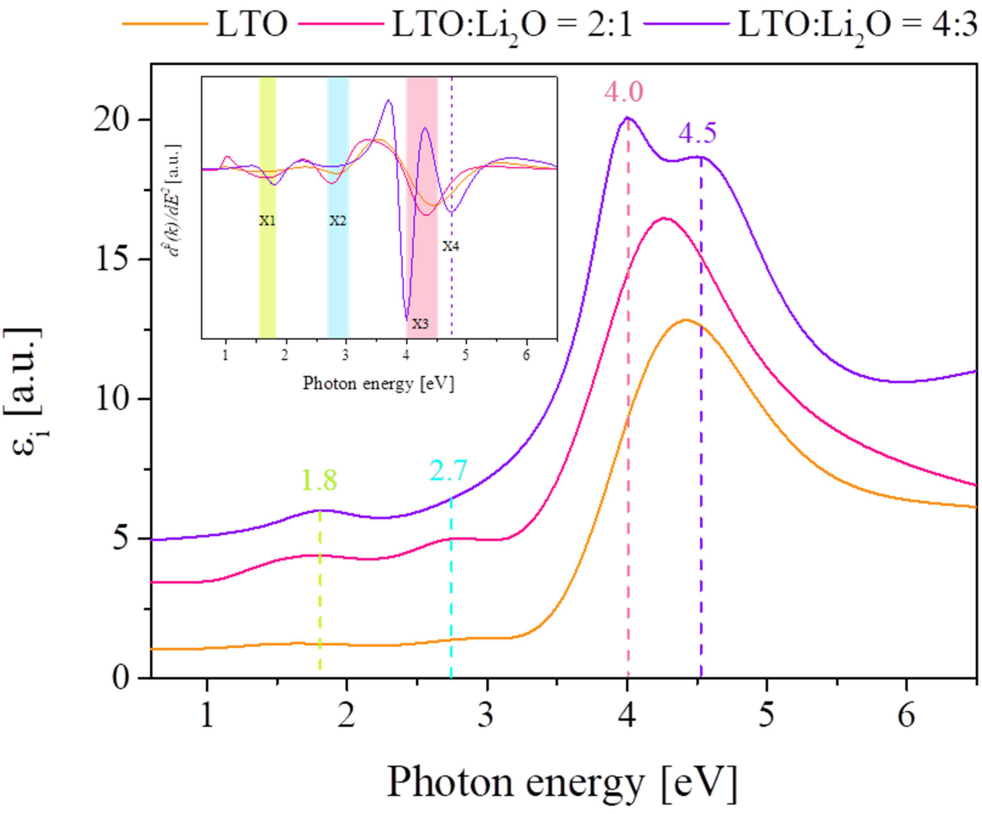

Fig. 4.3.3: Horizontally shifted traces of the imaginary (index i) part of the permittivity ε (absorption) over the corresponding photon energy of LTO thin films for different LTO:Li_2O ablation ratios. The second derivative of the extinction coefficient *k* is plotted over the photon energy as inset. The colored areas of X1 - X4 correspond to vertical, dashed lines in ε_i indicating significant changes in absorption bands upon lithium addition.

Absorption bands occurring in **Fig. 4.3.3** can be attributed to the electronic states of the Li_{2s} orbital and the hybridized molecule orbitals of O_{2p} and Ti_{3d} forming TiO_6 octahedra (see **Section 1.4.2** for further details).[56] The minima located in the second derivative of the extinction coefficient k at distinctive photon energies (shown as insert) are generally related to the electronic intraband transitions between O^{2-} (2p) and $Ti^{3+/4+}$ (3d) hybridized orbital states.[56] The position of X1 absorption band shifts with higher additional lithium content from 1.5 – 1.8 eV. Comparing to literature, this absorption band can be assigned by *Joshi et al.*[57] to electronic transitions in the $Ti^{3+/4+}$ (t_{2g} - e_g) d-orbital caused by the increased formation of Li-rich phases such as $Li_{4+x}Ti_2O_4$ with $x \neq 0$. This is supported by observations made by *Liu et al.*[56] for Li-rich phases, but has been attributed to the transitions between the O^{2-} (2p) and $Ti^{3+/4+}$ (3d) near the Fermi level. Hence X1 is a clear result of an increased presence for Li-rich phases upon lithium addition in the PLD deposition procedure. Further the band for X2 energetically shifts upon increasing lithium

content from 2.7 – 2.9 eV. *Joshi et al.* indicated this absorption band at 2.8 eV as transitions between the filled O (2p) valence band and vacant states in the Ti (t_{2g}) conduction band of $Li_4Ti_5O_{12}$ with an energetic increase upon further lithium intercalation.[57] Differences in the assigned energetic positions towards literature may result from the thin film character of the samples, which has proven to result in significant differences for e.g. titania compounds.[58] Another absorption band appears between 4.0 – 4.4 eV (X3), which can be assigned to the presence of titania, such as Rutile with absorptions between 4.1 – 4.3 eV, or Anatase with electronic transitions around 4.3 eV and 4.8 eV. With increasing lithium content the single peak at 4.4 eV splits shifts to lower energies of 4.0 eV and finally splits into two peaks. This new peak appearing around 4.5 eV may possibly be ascribed to newly introduced lattice defects and/or an additional secondary phase, as supported in GI-XRD patterns in **Fig. 4.3.2 (a)** and of similar absorption bands related to Anatase[58] and Li-rich phases such as $LiTi_2O_4$ or $Li_7Ti_5O_{12}$.[56]

For the determination of the bang gap energy E_g upon increasing lithium content the Tauc plot of $(\alpha hv)^{1/0.5}$ over the photon energy (hv) is shown in **Fig. 4.3.4**, with the absorption coefficient α and the reverse exponential of m = 0.5 describing the direct band gap of LTO.[33,59] The E_g calculated from the intercept of the linear extrapolation (dashed lines) with the x-axis at α = 0 is plotted over the Li_2O:LTO ratio and shown as insert.

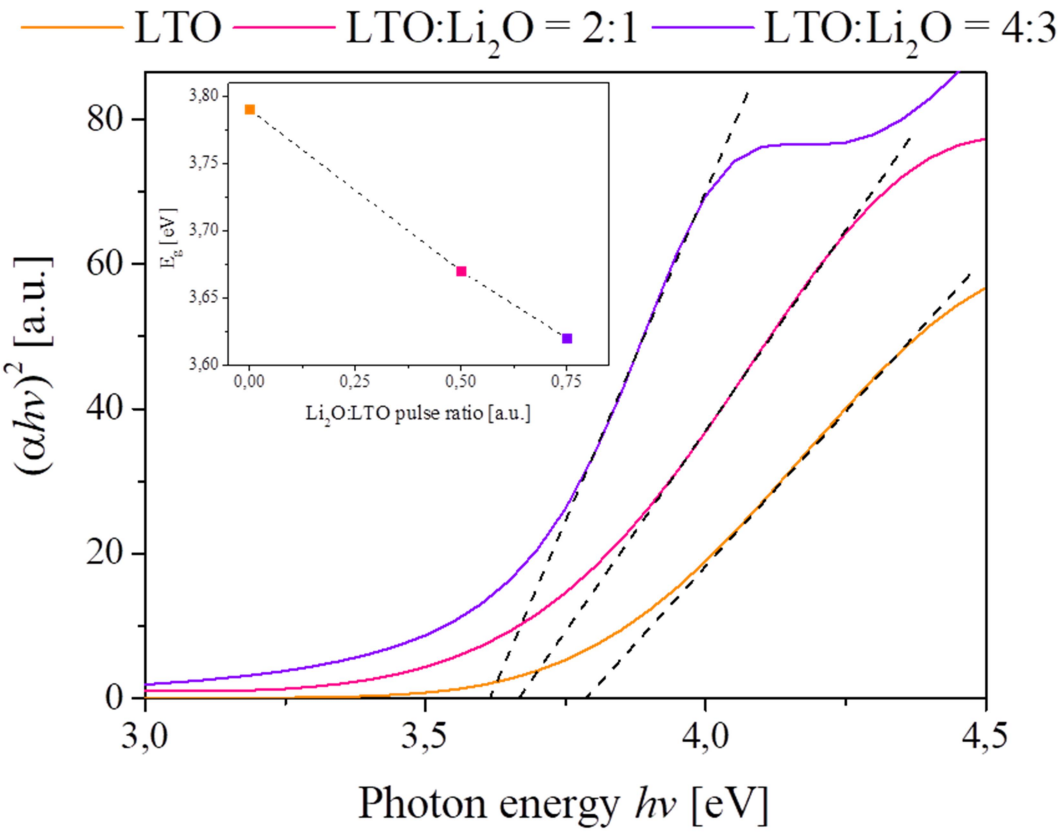

Fig. 4.3.4: Tauc plot of LTO with different additional lithium content added during PLD and the evolution of their band gap energy over the Li_2O:LTO pulse ratio as insert.

As the band gap of LTO has been reported to greatly vary between 1.8 and 3.8 eV due to the broad variety of energetic states in the O_{2p}-T_{3d} hybridized orbital, the resulting values of E_g in **Fig. 4.3.4** seem to align with literature for lithium titanates of high insulating character.[60–65] With the increasing fraction of ablation pulses distributed between Li_2O and LTO targets, higher amounts of additional lithium appear to decrease the resulting band gap energy from 3.8 eV with no additional Li_2O to 3.6 eV with a fraction of 0.75 of Li_2O:LTO respectively. This possibly leads to an improved rate performance and cyclability, as the low intrinsic electronic conductivity associated to greater band gaps has a delimiting effect on the materials diffusion coefficient.[3,62] Further the narrowing of the band gap can evolve from the formation of additional phases with stronger metallic behavior and hence higher electronic conductivity, such as Li-rich phases similar to $Li_7Ti_5O_{12}$ and titania.[57,58]

In addition the thicknesses of each layer could be obtained by modeling SE spectra and are summarized in **Tab. 4.3.1** in the following, which compile well with the previously obtained average thickness by SEM of 146 nm.

Tab. 4.3.1: Thickness determined by SE for different relative pulse ratios between LTO and Li_2O targets during PLD depositions, respectively, and the corresponding weighted sum of squared deviations χ^2 from the SE model.

Relative pulse ratio	Thickness [nm]	χ^2
1:0	131 ± 6	2
2:1	156 ± 3	2
4:3	130 ± 5	2

4.3.3 Electrochemical performance of LTO thin films

The electrochemical performance of all layers has been evaluated in 1 M $LiPF_6$ electrolyte with EC/DMC of 1:1 and lithium acting as counter and reference electrode in a classic three-electrode setup assembled in an open-cell under protective argon atmosphere. The thin films are assumed to be fully dense with ρ = 3.62 g cm^{-3}, which has been supported by SEM images in **Fig. 4.3.1**, and the theoretical capacity for $Li_7Ti_5O_{12}$ is known to be 634 mAh cm^{-3} when exchanging three lithium ions.[6] Cyclic voltammograms reveal different electrochemical reactions taking place, with the standard reaction potential for the intercalation of three Li^+ into spinel $Li_4Ti_5O_{12}$ is known to be 1.5 V vs. Li/Li^+ and follows the mechanism expressed in **Eq. 1.4.4** (see **Section 1.4.3**). Under continued discharge below 0.6 V vs. Li/Li^+, two additional lithium ions can be intercalated at tetrahedral 8a sites in $Li_7Ti_5O_{12}$ by reducing two remaining Ti^{4+} as described in **Eq. 1.4.5**, leading to a theoretical capacity of 866 mAh cm^{-3} (239 mAh g^{-1}) for $Li_9Ti_5O_{12}$.[60] Most research publications restrict to the limited potential window above 1.0 V vs. Li/Li^+ as the theoretical acceptance of Li^+ has been calculated to be dependent on the presence of vacant octahedral sites, which was believed to not be the case below 1.0 V.[52,66] On the contrary, current investigations by *Yi et al.*[53] and other groups[67] have proven the capability of $Li_7Ti_5O_{12}$ in hosting two additional Li^+ at vacant 8a sites in its lattice, when operating at potentials as low as 0.1 V vs Li/Li^+.

In this thesis, cyclic voltammograms and chronopotentiometric measurements have been collected at different current densities in the potential range of 0.3 – 3.5 V vs. Li/Li^+ and are shown in **Fig. 4.3.5** for LTO layers of ablation ratios with 1:0 **(a,b)**, 2:1 **(c,d)** and 4:3 **(e,f)** of LTO:Li_2O, respectively. For the calculation of volumetric capacities, the thicknesses determined by SE in **Tab. 4.3.1** have been utilized.

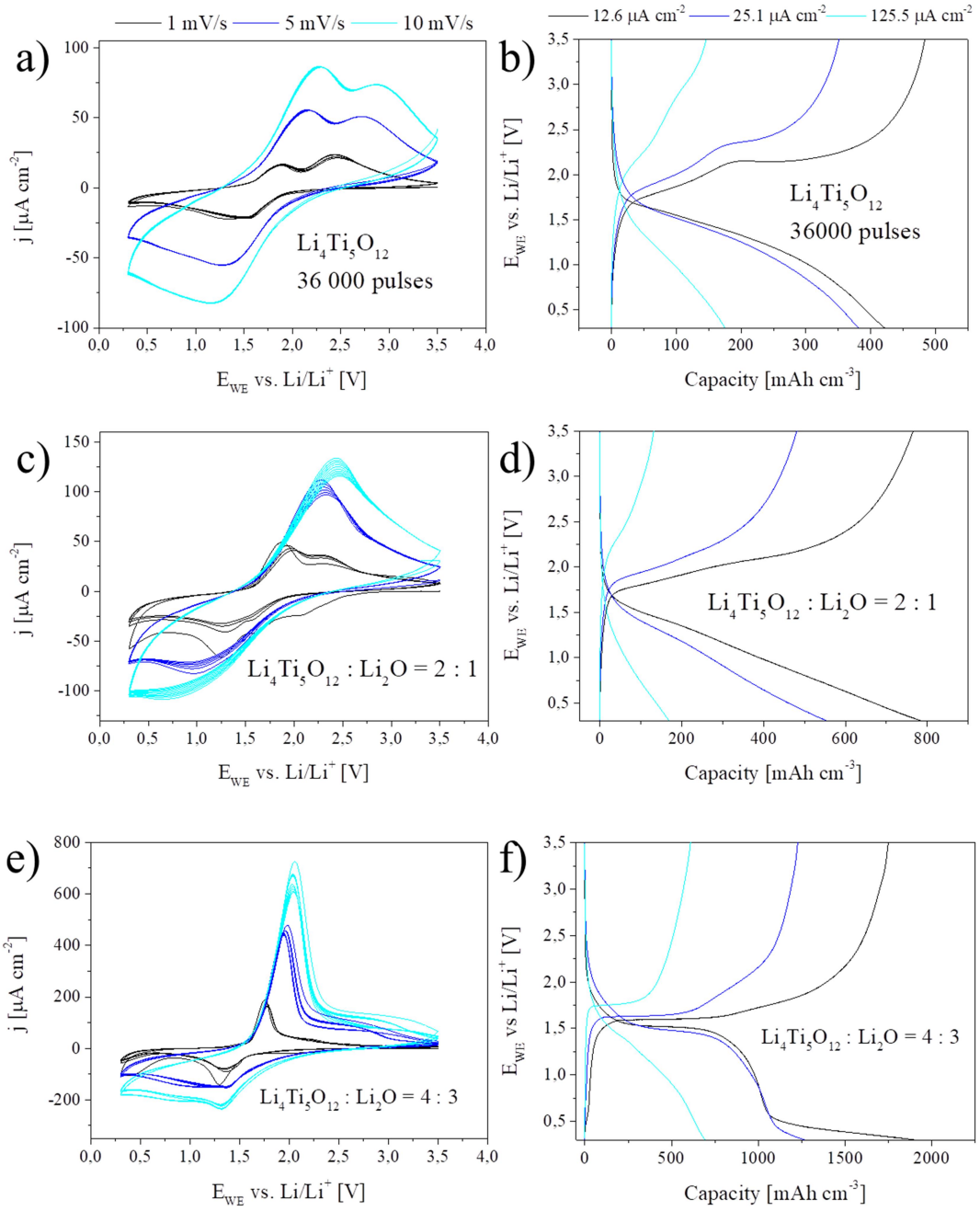

Fig. 4.3.5: Cyclic voltammograms (left) and constant current charge/discharge curves (right) of LTO layers without additional Li_2O in (a,b) and with additional Li_2O of a pulse ratio for 2:1 (c,d) and 4:3 (e,f) on LTO:Li_2O, respectively. The electrochemical window ranges between 0.3 – 3.5 V vs. Li/Li^+. The applied current densities are 12.6 µA cm^{-2}, 25.1 µA cm^{-2} and 125.5 µA cm^{-2}.

A clear improvement in the mass transport kinetics and specific capacities demonstrated in **Fig. 4.3.5** can be observed under the addition of Li_2O, which especially has an impact on the charge acceptable by the LTO lattice under application of high rates and fast cycling kinetics. The reversible redox peaks accounting to $Ti^{3+/4+}$ are visible for all layers in the CV of **Fig. 4.3.5** around 1.5 V

and lower for anodic currents (discharge), as well as around 2.0 V and higher for cathodic currents (charge), depending on the applied scan rate. An additional oxidation peak is present for layers of lower lithium content at a potential around 2.5 V vs. Li/Li^+, which in comparison with literature may be attributed to a differing local coordination of titanium atoms or nano-shapes introduced in the lattice.[54,68,69] Especially the CV collected in **Fig. 4.3.5 (e)** correlates strongly with black titania nano-particles (B-TiO_2) reported by *Patil et al.*[54], with XRD and Raman spectra additionally suggesting their presence, as discussed for **Fig. 4.3.2**. Those combine two different effects which have proven a positive effect on the electrochemical performance. First their nano-shape allows the formation of solid solutions of Li-rich and poor phases for particle sizes ≤ 120 nm, leading to the absence of physical domains inhibiting the charge transition between them.[38,70,71] Further B-TiO_2 is closely related to the anatase structure, which has shown excellent lithium storage capabilities, but reduced capacities evolve under formation of an irreversible SEI layer.[71] Similar behavior is observed for B-TiO_2 by *Patil et al.*, but electrochemical performance can further be advanced due to the oxygen vacancies narrowing the electronic band gap and hence increasing the electronic conduction as demonstrated by *Naldoni et al.*[55] Moreover Rutile also may appear as active intercalation material, as GI-XRD measurements in **Fig. 4.3.2 (a)** strongly suggest. *Bach et al.*[72] reported nano-sized Rutile to exhibit good electrochemical performance due to the lower energy barriers for the Li diffusion process in comparison to micro-sized materials of the same kind. Hence cyclic voltammograms represent a multitude of possible components and microstructural phenomena to be adding to the electrochemical performance of LTO thin films. As subsequent cycling proved the stability of the appearing oxidation and reduction peaks during charge and discharge, irreversible processes are excluded and the corresponding reduction reaction may be summarized in the anodic peak around 1.5 V vs. Li/Li^+, concluding full reversibility of the redox processes is present.

Constant current charge and discharge curves in **Fig. 4.3.5 (b, d, f)** exhibit a steady increase in the specific capacities correlated to the addition of Li_2O during PLD with the progressing pulse ratio of 1:0, 2:1 and 4:3 between LTO:Li_2O, respectively. For very low current densities of 12.6 μA cm^{-2} the specific capacity nearly doubles for each time more Li_2O is added during deposition. The broad

electrochemical window of 0.3 – 3.5 V vs. Li/Li^+ allows the lithitation of $Li_{7+x}Ti_5O_{12}$, with the theoretical capacity of 866 mAh cm^{-3} for x ~ 2, which is first approximated by compositions of 2:1 with 800 mAh cm^{-3} discharge capacity. Excellent charge/discharge profiles are reached with well-defined plateaus for the $Ti^{3+/4+}$ transition (**Fig 4.3.5 (f)**) with further Li_2O addition, resulting in the extraordinary high specific discharge capacity of 1080 mAh cm^{-3} at 0.5 V vs. Li/Li^+ for 4:3 relative ablation ratio between LTO:Li_2O. An additional plateau seems to commence below 0.5 V vs. Li/Li^+, which may be attributed to the additional lithium uptake described earlier by *Yi et al.*[53] under the occupation of octahedral 16c and tetrahedral 8a sites when lithiating below 1 V.[67] In order to stay comparative towards the layers of lower additional lithium content, this plateau is not further explored in this work and the calculated volumetric specific capacities are extracted at 0.5 V vs. Li/Li^+ and further plotted over their corresponding C-rates in **Fig. 4.3.6** for all layers deposited with different amounts of Li_2O.

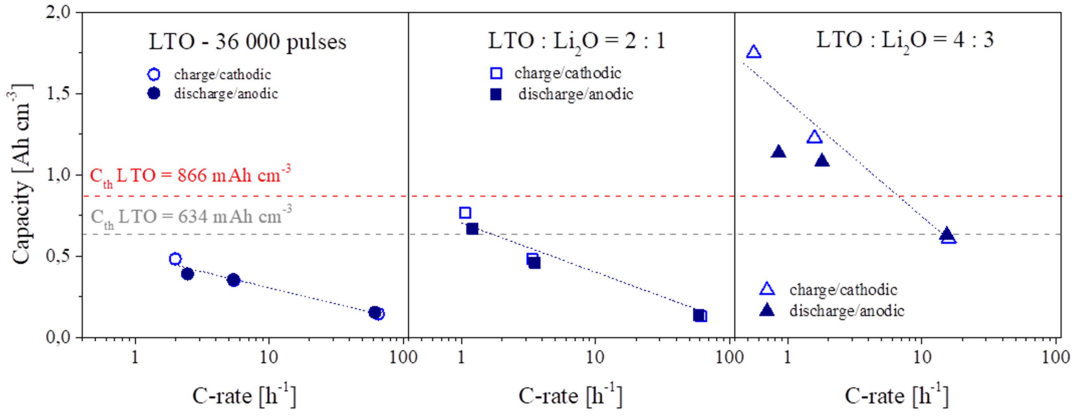

Fig. 4.3.6: Capacitive values taken at 3.5 V for charge curves (empty symbols), and at 0.5 V vs. Li/Li^+ for discharge curves (filled symbols) of LTO multilayers at different C-rates (logarithmic scale) for pulse ratios of 1:0 (circles), 2:1 (squares) and 4:3 (triangles) of LTO:Li_2O during PLD depositions, respectively. The theoretical specific capacities for LTO are indicated by horizontally dashed lines corresponding to 634 mAh cm^{-3} (grey) and 866 mAh cm^{-3}(red). The applied current densities are ascending with the C-rates and correspond to 12.6 µA cm^{-2}, 25.1 µA cm^{-2} and 125.5 µA cm^{-2} for all samples.

As it is observable for layers without or with relatively low amounts of additional lithium in **Fig. 4.3.6**, the theoretical specific capacities of $Li_7Ti_5O_{12}$ and $Li_9Ti_5O_{12}$ are indicated by the horizontally dashed lines at 634 mAh cm^{-3} (grey) and 866 mAh cm^{-3} (red), respectively, have been approached under application of low current densities between 12.6 µA cm^{-2} and 25.1 µA cm^{-2}, leading to C-rates below 4 C. Higher lithium content of 4:3 for the alternated target ablation of LTO:Li_2O is

giving for the same current densities much lower C-rates and exceptionally high specific discharge capacities with 1080 mAh cm^{-3}, exceeding the theoretical capacity at 0.5 V vs. Li/Li^+ of $Li_9Ti_5O_{12}$ by a multiple of 1.3 times around 0.5 C. Therefore the presence of B-TiO_2 appears reasonable, as the volumetric capacity presented by *Patil et al.*[54] at 0.5 C exhibits a reversible value of 1086 mAh cm^{-3}. This remarkable agreement strongly suggests the partial presence of nano-sized particles in the shape of B-TiO_2 inside the LTO multi-layered thin film anodes. With a higher current density, where layers of less additional lithium visibly tend to fail meeting the desired capacitive values, the layer with the highest lithium content still retains the theoretical capacity of $Li_7Ti_5O_{12}$ with 634 mAh cm^{-3} at 0.5 V, for a C-rate of 14 C in a potential window of 0.3 – 3.5 V vs. Li/Li^+. Again, this is in good accordance with data reported on the behavior of B-TiO_2 for a similar C-rate of 10 C. The apparent charge storage would possibly be maximized when reducing the layer down to 0.01V vs. Li/Li^+, as the reported capacitive values of LTO multi-layers have been collected at 0.5 V vs. Li/Li^+ but literature compares to capacities almost 500 mV below that. This depends on the layers stability, which has been reported to be quite good after a first capacitive drop upon the formation of a stable SEI in the incipient electrochemical cycles.[54] Therefore fast charge/discharge cycles have been repeated over various cycles at current densities of 125.5 µA cm^{-2} and the volumetric capacities reached for 0.5 V and 3.5 V for all layers in **Fig. 4.3.7**.

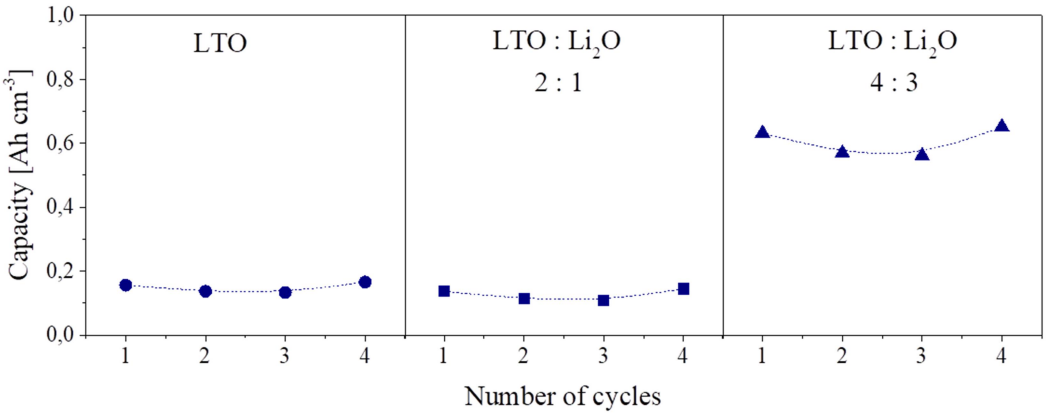

Fig. 4.3.7: Repeated discharge curves at a constant current density of 125.5 µA cm^{-2} at various cycles for LTO samples deposited with relative ablation pulse ratios of 1:0 (circles), 2:1 (squares) and 4:3 (triangles) between LTO:Li_2O respectively. Filled symbols correspond to the volumetric specific discharge capacities at 0.5 V vs. Li/Li^+.

As can be concluded from **Fig. 4.3.7**, all layers exhibit good charge/discharge stability (in this short term cycling test) with only minor changes in the specific

capacity over repeated galvanostatic cycling. Their initial capacitive values at a high current density of 126 μA cm^{-2} are largely preserved, supporting the hypothesis of nano-shapes presenting an improved electrochemical stability. All in all, the layer with the highest lithium content, deposited by multi-layering LTO and Li_2O targets in the relative ablation ratio of 4:3 in the PLD could demonstrate superior electrochemical properties in comparison to layers of less additional lithium content.

4.4 Conclusions

Thin films of intercalation materials for the application in lithium ion batteries such as $LiMn_2O_4$ and $Li_4Ti_5O_{12}$ have been successfully produced in a multi-layer approach for the LA-PLD under alternating ablation pulses between Li_2O with spinel targets of LMO and LTO, respectively.

Deposition parameters for the fabrication of LMO multi-layers could be optimized (refining previous seminal works from the group) in order to reduce impurities, leading to a stable spinel phase with good film quality and densification. The dependency of structure and microstructure on the film thickness has been studied and revealed to strongly impact the crystallite growth. Higher thicknesses supported the layer crystallization. Especially thick layers exhibit besides larger grains also an increased surface roughness and layer porosity. The resulting optical properties suggested a good suitability to study the optical transitions related to the change in Mn oxidation states, which in-situ/operando techniques could profit from for monitoring the lithium insertion and extraction for the LMO lattice. Excellent electrochemical performances in the aqueous Li_2SO_4 electrolyte under fast electrochemical cycling rates could be reproduced when comparing with previous publications from the group.[13] As thick electrodes are required in real microbatteries and a certain thickness dependency on the thin film electrochemical properties has been reported in the past by literature,[5,37] LMO was studied for various layer thicknesses of 180 nm, 340 nm and 1070 nm. In the analysis of the microstructure, the film thickness demonstrated a great influence on the grain size and layer densification, as there was a notable increase in crystallization upon subsequent layer growth. Under electrochemical cycling at 16 mV s^{-1} the area specific capacity increased with layer thickness, which is unexpected due to the usually increased film resistance with thickness. This effect was tentatively linked to the particle size, which is increasing upon layer thickness. Larger grains improve the mass transport, likely due to the lower presence of grain boundaries, and the apparent diffusion coefficient increases from 10^{-10} to 10^{-8} cm^2 s^{-1}, for LMO-180 to LMO-1070, respectively.

Further the stability of multi-layered LMO thin films in the extended potential range of 2.0 – 4.5 V vs. Li/Li^+ has been studied in non-aqueous electrolytes, leading

to the so-called overdischarge of the material. The thin layers deposited by PLD subjected to this extended range could sufficiently maintain 70 % of the initial capacity after 100 cycles at very high rates of 167 C, which represents a promising result in stability when comparing to literature.[5] Therefore, porous multi-layer thin films perform with acceptable losses in the full potential range of LMO under (de-) intercalation of three Li^+ and can be considered stable over a great amount of charge and discharge cycles. This may be improved by the fabrication of dense layers with higher degrees of crystallization, as previous studies on the reaction kinetics by DMFA in the aqueous limited potential range of multi-layered LMO thin films demonstrated.

Following the excellent results provided by multi-layering PLD for the compensation of volatile lithium compounds in LMO, $Li_4Ti_5O_{12}$ anode thin films have been realized. The alternated ablation of LTO and Li_2O targets provided a good control of the desired layer stoichiometry, which could be adjusted to the desired material properties. Hence the study of different LTO:Li_2O ablation ratios provided LTO thin films with Rutile as dominant secondary phase and small amounts of Anatase for all thin films. Crystallinity improves and the optical band gap decreases with higher lithium content, leading to presumably favorable conditions in the mass transport properties of the material. This was supported by electrochemical measurements, revealing a strong increase in the volumetric specific capacities upon higher additional lithium content. The maximum was obtained for layers with 4:3 of relative pulse ratio between LTO and Li_2O during PLD deposition, leading to an exceptionally high specific discharge capacity of 1080 mAh cm^{-3} at 0.5 V vs. Li/Li^+, for 0.5 C in the potential window of 0.3 – 3.5 V vs. Li/Li^+. The strong increase in capacity may not only be associated to the occupation of additional tetrahedral sites in such a broad electrochemical window, it is additionally supported by the increased content of active lithium charge and based on that, the further formation of Li-rich or electronically conducting phases. Moreover, the formation of electrochemically highly performing B-TiO_2 nano-particles could be supported by XRD, Raman and was finally evidenced in the electrochemical measurements revealing specific capacities to correspond very much with the multi-layered LTO thin films of maximized lithium content (with 4:3 relative pulse ratio during PLD deposition). Stabilities in the lower potential

region for the formation of $Li_9Ti_5O_{12}$ and the full intercalation of five Li^+ in the electrochemical potential window between 0.01 – 3.5 V vs. Li/Li^+ are interesting topics for future work in the performance of LTO anodes deposited by multi-layer LA-PLD.

References

(1) Mizushima, K.; Jones, P. C.; Wiseman, P. J.; Goodenough, J. B. Lix CoO2 (0 < x < 1): A New Cathode Material for Batteries of High Energy Density. *Mater. Res. Bull.* **1980**, *15*, 783–789.

(2) Broussely, M.; Biensan, P.; Simon, B. Lithium Insertion into Host Materials : The Key to Success for Li Ion Batteries. *Electrochim. Ac* **1999**, *45*, 3–22.

(3) Cai, Y.; Huang, Y.; Jia, W.; Wang, X.; Guo, Y.; Jia, D.; Sun, Z.; Pang, W.; Guo, Z. Super High-Rate, Long Cycle Life of Europium Modified Carbon Coated Hierarchical Mesoporous Lithium Titanate Anode Materials for Lithium Ion Batteries. *J. Mater. Chem. A* **2016**, *4* (25), 9949–9957. https://doi.org/10.1039/C6TA03162E.

(4) Armstrong, M. J.; O'Dwyer, C.; Macklin, W. J.; Holmes, J. D. Evaluating the Performance of Nanostructured Materials as Lithium-Ion Battery Electrodes. *Nano Research*. Tsinghua University Press December 4, 2014, pp 1–62. https://doi.org/10.1007/s12274-013-0375-x.

(5) Put, B.; Vereecken, P. M.; Labyedh, N.; Sepulveda, A.; Huyghebaert, C.; Radu, I. P.; Stesmans, A. High Cycling Stability and Extreme Rate Performance in Nanoscaled LiMn2O4 Thin Films. *ACS Appl. Mater. Interfaces* **2015**, *7* (40), 22413–22420. https://doi.org/10.1021/acsami.5b06386.

(6) Cunha, D. M.; Hendriks, T. A.; Vasileiadis, A.; Vos, C. M.; Verhallen, T.; Singh, D. P.; Wagemaker, M.; Huijben, M. Doubling Reversible Capacities in Epitaxial Li4 Ti5 O12 Thin Film Anodes for Microbatteries. *ACS Appl. Energy Mater.* **2019**, *2* (5), 3410–3418. https://doi.org/10.1021/acsaem.9b00217.

(7) Liu, Y.; Sun, Q.; Zhao, Y.; Wang, B.; Kaghazchi, P.; Adair, K. R.; Li, R.; Zhang, C.; Liu, J.; Kuo, L.-Y.; Hu, Y.; Sham, T.-K.; Zhang, L.; Yang, R.; Lu, S.; Song, X.; Sun, X. Stabilizing the Interface of NASICON Solid Electrolyte against Li Metal with Atomic Layer Deposition. *ACS Appl. Mater. Interfaces* **2018**, *10* (37), 31240–31248. https://doi.org/10.1021/acsami.8b06366.

(8) Maier, J. Size Effects on Mass Transport and Storage in Lithium Batteries. *J. Power Sources* **2007**, *174* (2), 569–574. https://doi.org/10.1016/j.jpowsour.2007.06.246.

(9) Lakshmi-Narayana, A.; Hussain, O. M.; Mauger, A.; Julien, C. Transport Properties of Nanostructured Li2 Ti O3 Anode Material Synthesized by Hydrothermal Method. *Sci* **2019**, *1* (39), 1–16.

(10) Liang, X.; Tan, F.; Wei, F.; Du, J. Research Progress of All Solid-State Thin Film Lithium Battery. *IOP Conf. Ser. Earth Environ. Sci.* **2019**, *218* (1), 12138. https://doi.org/10.1088/1755-1315/218/1/012138.

(11) Julien, C. M.; Mauger, A. Pulsed Laser Deposited Films for Microbatteries. *Coatings* **2019**, *9* (6), 386. https://doi.org/10.3390/coatings9060386.

(12) Fehse, M.; Trócoli, R.; Hernández, E.; Ventosa, E.; Sepúlveda, A.; Morata, A.; Tarancón, A. An Innovative Multi-Layer Pulsed Laser Deposition Approach for LiMn2O4 Thin Film Cathodes. *Thin Solid Films* **2018**, *648*, 108–112. https://doi.org/10.1016/j.tsf.2018.01.015.

(13) Fehse, M.; Trócoli, R.; Ventosa, E.; Hernández, E.; Sepúlveda, A.; Morata, A.; Tarancón, A. Ultrafast Dischargeable LiMn2O4 Thin-Film Electrodes with Pseudocapacitive Properties for Microbatteries. *ACS Appl. Mater. Interfaces* **2017**, *9* (6), 5295–5301.

(14) Kosilov, V. V; Potapenko, A. V; Kirillov, S. A. Effect of Overdischarge (Overlithiation) on Electrochemical Properties of Li Mn2 O4 Samples of Different Origin. *J. Solid State Electrochem.* **2017**, *21* (11), 3269–3279. https://doi.org/10.1007/s10008-017-3671-7.

(15) Dumont, T.; Lippert, T.; Döbeli, M.; Grimmer, H.; Ufheil, J.; Novák, P.; Würsig, A.; Vogt, U.; Wokaun, A. Influence of Experimental Parameter on the Li-Content of Li Mn2 O4 Electrodes Produced by Pulsed Laser Deposition. *Appl. Surf. Sci.* **2006**, *252* (13), 4902–4906. https://doi.org/10.1016/j.apsusc.2005.07.119.

(16) Trócoli, R.; Morata, A.; Fehse, M.; Stchakovsky, M.; Sepúlveda, A.; Tarancón, A. High Specific Power Dual-Metal-Ion Rechargeable Microbatteries Based on Li Mn2 O4 and Zinc for Miniaturized Applications. *ACS Appl. Mater. Interfaces* **2017**, *9* (38), 32713–32719. https://doi.org/10.1021/acsami.7b08883.

(17) Gallagher, K. G.; Nelson, P. A.; Dees, D. W. Simplified Calculation of the Area Specific Impedance for Battery Design. *J. Power Sources* **2011**, *196* (4), 2289–2297. https://doi.org/10.1016/j.jpowsour.2010.10.020.

(18) Park, S. H.; Sato, Y.; Kim, J. K. K.; Lee, Y. S. Powder Property and Electrochemical Characterization of Li2MnO3 Material. *Mater. Chem. Phys.* **2007**, *102* (2–3), 225–230. https://doi.org/10.1016/j.matchemphys.2006.12.008.

(19) Julien, C. M.; Massot, M. Lattice Vibrations of Materials for Lithium Rechargeable Batteries I. Lithium Manganese Oxides. *Mater. Sci. Eng. B Solid-State Mater. Adv. Technol.* **2003**, *100* (1), 69–78. https://doi.org/10.1016/S0921-5107(03)00077-1.

(20) Tang, S. B.; Lai, M. O.; Lu, L.; Tripathy, S. Comparative Study of LiMn 2 O 4 Thin Film Cathode Grown at High , Medium and Low Temperatures by Pulsed Laser Deposition. *J. Solid State Chem.* **2006**, *179*, 3831–3838. https://doi.org/10.1016/j.jssc.2006.08.025.

(21) Slautin, B.; Alikin, D.; Rosato, D.; Pelegov, D.; Shur, V.; Kholkin, A. Local Study of Lithiation and Degradation Paths in Li Mn2 O4 Battery Cathodes: Confocal Raman Microscopy Approach. *Batteries* **2018**, *4* (2), 21.

(22) Chiu, K.-F.; Hsiao, H. H.; Chen, G. S.; Liu, H. L.; Her, J. L.; Lin, H. C. Structural Evolution and Stability of RF Sputter Deposited Lix Mn2−y O4 Thin Film Cathodes. *J. Electrochem. Soc.* **2004**, *151* (3), A452. https://doi.org/10.1149/1.1644135.

(23) Amalraj, S. F.; Burlaka, L.; Julien, C. M.; Mauger, A.; Kovacheva, D.; Talianker, M.; Markovsky, B.; Aurbach, D. Phase Transitions in Li2 Mn O3 Electrodes at Various States-of-Charge. *Electrochim. Acta* **2014**, *123*, 395–404. https://doi.org/10.1016/j.electacta.2014.01.051.

(24) Susai, F. A.; Talianker, M.; Liu, J.; Paul, T.; Grinblat, Y.; Erickson, E.; Noked, M.; Burstein, L.; Frenkel, A. I.; Tsur, Y.; Markovsky, B.; Aurbach, D. Electrochemical Activation of Li2MnO3 Electrodes at 0 ◦ C and Its Impact on the Subsequent Performance at Higher Temperatures. *Materials (Basel).* **2020**, *13* (4388), 1–22.

(25) Müller, H. A.; Joshi, Y.; Hadjixenophontos, E.; Peter, C.; Csiszár, G.; Richter, G.; Schmitz, G. High Capacity Rock Salt Type Li2MnO3-: δ Thin Film Battery Electrodes. *RSC Adv.* **2020**, *10* (7), 3636–3645. https://doi.org/10.1039/c9ra10125j.

(26) Kim, K. J.; Park, Y. R. Sol-Gel Growth and Structural and Optical Investigation of Manganese-Oxide Thin Films: Structural Transformation by Zn Doping. *J. Cryst. Growth* **2004**, *270* (1–2), 162–167. https://doi.org/10.1016/j.jcrysgro.2004.06.019.

(27) Chakradhar, R. P. S.; Yasoda, B.; Rao, J. L.; Gopal, N. O. EPR and Optical Studies of Mn 2 + Ions in Li 2 O – Na 2 O – B 2 O 3 Glasses – An Evidence of Mixed Alkali Effect. *J. Non. Cryst. Solids* **2007**, *353*, 2355–2362. https://doi.org/10.1016/j.jnoncrysol.2007.04.002.

(28) Rudramadevi, B. H.; Buddhudu, S. Spectral Properties of Cu2+, Ni2+, Co2+ , Mn2+ & Cr3+ Ions Doped B2 3-BaO-LiF Glasses. *Ferroelectr. Lett.* **2009**, *36* (3–4), 82–91. https://doi.org/10.1080/07315170903152763.

(29) Halder, O.; Satpati, B.; Rajput, P.; Mohapatra, N.; Jha, S. N.; Suffczynski, J.; Pacuski, W.; Rath, S. Light Emitting Spin Active Electronic States in Ultra-Thin Mn Doped CdSe

Layered Nanosheets. *Sci. Rep.* **2019**, *9* (1804). https://doi.org/10.1038/s41598-019-38974-0.

(30) Kim, K. J.; Lee, J. H. Evolution of the Structural and the Optical Properties and the Related Electronic Structure of LiTxMn2-XO4 (T = Fe and Ni) Thin Films. *J. Korean Phys. Soc.* **2007**, *51* (3), 1166–1171. https://doi.org/10.3938/jkps.51.1166.

(31) Kim, K. J.; Lee, J. H. Effects of Nickel Doping on Structural and Optical Properties of Spinel Lithium Manganate Thin Films. *Solid State Commun.* **2007**, *141* (2), 99–103. https://doi.org/10.1016/j.ssc.2006.08.044.

(32) Zhou, W.; Wu, J.; Ouyang, C.; Gao, Y.; Xu, X.; Huang, Z. Optical Properties of Mn-Co-Ni-O Thin Films Prepared by Radio Frequency Sputtering Deposition. *J. Appl. Phys* **2014**, *114* (093512), 1–6. https://doi.org/10.1063/1.4867439.

(33) Tauc, J.; Grigorovici, R.; Vancu, A. Optical Properties and Electronic Structure of Amorphous Germanium. *Phys. status solidi* **1966**, *15*, 627–637.

(34) Eckhoff, M.; Blöchl, P. E.; Behler, J. Hybrid Density Functional Theory Benchmark Study on Lithium Manganese Oxides. *Phys. Rev. B* **2020**, *101* (205113). https://doi.org/10.1103/PhysRevB.101.205113.

(35) Paulraj, V.; Swami, B.; Bharathi, K. K. Growth Behavior, Work Function, and Band Gap Tuning of Nanocrystalline LiMn2O4 Thin Films Growth Behavior, Work Function, and Band Gap Tuning of Nanocrystalline LiMn 2 O 4 Thin Films. *Appl. Phys. Lett.* **2019**, *115* (093901). https://doi.org/10.1063/1.5109355.

(36) Erinmwingbovo, C. Kinetics of the Reversible Insertion of Cations in Positive Electrode Materials Under Dynamic Conditions https://media.suub.uni-bremen.de/handle/elib/4368 (accessed Oct 5, 2020).

(37) Wu, X.; Chen, S.; He, Z.; Ma, M.; Liu, J. Influence of Thickness on the Properties of Solution-Derived LiMn 2O4 Thin Films. *J. Wuhan Univ. Technol. Mater. Sci. Ed.* **2009**, *24* (5), 706–710. https://doi.org/10.1007/s11595-009-5706-0.

(38) Okubo, M.; Mizuno, Y.; Yamada, H.; Kim, J.; Hosono, E.; Zhou, H.; Kudo, T.; Honma, I. Fast Li-Ion Insertion into Nanosized LiMn 2 O 4 without Domain Boundaries. *ACS Nano* **2010**, *4* (2), 741–752.

(39) Lee, J.; Kim, S. T.; Cao, R.; Choi, N.; Liu, M.; Lee, K. T. Metal – Air Batteries with High Energy Density : Li – Air versus Zn – Air. *Adv. Energy Mater.* **2011**, 34–50. https://doi.org/10.1002/aenm.201000010.

(40) Feng, T.; Xu, W.; Liu, X.; Shao, M. Effect of Calcination Time on Lithium Ion Diffusion Coefficient. *Int. J. Electrochem. Sci.* **2018**, *13*, 1027–1028. https://doi.org/10.20964/2018.01.50.

(41) Erinmwingbovo, C.; Siller, V.; Nuñez, M.; Trócoli, R.; Brogioli, D.; Morata, A.; La Mantia, F. Dynamic Impedance Spectroscopy of LiMn2O4 Thin Films Made by Multi-Layer Pulsed Laser Deposition. *Electrochim. Acta* **2020**, *331*. https://doi.org/10.1016/j.electacta.2019.135385.

(42) Julien, C.; Haro-Poniatowski, E.; Camacho-Lopez, M. A.; Escobar-Alarcon, L.; Jimenez-Jarquin, J. Growth of LiMn2O4 Thin Films by Pulsed-Laser Deposition and Their Electrochemical Properties in Lithium Microbatteries. *Mater. Sci. Eng. B Solid-State Mater. Adv. Technol.* **2000**, *72* (1), 36–46. https://doi.org/10.1016/S0921-5107(99)00598-X.

(43) Hendriks, R.; Cunha, D. M.; Singh, D. P.; Huijben, M. Enhanced Lithium Transport by Control of Crystal Orientation in Spinel Li Mn2 O4 Thin Film Cathodes. *ACS Appl. energy Mater.* **2018**, *1* (12), 7046–7051. https://doi.org/10.1021/acsaem.8b01477.

(44) Rougier, A. Cyclic Voltammetry of Pulsed Laser Deposited Lix Mn2 O4 Thin Films. *J. Electrochem. Soc.* **1998**, *145* (9), 2975. https://doi.org/10.1149/1.1838750.

(45) Thackeray, M. M.; David, W. I. F.; Bruce, P. G.; Goodenough, J. B. Lithium Insertion into Manganese Spinels. *Mater. Res. Bull.* **1983**, *18* (4), 461–472. https://doi.org/10.1016/0025-5408(83)90138-1.

(46) Ates, M. N.; Mukerjee, S.; Abraham, K. M. A Search for the Optimum Lithium Rich Layered Metal Oxide Cathode Material for Li-Ion Batteries. **2015**, *162* (7), 1236–1245. https://doi.org/10.1149/2.0481507jes.

(47) Saroha, R.; Gupta, A.; Panwar, A. K. Electrochemical Performances of Li-Rich Layered-Layered Li 2 MnO 3 - LiMnO 2 Solid Solutions as Cathode Material for Lithium-Ion Batteries. *J. Alloys Compd.* **2017**, *696*, 580–589. https://doi.org/10.1016/j.jallcom.2016.11.199.

(48) Raju, K.; Nkosi, F. P.; Viswanathan, E.; Mathe, M. K.; Damodaran, K.; Ozoemena, K. I. Microwave-Enhanced Electrochemical Cycling Performance of the LiNi0.2Mn1.8O4 Spinel Cathode Material at Elevated Temperature. *Phys. Chem. Chem. Phys.* **2016**, *18* (18), 13074–13083. https://doi.org/10.1039/c6cp01873d.

(49) Guerrini, N.; Jin, L.; Lozano, J. G.; Luo, K.; Sobkowiak, A.; Tsuruta, K.; Massel, F.; Duda, L.; Roberts, M. R.; Bruce, P. G. Charging Mechanism of Li 2 MnO 3. *Chem.*

Mater. **2020**, No. 32, 3733–3740. https://doi.org/10.1021/acs.chemmater.9b04459.

(50) Ebin, B.; Battaglia, V.; Gürmen, S. Comparison of 4 V and 3 V Electrochemical Properties of Nanocrystalline LiMn 2 O 4 Cathode Particles in Lithium Ion Batteries Prepared by Ultrasonic Spray Pyrolysis. *Ceram. Int.* **2014**, *40* (5), 7029–7035. https://doi.org/10.1016/j.ceramint.2013.12.032.

(51) Guo, H.; Wei, Z.; Jia, K.; Qiu, B.; Yin, C.; Meng, F.; Zhang, Q. Abundant Nanoscale Defects to Eliminate Voltage Decay in Li-Rich Cathode Materials. *Energy Storage Mater.* **2019**, *16* (May 2018), 220–227. https://doi.org/10.1016/j.ensm.2018.05.022.

(52) Deng, J.; Lu, Z.; Chung, C. Y.; Han, X.; Wang, Z. Electrochemical Performance and Kinetic Behavior of Lithium Ion in Li 4 Ti 5 O 12 Thin Film Electrodes. *Appl. Surf. Sci.* **2014**, *314*, 936–941. https://doi.org/10.1016/j.apsusc.2014.06.162.

(53) Yi, T.-F.; Yang, S.-Y.; Xie, Y. Recent Advances of Li4 Ti5 O12 as Promising next Generation Anode Material for High Power Lithium-Ion Batteries. *J. Mater. Chem. A* **2015**, *3*, 5750−5777. https://doi.org/10.1039/C4TA06882C.

(54) Patil, S. B.; Phattepur, H.; Kishore, B.; Nagaraju, R. V. G. Robust Electrochemistry of Black - TiO 2 as Stable and High - Rate Negative Electrode for Lithium - Ion Batteries. *Mater. Renew. Sustain. Energy* **2019**, *8* (2), 1–10. https://doi.org/10.1007/s40243-019-0147-y.

(55) Naldoni, A.; Allieta, M.; Santangelo, S.; Marelli, M.; Fabbri, F.; Cappelli, S.; Bianchi, C. L.; Psaro, R.; Santo, V. D. Effect of Nature and Location of Defects on Bandgap Narrowing in Black TiO2 Nanoparticles. *J. Am. Chem. Soc.* **2012**, *134*, 7600–7603.

(56) Liu, Y.; Lian, J.; Sun, Z.; Zhao, M.; Shi, Y.; Song, H. The First-Principles Study for the Novel Optical Properties of LiTi2O4, Li4Ti5O12, Li2Ti2O4 and Li7Ti5O12. *Chem. Phys. Lett.* **2017**, *677*, 114–119. https://doi.org/10.1016/j.cplett.2017.04.009.

(57) Joshi, Y.; Saksena, A.; Hadjixenophontos, E.; Schneider, J. M.; Schmitz, G. Electrochromic Behavior and Phase Transformation in Li 4 + x Ti 5 O 12 upon Lithium-Ion Deintercalation / Intercalation. *ACS Appl. Mater. Interfaces* **2020**, *12*, 10616–10625. https://doi.org/10.1021/acsami.9b19683.

(58) Jellison, G. E.; Boatner, L. A.; Budai, J. D.; Jeong, B.-S.; Norton, D. P. Spectroscopic Ellipsometry of Thin Film and Bulk Anatase (Ti O2). *J. Appl. Phys.* **2003**, *93* (12), 9537–9541. https://doi.org/10.1063/1.1573737.

(59) Hao, M. I. Z.; Ian, J. I. E. L.; Ia, Y. A. J.; In, K. U. I. J.; Iping, L. X. U.; Higao, Z.; Ang, X. I. Y.; Ang, S. H. K. Investigation of the Optical Properties of LiTi 2 O 4 and Li 4 Ti 5

O 12 Spinel Films by Spectroscopic Ellipsometry. *Opt. Mater. Express* **2016**, *6* (10), 3366–3374.

(60) Raja, M. W.; Mahanty, S.; Kundu, M.; Basu, R. N. Synthesis of Nanocrystalline Li 4 Ti 5 O 12 by a Novel Aqueous Combustion Technique. *J. Alloys Compd.* **2009**, *468*, 258–262. https://doi.org/10.1016/j.jallcom.2007.12.072.

(61) Liu, D.; Ouyang, C.; Shu, J.; Jiang, J.; Wang, Z.; Chen, L. Theoretical Study of Cation Doping Effect on the Electronic Conductivity of Li 4 Ti 5 O 12. *Phys. status solidi* **2006**, *1841* (8), 1835–1841. https://doi.org/10.1002/pssb.200541404.

(62) Jhan, Y. R.; Duh, J. G. Electrochemical Performance and Low Discharge Cut-off Voltage Behavior of Ruthenium Doped Li 4Ti 5O 12 with Improved Energy Density. *Electrochim. Acta* **2012**, *63*, 9–15. https://doi.org/10.1016/j.electacta.2011.12.014.

(63) Meng, X.; Wang, X.; Zhou, Y.; Tong, L.; Zeng, X.; Chen, X. Spinel Lithium Titanate from Brookite Nanocrystallites. *Ceram. Int.* **2014**, *40* (3), 4989–4993. https://doi.org/10.1016/j.ceramint.2013.08.054.

(64) Özen, S.; Şenay, V.; Pat, S.; Korkmaz, Ş. Optical, Morphological Properties and Surface Energy of the Transparent Li4Ti5O12 (LTO) Thin Film as Anode Material for Secondary Type Batteries. *J. Phys. D. Appl. Phys.* **2016**, *49* (10). https://doi.org/10.1088/0022-3727/49/10/105303.

(65) Ge, H.; Tian, H.; Song, H.; Liu, D.; Wu, S.; Shi, X. Study on the Energy Band Structure and Photoelectrochemical Performances of Spinel Li 4 Ti 5 O 12. *Mater. Res. Bull.* **2014**, *61*, 459–462. https://doi.org/10.1016/j.materresbull.2014.10.064.

(66) Ge, H.; Li, N.; Li, D.; Dai, C.; Wang, D. Study on the Theoretical Capacity of Spinel Lithium Titanate Induced by Low-Potential Intercalation. *J. Phys. Chem. C* **2009**, *113*, 6324–6326.

(67) Liu, H.; Zhu, Z.; Huang, J.; He, X.; Chen, Y.; Zhang, R.; Lin, R.; Li, Y.; Yu, S.; Xing, X.; Yan, Q.; Li, X.; Frost, M. J.; An, K.; Feng, J.; Kostecki, R.; Xin, H.; Ong, S. P.; Liu, P. Elucidating the Limit of Li Insertion into the Spinel Li 4 Ti 5 O 12. *ACS Mater. Lett.* **2019**, *1*, 96–102. https://doi.org/10.1021/acsmaterialslett.9b00099.

(68) Subramanian, V.; Karki, A.; Gnanasekar, K. I.; Posey, F.; Rambabu, B. Nanocrystalline TiO 2 (Anatase) for Li-Ion Batteries. *J. Power Sources* **2006**, *159*, 186–192. https://doi.org/10.1016/j.jpowsour.2006.04.027.

(69) Wu, G.; Li, P.; Zhu, C.; Lei, Y.; Zhao, H.; Li, T.; Yue, H.; Dou, B.; Gao, Y.; Yang, X. Amorphous Titanium Oxide Passivated Lithium Titanium Phosphate Electrode for High

Stable Aqueous Lithium Ion Batteries with Oxygen Tolerance. *Electrochim. Acta* **2017**, *246*, 720–729. https://doi.org/10.1016/j.electacta.2017.06.093.

(70) Wagemaker, M.; Borghols, W. J. H.; Mulder, F. M. Large Impact of Particle Size on Insertion Reactions . A Case for Anatase Li x TiO 2. *J. Am. Chem. Soc.* **2007**, *11* (8), 4323–4327.

(71) Sudant, G.; Baudrin, E.; Larcher, D.; Tarascon, J. Electrochemical Lithium Reactivity with Nanotextured Anatase-Type TiO 2. *J. Mater. Chem.* **2005**, *15*, 1263–1269. https://doi.org/10.1039/b416176a.

(72) Bach, S.; Pereira-ramos, J. P.; Willman, P. Investigation of Lithium Diffusion in Nano-Sized Rutile TiO 2 by Impedance Spectroscopy. *Electrochim. Acta* **2010**, *55* (17), 4952–4959. https://doi.org/10.1016/j.electacta.2010.03.101.

5. In-situ and operando techniques

5.1 Introduction

Dynamic phenomena exceptionally occurring while device operation, such as interphase and lattice transformations, solid-electrolyte interphase (SEI) formation and Li-ion transport mechanisms, created the necessity to study and visualize in real time the kinetics of charge and mass transport taking place in battery materials.[1] The interest in developing suitable in-situ and operando characterization techniques therefore is great and mainly oriented on understanding those phenomena in their full complexity and further impact on the overall device performance. The current state-of-the-art has been described in detail in **Section 1.5** and ranges from highly sophisticated methods such as isotopic ion exchange,[2] in-situ TEM[2] and operando synchrotron X-ray analysis,[3–10] to more commonly available techniques such as in-situ X-Ray diffraction,[11–13] Atomic Force Microscopy (AFM)[14,15], Raman spectroscopy[16–18] and Fourier Transform Infrared (FTIR) Spectroscopy.[19,20] Non-destructive, optical methods such as Raman spectroscopy and spectroscopic ellipsometry, easy to apply in ambient conditions with low cost and little maintenance, are a sustainable choice and increase the popularity of such techniques due to their facile implementation. Nonetheless, Raman spectroscopy generously depends on the Raman activity of each material, which is complicated to predict in practical terms for non-stationary phases forming upon device operation. Complementary Spectroscopic Ellipsometry (SE) can build a good addition in the observation of phase and interphase transitions during charge and discharge, as it is especially sensitive to changes in the materials dispersion and absorption, directly correlated to the electronic band transitions of redox reactions and the resulting changes in volume.

As transitions of the LMO spinel phase in the full electrochemical potential range are rather complex, the different reactions observed from electrochemical characterization in **Section 4.2** are summarized in **Fig. 5.1.1** in order to support the following discussion on the operando optical characterization.

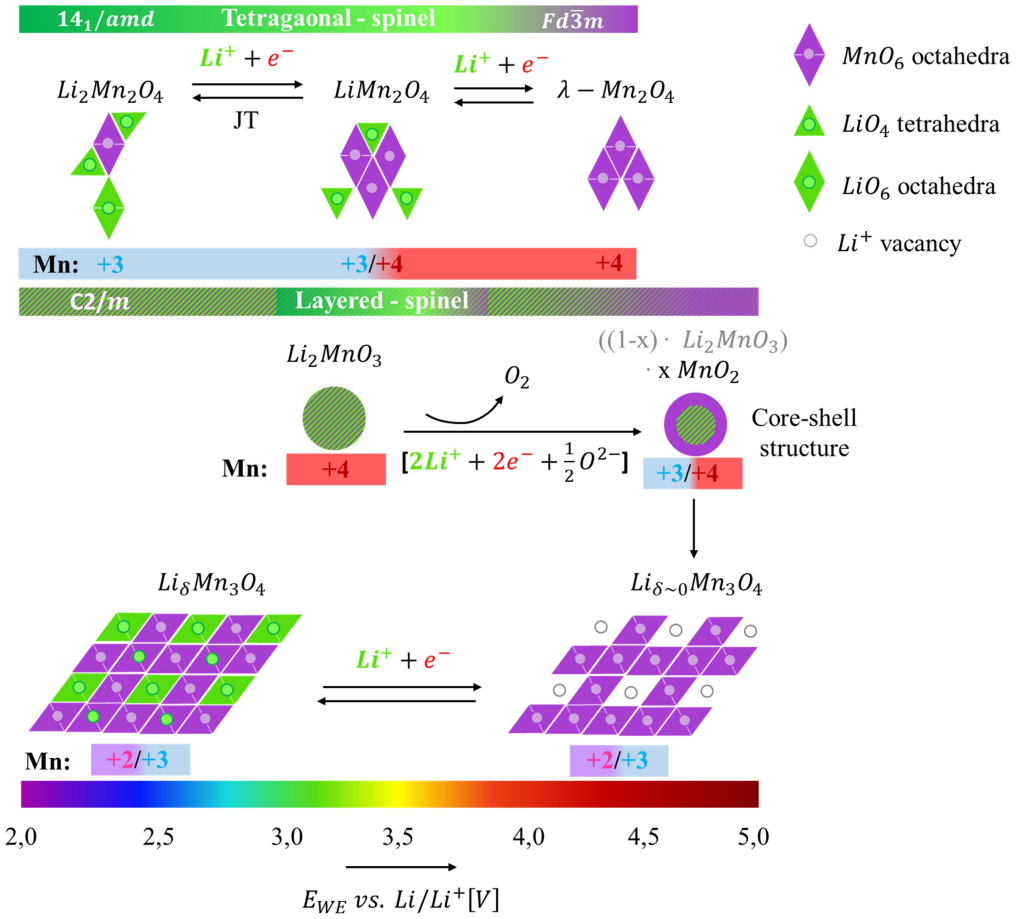

Fig. 5.1.1: Phase transformations for spinel LMO (tetragonal-spinel) and the monoclinic Li_2MnO_3 (layered-spinel) upon continuous de-intercalation and intercalation of Li^+ in the full electrochemical potential window of LMO cathode materials between 2.0 – 5.0 V vs. Li/Li^+.

A variety of phenomena occurs upon electrochemical cycling, especially when lithiating LMO below 3.5 V vs. Li/Li^+, leading to (i) the onset of a severe Jahn-Teller (JT) distortion,[21,22] (ii) the simultaneous dissolution of Mn^{2+} and formation of MnO as a result of the disproportionation of Mn^{4+} to Mn^{3+},[22,23] and (iii) the lattice transformation from spinel LMO ($Fd\bar{3}m$) to tetragonal $Li_2Mn_2O_4$ ($14_1/amd$).[24]

Additionally, the as-deposited layers have proven to consist of spinel LMO in co-existence with Li_2MnO_3 ($C2/m$), which is supported by previous observations based on Raman spectra and cyclic voltammograms for the extended voltage range of 2.0 – 5.0 V vs. Li/Li^+ (see **Section 4.2.4**). For Li_2MnO_3 the transform of the Mn^{4+} oxidation states occurs only under extraction of lithium and oxygen simultaneously at potentials above 4.5 V vs. Li/Li^+. This electrochemical activation transforms the layer into (1-x) Li_2MnO_3 · x $LiMnO_2$ with a mixed Mn^{3+}/Mn^{4+} oxidation state under oxygen evolution.[25,26] A core-shell structure is expected to form for polycrystalline

materials of nano-shaped crystallites, as demonstrated by *Guerrini et al.*[27] The core remains Li_2MnO_3, whereas the shell transforms into a highly disordered MnO_2. After various cycles the layer stabilizes, as the oxygen evolution from the layered transition decreases and the material is reduced to a stable defect-spinel of $Li_\delta Mn_3O_4$ with Mn^{2+} and Mn^{3+}, as reported by *Shimoda et al.*[26]

In the following sections, the in-time performance of multi-layer $LiMn_2O_4$ (LMO) thin films deposited by LA-PLD is studied by operando Raman spectroscopy in **Section 5.2**. Further LMO and RF-sputtered $LiMn_{1.5}Ni_{0.5}O_4$ (LMNO) cathode thin films are analyzed for the first time by operando SE in **Section 5.3**.

5.2 Operando Raman spectroscopy

Raman spectroscopy so far has been widely probed for the spatial and in-time resolution of mass transport correlated phenomena on several battery materials and devices,[17,28,29] using additionally surface enhanced (SERS)[30] and tip enhanced (TERS)[31] techniques or imaging approaches in combination with confocal microscopes.[32] Hence Raman scattering represents an already well-established method for tracking the in-time phase transformations upon redox reactions, following the SEI formation, as well as tracing lithiation paths and degradation mechanisms.[29]

5.2.1 In-time tracking of LMO phase transformations during electrochemical Li insertion/extraction

The operando evolution of Raman active vibrational modes in the LMO cathode materials upon lithium (de-) intercalation was previously studied by *Kanoh et al.*[33] and further refined by *Slautin et al.*[32] using confocal Raman microscopy, monitoring the state of charge (SOC) by a visualized local tracking of lithiation paths upon phase formation. In the light of these reports, the phase evolution of Raman active modes upon charge and discharge of LMO thin films deposited by LA-PLD is studied in the following, as specific nano-size related effects of the thin film microstructure may have an impact on the classical electrochemical performance. Therefore an optical chamber has been prepared as described in **Section 2.6.1** in order to contain the three-electrode setup of LMO (WE), the Ag/AgCl reference (RE) and a platinum mesh (CE), all jointly being introduced in

the aqueous electrolyte of 1 M Li_2SO_4. LMO thin films are consisting of 80 subsequent deposition cycles using the LA-PLD multi-layering approach described in **Section 4.2** and exhibit a thickness of 340 nm. Electrochemical characterization of these thin films has been performed separately and is described in **Section 4.2.3**, with the involved phenomena summarized in **Fig. 5.1.1**. The operando obtained Raman vibrational modes when cycling between 0.5 – 1.1 V vs. Ag/AgCl (corresponding to ~ 3.5 – 4.5 V vs. Li/Li^+) are shown in **Fig. 5.2.1**.

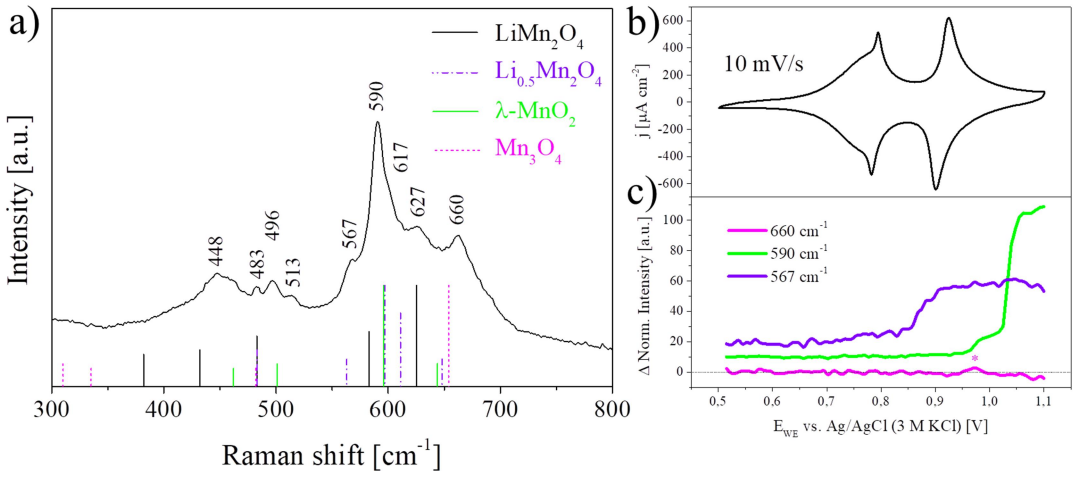

Fig. 5.2.1: Average of all Raman vibrational modes for $LiMn_2O_4$ cathode thin films in (a) occurring during the complete potential sweep in (b) from 0.5 – 1.1 V vs. Ag/AgCl (3 M KCl) in 1 M Li_2SO_4 aqueous solution. The change in the normalized intensity (horizontally shifted traces) for characteristic vibrational modes related to $Li_{0.5}Mn_2O_4$ (567 cm^{-1}), λ-MnO_2 (590 cm^{-1}) and Mn_3O_4 (660 cm^{-1}) is shown upon the applied electrochemical potential in (c).[34] The change in normalized intensity of the signal at 660 cm^{-1} has been amplified 3-times its initial value for demonstration purposes.

The real-time acquisition within a fraction of seconds efficiently monitors the evolution of each phase occurring upon lithium insertion and de-insertion over time, as demonstrated in **Fig. 5.2.1 (a)** for all active vibrational modes appearing during the cyclic voltammetry, averaged in one Raman spectrum. The strong bands appearing between 550 – 700 cm^{-1} could all be assigned to LMO (627 cm^{-1}) and its common intermediate de-intercalation phases such as $Li_{0.5}Mn_2O_4$ (617 cm^{-1}) and λ-MnO_2 (590 cm^{-1}), or typical secondary phases such as Mn_3O_4 (660 cm^{-1}), stemming from symmetrical stretching modes of the MnO_6 octahedra assigned to A_{1g} ($Fd\bar{3}m$) or A_1 ($F\bar{4}3m$).[35,36] Weaker bands are observed between 400 – 550 cm^{-1} for F_{2g} (F_2 for $F\bar{4}3m$) phonon modes of lower symmetry for the Mn-O and O-O bonds,[34,36] with additional bands occurring at 448 cm^{-1} and 513 cm^{-1}, which could not be assigned to any particular manganite phase, but are sharing similar peak positions

to monoclinic ordered LMO compounds and may be the result of locally distorted Mn-O bonds.[34] Slight peak shifts in comparison to the references shown in **Fig. 5.2.1 (a)** might be the result of some aging in the material, which can be affected by a difference up to 10 cm^{-1} from the initial peak position,[32] or some laser induced decomposition.[35,37]

Monitoring of the vibrational modes over the electrochemical potential in **Fig. 5.2.1 (c)** has been concentrated on the strongest or best definable phonon response for each material. The A_{1g} phonon at 627 cm^{-1} assigned to spinel LMO performed under a fluent peak shift upon lithium de-insertion of -10 cm^{-1}, resulting in two signals at 596 cm^{-1} and 617 cm^{-1} appearing around 0.7 V vs. Ag/AgCl, which then can be assigned to A_1 and F_2 phonons of $Li_{0.5}Mn_2O_4$, respectively.[36] This is in agreement with the two-step (de-) intercalation mechanism, leading to the fully or partial phase transformation from $Fd\bar{3}m$ to $F\bar{4}3m$ between $0.04 < x < 0.74$ in $Li_xMn_2O_4$,[38] as previously described in **Section 1.4.1** and **4.2.3**. In order to better distinguish the intermediate phase from others, the well separated Raman shift at 567 cm^{-1}, corresponding equally to A_1 phonons from $Li_{0.5}Mn_2O_4$, is monitored in **Fig. 5.2.1 (c)**. Its intensity starts to increase around 0.70 V as the initiation of the first Li de-intercalation step and further shows a strong increment when passing to the second step around 0.85 V. It remains constantly intense, even during the onset of λ-MnO_2 formation around 0.98 V, which is clearly indicated by the sudden rise in intensity for the A_{1g} phonon at 590 cm^{-1}. Hence a mixed state of two-phases is present at higher voltages between 0.98 – 1.10 V, which is a classical phenomenon of stoichiometric $LiMn_2O_4$ and may also be attributed to the difficulties of de-lithiating the layer completely.[38–40] Further the A_{1g} mode at 660 cm^{-1} exhibits a minor peak (indicated by an asterisk) at 0.98 V during the simultaneous onset of λ-MnO_2 formation. This could result from Mn_3O_4 formation and dissolution upon charge and discharge,[32] strong local heat evolution during laser excitation and the subsequent formation of Mn_3O_4,[37] or amount to the A_1 mode of $Li_{0.5}Mn_2O_4$ having a weak band at 657 cm^{-1}.[32,36]

The assignment and monitoring of broad or weak vibrational modes can be challenging, due to unfavorable signal-to-noise ratios during the operando acquisition on thin films. Those arise from the thin film character itself, as well as from relatively short acquisition times in order to follow as precisely as possible the

evolution of separate Raman bands. Hence, Raman acquisitions demand time, usually in the magnitude of seconds, as their spectra need to be repeated at least twice for eliminating eventual disturbances from random noise and spikes.

5.2.2 Real-time monitoring the state of charge (SOC)

The state of charge (SOC) is a measure of the charge occupancy at the interstitial sites of the intercalation battery material normalized to the specific capacity of the active material, giving information about the entire charge or discharge status of the battery device. *Slautin et al.*[32] evaluated the peak ratio of F_{2g}/A_{1g} intensities monitoring the charge transfer upon operation, whereas the vibrational mode of $F_{2g}(1)$ at 370 cm^{-1} has been related to lithium sublattice vibrations and therefore acts as suitable indicator for lithium occupancy. For LMO thin films in this work, no peak could be detected at 370 cm^{-1}, as it has been demonstrated in **Fig. 5.2.1**., possibly resulting from a low signal-to-noise ratio or material aging effects.[32] *Kanoh et al.*[33] instead could demonstrate the logarithmic ratio of A_{1g} intensities at 590 cm^{-1} and 627 cm^{-1} to deliver some approach in monitoring the state of charge at different electrochemical potentials. The evolution of the operando Raman spectra over the full electrochemical voltammetry cycle between 0.5 – 1.1 V vs. Ag/AgCl is shown in **Fig. 5.2.2 (a)** with the change in $Log(I_{590}/I_{627})$ during the galvanostatic sweep of the electrochemical potential plotted in **(b)**.

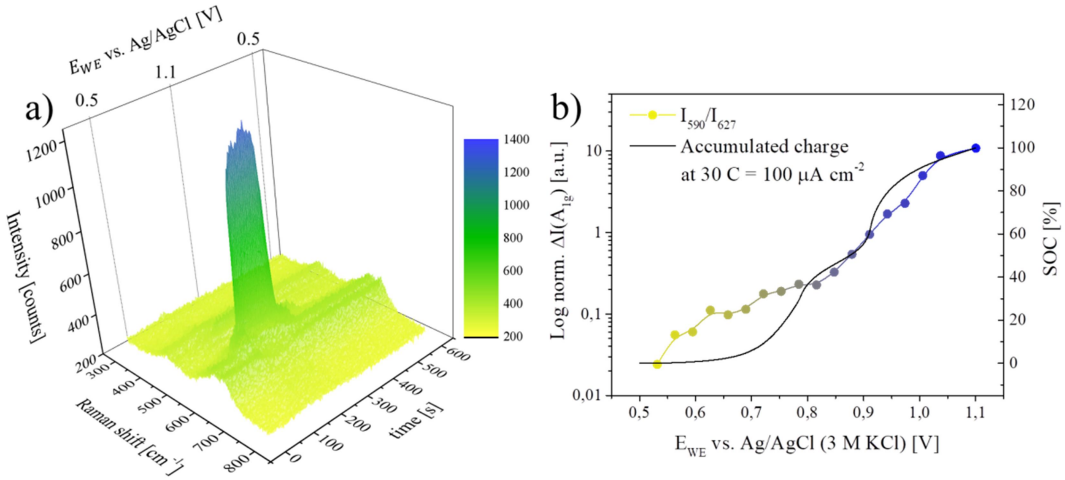

Fig. 5.2.2: Evolution of time-resolved Raman spectra in the potential range of 0.5 – 1.1 V vs. Ag/AgCl for LMO thin films deposited by multi-layer PLD in (a). Logarithmic intensity ratio of A_{1g} vibrational modes at 590 cm^{-1} and 627 cm^{-1} in (b) and its evolution over the electrochemical potential under the application of a constant current at 100 µA cm^{-2}. In addition the correlated electrochemical state of charge (SOC) is shown over the potential.

The signal of λ-MnO_2 at 590 cm^{-1} experiences a certain resonance enhancement, which *Ammundsen et al.*[36] related to the scattering of Mn^{4+} vibronic states. It dominates with its very high relative intensity the Raman spectra between 1.0 – 1.1 V vs. Ag/AgCl, especially having a great effect on the A_{1g} (A_1) vibrational modes between 550 – 700 cm^{-1}, as shown in **Fig. 5.2.2 (a)**. This is attributed to higher symmetries around the Mn^{4+} - O bonding and smaller ionic radii, whereas the Mn^{3+} formation is locally accompanied by a slight Jahn-Teller (JT) distortion, resulting in peak broadening and more peaks occurring than expected from the calculated spectra of cubic LMO.[34] Following the logarithmic intensity ratio of A_{1g} modes in **Fig. 5.2.2 (b)** for LMO and λ-MnO_2 over the potential, the state of charge can be estimated under the continuous change of ΔI.

Nonetheless, the discrepancy between the intensity ratio and the evolution of the accumulated charge is not negligible and reveals a lack in accuracy. Possible explanations result from multiple effects coming together, forming a disadvantageous signal-to-noise ratio. First, Raman signals depend on the cation order and covalence of the molecule bonding in spinels, as described by *D'Ippolito et al.*[41] Therefore the low symmetry for mixed-valent LMO, as a result of the JT distorted molecule of trivalent Mn^{3+} octahedra (see details in **Section 1.4.1**), and the low degree of Mn covalency (similar to Fe) are causing a low intensity in the Raman scattering.[36,41,42] In combination with less material available due to the thin film character and the fast acquisition within a few seconds, the overall signal of LMO thin films is damped and an insufficient accuracy for a fast monitoring of the real SOC results.

5.3 Operando spectroscopic ellipsometry

Spectroscopic ellipsometry (SE) is a powerful technique in observing the change of polarization when linear polarized light is passing through matter. The resulting optical signal is fitted to a physical model and directly related to material specific properties such as the complex permittivity ε (see **Section 2.5.3.1**), which can be therefore calculated as a function of the photon energy.[43] Hence the resulting optical dispersion and absorption can be determined at specific energies, being directly correlated to the electronic band structure of each material.[44,45] Accordingly, information concerning the materials band gap, crystallinity,

thickness, surface and interface roughness can be deduced, especially valuable for complex ultrathin multi-layer materials.[46]

Compositional ratios involving materials with different optical properties can be obtained by SE under application of the Bruggeman effective-medium approximation (EMA) for intermixed materials of more than one constituent. This approach has shown in the past to provide reliable results for crystalline thin film materials.[47,48] Despite all the valuable information yielding from SE, its implementation for operando studies in the field of lithium-ion batteries has seen very few applications so far, which have mainly been concentrated on the SEI characterization.[49,50] Only recently, our group has published a seminal work on the operando monitoring of lithium (de-) intercalation by SE based on the electrochemical analysis of LMO cathode thin films.[51]

In this thesis, the non-destructive optical tracking of the charge and discharge process of lithium manganite cathodes has been carried out using two complementary approaches, namely, one employing a monochromator combined with a triggering strategy and another, more straightforward, using a multi-wavelength (MWL) enhanced SE acquisition system. In both cases, it was possible to implement an innovative method for the time-resolved monitoring of the optical absorption assigned to the $Mn^{3+/4+}$ transition upon lithium insertion and extraction in LMO. Experiments have been carried out in a suitable custom-made optical chamber as described in **Section 2.6.1** in order to meet the requirements of the optical geometries for SE. Measurements were collected in aqueous electrolytes in ambient air for LMO cathode thin films in **Section 5.3.1**, and further in solvent based electrolytes assembled in protected Ar-atmosphere with subsequent air-tight sealing of the optical chamber. Aprotic solvent based electrolytes are implemented due to their extended electrochemical stability window and hence are applied in **Section 5.3.1** for monitoring the 3 V plateau of LMO and in **Section 5.3.2** the electrochemical performance of sputter deposited LMNO layers as high-voltage cathodes.

5.3.1 Operando studies on LMO thin film cathodes

First observations of the LMO multi-layer thin films by operando SE for the lithium (de-) intercalation in aqueous and solvent based electrolytes are provided in the

following sections, concerning the accurate monitoring of the state of charge and the phase transitions upon changes in the Mn oxidation states.

5.3.1.1 Monochromator triggering acquisition

Electrochemical (de-) insertion of Li^+ ions in LMO causes a change in the mixed-valent Mn oxidation state of +III/+IV (see **Fig. 5.1.1**), which can be followed in the optical absorption of the material upon interaction with linearly polarized UV-light. In **Fig. 5.3.1** the change in phase Δ and amplitude ratio Ψ of the wave is detected by the SE monochromator at different potential instants over the entire voltage sweep between 0.5 – 1.1 V vs. Ag/AgCl.

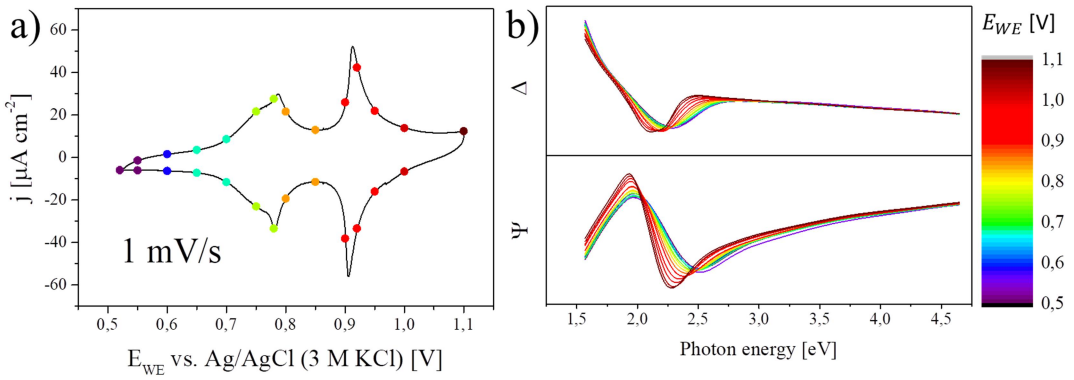

Fig. 5.3.1: Electrochemical potential sweep in (a) of the LMO thin film cathode at 1 mV s^{-1} between 0.5 – 1.1 V vs. Ag/AgCl in 1 M Li_2SO_4 aqueous electrolyte with the potential instants (circles) of spectroscopic ellipsometry monochromator acquisition indicated. The evolution of the spectroscopic ellipsometry raw signals (Δ and Ψ) is shown operando for a single charge/discharge process upon voltage sweep in (b). The colors in a) and b) refer to the voltage of the WE and are represented in the scale bar on the right.

As shown in **Fig. 5.3.1 (a)**, the electrochemical cycling clearly reveals the redox-peaks for the two-step (de-) intercalation of lithium, described in **Section 1.4.1**, and the optical signal represented by Δ and Ψ in **(b)** follows the changing potential accordingly. The correlation of the optical absorption ε_i to Δ and Ψ is described in **Eq. 2.5.11** and **2.5.12**, resolving in the complex dielectric function (see **Section 2.5.3.1** for further details). Optical spectra are modeled with a series of Tauc-Lorentz oscillators, as described in **Section 2.5.3.2**, forming a single material model which is embedded in the Bruggeman effective-medium approximation (EMA), in order to describe the complex multi-layer system of substrate, layer, surface and ambient. This approximation has shown reliable results for obtaining a reasonable approximation on physicochemical material properties, especially concerning

polycrystalline dielectrics with a certain surface roughness.[47,48,52] In **Fig. 5.3.2** the comparison is shown for a single layer model **(a)** and two different versions of the Bruggeman EMA used in this work **(b,c)**.

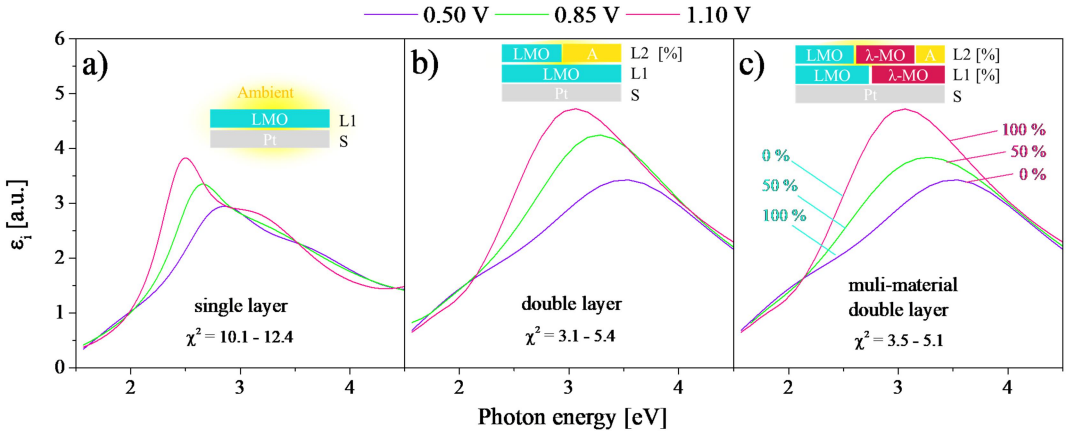

Fig. 5.3.2: Different modeling approaches for in-situ SE spectra, with (a) LMO single layer (L1) on the Pt-substrate (S) and (b) the Bruggeman EMA double layer approach of a pure LMO layer (L1) and a mixed layer (L2) of LMO and the ambient (A). In (c) an extension of the Bruggeman EMA is shown, adapted to the in-situ modeling of non-stationary material properties including multi-material layers. The suitability to model the electrochemical voltage dependent optical properties at 0.50 V, 0.85 V and 1.10 V vs. Ag/AgCl is expressed by the weighted sum of squared deviations χ^2.

The obtained spectra in **Fig. 5.3.2 (a)** for a single layer differ very much from the optical absorption of the layers approximated by the Bruggeman EMA and exhibit relatively high values for the weighted sum of squared deviations $\chi^2 \approx 12$, serving as indicator for the goodness of a fit and is recommended to range around 1.[47] Hence an additional layer is added, in order to involve the surface roughness, simplified by a mixed material proportional to the LMO material model and the optical properties of the ambient. For operando measurements the ambient is adapted to the optical properties of the surrounding ionic liquid (see **Section 2.5.3.2**). Under electrochemical polarization, the material properties change and the material model is fitted, resulting in the optical properties of LMO in the bulk layer (L1) and the mixed surface layer (L2) at different electrode potentials in **Fig. 5.3.2 (b)**. The modeled optical absorption is much more accurate, as the quality of the fit improved to $\chi^2 \leq 5.4$. The EMA model in **(b)** can be further modified, under consideration of the reversible material transformation taking place for electrochemical redox reactions. Material models are fixed for the lithiated LMO and the de-lithiated λ-MnO_2 (λ-MO) in **Fig. 5.3.2 (c)** at their corresponding potentials. Upon electrode polarization their partial concentration in the double

layer is modeled and can be expressed as a certain percentage. This perfectly reflects the transition between Mn^{3+} and Mn^{4+} oxidation states and can be directly correlated to the exchange of one Li^{+} ion. The goodness of the fit appears slightly improved with $\chi^2 \leq 5.1$, but the main advantage of this approach lies in the fast and direct in-situ monitoring of the Li concentration in the cathode material. This approximation becomes specifically valuable for MWL acquisitions, as further described in **Section 5.3.1.2**, where a multitude of hundreds or thousands of spectra need data processing.

For the modeling of single SE spectra obtained in-situ by the monochromator acquisition, the approach demonstrated in **Fig. 5.3.2 (b)** has been chosen. The optical properties of LMO are represented in a single material model consisting of 4 Tauc-Lorentz oscillators, with each oscillator ascribed to classic transition energies of the electronic states present in the hybridized molecule orbital of O^{2-} (2p) and $Mn^{3+/4+}$ (3d) forming the MnO_6 octahedra constituting LMO. Based on the crystal field theory concerning the 3d-orbitals of manganese, their energetic levels split into t_{2g} and e_g bands upon hybridization with oxygen.[53] As the Li^{+} (de-) intercalation is accompanied by a change in the manganese oxidation state (compare **Fig. 5.1.1**), three absorption bands are included in the models correlated to $Mn^{3+/4+}$ (t_{2g}) interband transitions at low energies between 1.9 – 2.3 eV, Mn^{4+} (e_g) around 2.8 - 3.0 eV and Mn^{3+} (e_g) transitions at 3.4 – 3.6 eV,[44,45] as indicated in **Fig. 5.3.3 (a)**. The good agreement between fitting and experimentally obtained data is shown in **Fig. 2.5.4** (see **Section 2.5.3.2**) for the pristine layer of LMO in air, which is transferable to the modeling results in-situ.

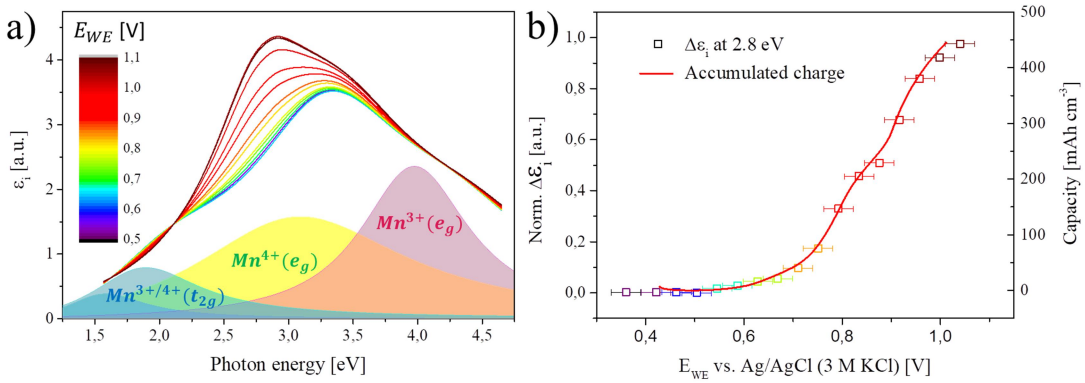

Fig. 5.3.3: Imaginary part of the dielectric constant (ε_i) extracted from fitted spectra at different working electrode (WE) potentials in (a), using the model containing several Tauc-Lorentz oscillators at different photon energies for $Mn^{3+/4+}$ correlated band

transitions. The evolution of accumulated charge in (b) upon the galvanostatic potential sweep is compared to the normalized change in ε_i at 2.8 eV photon energy.

In **Fig. 5.3.3** optical spectra have been obtained from a series of quasi-stationary electrochemical potentials upon the constant application of a cathodic current. The observable optical absorption in **(a)** follows the electrochemical potential when extracting lithium from the $Li_xMn_2O_4$ lattice, which is visible in the peak shift of Mn^{3+} (e_g) to lower energies of Mn^{4+} (e_g) around 2.8 eV, summarized in **(b)**. The decrease in energy stems from the stronger Coulomb attraction between the d electrons of Mn^{4+} than for Mn^{3+}, resulting in higher binding energies and a decrease in the energy necessary for charge-transfer transitions.[45] In **Fig. 5.3.3 (b)** the evolution of the intensity for the optical absorption at 2.8 eV follows precisely the accumulated charge between 0.35 – 1.05 V vs. Ag/AgCl, giving an accurate insight in the materials current state of charge by tracking the presence of Mn^{4+}. Following the accumulated charge in **Fig. 5.3.3 (b)**, it can be evidenced that operando SE allows an excellent monitoring of the SOC in thin film battery electrodes, which is much more accurate, than the operando Raman spectra obtained in **Fig. 5.2.3**.

Relevant mass transport properties, such as the diffusivity, require the analysis of a transient between different states of charge as a function of time. However, SE measurements are facing challenges in the timescale below seconds, typical for the diffusion phenomena in thin films, due to the extended time consumption required by the monochromator to shift the frequency range. Solutions based on advanced multi-wavelength ellipsometers (able to acquire the whole spectra in 100 ms) or conventional single-wavelength ellipsometry combined with triggering strategies along different cycles are presented in the following. An innovative triggering strategy of the monochromator guided acquisition has been used in this work to reconstruct the fast transient signal along a single potential step carried out between 0.35 V and 1.05 V vs. Ag/AgCl for 19 repetitive times, each at a different photon energy in the optical window between 1.4 eV to 4.2 eV (see **Section 2.6.2** for more details on the triggered optical acquisition method). This single-wavelength monitoring requires sufficiently stable samples during all the acquisition procedure, which LMO multi-layer thin films have proven to fulfill when comparing to the electrochemical experiments conducted in **Section 4.2.3** and in previous publications on their electrochemical stability.[54,55] The resulting optical spectra of ε_i

and their evolution upon a single voltage step in time are collected in **Fig. 5.3.4 (a)**, following the complete de-lithiation of the thin layer.

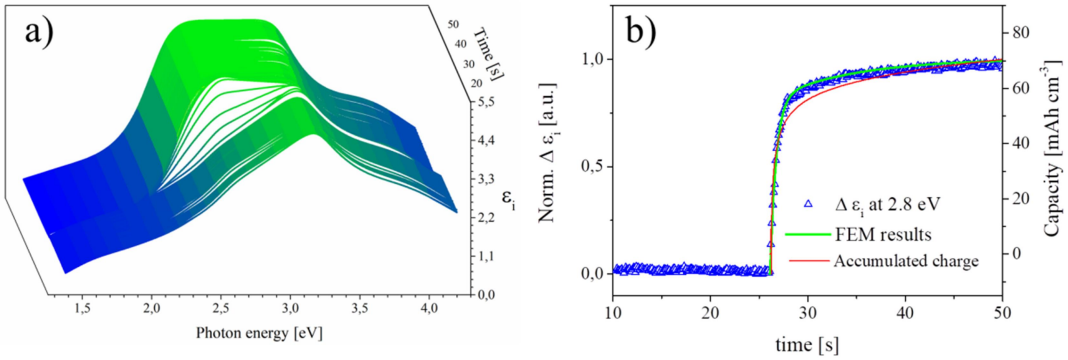

Fig. 5.3.4: Optical absorption ε_i evolving over time when passing from 0.35 V to 1.05 V vs. Ag/AgCl in a sudden potential step in (a). The change in ε_i at 2.8 eV is monitored during that time in (b), whereas the red line corresponds to the experimentally obtained accumulated charge and the green line results from the FEM model for such sudden de-lithiation, shown in the inset for a cylindrical grain of 60 nm diameter. The color scale indicates the normalized lithium content with its minimum (blue) and maximum (red).

The shift of optical absorption bands to lower photon energies in **Fig. 5.3.4 (a)** again indicates the transition of manganese oxidation states from +III to +IV. The potentiostatic de-lithiation of the layer can further be corroborated, when extracting the signal of ε_i at 2.8 eV over time and plotting it together with the accumulated charge (capacity) during the potential step from 0.35 V to 1.05 V vs. Ag/AgCl in **Fig. 5.3.4 (b)**. The transient in optical absorption and charge coincide very much, enabling the tracking of Li^+ occupation in the spinel lattice at every moment. As can be seen in the normalized change of the optical absorption, a fast Mn oxidation takes place immediately after the sudden potential step, leading to an extraction of more than 80% of the final charge within the first 2 seconds. Subsequently a less pronounced variation follows, leading to the charge saturating at a constant level around 70 mAh cm^{-3} in the remaining 28 seconds. This extremely fast charge-transfer has been linked in the past to the possibility of some pseudo-capacitive behavior of LMO thin film cathodes,[54,56–61] typically attributed to (i) charge-transfer processes with surface atoms and (ii) less pronounced contributions from a purely capacitive double layer. However, operando SE is able to relate the observed charge-transfer to the transition of the manganese oxidation state in the LMO bulk, by definition acting as faradaic contribution to the accumulated charge (red line in **Fig. 5.3.4 (b)**). Hence the hypothesis of pseudo-capacitive charge storage in LMO thin films is not further supported, as all the introduced charge appears to be

immediately invested in the bulk electrochemical oxidation, needless of additional surface governed capacitive phenomena.

To further corroborate this point, the results have been contrasted with a finite element study (FEM), which provides quantitative information in such a complex system. A 2D model has been used consisting of cylindrical grains on an ion-blocking substrate (see **Section 2.7** for details on the fitting procedure). The best fit obtained is represented by a green line in **Fig. 5.3.4 (b)**, corresponding to a chemical diffusivity (D_{Li}) for Li^+ ion in LMO of $3.5 \cdot 10^{-12}$ cm^2 s^{-1}. A wide range of values for D_{Li} are found in literature for this material, which can be partially explained by factors like microstructure, stress, etc.[62] that have a huge impact on the Li^+ diffusivity, but also in the particularities of the experimental conditions, hence providing D_{Li} values on similar LMO thin films in a range of 10^{-12} to 10^{-10} cm^2 s^{-1} for different techniques and microstructures.[63–71] Therefore, the here presented results demonstrate the apparent Li^+ de-insertion to be guided by faradaic and therefore diffusion limited charge transfer phenomena, potentially supported by a high diffusivity of LMO.

5.3.1.2 Multi-wavelength acquisition

The very same layers discussed in the previous section have been used to study their change in optical properties upon galvanostatic charge and discharge curves at different C-rates, using the multi-wavelength acquisition where spectra could be obtained every 100 ms, as demonstrated in **Fig. 5.3.5**.

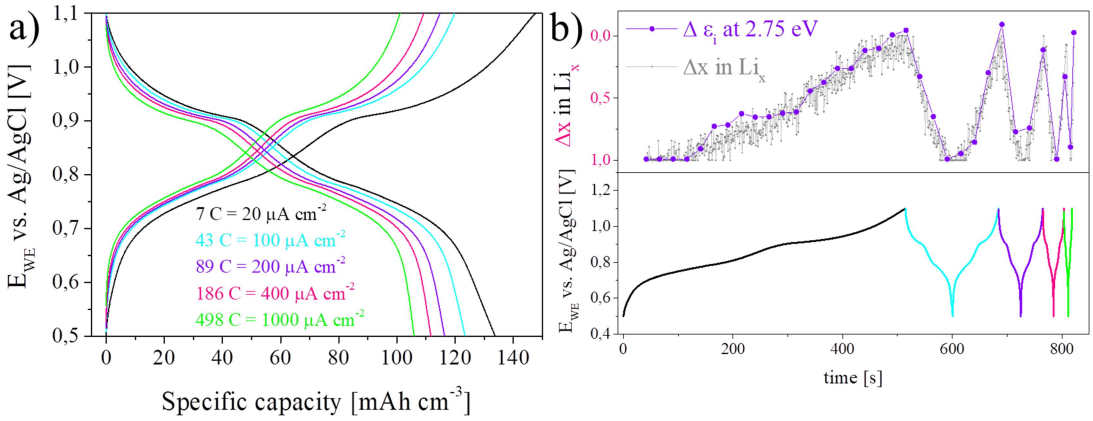

Fig. 5.3.5: Galvanostatic charge and discharge curves at different C-rates (7 – 498 C) in (a) and the correlated evolution of the optical absorption ε_i extracted from optical models at 2.8 eV every 50 s following the charge/discharge in (b) during multi-wavelength

acquisition. Additionally the variation of x in Li_x is modeled for all spectra obtained at every 100 ms.

Besides the great advantage of fast MWL acquisition providing the possibility of monitoring rapid electrochemical phenomena, it also creates a vast amount of optical spectra within a very short time, which are in need of an accurate and efficient modeling approach. For this reason the model described earlier in **Fig. 5.3.2 (c)** is applied, based on the Bruggeman EMA in a modified multi-material approach. This allows for the extraction of the nominal concentration of the involved compounds, which for LMO can be correlated to the amount of lithium ranging between $0 \leq x \leq 1$ in $Li_xMn_2O_4$. The full evolution of Δx during MWL acquisition is shown for each spectrum collected every 100 ms in **Fig. 5.3.5 (b)**. The values perfectly reflect the time dependent evolution of the electrochemical potential for C-rates as high as ~ 500 C. In addition, the evolution of the optical absorption at 2.8 eV is extracted for every 50 s, which overlaps with Δx and indicates the values to be directly correlated to the materials electronic band structure.

Both ε_i and Δx follow precisely the corresponding galvanostatic charge and discharge curves in **Fig. 5.3.5 (c)**. As a result, besides the single-wavelength triggering approach previously presented for fast data acquisition during electrochemical cycling, the MWL ellipsometry provides a more facile and equally fast method for operando monitoring of redox-reactions within a fraction of seconds. The only drawback in the capabilities of the MWL technique results from the pre-determined selection and limited amount of energy channels, which complicate and partially aggravate the signal-to-noise ratio combined with the short acquisition times required. Especially when dealing with an additional absorption coming from the electrolyte, a further limitation in the spectral window and less points in the optical spectra can lead to further uncertainties in the already complex modeling of SE optical spectra.

5.3.1.3 Monitoring of the phase transitions in the 3 V plateau

In order to gain insight into the evolution of optical properties upon the charge transfer process of LMO thin films in their full electrochemical potential range between 2.0 – 5.0 V vs. Li/Li^+, the samples have been introduced in the electrolyte solution of $LiPF_6$ EC/DMC (1:1) under protective Ar-atmosphere (see details in

Section 2.6.2) and transferred to ambient under air-tight sealing of the optical chamber. Purely electrochemical measurements for the extended voltage range of LMO multi-layers deposited by PLD, exploring the 3 V and 4 V plateau vs. lithium, have been presented in **Section 4.2.4** and related electrochemical phenomena are summarized in **Fig. 5.1.1**.

Cyclic voltammograms collected in **Fig. 5.3.6 (a)** are in good accordance with previously reported data in **Fig. 4.2.10**, showing good reversibility of significant redox-peaks over the full potential range. A certain layer-activation as expected from Li_2MnO_3 can be observed in **Fig. 5.3.6 (a)** when comparing the cyclic voltammograms collected before (start) and after (end) the operando SE data acquisition. Colored points in the CV symbolize the voltage instants at which optical spectra were obtained by using the monochromator SE acquisition, as for the modeling of the material a good resolution especially at low photon energies was desired. The optical absorption has been calculated under the use of the Bruggeman EMA demonstrated in **Fig. 5.3.2 (c)** and resulted in $\chi^2 \sim 5$ as fairly reliable fitting.

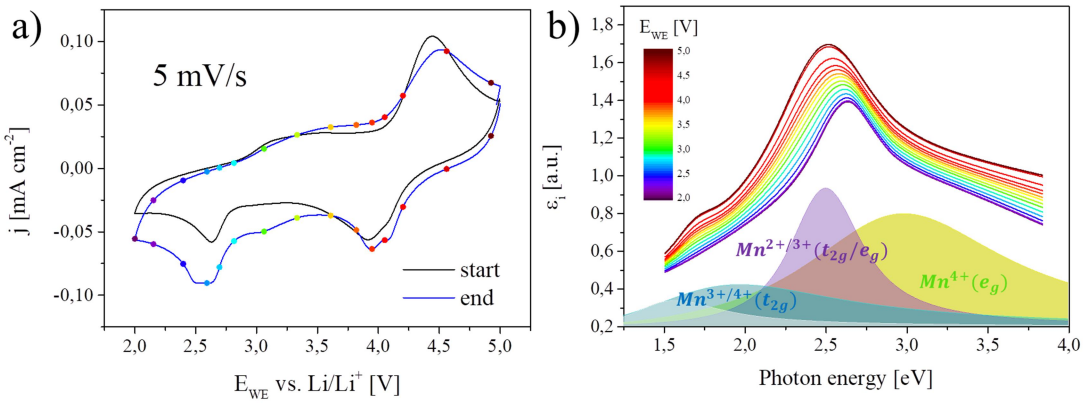

Fig. 5.3.6: Cyclic voltammetry of LMO cathode thin films between 2.0 – 5.0 V vs. Li/Li$^+$ in 1 M $LiPF_6$ EC/DMC (1:1) in (a) at 5 mV s^{-1} scan rate before (start) and after (end) the operando monitoring by SE monochromator acquisition. Voltage instants for the SE spectra are shown as circles with the color of the corresponding voltage. The related change in optical absorption ε_i and the correlated Tauc-Lorentz oscillators for the charge-transfer transitions of $Mn^{3+/4+}$ are shown in (b).

Multiple changes can be observed in the evolution of the optical absorption bands in **Fig. 5.3.6 (b)** upon lithium extraction, dominated by a very intense band between 2.5 – 2.7 eV, which increases in intensity and shifts to lower photon energies with higher electrochemical potentials. Additionally, the overall intensity of the optical

absorption increases with lithium de-intercalation. Possible associations to electrochemical phenomena are made in the following, in strong correlation to the mechanisms defined in **Fig. 5.1.1**:

(i) Layer activation: During electrochemical lithium de-intercalation in **Fig. 5.3.6 (b)**, the optical absorption obtained from the multi-material uncovers an intense signal of ε_i at photon energies ~ 2.6 eV for the 3 V plateau. This absorption band shifts upon lithium de-intercalation towards lower photon energies ~ 2.4 eV with continuous increase in the intensity. Comparing to literature,[44,72,73] the absorption band between 2.3 - 2.6 eV can further be attributed to the octahedral Mn^{3+} environment of $(MnO_6)^{9-}$ for $A_xMn_{2-x}O_3$ (A is a metal or transition metal cation) with a variety of interband transitions in the O^{2-} (2p) - M^{3+} (3d) hybridized orbital. Electronic states of the Mn^{2+} oxidation may form according to a certain disproportionation of the Mn^{4+}. Those are difficult to separate, as absorption bands due to Mn^{2+} transitions have shown certain overlap with the absorption band around 2.7 eV,[74–76] or have been reported at much lower photon energies,[44,77] which are outside the observable spectral range in **Fig. 5.3.6 (b)**. Therefore, the shift of the dominant absorption band from 2.7 eV to 2.5 eV upon lithium de-intercalation can be assigned to a change in the ligand field of Mn^{4+} upon layer activation and Mn-disproportionation under oxygen loss, creating Mn^{3+} with the formation of $LiMnO_2$ around 2.3 – 2.6 eV[27,78–80] and Mn^{2+} at 2.7 eV.[74–76]

(ii) Layered-to-spinel transformation: During electrochemical cycling, Li_2MnO_3 tends to form some core-shell structure as shown in **Fig. 5.1.1**, maintaining the pristine Li_2MnO_3 on the inside and forming some highly disordered MnO_2 on the outside.[79] The overall absorption may increase upon the high defect density in the Li-poor outer shell, as it has been observed for large defects in LMO thin films sputtered at room temperature by *Paulraj et al.*[81] This appears to be reversible when lithium is intercalated and may indicate a stabilization of the defect-spinel $Li_\delta Mn_3O_4$, which is fairly similar to the tetragonal Mn_3O_4 and has been reported by *Kim et al.*[44] to exhibit no strong absorption bands above 3.0 eV. Therefore the appearance of an additional feature upon lithium de-intercalation ~ 1.8 eV, which has previously been

attributed to Mn^{4+} d-d transitions of Li_2MnO_3 by *Tamilarasan et al.*,[78] could also describe the layered-to-spinel lattice transformation with resulting absorption bands below 2.3 eV related to Mn_3O_4.[44]

Nonetheless, the co-existing LMO spinel structure is also taking place in the redox-phenomena, although the absorption bands for Mn^{4+} (e_g) – O^{2-} (2p) appear damped in **Fig. 5.3.6 (b)**. In order to demonstrate that both materials are acting as active cathode materials during lithium (de-) intercalation, the optical absorption is extracted at 2.5 eV and 2.8 eV in **Fig. 5.3.7 (a)**, for the galvanostatic lithium de-intercalation between 2.0 – 5.0 V vs. Li/Li^+.

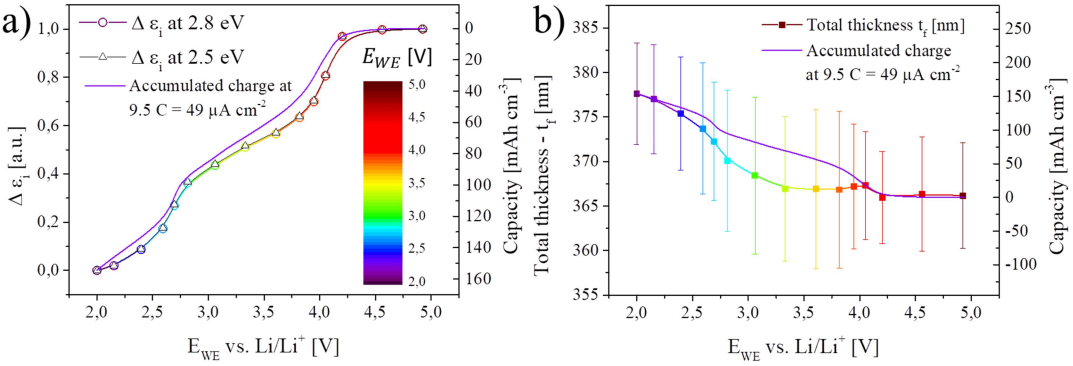

Fig. 5.3.7: The normalized change of ε_i at 2.8 eV and 2.5 eV during galvanostatic de-lithiation at 9.5 C is shown in (a) and the corresponding change in the (total) thickness upon lithium extraction in (b), for both the same C-rate and accumulated charge.

The resulting optical absorption obtained from multi-material models (see **Fig. 5.3.2 (c)**) of different oxidation states for Mn at 2.0 V and 5.0 V vs. Li/Li^+ is monitored in **Fig. 5.3.7 (a)** by following ε_i at 2.8 eV, as previously introduced for being a good indicator of Mn^{4+} (e_g) presence upon lithium extraction for $LiMn_2O_4$. In addition the optical absorption at 2.5 eV is shown, as the average position of the most intense absorption band in **Fig. 5.3.6 (b)**, which could not directly be attributed to spinel LMO. A good agreement turns out to be existent between the accumulated charge and the change in the normalized intensity of the optical absorption at 2.8 eV and 2.5 eV, both precisely following the current state of charge in the battery material.

In this model, an invariant surface layer as mixed component of LMO and $LiPF_6$ reference materials is implemented as SEI layer (~ 1.5 nm)[49] or as defective surface layer resulting from Li_2MnO_3 activation (~ 6 nm).[27] This intermediate layer is assumed to have stably formed upon former layer cycling and therefore is fixed at

an intermediate of 3 nm. This additional layer simplifies the variants in the model and supports the representation of a rough layer.[48] This allows an approximation for the change in layer thicknesses upon charge transfer, which is plotted over the corresponding electrochemical potential in **Fig. 5.3.7 (b)**. Despite the large errors, the trends of the evolution in thickness are visible and correlate with the accumulated charge especially at low and high voltages, for which the material models were created. Thickness values for intermediate potential steps are evolving with the accumulated charge. The major decrease from 378 nm to 367 nm is observed for the entire 3 V plateau between 2.0 – 3.5 V vs. Li/Li^+, amounting to ~3 % of averaged thickness change, whereas the 4 V plateau only changes the thickness for additional 0.3 %, which is negligible considering the huge errors resulting from the modeled thickness. This is in good agreement with the majority of expected lattice volume changes from literature, being attributed to the Jahn-Teller distortion and the greater acceptance of lithium in the LMO lattice, with up to 5.6 % of total volume changes in the 3 V region.[22,82,83] A further decrease in thickness upon Mn-dissolution is expectable and should be taken into consideration.[49] Hence, the variation in thickness upon electrochemical cycling appears to be a sensitive parameter in the multi-material modeling approach by Bruggeman EMA, suffering complex dependencies resulting from the surface roughness, layer porosity and systematic obstacles in obtaining a sufficiently good signal-to-noise ratio. Nonetheless, the resulting decrease of layer thickness upon lithium extraction is in the acceptable range according to literature,[49,83] and the implemented modeling approach enables the tracking of lithium occupation related volumetric expansion and compression of the layer in their tendencies.

5.3.2 Operando studies on LMNO thin film cathodes

The cathode material $LiMn_{1.5}Ni_{0.5}O_4$ (LMNO) is known for its high reversible capacity of 658 mAh cm^{-3} (147 mAh g^{-1}) and high operational voltage around 4.7 V vs. Li/Li^+, allowing high power densities in battery applications.[84,85] It is constituted of 25 % Ni^{2+} ions replacing Mn^{4+} in the 16d octahedral sites, leading to a cationic ordering of the spinel structure in $P4_332$. This resolves in the stabilization of the tetravalent Mn cations and $Ni^{2+/4+}$ being the active redox couple upon charge and discharge, explaining the higher operational window of LMNO (see DOS in **Section 1.4.1**).[86] The stoichiometry of the partial replacement of Mn with Ni is

highly dependent on the synthesis route elected, whereas usually an annealing around 700 ºC is chosen to obtain the ordered spinel structure and to eliminate the remaining Mn^{3+} from the lattice.[85]Any deviation from the Mn:Ni ratio of 3:1 will increase the cation disorder under transformation of the lattice to $Fd\bar{3}m$, allowing trivalent cations of Ni and Mn to participate in the electrochemical redox reactions at lower potentials. This may cause certain instabilities associated to Jahn-Teller distortions and the Mn-disproportion reaction of Mn^{3+} into Mn^{4+} and soluble Mn^{2+}, forming MnO which is easily dissolved in the electrolyte.[23]

In this thesis, RF-sputtered LMNO* thin films have been fabricated and annealed at 700 ºC in air and will be evaluated by Raman spectroscopy and operando spectroscopic ellipsometry in the following section. Further details on the sample fabrication are provided in **Section 2.3.7**.

5.3.2.1 Cation ordering of LMNO for optical models

Dense and smooth layers, as shown in **Fig. 5.3.8 (a)**, have been fabricated with resulting thicknesses ~ 100 nm. As the stoichiometry of LMNO strongly determines its physicochemical properties, Raman spectroscopy is chosen in order to obtain first reference points for the analysis of ellipsometry spectra. Raman spectra have proven to provide valuable insight in the cation ordering of LMNO, as reported in literature,[84,86] and are shown exemplary for the sputtered thin films used in this work in **Fig. 5.3.8 (b)**.

* RF-sputtered LMNO thin films have been fabricated by Imec (Leuven, Belgium) using the synthesis described in **Section 2.3.7**.

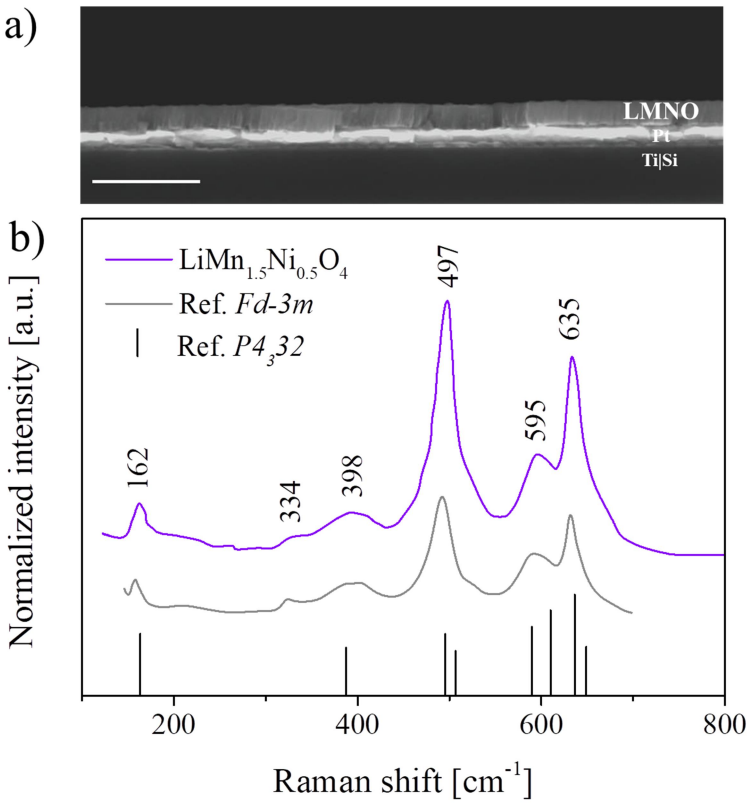

Fig. 5.3.8: SEM cross-sections of RF-sputtered LMNO thin films are shown in (a). Corresponding Raman spectra of the thin films (violet line) are shown in (b) with comparison to the cation disordered, oxygen deficient $LiMn_{1.5}Ni_{0.5}O_{4-\delta}$ in $Fd\bar{3}m$ (grey line) obtained by *Samarasingha et al.*[86] Both are compared to the ordered spinel in $P4_332$ (vertical black lines) reported by *Hallot et al.*[84]

The Raman vibrational modes occurring can be mainly assigned to the A_{1g} and F_{2g} active modes of the ordered spinel ($P4_332$) evolving from the cation ratio 3:1 of Mn:Ni in stoichiomtetric $LiMn_{1.5}Ni_{0.5}O_4$.[84] The band appearing at 595 cm^{-1} is stronger than expected for the ordered spinel and is associated in literature to the lattice disorder of $Fd\bar{3}m$.[86] This disordered spinel evolves from an oxygen deficiency, forming $LiMn_{1.5}Ni_{0.5}O_{4-\delta}$,[87] and contains notable amounts of Mn^{3+} in the structure (~ 0.21 mol per LMNO unit).[86] The effect on this cationic disordering during electrochemical cycling is evaluated in the following section by operando spectroscopic ellipsometry.

5.3.2.2 Operando SE on LMNO

The electrochemical properties of LMNO sputtered thin films are shown in **Fig. 5.3.9 (a)** upon voltage sweep in the potential range of 3.5 – 5.0 V vs. Li/Li^+ with very clear redox couples, corresponding to the reversible $Ni^{2+/4+}$ transitions. The points appearing in the CV are symbolizing the potential instants where optical

spectra have been obtained using the monochromator SE acquisition. Monochromator acquisition is chosen above the multi-wavelength at first, in order to obtain sufficiently enough points for an accurate modeling of the optical absorption. A model has been chosen accordingly, described in **Section 2.5.3.2**, and oscillator positions determined based on the previous experience with LMO thin films of very similar structure. The material model was included in a similar Bruggeman EMA demonstrated in **Fig. 5.3.2 (c)** and the resolving optical spectra are shown in **Fig. 5.3.9 (b)** with a goodness of fit between $2 \leq \chi^2 \leq 6$.

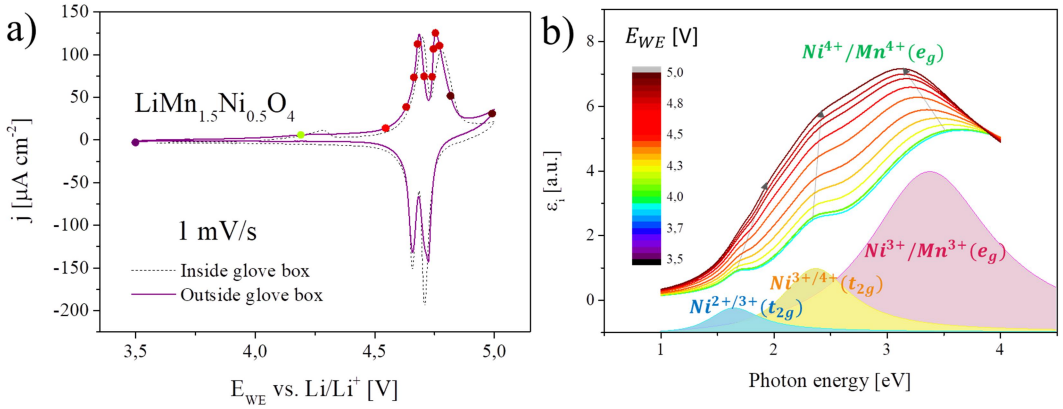

Fig. 5.3.9: Cyclic voltammetry of sputter deposited $LiMn_{1.5}Ni_{0.5}O_4$ thin film cathodes at a scan rate of 1 mV s^{-1} in 1 M $LiPF_6$ EC/DMC (1:1) in (a) when mounted in the glove box (dashed line), placed in ambient (purple line) and after the SE acquisition (red line). The evolution of the optical absorption ε_i upon voltage sweep is shown in (b) with corresponding Tauc-Lorentz oscillators for the charge-transfer transitions indicated.

The LMNO thin film is considered to be very stoichiometric when comparing the CV shown in **Fig. 5.3.9 (a)**, as there are no major features of the $Mn^{3+/4+}$ transitions visible in the potential window of 3.5 – 4.4 V vs. Li/Li^+, which assumes all the manganese and charge to be stabilized in the (IV) oxidation state.[88] After repeated electrochemical cycling, in order to ensure the thin film stability when transferring the air-tight chamber to ambient, the evolution of ε_i is monitored during the entire electrochemical window in **(b)**.

The optical features appearing at 3.5 V vs. Li/Li^+ are showing good agreement with literature,[45,89,90] and are located at photon energies of 1.6, 2.4 and 3.4 eV, as indicated by the corresponding oscillators in **Fig. 5.3.9 (b)**. The feature appearing at 1.6 eV can be assigned to the stabilization of Mn^{4+}, which in reverse indicates $Ni^{2+/3+}$ orbital to be occupied (see DOS in **Fig. 1.4.3 (b)** in **Section 1.4.1**), whereas absorption bands at higher energies account to the transitions of $Ni^{4+/3+}$ (3d) – O^{2-}

(2p) at reduced photon energies for the Mn (3d) assignments previously made for LMO by *Kim et al.*[44] and by *Rudramadevi et al.*[75] Energies of Mn (3d) band transitions in LMNO are generally lower, due to the higher binding energies of Mn^{4+}.[90] Upon electrochemical de-lithiation up to 5 V vs. Li/Li^+ the typical absorption band associated to λ-MnO_2 appears around 2.8 eV, which for LMNO accounts to the transition of Ni^{4+} (e_g) and O^{2-} (2p) in λ-$Mn_{1.5}Ni_{0.5}O_2$. Simultaneously, the absorption around 3.2 eV diminished, which is associated to the Ni^{3+}/Mn^{3+} (e_g) transitions with O^{2-} (2p) to decrease as the tetravalent charges are stabilized.[45] The absorption band shift appearing around 2.0 eV upon lithium extraction can be attributed to the Ni^{4+} (t_{2g}) electronic states evolving from lower oxidation states. The overall increase in intensity of the optical absorption in **Fig. 5.3.9 (b)** may be due to the reduced JT distortion evolving from the Ni^{4+} octahedra.[45]

Taking these observations into consideration, the first impression from cyclic voltammograms in **Fig. 5.3.9 (a)** that only the $Ni^{2+/4+}$ species are being oxidized and reduced, cannot be further supported, as the evolution of the optical signal around 3.2 eV indicates the presence of trivalent Ni^{3+}/Mn^{3+} charges in the lattice.[45,90] This is supported by the Raman spectra shown in **Fig. 5.3.8**, which indicated some oxygen deficient $LiMn_{1.5}Ni_{0.5}O_{4-\delta}$ to be present, with a cation disordered lattice of $Fd\bar{3}m$.[86,87] Although stoichiometric LMNO is known for inheriting a great resistance towards NiO and MnO formation for potentials ≥ 4.5 V, the electrochemical cycling above 4.8 V may anyway cause some lattice disordering (similar to the electrochemical activation mechanism as reported for layered Li_2MnO_3 cathodes in **Fig. 5.3.2**), dissolving oxygen coordinated at the Mn^{4+} and Li^+ cations under creation of electron holes located above the O^{2-} (2p) valence band.[27,91] This could lead to the a re-creation of active Mn^{3+} sites taking part in the redox-reactions and therefore an increased risk of MnO formation. Additionally, cycling at such high potentials may degrade the $LiPF_6$ electrolyte and its organic compounds (EC and DMC), forming an SEI layer (~3 nm) on the LMNO surface consisting of alkyl carbonates (Li-$ROCO_2$) rich in F and P, mediating the ionic diffusion and cycling stability of the cathode material.[92]

Concluding from **Fig. 5.3.9 (a)**, the evolution of the optical absorption at 2.8 eV in LMNO thin films is correlated to the accumulated charge over the galvanostatic potential sweep between 3.5 -5.0 V vs. Li/Li^+ in **Fig. 5.3.10 (a)**.

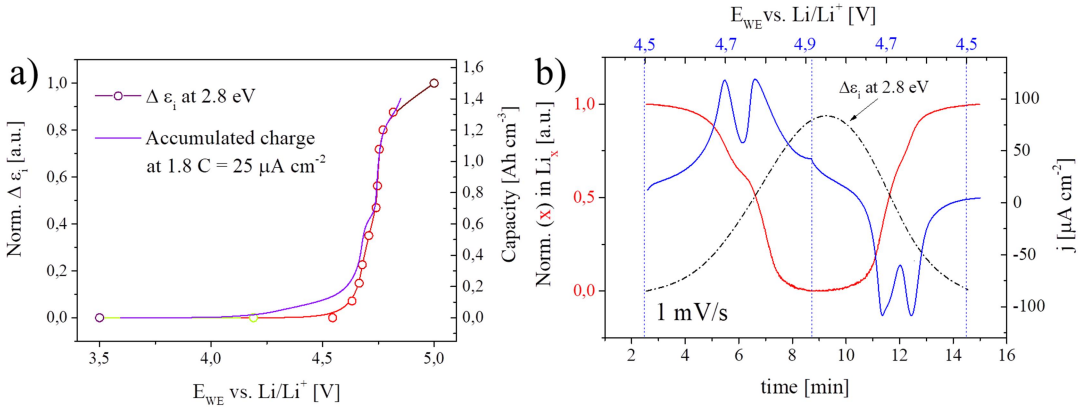

Fig. 5.3.10: Change of the normalized optical absorption at 2.8 eV during the galvanostatic potential sweep at 1.8 C and the corresponding accumulated charge in (a) obtained with monochromatic acquisition. Monitoring of the potentiostatic voltage sweep at 1 mV s^{-1} over time with the multi-wavelength acquisition is shown in (b). The Normalized change in x for $Li_xMn_{1.5}Ni_{0.5}O_4$ is extracted from the model and compared to the optical absorption extracted for every 2 min at 2.8 eV (dash dot – B-spline).

The optical absorption at 2.8 eV follows the cathodic charge in **Fig. 5.3.10 (a)** very precisely, with only a small deviation around 4.5 V vs. Li/Li^+. Hence the model created for LMNO appears to be a sufficient approximation for monitoring the SOC in the LMNO cathode thin film, as the multi-wavelength acquisition in **Fig. 5.3.10 (b)** further confirms.

The transfer of a single Li^+ ion is followed under calculation of the compositional fraction of LMNO and λ-MNO in the multi-material layer (as described for the model in **Fig. 5.3.2 (c)**), resolving in the concentration x in $Li_xMn_{1.5}Ni_{0.5}O_4$ at every 100 ms during the electrochemical cycling at 1 mV s^{-1}. As the tetra-valent oxidation state of the cationic Mn/Ni species should show the most intense absorption around 2.8 eV when $x \approx 0$, the $x \cdot Li^+$ concentration calculated from the model (red line) is correlated to the optical absorption (dashed line) at 2.8 eV in **Fig. 5.3.10 (b)**. As both show a reversed correlation to each other in good agreement with the physicochemical models, the capability of fast in-time acquisition by multi-wavelength SE is proven to give reliable results on the SOC of the cathode material.

5.4 Conclusions

Optical, non-destructive operando techniques based on Raman spectroscopy and spectroscopic ellipsometry have successfully been implemented in the study of electrochemical performances upon lithium (de-) intercalation for cathode thin films in the spinel phase.

Operando Raman spectroscopy was able to reveal the phase transformations of LMO multi-layered thin films in an aqueous environment, when passing a voltage or current through the layers, changing the lithium occupation of the spinel lattice. Hence, the appearance of various Raman active modes and their continuous change upon charge and discharge was assigned with clarity to the common spinel phases of $LiMn_2O_4$, $Li_{0.5}Mn_2O_4$ and λ-MnO_2. An unfavorable signal-to-noise ratio arises from the thin film nature itself and relative short acquisition times (magnitude of seconds) necessary for in-time tracking of changes in the vibrational modes. Therefore the current state of charge (SOC) could be followed by operando Raman spectroscopy, but still lacks in accuracy when trying to reflect the complex two-step (de-) intercalation mechanisms taking place.

In order to gain better insight in the real SOC during battery operation, operando spectroscopic ellipsometry has been established to perform during electrochemical cycling. The optical absorption of the material can be tracked at any moment, using the common, time-consuming but well-resolved monochromator acquisition (magnitude of minutes) or an innovative triggering approach at a fixed, manually definable photon energy, allowing the decrease in acquisition times below seconds. The technological equivalent to that is the multi-wavelength acquisition, enabling the simultaneous monitoring of multiple, pre-defined photon energy channels at the same time (~ 100 ms). The obtained results are converted into optical models and implemented in the frame of the Bruggeman EMA, calculating the optical absorption spectra of the material at any moment of charge. The SOC can be precisely followed, when tracing the Mn^{4+} (e_g) – O^{2-} (2p) transitions at the correlated absorption band around 2.8 eV. As new approach, the 3 V plateau of LMO vs. Li/Li^+ has been explored using operando SE, resolving features during electrochemical cycling which can be associated to a certain activation process of the layer.

In addition, the approach has been extended to high voltage electrodes by the study of the electrochemical behavior of $LiMn_{1.5}Ni_{0.5}O_4$ cathodes. Thin films prepared by RF-sputtering have been monitored under application of operando SE. With the precise information obtained on the materials optical absorption, it was possible to detect remaining trivalent cationic states in the lattice, participating in the charge and discharge processes.

The use of operando techniques is very much promising for the accurate real-time analysis of battery degradation and material performance upon operation, which has already made Raman spectroscopy a popular technique, due to its commonness and facile implementation. Spectroscopic ellipsometry has shown a great potential for future applications in the field of operando material and device analysis, as it is widely implemented, easy to transfer and maintain. Moreover, it exhibits a broad variety of possible materials to be applied (especially for transition metal oxides) and further allows for the materials to remain as close as possible to their real environment conditions. Together with its high surface and interface sensitivity, underlining its great capability in the monitoring of SEI layer properties and multi-layer solid-solid interfaces, operando SE is capable of becoming a very powerful, in-expensive and widely applicable technique in the field of lithium-ion thin film batteries.

References

(1) Liu, D.; Shadike, Z.; Lin, R.; Qian, K.; Li, H.; Li, K.; Wang, S.; Yu, Q.; Liu, M.; Ganapathy, S.; others; Qin, X.; Yang, Q.-H.; Wagemaker, M.; Kang, F.; Yang, X.-Q.; Li, B. Review of Recent Development of In Situ/Operando Characterization Techniques for Lithium Battery Research. *Adv. Mater.* **2019**, *31* (28), 1806620. https://doi.org/10.1002/adma.201806620.

(2) Zhu, Z.; Zhou, Y.; Yan, P.; Vemuri, R. S.; Xu, W.; Zhao, R.; Wang, X.; Thevuthasan, S.; Baer, D. R.; Wang, C.-M. In Situ Mass Spectrometric Determination of Molecular Structural Evolution at the Solid Electrolyte Interphase in Lithium-Ion Batteries. *Nano Lett.* **2015**, *15* (9), 6170–6176. https://doi.org/10.1021/acs.nanolett.5b02479.

(3) Mukerjee, S.; Thurston, T. R.; Jisrawi, N. M.; Yang, X. Q.; McBreen, J.; Daroux, M. L.; Xing, X. K. Structural Evolution of Li x Mn2 O 4 in Lithium-Ion Battery Cells Measured In Situ Using Synchrotron X-Ray Diffraction Techniques. *J. Electrochem. Soc.* **1998**, *145* (2), 466–472. https://doi.org/10.1149/1.1838286.

(4) Bressler, C.; Chergui, M. Ultrafast X-Ray Absorption Spectroscopy. *Chem. Rev.* **2004**, *104* (4), 1781–1812. https://doi.org/10.1021/cr0206667.

(5) Chen, Y.-C.; Chen, J.-M.; Hsu, C.-H.; Lee, J.-F.; Yeh, J.-W.; Shih, H. C. In-Situ Synchrotron X-Ray Absorption Studies of LiMn0.25Fe0.75PO4 as a Cathode Material for Lithium Ion Batteries. *Solid State Ionics* **2009**, *180* (20), 1215–1219. https://doi.org/https://doi.org/10.1016/j.ssi.2009.06.013.

(6) Robert, R.; Zeng, D.; Lanzirotti, A.; Adamson, P.; Clarke, S. J.; Grey, C. P. Scanning X-Ray Fluorescence Imaging Study of Lithium Insertion into Copper Based Oxysulfides for Li-Ion Batteries. *Chem. Mater.* **2012**, *24* (14), 2684–2691. https://doi.org/10.1021/cm3005375.

(7) Finegan, D. P.; Scheel, M.; Robinson, J. B.; Tjaden, B.; Hunt, I.; Mason, T. J.; Millichamp, J.; Di Michiel, M.; Offer, G. J.; Hinds, G.; Brett, D. J. L.; Shearing, P. R. In-Operando High-Speed Tomography of Lithium-Ion Batteries during Thermal Runaway. *Nat. Commun.* **2015**, *6*, 6924.

(8) Ding, Y.; Li, Z.-F.; Timofeeva, E. V; Segre, C. U. In Situ EXAFS-Derived Mechanism of Highly Reversible Tin Phosphide/Graphite Composite Anode for Li-Ion Batteries. *Adv. Energy Mater.* **2018**, *8* (9), 1702134. https://doi.org/10.1002/aenm.201702134.

(9) Boesenberg, U.; Fittschen, U. E. A. 2D and 3D Imaging of Li-Ion Battery Materials Using Synchrotron Radiation Sources. In *Rechargeable Batteries: Materials,*

Technologies and New Trends; Zhang, Z., Zhang, S. S., Eds.; Springer International Publishing: Cham, 2015; pp 393–418. https://doi.org/10.1007/978-3-319-15458-9_14.

(10) Lin, F.; Liu, Y.; Yu, X.; Cheng, L.; Singer, A.; Shpyrko, O. G.; Xin, H. L.; Tamura, N.; Tian, C.; Weng, T.-C.; Yang, X.-Q.; Meng, Y. S.; Nordlund, D.; Yang, W.; Doeff, M. M. Synchrotron X-Ray Analytical Techniques for Studying Materials Electrochemistry in Rechargeable Batteries. *Chem. Rev.* **2017**, *117* (21), 13123–13186. https://doi.org/10.1021/acs.chemrev.7b00007.

(11) Shearing, P.; Wu, Y.; Harris, S. J.; Brandon, N. In Situ X-Ray Spectroscopy and Imaging of Battery Materials. *Electrochem. Soc. Interface* **2011**, *20* (3), 43–47. https://doi.org/10.1149/2.F03113if.

(12) Buchberger, I.; Seidlmayer, S.; Pokharel, A.; Piana, M.; Hattendorff, J.; Kudejova, P.; Gilles, R.; Gasteiger, H. A. Aging Analysis of Graphite/LiNi1/3Mn1/3Co1/3O2 Cells Using XRD, PGAA, and AC Impedance. *J. Electrochem. Soc.* **2015**, *162* (14), A2737–A2746. https://doi.org/10.1149/2.0721514jes.

(13) Yang, X. Q.; Sun, X.; Lee, S. J.; McBreen, J.; Mukerjee, S.; Daroux, M. L.; Xing, X. K. In Situ Synchrotron X-Ray Diffraction Studies of the Phase Transitions in Li x Mn2 O 4 Cathode Materials. *Electrochem. Solid-State Lett.* **1999**, *2* (4), 157–160. https://doi.org/10.1149/1.1390768.

(14) Breitung, B.; Baumann, P.; Sommer, H.; Janek, J.; Brezesinski, T. In Situ and Operando Atomic Force Microscopy of High-Capacity Nano-Silicon Based Electrodes for Lithium-Ion Batteries. *Nanoscale* **2016**, *8* (29), 14048–14056. https://doi.org/10.1039/C6NR03575B.

(15) Yang, S.; Yan, B.; Lu, L.; Zeng, K. Grain Boundary Effects on Li-Ion Diffusion in a Li1.2Co0.13Ni0.13Mn0.54O2 Thin Film Cathode Studied by Scanning Probe Microscopy Techniques. *RSC Adv.* **2016**, *6* (96), 94000–94009. https://doi.org/10.1039/C6RA17681J.

(16) Drewett, N. E.; Aldous, I. M.; Zou, J.; Hardwick, L. J. In Situ Raman Spectroscopic Analysis of the Lithiation and Sodiation of Antimony Microparticles. *Electrochim. Acta* **2017**, *247*, 296–305. https://doi.org/https://doi.org/10.1016/j.electacta.2017.07.030.

(17) Krause, A.; Tkacheva, O.; Omar, A.; Langklotz, U.; Giebeler, L.; Dörfler, S.; Fauth, F.; Mikolajick, T.; Weber, W. M. In Situ Raman Spectroscopy on Silicon Nanowire Anodes Integrated in Lithium Ion Batteries. *J. Electrochem. Soc.* **2019**, *166* (3), A5378–A5385. https://doi.org/10.1149/2.0541903jes.

(18) Lei, J.; McLarnon, F.; Kostecki, R. In Situ Raman Microscopy of Individual LiNi0.8Co0.15Al0.05O2 Particles in a Li-Ion Battery Composite Cathode. *J. Phys. Chem. B* **2005**, *109* (2), 952–957. https://doi.org/10.1021/jp046027c.

(19) Matsui, M.; Kuwata, H.; Imanishi, N. In Operando FTIR Spectroscopy for Lithium-Ion Batteries. *Meet. Abstr.* **2014**, *MA2014-02* (4), 247.

(20) Streich, D.; Novák, P. Electrode-Electrolyte Interface Characterization of Carbon Electrodes in Li-O2 Batteries: Capabilities and Limitations of Infrared Spectroscopy. *Electrochim. Acta* **2016**, *190*, 753–757. https://doi.org/https://doi.org/10.1016/j.electacta.2015.12.061.

(21) Kosilov, V. V; Potapenko, A. V; Kirillov, S. A. Effect of Overdischarge (Overlithiation) on Electrochemical Properties of Li Mn2 O4 Samples of Different Origin. *J. Solid State Electrochem.* **2017**, *21* (11), 3269–3279. https://doi.org/10.1007/s10008-017-3671-7.

(22) Put, B.; Vereecken, P. M.; Labyedh, N.; Sepulveda, A.; Huyghebaert, C.; Radu, I. P.; Stesmans, A. High Cycling Stability and Extreme Rate Performance in Nanoscaled LiMn2O4 Thin Films. *ACS Appl. Mater. Interfaces* **2015**, *7* (40), 22413–22420. https://doi.org/10.1021/acsami.5b06386.

(23) Raju, K.; Nkosi, F. P.; Viswanathan, E.; Mathe, M. K.; Damodaran, K.; Ozoemena, K. I. Microwave-Enhanced Electrochemical Cycling Performance of the LiNi0.2Mn1.8O4 Spinel Cathode Material at Elevated Temperature. *Phys. Chem. Chem. Phys.* **2016**, *18* (18), 13074–13083. https://doi.org/10.1039/c6cp01873d.

(24) Liu, C.; Neale, Z. G.; Cao, G. Understanding Electrochemical Potentials of Cathode Materials in Rechargeable Batteries. *Mater. Today* **2016**, *19* (2), 109–123. https://doi.org/10.1016/j.mattod.2015.10.009.

(25) Susai, F. A.; Talianker, M.; Liu, J.; Paul, T.; Grinblat, Y.; Erickson, E.; Noked, M.; Burstein, L.; Frenkel, A. I.; Tsur, Y.; Markovsky, B.; Aurbach, D. Electrochemical Activation of Li2MnO3 Electrodes at 0 ◦ C and Its Impact on the Subsequent Performance at Higher Temperatures. *Materials (Basel).* **2020**, *13* (4388), 1–22.

(26) Shimoda, K.; Oishi, M.; Matsunaga, T.; Murakami, M.; Yamanaka, K.; Arai, H.; Ukyo, Y.; Uchimoto, Y.; Ohta, T.; Matsubara, E.; Ogumi, Z. Direct Observation of Layered-to-Spinel Phase Transformation in Li2MnO3 and the Spinel Structure Stabilised after the Activation Process. *J. Mater. Chem. A* **2017**, *5*, 6695–6707. https://doi.org/10.1039/C6TA11151C.

(27) Guerrini, N.; Jin, L.; Lozano, J. G.; Luo, K.; Sobkowiak, A.; Tsuruta, K.; Massel, F.;

Duda, L.; Roberts, M. R.; Bruce, P. G. Charging Mechanism of Li 2 MnO 3. *Chem. Mater.* **2020**, No. 32, 3733–3740. https://doi.org/10.1021/acs.chemmater.9b04459.

(28) Luo, Y.; Cai, W. Bin; Xing, X. K.; Scherson, D. A. In Situ, Time-Resolved Raman Spectromicrotopography of an Operating Lithium-Ion Battery. *Electrochem. Solid-State Lett.* **2004**, *7* (1), 1–5. https://doi.org/10.1149/1.1627972.

(29) Julien, C. M.; Mauger, A. In Situ Raman Analyses of Electrode Materials for Li-Ion Batteries. *AIMS Mater. Sci.* **2018**.

(30) Hy, S.; Felix; Chen, Y. H.; Liu, J. Y.; Rick, J.; Hwang, B. J. In Situ Surface Enhanced Raman Spectroscopic Studies of Solid Electrolyte Interphase Formation in Lithium Ion Battery Electrodes. *J. Power Sources* **2014**, *256*, 324–328. https://doi.org/10.1016/j.jpowsour.2014.01.092.

(31) Touzalin, T.; Joiret, S.; Maisonhaute, E.; Lucas, I. T. Capturing Electrochemical Transformations by Tip-Enhanced Raman Spectroscopy. *Curr. Opin. Electrochem.* **2017**.

(32) Slautin, B.; Alikin, D.; Rosato, D.; Pelegov, D.; Shur, V.; Kholkin, A. Local Study of Lithiation and Degradation Paths in Li Mn2 O4 Battery Cathodes: Confocal Raman Microscopy Approach. *Batteries* **2018**, *4* (2), 21.

(33) Kanoh, H.; Tang, W.; Ooi, K. In Situ Raman Spectroscopic Study on Electroinsertion of Li+ into a Pt/λ-MnO2 Electrode in Aqueous Solution. *Electrochem. Solid-State Lett.* **1998**, *1* (1), 17–19. https://doi.org/10.1149/1.1390620.

(34) Julien, C. M.; Massot, M. Lattice Vibrations of Materials for Lithium Rechargeable Batteries I. Lithium Manganese Oxides. *Mater. Sci. Eng. B Solid-State Mater. Adv. Technol.* **2003**, *100* (1), 69–78. https://doi.org/10.1016/S0921-5107(03)00077-1.

(35) Tang, S. B.; Lai, M. O.; Lu, L.; Tripathy, S. Comparative Study of LiMn 2 O 4 Thin Film Cathode Grown at High , Medium and Low Temperatures by Pulsed Laser Deposition. *J. Solid State Chem.* **2006**, *179*, 3831–3838. https://doi.org/10.1016/j.jssc.2006.08.025.

(36) Ammundsen, B.; Burns, G. R.; Islam, M. S.; Kanoh, H.; Rozière, J. Lattice Dynamics and Vibrational Spectra of Lithium Manganese Oxides: A Computer Simulation and Spectroscopic Study. *J. Phys. Chem. B* **1999**, *103* (25), 5175–5180. https://doi.org/10.1021/jp984398l.

(37) Paolone, A.; Sacchetti, A.; Corridoni, T.; Postorino, P.; Cantelli, R.; Rousse, G.; Masquelier, C. MicroRaman Spectroscopy on LiMn2O4: Warnings on Laser-Induced Thermal Decomposition. *Solid State Ionics* **2004**, *170* (1–2), 135–138.

https://doi.org/10.1016/j.ssi.2004.02.002.

(38) Bianchini, M.; Suard, E.; Croguennec, L.; Masquelier, C. Li-Rich Li1+x Mn2-x O4 Spinel Electrode Materials: An Operando Neutron Diffraction Study during Li+ Extraction/Insertion. *J. Phys. Chem. C* **2014**, *118* (45), 25947–25955.

(39) Berg, H.; Rundlöv, H.; Thomas, J. O. The LiMn2O4 to λ-MnO2 Phase Transition Studied by in Situ Neutron Diffraction. *Solid State Ionics* **2001**, *144* (1–2), 65–69. https://doi.org/10.1016/S0167-2738(01)00894-3.

(40) Baehtz, C.; Buhrmester, T.; Bramnik, N. N.; Nikolowski, K.; Ehrenberg, H. Design and Performance of an Electrochemical In-Situ Cell for High Resolution Full-Pattern X-Ray Powder Diffraction. *Solid State Ionics* **2005**, *176* (17–18), 1647–1652. https://doi.org/10.1016/j.ssi.2005.03.021.

(41) D'Ippolito, V.; Andreozzi, G. B.; Bersani, D.; Lottici, P. P. Raman Fingerprint of Chromate, Aluminate and Ferrite Spinels. *J. Raman Spectrosc.* **2015**. https://doi.org/10.1002/jrs.4764.

(42) Dokko, K.; Mohamedi, M.; Anzue, N.; Itoh, T.; Uchida, I. In Situ Raman Spectroscopic Studies of LiNix Mn2-x O4 Thin Film Cathode Materials for Lithium Ion Secondary Batteries. *J. Mater. Chem.* **2002**, *12*, 3688–3693. https://doi.org/10.1039/b206764a.

(43) Tompkins, H. G.; Irene, E. A. *Handbook of Ellipsometry*; William Andrew, 2005.

(44) Kim, K. J.; Park, Y. R. Sol-Gel Growth and Structural and Optical Investigation of Manganese-Oxide Thin Films: Structural Transformation by Zn Doping. *J. Cryst. Growth* **2004**, *270* (1–2), 162–167. https://doi.org/10.1016/j.jcrysgro.2004.06.019.

(45) Kim, K. J.; Lee, J. H. Effects of Nickel Doping on Structural and Optical Properties of Spinel Lithium Manganate Thin Films. *Solid State Commun.* **2007**, *141* (2), 99–103. https://doi.org/10.1016/j.ssc.2006.08.044.

(46) Woollam, J. A.; Snyder, P. G.; Rost, M. C. Variable Angle Spectroscopic Ellipsometry: A Non-Destructive Characterization Technique for Ultrathin and Multilayer Materials. *Thin Solid Films* **1988**, *166* (C), 317–323. https://doi.org/10.1016/0040-6090(88)90393-8.

(47) Jellison, G. E. Data Analysis for Spectroscopic Ellipsometry. *Handb. Ellipsom.* **2005**, *234*, 237–296. https://doi.org/10.1016/B978-081551499-2.50005-8.

(48) Aspens, D. E.; Theeten, J. B. Investigation of Effective-Medium Models of Microscopic Surface Roughness by Spectroscopic Ellipsometry. *Phys. Rev. B* **1979**, *20* (8), 3292–

3302.

(49) Lei, J.; Li, L.; Kostecki, R.; Muller, R.; McLarnon, F. Characterization of SEI Layers on LiMn2O4 Cathodes with In Situ Spectroscopic Ellipsometry. *J. Electrochem. Soc.* **2005**, *152* (4), A774–A777. https://doi.org/10.1149/1.1867652.

(50) McArthur, M. A.; Trussler, S.; Dahn, J. R. In Situ Investigations of SEI Layer Growth on Electrode Materials for Lithium-Ion Batteries Using Spectroscopic Ellipsometry. *J. Electrochem. Soc.* **2012**, *159* (3), A198–A207. https://doi.org/10.1149/2.004203jes.

(51) Morata, A.; Siller, V.; Chiabrera, F.; Nuñez, M.; Trocoli, R.; Stchakovsky, M.; Tarancon, A. Operando Probing of Li-Insertion into LiMn2O4 Cathodes by Spectroscopic Ellipsometry. *J. Mater. Chem. A* **2020**, 1–7.

(52) Bruggeman, D. A. G. Berechnung Verschiedener Physikalischer Konstanten von Heterogenen Substanzen. *Ann. Phys.* **1935**, *5* (24), 636–664.

(53) Berg, H.; Göransson, K.; Noläng, B.; Thomas, J. O. Electronic Structure and Stability of Li1+(x)Mn2-(x)O4 Spinels. *J. Mater. Chem.* **2000**, *10* (6), 1437–1441. https://doi.org/10.1039/a908746j.

(54) Fehse, M.; Trócoli, R.; Ventosa, E.; Hernández, E.; Sepúlveda, A.; Morata, A.; Tarancón, A. Ultrafast Dischargeable LiMn2O4 Thin-Film Electrodes with Pseudocapacitive Properties for Microbatteries. *ACS Appl. Mater. Interfaces* **2017**, *9* (6), 5295–5301.

(55) Trócoli, R.; Morata, A.; Fehse, M.; Stchakovsky, M.; Sepúlveda, A.; Tarancón, A. High Specific Power Dual-Metal-Ion Rechargeable Microbatteries Based on Li Mn2 O4 and Zinc for Miniaturized Applications. *ACS Appl. Mater. Interfaces* **2017**, *9* (38), 32713–32719. https://doi.org/10.1021/acsami.7b08883.

(56) Tang, W.; Hou, Y.; Wang, F.; Liu, L.; Wu, Y.; Zhu, K. Li Mn2 O4 Nanotube as Cathode Material of Second-Level Charge Capability for Aqueous Rechargeable Batteries. *Nano Lett.* **2013**, *13* (5), 2036–2040.

(57) Tang, W.; Liu, L.; Zhu, Y.; Sun, H.; Wu, Y.; Zhu, K. An Aqueous Rechargeable Lithium Battery of Excellent Rate Capability Based on a Nanocomposite of MoO3 Coated with PPy and LiMn2O4. *Energy Environ. Sci.* **2012**, *5* (5), 6909–6913. https://doi.org/10.1039/C2EE21294C.

(58) Jiao, F.; Bao, J.; Hill, A. H.; Bruce, P. G. Synthesis of Ordered Mesoporous Li–Mn–O Spinel as a Positive Electrode for Rechargeable Lithium Batteries. *Angew. Chemie Int. Ed.* **2008**, *47* (50), 9711–9716. https://doi.org/10.1002/anie.200803431.

(59) Young, M. J.; Schnabel, H.-D.; Holder, A. M.; George, S. M.; Musgrave, C. B. Band Diagram and Rate Analysis of Thin Film Spinel Li Mn2 O4 Formed by Electrochemical Conversion of ALD-Grown MnO. *Adv. Funct. Mater.* **2016**, *26* (43), 7895–7907.

(60) Okubo, M.; Mizuno, Y.; Yamada, H.; Kim, J.; Hosono, E.; Zhou, H.; Kudo, T.; Honma, I. Fast Li-Ion Insertion into Nanosized LiMn2O4 without Domain Boundaries. *ACS Nano* **2010**, *4* (2), 741–752. https://doi.org/10.1021/nn9012065.

(61) Quan, Z.; Ohguchi, S.; Kawase, M.; Tanimura, H.; Sonoyama, N. Preparation of Nanocrystalline LiMn2O4 Thin Film by Electrodeposition Method and Its Electrochemical Performance for Lithium Battery. *J. Power Sources* **2013**, *244*, 375–381. https://doi.org/10.1016/j.jpowsour.2012.12.087.

(62) Zhao, Y. F.; Lu, B.; Zhang, J. Lithium Diffusion and Stress in a Polycrystalline Film Electrode. *Acta Mech. Solida Sin.* **2018**, *31* (3), 290–309. https://doi.org/10.1007/s10338-018-0018-6.

(63) Kuwata, N.; Nakane, M.; Miyazaki, T.; Mitsuishi, K.; Kawamura, J. Lithium Diffusion Coefficient in LiMn2O4 Thin Films Measured by Secondary Ion Mass Spectrometry with Ion-Exchange Method. *Solid State Ionics* **2018**, *320*, 266–271. https://doi.org/10.1016/j.ssi.2018.03.012.

(64) Shu, D.; Chung, K. Y.; Cho, W. Il; Kim, K.-B. Electrochemical Investigations on Electrostatic Spray Deposited LiMn2O4 Films. *J. Power Sources* **2003**, *114* (2), 253–263. https://doi.org/10.1016/S0378-7753(02)00602-X.

(65) Nishizawa, M.; Uchiyama, T.; Dokko, K.; Yamada, K.; Matsue, T.; Uchida, I. Electrochemical Studies of Spinel LiMn2O4 Films Prepared by Electrostatic Spray Deposition. *Bull. Chem. Soc. Jpn.* **1998**, *71* (8), 2011–2015. https://doi.org/10.1246/bcsj.71.2011.

(66) Xie, J.; Tanaka, T.; Imanishi, N.; Matsumura, T.; Hirano, A.; Takeda, Y.; Yamamoto, O. Li-Ion Transport Kinetics in LiMn2O4 Thin Films Prepared by Radio Frequency Magnetron Sputtering. *J. Power Sources* **2008**, *180* (1), 576–581. https://doi.org/10.1016/j.jpowsour.2008.02.049.

(67) Okumura, T.; Fukutsuka, T.; Uchimoto, Y.; Sakai, N.; Yamaji, K.; Yokokawa, H. Determination of Lithium Ion Diffusion in Lithium-Manganese-Oxide-Spinel Thin Films by Secondary-Ion Mass Spectrometry. *J. Power Sources* **2009**, *189* (1), 643–645. https://doi.org/10.1016/j.jpowsour.2008.09.043.

(68) Striebel, K. A.; Deng, C. Z.; Wen, S. J.; Cairns, E. J. Electrochemical Behavior of

LiMn2 O 4 and LiCoO2 Thin Films Produced with Pulsed Laser Deposition. *J. Electrochem. Soc.* **1996**, *143* (6), 1821–1827. https://doi.org/10.1149/1.1836910.

(69) Julien, C.; Haro-Poniatowski, E.; Camacho-Lopez, M. A.; Escobar-Alarcon, L.; Jimenez-Jarquin, J. Growth of LiMn2O4 Thin Films by Pulsed-Laser Deposition and Their Electrochemical Properties in Lithium Microbatteries. *Mater. Sci. Eng. B Solid-State Mater. Adv. Technol.* **2000**, *72* (1), 36–46. https://doi.org/10.1016/S0921-5107(99)00598-X.

(70) Tang, S. B.; Lai, M. O.; Lu, L. Study on Li+-Ion Diffusion in Nano-Crystalline LiMn2O4 Thin Film Cathode Grown by Pulsed Laser Deposition Using CV, EIS and PITT Techniques. *Mater. Chem. Phys.* **2008**, *111* (1), 149–153. https://doi.org/https://doi.org/10.1016/j.matchemphys.2008.03.041.

(71) Takai, S.; Yoshioka, K.; Iikura, H.; Matsubayashi, M.; Yao, T.; Esaka, T. Tracer Diffusion Coefficients of Lithium Ion in LiMn2O 4 Measured by Neutron Radiography. *Solid State Ionics* **2014**, *256*, 93–96. https://doi.org/10.1016/j.ssi.2014.01.013.

(72) Jung, J. H.; Kim, K. H.; Eom, D. J.; Noh, T. W.; Choi, E. J.; Yu, J.; Kwon, Y. S.; Chung, Y. Determination of Electronic Band Structures of CaMnO3 and LaMnO3 Using Optical-Conductivity Analyses. *Phys. Rev. B* **1997**, *55* (23), 15489–15493.

(73) Sherman, D. M. The Electronic Structures of Manganese Oxide Minerals. *Amerian Mineral.* **1984**, *69*, 788–799.

(74) Chakradhar, R. P. S.; Yasoda, B.; Rao, J. L.; Gopal, N. O. EPR and Optical Studies of Mn 2 + Ions in Li 2 O – Na 2 O – B 2 O 3 Glasses – An Evidence of Mixed Alkali Effect. *J. Non. Cryst. Solids* **2007**, *353*, 2355–2362. https://doi.org/10.1016/j.jnoncrysol.2007.04.002.

(75) Rudramadevi, B. H.; Buddhudu, S. Spectral Properties of Cu2+, Ni2+, Co2+ , Mn2+ & Cr3+ Ions Doped B2 3-BaO-LiF Glasses. *Ferroelectr. Lett.* **2009**, *36* (3–4), 82–91. https://doi.org/10.1080/07315170903152763.

(76) Halder, O.; Satpati, B.; Rajput, P.; Mohapatra, N.; Jha, S. N.; Suffczynski, J.; Pacuski, W.; Rath, S. Light Emitting Spin Active Electronic States in Ultra-Thin Mn Doped CdSe Layered Nanosheets. *Sci. Rep.* **2019**, *9* (1804). https://doi.org/10.1038/s41598-019-38974-0.

(77) Marco, A. T.; Dantas, N. O.; Cano, N. F.; Rastrello, L. R.; Guimar, E. V; Lourenço, S. A.; Ricardo, S. Effect of Thermal Annealing and Sp-d Exchange Interaction in the Optical Properties of Mn 2+ -Doped PbS Nanocrystals Embedded in a Glass Matrix. *J.*

Lumin. **2020**, *222* (117144). https://doi.org/10.1016/j.jlumin.2020.117144.

(78) Tamilarasan, S.; Laha, S.; Natarajan, S.; Gopalakrishnan, J. Li2MnO3: A Rare Red-Coloured Manganese(Iv) Oxide Exhibiting Tunable Red-Yellow-Green Emission. *J. Mater. Chem. C* **2015**, *3* (18), 4794–4800. https://doi.org/10.1039/c5tc00616c.

(79) Amalraj, S. F.; Burlaka, L.; Julien, C. M.; Mauger, A.; Kovacheva, D.; Talianker, M.; Markovsky, B.; Aurbach, D. Phase Transitions in Li2 Mn O3 Electrodes at Various States-of-Charge. *Electrochim. Acta* **2014**, *123*, 395–404. https://doi.org/10.1016/j.electacta.2014.01.051.

(80) Saroha, R.; Gupta, A.; Panwar, A. K. Electrochemical Performances of Li-Rich Layered-Layered Li 2 MnO 3 - LiMnO 2 Solid Solutions as Cathode Material for Lithium-Ion Batteries. *J. Alloys Compd.* **2017**, *696*, 580–589. https://doi.org/10.1016/j.jallcom.2016.11.199.

(81) Paulraj, V.; Swami, B.; Bharathi, K. K. Growth Behavior, Work Function, and Band Gap Tuning of Nanocrystalline LiMn2O4 Thin Films Growth Behavior, Work Function, and Band Gap Tuning of Nanocrystalline LiMn 2 O 4 Thin Films. *Appl. Phys. Lett.* **2019**, *115* (093901). https://doi.org/10.1063/1.5109355.

(82) Ohzuku, T.; Kitagawa, M.; Hirai, T. Electrochemistry of Manganese Dioxide in Lithium Nonaqueous Cell: III. X-Ray Diffractional Study on the Reduction of Electrolytic Manganese Dioxide. *J. Electrochem. Soc.* **1989**, *136* (11), 3169–3174. https://doi.org/10.1149/1.2096421.

(83) Van Der Ven, A.; Marianetti, C.; Morgan, D.; Ceder, G. Phase Transformations and Volume Changes in Spinel LixMn2O4. *Solid State Ionics* **2000**, *135* (1–4), 21–32. https://doi.org/10.1016/S0167-2738(00)00326-X.

(84) Hallot, M.; Demortière, A.; Roussel, P.; Lethien, C. Sputtered Li Mn1.5 Ni0.5 O4 Thin Films for Li-Ion Micro-Batteries with High Energy and Rate Capabilities. *Energy Storage Mater.* **2018**, *15* (August), 396–406. https://doi.org/10.1016/j.ensm.2018.08.012.

(85) Manthiram, A.; Chemelewski, K.; Lee, E. A Perspective on the High-Voltage Li Mn1.5 Ni0.5 O4 Spinel Cathode for Lithium-Ion Batteries. *Energy Environ. Sci.* **2014**, *7*, 1339–1350. https://doi.org/10.1039/c3ee42981d.

(86) Samarasingha, P. B.; Andersen, N. H.; Sørby, M. H.; Kumar, S.; Nilsen, O.; Fjellvåg, H. Neutron Diffraction and Raman Analysis of Li Mn1.5 Ni0.5 O4 Spinelt Type Oxides for Use as Lithium Ion Battery Cathode and Their Capacity Enhancements. *Solid State Ionics* **2016**, *284*, 28–36. https://doi.org/10.1016/j.ssi.2015.11.018.

(87) Kim, J.-H.; Myung, S.-T.; Yoon, C. S.; Kang, S. G.; Sun, Y.-K. Comparative Study of Li Ni0.5 Mn 1.5 O4-d and Li Ni0.5 Mn1.5 O4 Cathodes Having Two Crystallographic Structures : Fd-3m and P4(3)32. *Chem. Mater.* **2004**, *16*, 906–914.

(88) Zhong, Q.; Bonakdarpour, A.; Zhang, M.; Gao, Y.; Dahn, J. R. Synthesis and Electrochemistry of Li Nix Mn2-x O4. *J. Electrochem. Soc.* **1997**, *144* (1), 205–213.

(89) Sanad, M. M. S.; Abdellatif, H. A.; Elnaggar, E. M.; El-Kady, G. M.; Rashad, M. M. Understanding Structural, Optical, Magnetic and Electrical Performances of Fe- or Co-Substituted Spinel Li Mn1.5 Ni0.5 O4 Cathode Materials. *Appl. Phys. A* **2019**, *125* (139), 1–10. https://doi.org/10.1007/s00339-019-2445-8.

(90) Zhou, W.; Wu, J.; Ouyang, C.; Gao, Y.; Xu, X.; Huang, Z. Optical Properties of Mn-Co-Ni-O Thin Films Prepared by Radio Frequency Sputtering Deposition. *J. Appl. Phys.* **2014**, *114* (093512), 1–6. https://doi.org/10.1063/1.4867439.

(91) Luo, K.; Roberts, M. R.; Hao, R.; Guerrini, N.; Pickup, D. M.; Liu, Y.; Edström, K.; Guo, J.; Chadwick, A. V; Duda, L. C.; Bruce, P. G. Charge-Compensation in 3d-Transition-Metal-Oxide Intercalation Cathodes through the Generation of Localized Electron Holes on Oxygen. *Nat. Chem.* **2016**, *8* (7), 684–691. https://doi.org/10.1038/nchem.2471.

(92) Browning, J. F.; Baggetto, L.; Jungjohann, K. L.; Wang, Y.; Tenhaeff, W. E.; Keum, J. K.; Wood, D. L.; Veith, G. M. In Situ Determination of the Liquid/Solid Interface Thickness and Composition for the Li Ion Cathode LiMn1.5Ni0.5O4. *ACS Appl. Mater. Interfaces* **2014**.

6. Conclusions of the thesis

This thesis has been devoted to the fabrication of all-solid-state thin film battery (TFB) components and their operando optical characterization for a better understanding of lithium-ion migration and reaction kinetics. Three main topics have been derived concerning (i) the synthesis of a solid-state electrolyte thin film of $Li_{1+x}Al_xTi_{2-x}(PO_4)_3$ (LATP) for the application in large-area PLD and investigations on the role of microstructure in the ionic conduction mechanism, (ii) the deposition of spinel intercalation materials by PLD as suitable electrodes in TFBs and their electrochemical characterization, and (iii) the operando probing of lithium (de-) intercalation using facile optical spectroscopic methods for deeper insight in material transitions during device operation. Most relevant results are summarized in the following.

- **$Li_{1+x}Al_xTi_{2-x}(PO_4)_3$ glass-ceramics as thin film solid-state electrolyte:** Dense, nano-crystalline LATP thin films of good phase purity, high stability in ambient and low surface roughness were successfully deposited by large-area PLD, from a target composed of $x \approx 0.5$. Tuning of the partial background gas pressure has led to the optimization of electrochemical performances for as-deposited and annealed thin films. This optimization of the LATP deposition by PLD and the subsequent electrochemical characterization represent the first time report on this particular. Characteristic achievements namely resulted in:

    - Ionic conductivities of ~ 10^{-6} S cm^{-1} and activation energies about 0.58 eV have been reached for as-deposited thin films, comparable with the state-of-the art in TFBs, e.g. LiPON compounds.

    - Annealing with a minimum of 800 ºC has shown to significantly increase the ionic conductivity of thin films, with values close to the bulk conductivity of LATP ~ 10^{-4} S cm^{-1} and activation energies of 0.37 eV.

    - Contact between nano-crystallites improved upon heat treatment with the formation of an ion conductive intergranular glassy matrix, having a great impact on a better layer densification, resulting in advanced lithium-ion mobilities.

- E**lectrochemical performance of spinel intercalation materials deposited by multi-layer PLD approach:** The co-deposition of two targets to compensate for volatile lithium allows high flexibility and increased precision in the study of material compositions and structures evolving from different ablation pulse ratios in the PLD. Electrochemical performances have been studied for:

    - *$LiMn_2O_4$ (LMO) thin films.* Thickness, crystallinity and specific cathode capacity seem to be directly correlated. Potentiostatic voltage sweep over the complete electrochemical potential window (2.0 – 4.5 V vs. Li/Li^+) revealed a certain layer activation. The capacity retention and cycling stability for the extended potential window are high, with only 30 % loss over 100 cycles and rates as high as 167 C.

    - *$Li_4Ti_5O_{12}$ (LTO) thin films.* Specific capacities and lithium content are directly correlated, achieving extraordinary high discharge capacities of 1080 mAh cm^{-3} when galvanostatic cycling is carried out between 0.3 – 3.5 V vs. Li/Li^+ at 0.5 C. As hypothesis, the presence of titania secondary phases may create interband transitions, lowering electronic band gaps, but also increase the available lithium storage capacity.

- **Operando probing of lithium-ion migration in thin films:** Both Raman spectroscopy and Spectroscopic Ellipsometry (SE) are capable of real-time monitoring phase transitions and the state of charge (SOC) in intercalation material based thin films. Specific setup and methodology for operando measurements were developed during the thesis. In the particular case of operando SE, the method was proposed here for the first time for application in lithium ion (de-) intercalation studies. Details on the achievements are as follows:

    - Operando Raman spectroscopy allows for real-time observations in phase transitions upon (de-) lithiation. However, a lack of accuracy is observed when it comes to precise monitoring of the real SOC.

    - Operando Spectroscopic Ellipsometry was demonstrated to be a powerful technique for determining the SOC in real-time, given its highly accurate probing of lithium-ion occupancy by changes in the

materials electronic band structure. Moreover, multi-wavelength analysis allows a complete investigation of the transient phenomena, with an acquisition time in the order of hundreds of milliseconds.

- Lithium intercalation and extraction for spinel LMO in its full potential region was directly connected to changes in the optical absorption assigned to the $Mn^{3+/4+}$ transitions.

- $LiMn_{1.5}Ni_{0.5}O_4$ (LMNO) sputtered cathode thin films were proven to consist of disordered cubic $Fd\bar{3}m$ with a slightly off-stoichiometric cation order. The presence of trivalent charges in the redox reactions was verified by operando SE and gave a good probing of the SOC.

- Minimal changes in the thickness, on the range of few nanometers, were extracted from optical models and gave tendencies possibly correlated to lattice volume changes upon lithium (de-) intercalation or the formation of solid-electrolyte interphases (SEI). Thickness monitoring is presented as a powerful technique for analysis of SOC and mechanical matching of multi-layer devices in operando.

As concluding remark for future investigations, LATP thin films appear to greatly profit from the stabilization of an amorphous interface at the grain boundaries, which can be tailored with precise control of the segregating compounds. The glass-ceramic nature of NASICON-like compounds allows the combination of amorphous and crystalline material properties, which in thin film shape holds promising capabilities in the application of TFBs. Despite the electrochemical window limitations of LATP as an electrolyte, this material is a promising candidate for protective coatings of more atmosphere sensitive materials.

Future electrochemical characterization of LMO and LTO multi-layered thin films should be extended to their full stability windows, providing much higher specific capacities. Furthermore, the possibility of nano-size effects providing extraordinary high specific capacities, high rate capabilities and stable capacity retention need deeper understanding. The fabrication of full all-solid-state batteries in thin film form is expected on the basis of this thesis.

The special sensitivity to surfaces and interfaces, together with fast acquisition times of 100 ms, relatively low cost and facile implementation, should pave the way for operando SE to become a popular probing technique for battery characterization upon device operation. Hence future investigations may provide a better understanding of the optical transitions upon device operation and give deeper insight on the nature of buried solid-solid interfaces in a non-destructive manner.

Scientific contributions

Peer reviewed articles:

(1) Morata, A., Siller, V., Chiabrera, F., Nuñez, M., Trocoli, R., Stchakovsky, M., & Tarancón, A. (2020). Operando probing of Li-insertion into $LiMn_2O_4$ cathodes by spectroscopic ellipsometry. *Journal of Materials Chemistry A*.

(2) Erinmwingbovo, C., Siller, V., Nuñez, M., Trócoli, R., Brogioli, D., Morata, A., & La Mantia, F. (2020). Dynamic impedance spectroscopy of $LiMn_2O_4$ thin films made by multi-layer pulsed laser deposition. *Electrochimica Acta*, *331*, 135385.

Contributions in conferences:

- *Oral presentation:*

(1) Siller, V., Morata, A., Chiabrera, F., Stchakovsky, M., Tarancón, A. (2019). In-operando studies of electrochemical evolution of thin film LMO spinel cathodes by means of spectroscopic ellipsometry. Joint IEEE ISAF/EMF/ICE/IWPM/PFM meeting (f^2cPi^2 -Lausanne 2019)